Identifying key features for improving activity and durability of metal-free and non-precious-metal catalysts for the oxygen reduction reaction

PhD Thesis

Carlota Domínguez Fernández

•

Supervised by

Dr. Francisco José Pérez Alonso
Dr. Sergio Rojas Muñoz

•

Grupo de Energía y Química Sostenibles
Instituto de Catálisis y Petroleoquímica (ICP)
Consejo Superior de Investigaciones Científicas (CSIC)

•

Programa de Doctorado en Electroquímica. Ciencia y Tecnología.
Departamento de Química Física Aplicada
Facultad de Ciencias
Universidad Autónoma de Madrid (UAM)

•

2016

Identifying key features for improving activity and durability of metal-free and non-precious-metal catalysts for the oxygen reduction reaction

Dissertation submitted to obtain the Ph. D. Degree by

Carlota Domínguez Fernández

Supervised by

Dr. Francisco José Pérez Alonso
Dr. Sergio Rojas Muñoz

Grupo de Energía y Química Sostenibles
Instituto de Catálisis y Petroleoquímica (ICP)
Consejo Superior de Investigaciones Científicas (CSIC)

•

Programa de Doctorado en Electroquímica. Ciencia y Tecnología.
Departamento de Química Física Aplicada
Facultad de Ciencias
Universidad Autónoma de Madrid (UAM)

•

2016

Take the time, look around you
And the world will be better

Agradecimientos

Después de estos años ha llegado el momento de presentar esta tesis y agradecer a todos los que me han acompañado durante este tiempo, su apoyo y sus consejos.

Gracias en especial a las personas que han ayudado a que este trabajo vea la luz, a Paco por sus explicaciones, sus consejos, sus bromas, gracias por enseñarme electroquímica, por ser mi amigo y por estar siempre ahí. Gracias a Sergio por darme la oportunidad de hacer este trabajo, por intentar enseñarme que lo importante es lo que sale bien y no lo que sale mal, por sus consejos, sus bromas, su dedicación. Gracias a los dos por todo lo que me habéis enseñado estos años y por los buenos momentos que he disfrutado con vosotros.

Gracias a Gofuen por alegrarme cada mañana con sus palabras y sus chistes malos, por estar siempre dispuesto a ayudarme en lo que sea y por nunca dejar de sorprenderme. Gracias a Miguel por sus explicaciones, sus ideas constantes y por la magia. Gracias a Jorge por animar el laboratorio con su buen humor infinito y por nuestras clases de baile. Gracias a María Retuerto por estar siempre dispuesta a ayudarme y enseñarme nuevas cosas. Gracias a María Roca por ser mi compañera de viajes y por estar siempre dispuesta a ayudarme.

Gracias a mis compañeros de comidas, Dalia, Gema, Inma, Noelia A., Noelia M., Fernando, María José, Mayka, Erika, Marta, Cristina gracias por compartir tantos momentos de tuppers y risas.

Gracias al grupo de la Autónoma por abrirme sus puertas a Pilar Ocón, Manu, Mikel y a Ricardo por sus días de cotilleos y trabajo.

Gracias a mis amigos en Madrid, con los que he compartido tantas cervezas, comidas y viajes y que han conseguido hacer de esta ciudad mi nueva casa, gracias Rubén, Gonzalo, Gelines y Eduardo. Gracias a toda la

gente maravillosa que he conocido aquí, mis compañeros de master, mis compañeras de piso Eli y Lucía, a los amigos de siempre que me he reencontrado Tara, Fresa, Antón, Carmen, Jurjo,...

Gracias a los amigos de siempre María, Fely, Vero, José, Antón, Brais, Manso, Úrsula, Miguel, Héctor, Tato, María de Peré, Jéssica,... gracias por hacer que cada vuelta a casa sea como si no pasase el tiempo. Gracias a mis grandes amigas Mónica y Vanessa por nuestras comidas y cotilleos.

E sobre todo gracias a miña familia, os meus pais por ensinarme que podo facer o queira, que o importante é que me guste, por anímame a ir a todas partes e seguir aprendendo e por intentar entender o que fago aínda que non sempre teña paciencia para explicárvo-lo. Gracias a Celtia por ser a primeira en escoitar as miñas charlas sobre pilas de hidróxeno e por estar sempre ahí.

Y por último no podía olvidarme de la persona que mejor me ha entendido y más me ha aguantado durante este tiempo. *Graciñas* Raúl, por hacer que contigo me olvide de todo, por hacerme reír siempre y por estar a mi lado.

Abstract

The exponential increase in the energy consumption due to the economic and technological progress is leading to a high increment in the greenhouse gas emissions, resulting in severe climate changes. This is because the current energy model is based upon the use (combustion) of fossil sources, such as coal, oil and natural gas. In addition, since the amount of fossil sources is limited, is leading to an increased risk of geopolitical conflicts as nations attempt to secure energy resources.

The transformation of the energy sector goes through the increment in the use of renewable energies for the power generation and the decarbonisation of the road transport sector. Nowadays, the transition from combustion energy conversion technologies to clean technologies is still a challenge. To do so, fuel cells and specially proton exchange membrane fuel cells (PEMFCs) are being named to play a key role in transportation and portable devices sectors. For the time being, economic and technological drawbacks have slowed down their implementation at the commercial level. In the actual state-of-the-art of these devices, Pt based catalysts are used in both the anode and the cathode electrodes of PEMFCs. As a consequence, around half of the cost of a fuel cell stack accounts to the use of Pt-based catalysts, especially in the cathode electrode where the oxygen reduction reaction (ORR) takes place. However, due to the sluggish kinetics of the ORR, decreasing Pt loading in the cathode electrode results in severe power density losses. An approach to achieve fuel cell devices economically competitive, goes through to the replacement of Pt (and other Pt-group-metals, PGM) altogether from the cathode electrode of fuel cells with non-expensive, more abundant non-precious metals catalysts (NPMCs). Although NPMCs have intrinsic slower kinetics for the ORR than Pt-based catalyst, their performance can be offset by the use of higher amounts of catalyst without serious

economic consequences.

The present thesis is focused on the study of different Pt-free catalysts for the ORR in acid and alkaline electrolytes. Different types of noble metal-free catalysts have been prepared, *e.g.*, nitrogen/carbon or nitrogen/sulfur/carbon composites, and NPMCs based mainly on iron/nitrogen/carbon composites. Amongst other features, the effect of the nature of the nitrogen, carbon and metal-containing precursors, the synthetic route and their repercussion for the ORR has been studied in this thesis.

The catalysts have been thoroughly characterized by using a battery of complementary techniques including elemental analysis, X-ray diffraction (XRD), X-ray photoelectron spectroscopy, N_2 adsorption-desorption isotherms, X-ray absorption (XANES and EXAFS). The characterization data have been used to elucidate catalyst activity-structure relationships which, in turn, lead to a rational designing of NPMCs. The electrochemical studies to determine the ORR activity of the catalysts have been carried out by means of the cyclic voltammetry technique using a rotating ring disk electrode (RRDE). *In situ* techniques, as electrochemical cell coupled to infrared spectroscopy (EC-SPAIRS), were also employed to establish the mechanism of catalyst degradation during the ORR.

First, this thesis addressed the effect of N-doping of carbon nanotubes (CNTs) in **paper III**. The aim of this work was to understand the relationship between the amount of defects created in CNTs via mechano-chemical treatments and the incorporation of N into the carbon network. In addition, this work studied the effect of N-doping for the ORR activity of the composites N/CNT.

Specifically, N was incorporated onto the treated-CNTs by successive ballmilling of a mixture of CNTs and urea as the N precursor followed by a thermal treatment in a N_2 flow at 800 ^{o}C. The results obtained showed that CNT structure remains stable for ballmilling periods shorter than 48 h. By contrary, subjecting CNTs to longer ballmilling periods results in the collapse of the nanotubes leading to a carbonaceous material composed by short CNTs and amorphous microporous carbon. The incorporation of N is only moderate for the CNTs subjected to ballmilling periods up to 48 h increasing significantly when longer ballmilling treatments are employed. The results obtained in this work showed that the N/CNTs are active for the ORR, both in acid and alkaline electrolytes. The N/CNTs catalysts recorded

after longer ballmilling treatments were the more active ones for the ORR in acid electrolyte. Surprisingly, the N/CNTs catalyst contained very little amount of Fe surface species probably incorporated during the ballmilling step. The effect of the presence of such residual Fe species for the ORR was elucidated/discussed by using NaSCN to poisoning the iron-containing active sites. These results concluded that the participation of these Fe species for the total ORR activity is only marginal.

The results prove that N-doped CNTs are active catalysts for the ORR, although the generation of micropores results in more active catalysts for the ORR.

The activity of the N-doped carbon nanotubes can be enhanced by the co-doping of nitrogen and sulfur, especially in alkaline electrolytes. This thesis studies in **paper IV**, the incorporation of N and S into CNTs. In order to compare accurately the effect of the incorporation of S and N on CNTs, thiourea was used as the source of N and S. The results were compared with that of a N/CNT prepared with urea. The use of thiourea as the S and N precursor results in a greater distortion of the graphitic structure. In addition, the incorporation of N is promoted by the presence of S during the synthesis. Thus, the N content of the catalysts prepared with thiourea is twofold higher than that of the catalysts prepared with urea. The incorporation of N and S takes place in defect sites in the C-C network of CNTs, especially in amorphous carbon. The results clearly showed that the ORR activity of (S)/N/CNT catalysts increases with the increasing surface N content in the catalysts, both in acid and in alkaline media. The promotional effect of S is more evident in alkaline medium.

On the other hand, the incorporation of transition metals to the nitrogen/carbon composites, results in highly active catalysts for the ORR. In the absence of consensus about the nature of the transition metal for the ORR, this thesis addressed the study of the influence of transition metals, such as Fe, Co or Mn in NPMCs, for the ORR in **paper I**. Fe, Co or Mn containing NPMCs were prepared with similar N and transition metal loadings by the wet-impregnation of the precursors over the carbon matrix. This work established an activity sequence of Fe $>$ Co $>$ Mn for the final catalysts prepared. The results obtained in this thesis indicate that the activity of NPMCs is dominated by the nature of the transition metal, and that Fe renders more active catalysts than Co and Mn. Moreover, the study of the

different stages of catalyst preparation showed that catalysts are only active and stable in the ORR in acid medium after the pyrolysis step which leads to the incorporation of the transition metal along with the creation of graphitic-N groups.

Once the iron-based catalysts were demonstrated as the most active for the ORR, other approaches for the preparation of these NPMCs were explored. The use of a mechano-chemical method for the synthesis of Fe/N/C catalysts was reported to lead very active ORR catalysts in **paper II**. In this work the influence of anion and cation adsorption for the ORR with Fe-based electrocatalysts in different acid and basic electrolytes was investigated. The results showed that the performance of Fe/N/C for the ORR is affected by the pH of the electrolyte but not by the counterion present in the electrolyte. Higher ORR activities were recorded in alkaline electrolytes. Furthermore, if acid treatments are used during catalyst preparation, a fraction of iron is removed from the catalyst and anions such as sulphates are adsorbed onto the active sites resulting in a severe decrease of the ORR performance. The effect of the sulphates from the acid leaching was also addressed, studying the nature of the interaction between the adsorbed sulphates and the catalyst by DRIFT spectroscopy at different temperatures. The results obtained indicate that sulphates are chemically bonded to the active sites rather than physically adsorbed thus producing a simply blockage of the micropores where active sites are hosted.

The nature of the carbon matrix (C) in Fe/N/C was addressed in a further paper. Thus, Fe/N/C catalysts were prepared using different carbon matrixes, e.g., active carbon (AC), carbon nanotubes (CNT) and graphene (G). This study has provided useful information about the possible active Fe-N_x moieties formed during the synthesis and the degradation mechanism during ORR of this type of catalysts (see **paper VI**). The nature of the iron species formed in Fe/N/AC, Fe/N/CNT and Fe/N/G was thoroughly studied by different characterization techniques such as X-ray absorption spectroscopy among others. EXAFS spectra suggested that the fraction of Fe-N_x ensembles varies with the nature of the carbon matrix following the order Fe/N/G > Fe/N/CNT > Fe/N/AC. Nevertheless, EXAFS indicates that the Fe_3C is the most abundant iron species in the catalysts. Iron carbides, however, were not detected by XPS, indicating that they are encapsulated within the carbon matrix rather than at the surface of the catalysts. Fe/N/G

is the most active and durable catalyst for the ORR in the series showing 3.1 $A \cdot g^{-1}$ at 0.9 V *vs.* RHE in alkaline electrolyte and excellent stability (10% loss mass activity) after recording 3000 consecutive cycles up to 1.4 V. These observations lead to the conclusion that the activity and durability of Fe/N/C increases with the use of more graphitic carbon materials such as carbon nanotubes or graphene.

In order to understand the degradation mechanism during the ORR the performance of the catalysts was monitored *in situ* with EC-SPAIRS. The obtained results clearly show that the oxidation of the carbon matrix to CO_2 is responsible for the loss of activity and that both graphene and CNT are more stable than AC towards oxidation thus rendering more durable catalyst.

In view of the importance of the Fe-N_x moieties as the species responsible of the catalytic activity, a systematic study about the influence of the relative amounts of N and C precursors used during the synthesis of Fe/N/-Graphene catalysts and the influence for the ORR activity is presented in **paper V**. The characterization results showed that the N/C ratio in the precursor mixture used for the preparation of Fe/N/Graphene catalysts has a strong influence on their textural properties, elemental composition and nature of the surface and bulk phases in the catalysts. As in previous studies of this type of materials, Fe-N_x moieties are the most abundant species at the surface of the Fe/N/Graphene catalysts which are the active sites for the ORR. Increasing the N/C ratio used for the synthesis of the N/Graphene composites results in materials with lower BET surface areas and as a consequence with less accessible Fe-N_x sites. Thus, the adequate choice of the N/C atomic ratio of precursors to prepare Fe/N/Graphene based materials is crucial to obtain electrocatalysts with an optimal amount of accessible Fe-N_x moieties.

Resumen

El aumento exponencial en el consumo de energía debido al actual progreso económico y tecnológico está dando lugar a un importante incremento en las emisiones de gases de efecto invernadero, produciendo graves cambios climáticos. Este efecto está causado por el actual modelo energético basado en el uso (combustión) de fuentes de tipo fósil, como carbón, petróleo y gas natural. Además, debido al origen limitado de este tipo de fuentes fósiles se está produciendo un aumento en el número de conflictos geopolíticos con el fin de intentar asegurar estas fuentes de energía.

La transformación del sector energético actual pasa por un incremento en el uso de energías renovables para la generación de energía y por la descarbonización del sector del transporte por carretera. Hoy en día, la transición de tecnologías de conversión de energía por combustión hacía energías limpias es todavía un reto. Para lograr este fin, se espera que las celdas de combustible y en especial las celdas de combustible de membrana de intercambio protónico (PEMFCs) jueguen un papel importante tanto en el sector del transporte como para su aplicación en dispositivos portátiles. Hasta el momento, su puesta en práctica a nivel comercial no ha sido posible debido a una serie de desventajas económicas y tecnológicas que han ralentizado su completo desarrollo. En el actual estado del arte de estos dispositivos, los catalizadores basados en Pt son los que se emplean como electrodos tanto para el ánodo como para el cátodo de las PEMFCs. Como consecuencia del uso de estos materiales, alrededor de la mitad del coste de una celda de combustible se debe al uso de catalizadores basados en Pt, especialmente para el electrodo del cátodo, donde se lleva a cabo la reacción de reducción de oxígeno (ORR). Debido a la lenta cinética de la ORR, la disminución de la carga de Pt en el cátodo produce graves pérdidas de densidad de potencia. Una propuesta para lograr dispositivos de celda de combustible económi-

camente competitivos, pasa por la sustitución del Pt (y otros metales del grupo del Pt, PGM) utilizado como catalizador en el cátodo de las celdas de combustible por otros metales no preciosos, más abundantes y más baratos (NPMCs). Aunque los NPMCs tienen una cinética más lenta para la ORR que los catalizadores basados en Pt, su bajo rendimiento puede ser compensado por un incremento en la cantidad de catalizador empleada sin graves repercusiones económicas.

Esta tesis se centra en el estudio de diferentes catalizadores sin Pt para la ORR tanto en electrolitos ácidos como alcalinos. Se han preparado distintos tipos de catalizadores sin metales nobles, como por ejemplo, catalizadores basados en composites de nitrógeno/carbón o nitrógeno/azufre/carbón y NPMCs basados principalmente en composites de hierro/nitrógeno/carbón. En esta tesis se han estudiado el efecto de la naturaleza de los precursores de nitrógeno, carbón y metal, la ruta de preparación de estos materiales y su repercusión para la ORR.

Los catalizadores preparados se han caracterizado utilizando una serie de técnicas experimentales que incluyen, análisis elemental, difracción de rayos-X, espectroscopia fotoelectrónica de rayos-X, isotermas de adsorción-desorción de N_2 y absorción de rayos-X (XANES y EXAFS). Los datos obtenidos de las técnicas de caracterización se han usado para elucidar la relación actividad-estructura de los catalizadores, lo cual da lugar a una racionalización del diseño de los NPMCs. Se han realizado estudios electroquímicos para determinar la actividad para la ORR de los catalizadores, mediante el uso de la técnica de la voltametría cíclica usando un electrodo rotatorio de disco anillo (RRDE). También se han usado técnicas electroquímicas *in situ* como la espectroscopia de infrarrojo acoplada a una celda electroquímica (EC-SPAIRS), que permite el estudio del mecanismo de degradación durante la ORR.

Primeramente, esta tesis ha abordado el estudio del efecto del dopaje de nanotubos de carbón (CNTs) con átomos de N en el **artículo III**. El objetivo de este trabajo ha sido entender la relación entre la cantidad de defectos creados en los CNTs mediante el uso de tratamientos mecano-químicos y la incorporación de N dentro de la red de carbonos. Además, este trabajo ha estudiado el efecto del dopaje con átomos de N de los composites N/CNT, en la actividad para la ORR.

Los átomos de N se incorporaron en los CNTs, previamente tratados,

por sucesivos tratamientos de la mezcla CNTs y urea como precursor de N en un molino de bolas, seguido por un tratamiento térmico a 800 ^{o}C en flujo de N_2. Los resultados obtenidos mostraron que la estructura de los CNTs permanece estable para tratamientos en el molino de bolas inferiores a 48 h. Por el contrario, sometiendo los CNTs a tratamientos más largos en el molino de bolas se produce el colapso de la estructura de los nanotubos transformándose en un material carbonoso formado por CNTs más cortos y carbón amorfo microporoso. La incorporación de N es solamente moderada para los CNTs sometidos a tratamientos en molino de bolas hasta un máximo de 48 h, aumentando considerablemente cuando se emplean tratamientos en molino de bolas más largos. Los resultados obtenidos en este trabajo mostraron que los N/CNTs son activos para la ORR, tanto en electrolitos ácidos como alcalinos. Los catalizadores N/CNTs después de largos periodos de tratamiento en el molino de bolas registraron la mayor actividad medida en electrolito ácido. Sorprendentemente, los catalizadores N/CNTs contenían una pequeña cantidad de Fe superficial, probablemente incorporado durante el tratamiento en el molino de bolas. El efecto de la presencia de este Fe residual para la ORR fue elucidado/discutido mediante el uso de NaSCN como veneno de los centros activos que pudiesen contener hierro. Estos resultados concluyeron que la participación de estas especies de Fe para la actividad total de estos catalizadores en la ORR es mínima.

Los resultados obtenidos prueban que los CNTs dopados con N son activos para la ORR, y que con la generación de microporos se obtienen catalizadores más activos para la ORR.

La actividad de los nanotubos de carbón dopados con N puede mejorarse haciendo un co-dopaje de nitrógeno y azufre, especialmente para medidas en electrolitos alcalinos. Esta tesis estudia en el **artículo IV**, la incorporación de N y S dentro de los CNTs. Para comparar precisamente el efecto de la incorporación del S y N en CNTs, se usó la tiourea como fuente de N y S. Los resultados obtenidos se compararon con los de los catalizadores preparados solo con urea. El uso de tiourea como precursor de S y N produce una mayor distorsión de la estructura grafítica obtenida. Además, la incorporación del N se favorece por la presencia de S durante la síntesis. De este modo, el contenido de N en los catalizadores preparados con tiourea es dos veces mayor que en los catalizadores preparados solo con urea. La incorporación de N y S se produce en los defectos de la red C-C de los CNTs, especialmente en el

carbón amorfo. Los resultados mostraron claramente que la actividad de los catalizadores (S)/N/CNT en la ORR aumenta a medida que se incrementa el contenido superficial de N en los catalizadores, tanto para electrolitos ácidos como alcalinos. El efecto de mejora producido por la incorporación de S es más evidente en medio alcalino.

Por otra parte, con la incorporación de metales de transición a los composites nitrógeno/carbón, se obtienen catalizadores altamente activos para la ORR. Debido a la controversia sobre la naturaleza del metal de transición que debe ser empleado para catalizadores activos en la ORR, esta tesis aborda, en el **artículo I**, el estudio de la influencia de los metales de transición como Fe, Co o Mn en NPMCs para la ORR. Los NPMCs que contienen Fe, Co o Mn se prepararon con similares cargas de N y metal de transición usando el método de impregnación húmeda de los precursores sobre la matriz de carbón. Este trabajo establece una secuencia de actividad para los catalizadores finales de Fe $>$ Co $>$ Mn. Los resultados obtenidos en esta tesis indican que la actividad de los NPMCs está dominada por la naturaleza del metal de transición, y que el Fe produce catalizadores más activos que el Co y el Mn. Además, el estudio de las diferentes etapas de preparación de los catalizadores mostró que estos catalizadores solo son activos y estables para la ORR en medio ácido, después de la etapa de pirólisis, en la cual se produce la incorporación del metal de transición a las estructura junto con la creación de grupos de N-grafítico.

Una vez demostrado que los catalizadores basados en hierro son los más activos para la ORR, se exploraron otras propuestas para la preparación de estos NPMCs. En el **artículo II** se presentó el uso de un método mecanoquímico para la síntesis de catalizadores Fe/N/C como una posibilidad para obtener catalizadores muy activos para la ORR. En este trabajo se estudió la influencia de la adsorción de los aniones y cationes procedentes de diferentes electrolitos en electrocalizadores basados en Fe y su efecto en la ORR. Los resultados mostraron que la actividad de los catalizadores Fe/N/C en la ORR se ve afectada por el pH del electrolito empleado pero no por el contraión presente en este electrolito. Se observó una mayor actividad de estos catalizadores en electrolitos alcalinos. Además, si se llevan a cabo tratamientos ácidos durante la etapa final de la preparación de los catalizadores, parte del hierro incorporado se elimina del catalizador y los aniones sulfatos se adsorben sobre los centros activos dando lugar a una fuerte pérdida de actividad

en la ORR. En este artículo también se abordó el efecto de los sulfatos procedentes del lavado en ácido de los catalizadores, estudiando la naturaleza de la interacción entre los sulfatos adsorbidos y el catalizador para lo que se utilizó la espectroscopia DRIFT a diferentes temperaturas. Los resultados obtenidos indican que los sulfatos se enlazan químicamente a los centros activos en lugar de adsorberse de forma física produciendo simplemente el bloqueo de los micropores donde se alojan los centros activos.

La naturaleza de la matriz de carbón (C) en los catalizadores Fe/N/C se estudió en un nuevo artículo. En este caso se prepararon catalizadores Fe/N/C usando diferentes matrices de carbón como carbón activo (AC), nanotubos de carbón (CNT) y grafeno (G). Este estudio ha proporcionado información útil acerca las posibles fracciones Fe-N_x activas para la ORR formadas durante la síntesis de los catalizadores y sobre su mecanismo de degradación en esta reacción (ver **artículo VI**). La naturaleza de las especies de hierro formadas en los catalizadores Fe/N/AC, Fe/N/CNT y Fe/N/G ha sido ampliamente estudiada mediante el uso de técnicas de caracterización como la absorción de rayos-X entre otras. Los espectros EXAFS sugirieron que la fracción de especies Fe-N_x varía con la naturaleza de la matriz de carbón, siguiendo la siguiente secuencia Fe/N/G > Fe/N/CNT > Fe/N/AC. Sin embargo, los espectros EXAFS indican que la especie Fe_3C es la más abundante de las especies de hierro en estos catalizadores. Los carburos de hierro, sin embargo, no se detectaron por la técnica XPS, indicando que estas especies están encapsuladas dentro de la matriz de carbón en lugar de en la superficie del catalizador. Fe/N/G es el catalizadores más activo y estable para la ORR en esta serie, mostrando una actividad de $3.1 A \cdot g^{-1}$ a 0.9 V *vs.* RHE en electrolito alcalino y una excelente estabilidad (pérdida de actividad del 10%) después de 3000 ciclos consecutivos hasta un potencial de 1.4 V. Estas observaciones llevan a la conclusión de que la actividad y durabilidad de los catalizadores Fe/N/C aumenta con el uso de materiales carbonosos más grafíticos como nanotubos de carbón o grafeno.

Con el fin de comprender el mecanismo de degradación de los catalizadores durante la ORR, su actividad se monitorizó mediante el uso de la técnica *in situ* EC-SPAIRS. Los resultados obtenidos mostraron claramente que la oxidación de la matriz de carbón a CO_2 es la responsable de la pérdida de actividad y que tanto el grafeno como los CNTs son más estables a esta oxidación que el AC dando lugar a catalizadores más estables.

En vista de la importancia de las especies Fe-N_x como las responsables de la actividad catalítica, en el **artículo V** se realizó un estudio sistemático acerca de la influencia de la cantidad relativa de los precursores de N y C usados durante la síntesis de los catalizadores Fe/N/Grafeno y de su influencia para la actividad de la ORR. Los resultados de caracterización mostraron que la relación N/C en la mezcla de precursores usada para la preparación de los catalizadores Fe/N/Grafeno tiene una fuerte influencia en sus propiedades texturales, en su composición elemental y en la naturaleza de las fases formadas tanto en la superficie como en el volumen de los catalizadores. Al igual que en estudios anteriores de este tipo de materiales, las fracciones Fe-N_x son las especies más abundantes en la superficie de los catalizadores Fe/N/G, las cuales forman los centros activos en la ORR. Aumentando la relación N/C empleada en la síntesis de los composites N/Grafeno se obtienen materiales con una menor área superficial BET y como consecuencia con un menor número de centros Fe-N_x accesibles. Por lo tanto, la elección de una adecuada relación atómica N/C de los precursores para la preparación de los materiales basados en Fe/N/Grafeno es crucial para obtener electrocatalizadores con la cantidad óptima de especies Fe-N_x accesibles.

Contents

List of Figures

List of Tables

Chapter 1

Introduction

Since the Industrial Revolution, the energy model has been based on the use (combustion) of fossil sources, such as coal, oil and natural gas. Although this energy model has led to economic and technological progress, it has been clearly demonstrated that relying on the combustion of fossil fuels is not sustainable. On the one hand, fossil fuels are finite, and eventually, they will be either prohibitively expensive or no longer available, thus resulting in serious geopolitical issues. On the other hand, and arguably more important in the short term, the current model of using fossil fuels results in a severe increase in greenhouse gas emissions, causing Earth's average temperature to continuously increase. Continuing with the current energy model and no further actions to reduce greenhouse gas emissions would lead to catastrophic climate change and no longer being able to ensure energy security in the face of declining supplies of the conventional fossil fuels [1]. Fortunately, concerns about the greenhouse gas emissions produced from the use of fossil fuels are increasingly being taken into account. The International Energy Agency reported a new global agreement to limit greenhouse gas emissions that was reached at the 21^{st} Conference of the Parties of the UNFCCC meeting in Paris in December 2015. The objective adopted by governments is to limit global warming to an average of no more than 2 ^{o}C relative to pre-industrial levels. This implies a deep transformation of the energy sector, with the goal of reducing CO_2 emissions by 80% in 2050 [2].

The transformation of the energy sector consists of using renewable energy sources for power generation and a 95% decarbonisation of the road transport sector [3]. Currently, renewable technologies are becoming in-

creasingly cost competitive, and they increased the global power generation capacity by 128 GW in 2014. This level amounted to more than 45% of the global power generation capacity additions in 2014 [2]. However, despite the efforts and development of this new energy model based on renewable sources, there are still some challenges to achieve the targets established in the last agreement of 2015. On the one hand, there is the problem of storing energy from various renewable sources; on the other hand, the use of this type of energy in the transport sector or portable devices is not a simple task. In this sense, the use of hydrogen should be part of this new energy model. The hydrogen molecule is considered to be a possible technology for reaching the target for environmental issues due to its energy power. Hydrogen can be used to store electricity exceedingly produced by renewable sources, thus obtaining a useful product that can be stored in large quantities.

Currently, approximately one billion vehicles are on the roads, and this number could rise due to the rapid technological developments in emerging countries such as China and India. Moreover, 95% of the fuel used by this fleet is produced using fossil fuels, causing a higher crude oil demand and higher CO_2 emissions and other harmful contaminants as NO_x.

Hydrogen fuel cell vehicles can also contribute to decarbonisation of the road transport sector. The concept of using hydrogen as a transport fuel for vehicles has attracted the interest of industries, government and the public since the 1960s. The first fuel cell electric vehicle (EV) was developed by General Motors, the GM Electrovan of 1966, based on an alkaline fuel cell and fuel cell storage in the form of cryogenic hydrogen and oxygen [4]. Over the past 20 years, there have been signs of reactivation in the development of hydrogen fuel cells. Several global public-private partnerships have been created to secure funding for coordinated action to promote the application of fuel cell technology beyond the automotive industry (*e.g.*, in California, Europe, Japan, Korea and recently in Dubai). This has been reflected in recent commercial launches, for example, Toyota just launched the Mirai for 2016 in Japan, the first commercially available hydrogen fuel cell car; Hyundai is aiming to sell several thousand vehicles soon (the Hyundai Tucson Fuel Cell Electric Vehicle has been available for lease since mid-2014); and Honda has announced its intention to launch a hydrogen-powered car in 2016 [2].

One considerable potential advantage of hydrogen-fuelled vehicles is that

their range is not limited like that of an EV, which is a subject of considerable consumer anxiety. The refuelling time is also generally much lower than the charging time of a battery. If hydrogen is produced from low-carbon sources, then the CO_2 benefits offered are comparable to those of EVs [2]. The limitations of pure EV are even greater when the operation range is greater than 150 km. It is estimated that the current technology for a pure EV requires a weight close to 840 kg for complete energy storage using advanced Li-ion batteries. In addition, the re-charging of a 100 kW h battery takes hours; even when using a fast charger, the re-charging takes 2 h, and to provide less than 500 km of operation, the cost of production ranges from US$ 30000 to 50000. Conversely, the tank system for a hydrogen-fuelled vehicle would have a weight of *ca.* 125 kg (based on 70 MPa compressed hydrogen gas, which is considered the current optimal storage pressure) when containing 5 kg of hydrogen (200 kW h of chemical energy), and it can be re-fuelled in 5 minutes. The industry estimates that the production of a tank system based on a 70 MPa compressed hydrogen gas cost approx. US$ 3000 [4] and the cost of decentralized H_2 production is US$ 50 / GJH_2 so the cost of re-fuelling would be US$ 30 / tank [5]. Hence, the use of hydrogen-fuelled vehicles is a plausible alternative for replacing the actual vehicle fleet because of their advantages in terms of operation range, re-fuelling and fuel production. Out up of that, fuel cells can also be used in portable application like laptops, radios, sonotones, etc.

1.1 Fuel Cells

1.1.1 Principles and classification

Fuel cells are devices that convert chemical energy from a fuel (such as hydrogen, methanol or ethanol) into electrical energy, producing only water when the fuel used is hydrogen as a by-product. Studies of fuel cells began in the nineteenth century, when Christian F. Shöbein and Sir Willian R. Grove simultaneously discovered the working principle of fuel cells, observing that the combination of hydrogen with oxygen in the presence of platinum (Pt) produced an electrical current.

The operating principle of fuel cells is based on the catalytic oxidation of the fuel at the anode and the catalytic reduction of an oxidant at the cathode.

In particular, in a proton exchange membrane fuel cell (PEMFC), which is the most studied type of fuel cell for portable or transportation devices, the operation is based on the catalytic oxidation of hydrogen (hydrogen oxidation reaction, HOR), releasing protons and electrons. The protons from the anode pass through the polymeric membrane, whereas the electrons pass through an external circuit to the cathode. At the cathode side, oxygen is catalytically reduced with the electrons and protons from the anode, (oxygen reduction reaction, ORR), producing water (see Figure 1.1 and Eq. 1.1). Fuel cells can continuously produce energy as long as fuel and oxidant are fed to the electrodes.

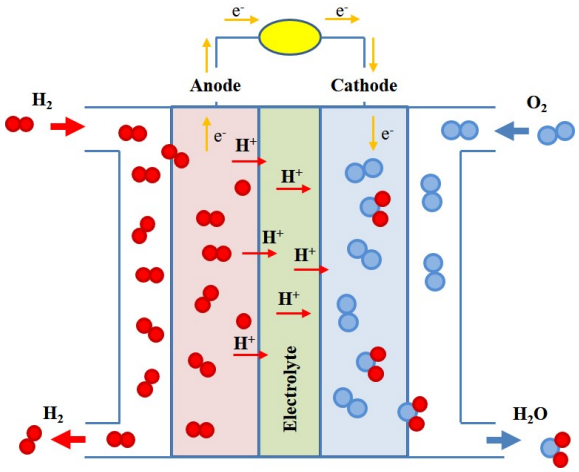

Figure 1.1: Scheme of a fuel cell.

$$\text{Hydrogen Oxidation Reaction (HOR): } 2H_2 \rightarrow 4H^+ + 4e^-$$

$$\text{Oxygen Reduction Reaction (ORR): } O_2 + 4H^+ + 4e^- \rightarrow 2H_2O$$

$$\text{Overall Reaction: } 2H_2 + O_2 \rightarrow 2H_2O \tag{1.1}$$

The core of a fuel cell is formed by the electrodes and the electrolyte located between the electrodes, forming the membrane electrode assembly (MEA). Chemical reactions occur at the electrodes, while the electrolyte acts as an ionic conductor and an electronic insulator between the anode and cathode electrodes. Fuel cells can be classified according to different

criteria, such as the type of electrolyte, the conduction ion or the operating temperature. Based on the type of electrolyte, fuel cells are classified as follows (see Table 1.1):

- Solid oxide fuel cell (SOFC) [6]: The electrolyte used is a metallic and porous solid material composed of Y_2O_3-stabilized ZrO_2. The operating temperature ranges from 600 °C to 1000 °C. The catalysts used are Co-ZrO_2 or Ni-ZrO_2 as the anode and Sr-doped with $LaMnO_3$ as the cathode. Due to the high operating temperature of SOFCs, their overall efficiency becomes very high if the heat produced is harnessed.

- Molten carbonate fuel cell (MCFC) [6]: The electrolyte is formed by alkaline ceramic carbonates that are retained in a matrix of $LiAlO_3$. The operating temperature is approximately 650 °C. The catalysts employed are composed of nickel for the anode reactions and nickel oxide for the cathode. The advantages of these types of fuel cells are the low cost of the catalysts and the use of no highly pure H_2 flow to feed the cell.

- Phosphoric acid fuel cell (PAFC) [6]: This type of fuel cell uses phosphoric acid retained in a matrix of SiC as the electrolyte The operating temperature ranges from 100 °C to 200 °C. The catalyst employed is Pt. At lower operating temperatures, the phosphoric acid is not an ionic conductor material, and CO poisoning of the Pt catalysts used in the anode side could occur.

- Proton exchange membrane fuel cell (PEMFC) [6, 7]: The electrolyte is a solid polymer membrane in which protons are mobile, which is similar to an acid electrolyte from a chemical perspective. These types of fuel cells operate at relatively low temperatures, up to 120 °C. In this case, the operating temperature is limited by degradation of the polymer membrane, thus making the use of very active catalysts capable of working at low temperatures and of improving the reaction rate necessary. In the actual state-of-the-art, Pt and Pt-alloys are the only suitable catalysts that can satisfy the current requirements. The fuel used is hydrogen gas with a CO content lower than 10 ppm because higher CO concentrations lead to poisoning of the catalyst.

Table 1.1: Summary of the different types of fuel cells.

Fuell cell type	Operation temperature	Anode reaction	Conducting ion(Electrolyte)	Cathode reaction	Catalyst
SOFC	$\approx$ 1000 °C	$H_2 + O^{2-} \rightarrow H_2O + 2e^-$	$\leftarrow O^{2-}$ (Y-stabilized ZrO2)	$1/2O_2 + 2e^- \rightarrow O^{2-}$	Ni/YSZ-Perovskitas
MCFC	$\approx$ 650 °C	$H_2 + CO_3^{2-} \rightarrow H_2O + CO_2 + 2e^-$	$\leftarrow CO_3^{2-}$ (alkali carbonates)	$1/2O_2 + CO_2 + 2e^- \rightarrow CO_3^{2-}$	$Ni - NiO_2$
PAFC	$\approx$ 200 °C	$H_2 \rightarrow 2H^+ + 2e^-$	$H^+ \rightarrow$ (H_3PO_4)	$1/2O_2 + 2H^+ + 2e^- \rightarrow H_2O$	$Pt/C - Pt/C$
PEMFC	$\approx$ 80 °C	$H_2 \rightarrow 2H^+ + 2e^-$	$H^+ \rightarrow$ (solid polymer)	$1/2O_2 + 2H^+ + 2e^- \rightarrow H_2O$	$Pt/C - Pt/C$
DMFC (subclass of PEMFC)	$\approx$ 80 °C	$CH_3OH + H_2O \rightarrow CO_2 + 6H^+ + 6e^-$	$H^+ \rightarrow$ (solid polymer)	$1.5O_2 + 6H^+ + 6e^- \rightarrow 3H_2O$	$PtRu/C - Pt/C$
AFC	$\approx$ 80 °C	$H_2 + 2OH^- \rightarrow 2H_2O + 2e^-$	$\leftarrow OH^-$ (KOH)	$1/2O_2 + H_2O + 2e^- \rightarrow 2OH^-$	$Pt/C - Pt/C, Ni, Ag,$ spinels

- Direct methanol fuel cell (DMFC) [6]: These types of fuel cells are a subclass of PEMFCs that use methanol (liquid) rather than H_2 as the fuel. The employed electrolyte is the same as in PEMFCs, and the operating temperature ranges from 20 to 90 °C. The employed catalysts are also based on Pt, although for the anode reaction, the best catalyst is PtRu. The PtRu catalyst avoids the formation of intermediate-CO species from the oxidation of methanol, which act as catalyst poison. These fuel cells generate less power than PEMFCs operated using H_2 despite the high energy contained in methanol molecules. This fact is due to the low kinetics of the reactions occurring in DMFCs and the crossover of methanol from the anode to the cathode.

- Alkaline fuel cell (AFC)[6]:. The electrolyte used is a KOH solution. This type of fuel cell operates between 50 and 200 °C, but it generally operates below 100 °C. The primary advantage of the AFC is that the kinetics for the oxygen reduction reaction are faster, thus improving the reaction rate. This advantage is because the activation overvoltage at the cathode is generally less than that for an acid electrolyte, which results in less potential losses on the cathode site. Because the ORR is faster in alkaline electrolytes, metals such as Ni, Ag, metal oxides, spinels or non-noble metals can be used as catalysts. The fuel is highly pure H_2 because CO acts as a poison and because CO_2 reacts with the KOH solution to form K_2CO_3, thereby modifying the properties of the electrolyte. The use of C-containing catalysts could also lead to the formation of K_2CO_3 due to the corrosion of the carbon catalyst support. Anion exchange membrane fuel cells (AEMFCs) are a type of AFCs that operate through the same principle as AFCs but using an alkaline solid polymer electrolyte rather than the aqueous KOH electrolyte.

Among the different fuel cells, proton exchange membrane fuel cells (PEMFCs) are the best choice for portable and mobile applications and in the transportation sector. This is because they provide a high current density at low temperatures using a solid electrolyte.

Nafion® is the most commonly used proton electrolyte membrane (PEM); it is a commercial ionomer based on persulfonic acid (PFSA) [8]. The operating temperature in a PEM fuel cell ranges from 60 to 120 °C. The operating

conditions must be well controlled, keeping the membrane under the optimal hydration conditions to maximize its conductivity. Hydration is typically achieved by humidifying the inlet reactant gases by bubbling them through saturators that contain water at a fixed temperature [9].

A fuel cell is formed by bipolar plates, which collect the electrons from the anode to the cathode site; gas diffusion layers, which homogenously spread the gas through the catalyst layer; gaskets, which keep the system sealed; and the membrane electrode assembly (MEA) formed by the electrolyte membrane and the catalyst layer (Figure 1.2).

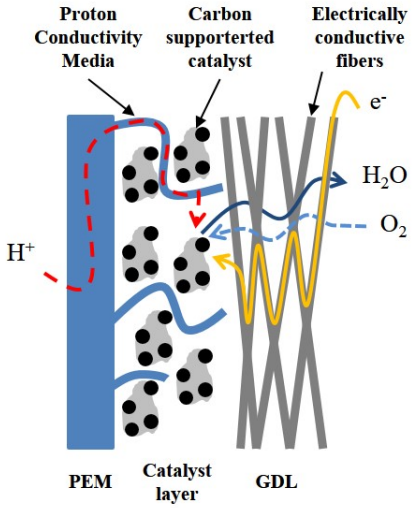

Figure 1.2: Cathode side of a membrane electrode assembly (MEA).

1.1.2 Thermodynamics and kinetics of fuel cells

The work potential of a fuel cell is related to the Gibbs free energy (G). G can be considered as the net energy that has to be transferred to create a system; therefore, G represents the maximum energy that you can get back out of the system. Thus, the maximum amount of electrical work of a fuel cell is given by the Gibbs free energy as follows:

$$\Delta G = -\Delta W_{elec} \tag{1.2}$$

The electrical work done is given by the movement of a charge Q, measured in Coulombs, through an electrical potential difference E, measured

in volts:

$$W_{elec} = EQ \tag{1.3}$$

If the charge is defined by the number of electrons transferred:

$$Q = nF \tag{1.4}$$

where n is the number of electrons transferred and F is Faraday's constant (96485 C·mol^{-1}). Therefore, ΔG is:

$$\Delta G = -nFE_{cell} \tag{1.5}$$

Gibbs free energy sets the magnitude of the reversible voltage for an electrochemical reaction. The most simple and common reaction of a hydrogen-oxygen fuel cell (Eq. 1.6) has a ΔG of -237.1 kJ·mol^{-1} under standard conditions for liquid water as the product

$$H_2 + 1/2O_2 \rightarrow H_2O \tag{1.6}$$

The standard free energy change of the fuel cell reaction is indicated by the following equation:

$$\Delta G^0 = -nFE^0 \tag{1.7}$$

The change in the Gibbs free energy can be used to calculate the reversible cell voltage, E^0, under standard conditions.

$$E^0 = -\frac{\Delta G^0}{nF} = \frac{-237.1kJ \cdot mol^{-1}}{2 \cdot 96485C \cdot mol^{-1}} = 1.23\ V \tag{1.8}$$

Considering the overall reaction for the formation of one molecule of water (liquid state) under standard conditions (the number of electrons exchanged is 2), the highest voltage from a hydrogen-oxygen fuel cell is $E^0 = 1.23$ V.

Electrochemical reactions are heterogeneous processes. The reactions only occur at the interface between an electrode and an electrolyte, through which the charge transfer occurs. In particular, electrochemical reactions occur at the interface, and the current produced is proportional to the area of the interface. In this case, the current density, j, allows the electrochemical

activities of different surfaces to be compared.

In an electrochemical reaction, the rate of conversion of reactants to products depends on the ease with which the reactants reach their activated state. The energy required to reach this activated state determines the reaction rate of the process, and it is referred to as activation energy.

At thermodynamic equilibrium, the forward and reverse current densities are the same, which implies that there is no net current density in the electrochemical reaction. However, both forward and reverse reactions are occurring at a rate that is determined by j_0. Therefore, at equilibrium, $j_1 = j_2 = j_0$.

Away from thermodynamic equilibrium, the current densities for the forward and reverse reactions are given by the exchange current density of the reaction, j_0, and by the activation energy of each reaction. Therefore, the net current is given by the Butler-Volmer equation (assuming that the concentration of reactant and product species at the electrode are unaffected by the presence of a net reaction rate):

$$j = j_1 - j_2 \tag{1.9}$$

$$j = j_0 \left(e^{\alpha n F \eta / RT} - e^{-(1-\alpha) n F \eta / RT} \right) \tag{1.10}$$

where η is the voltage loss to overcome the activation energy, namely, overvoltage or overpotential; n is the number of electrons transferred; j_0 is the exchange current density; and α is the transfer coefficient, α expresses how the change in the electrical potential across to the reaction interface changes the sizes of the forward versus the reverse activation barrier. The value of α is always between 0 and 1. The behaviour predicted by Eq. 1.10 is depicted in Figure 1.3. The solid curve shows the actual total current density j, which is the sum of the components j_1 and j_2, which are shown as dashed traces. For large negative overpotentials, the anodic component is negligible; hence, the total current density curve merges with that for j_2. At large positive overpotentials, the cathodic component is negligible, and the total current density is essentially the same as j_1. When going either direction from equilibrium, the magnitude of the current density rapidly increases because the exponential factors dominate its behaviour, but at extreme η, the current plateaus. In these plateau regions, the current density is limited

by mass transfer rather than kinetics [10].

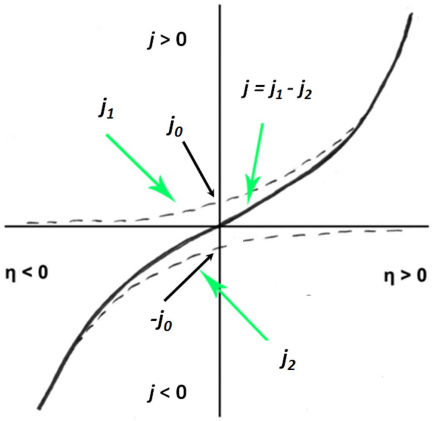

Figure 1.3: Relationship between η and j given by the Butler-Volmer equation.

The Butler-Volmer equation expresses the kinetics of electrochemical reactions. To simplify this expression for fuel cells, it is possible to apply the approximation corresponding to irreversible reactions, in which the forward reaction dominates the process and the activation overpotential is higher than $50 - 100$ mV, giving the equation:

$$j_1 = j_0 e^{(\alpha_1 nF\eta)/RT} \tag{1.11}$$

Solving this equation for η yields:

$$\eta = -\frac{RT}{\alpha nF} ln j_0 + \frac{RT}{\alpha nF} ln j \tag{1.12}$$

which is generalized as the Tafel equation:

$$\eta = a + b log j \tag{1.13}$$

where b is the Tafel slope.

Through the Tafel plot (Figure 1.4), it is possible to extract the kinetic parameters α and j_0 from the slope and the intercept of the linear fit, respectively. The kinetics of fuel cell reactions can be evaluated according to these parameters, In this way, sluggish reaction kinetics (low α and j_0 val-

ues) result in severe performance losses of the fuel cell, whereas fast reaction kinetics (high α and j_0 values) result in lower losses. Nevertheless, in a more practical way the kinetics of a fuel cell is also evaluated comparing the value of the density current density, j, at a fixed potentials in the kinetic region of the reaction.

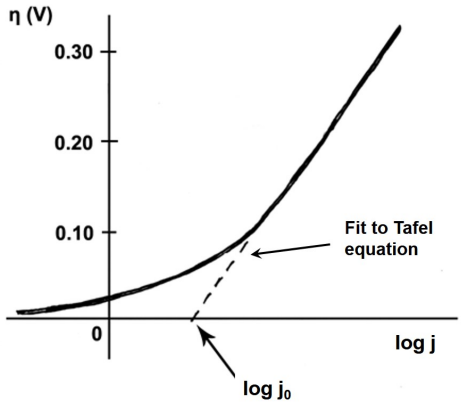

Figure 1.4: The $j - \eta$ representation. At high overpotentials, a linear fit of the kinetics to the Tafel approximation allows determination of j_0 and α.

In a typical redox reaction, the equilibrium state is governed by the Nernst equation. This equation relates the Gibbs free energy and consequently the equilibrium potential (E_{cell}) with the concentrations of reduced and oxidized species.

$$E_{cell} = E^0 - \frac{RT}{nF}\left(ln\frac{C_R}{C_O}\right) \tag{1.14}$$

where E_{cell} is the equilibrium voltage, R is the ideal gas constant, F is Faraday's constant, n is the number of electrons transferred, C_R is the concentration of reduced species, and C_O is the concentration of oxidized species. The equilibrium cell voltage, E_{cell} , of a fuel cell cannot be measured in practice. This is because there are several sources of performance loss during operation. When current is drawn from the fuel cell, the cell voltage, E_{cell}, decreases with increasing current density, j:

$$E_{cell} = E^0 - iR_\Omega - \eta_{an} - \eta_{cat} - \eta_{tx} \tag{1.15}$$

where R_Ω refers to the ohmic losses due to the ion conduction resistance and contact resistance losses. η_{an} and η_{cat} are the current-dependent kinetic losses at the anode and cathode, respectively, whose effects are observed at low current densities, as shown in Figure 1.5. For electrochemical reactions with overpotentials higher than $50-100$ mV, the voltage loss can be expressed according the Tafel equation (Eq. 1.13). At high current densities, the voltage loss, η_{tx}, is dominated by the concentration polarization due to the reactant transport resistances (see Figure 1.5).

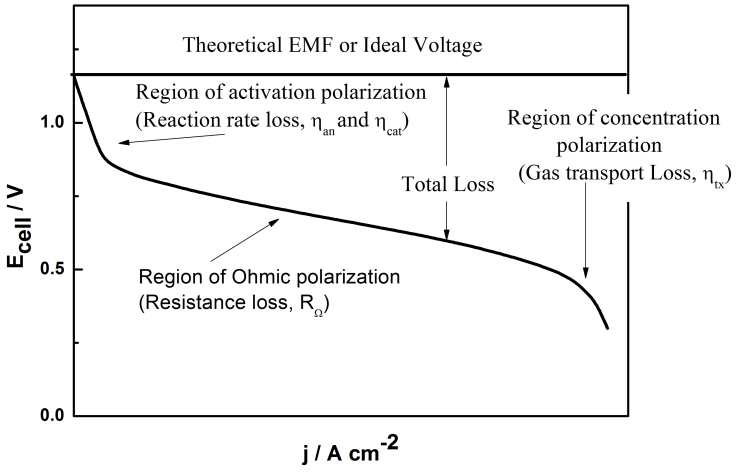

Figure 1.5: Cell voltage *vs.* current density for a PEMFC [11].

1.1.3 Cathodic Reaction. Oxygen Reduction Reaction (ORR)

In a typical fuel cell, in which H_2 is used as the fuel at the anode and O_2 is used as the oxidant at the cathode, the H_2 oxidation (HOR) overpotential from the anode ($\eta_{an} = \eta_{HOR}$) can be negligible for operation with pure H_2. The term η_{tx} includes the mass transport-induced potential losses, which using well-defined electrodes and operating with the optimal humidification of the gases can also be negligible. Hence, the O_2 reduction overpotential $\eta_{cat} = \eta_{ORR}$ produces the greatest loss of potential in a fuel cell due to the sluggish kinetics of this reaction.

The kinetics for the oxygen reduction reaction (ORR) are very slow,

even when using Pt as catalysts. Although Pt is the most active single metal catalyst to date, the kinetic parameter j_0 is still at least six orders of magnitude lower than that in the HOR (see Table 1.2 and Table 1.3). This is why the η_{ORR} produces the greatest loss of potential in a PEMFC, as schematically shown in Figure 1.6.

Table 1.2: Standard state (T = 300 K and 1 atm). Exchange current densities for the hydrogen oxidation reaction (HOR) on various metal surfaces [12].

Surface	**Electrolyte**	$\mathbf{j_0/A \cdot cm^{-2}}$
Pt	Acid	10^{-3}
Pt	Alkaline	10^{-4}
Pd	Acid	10^{-4}
Rh	Alkaline	10^{-4}
Ir	Acid	10^{-4}
Ni	Alkaline	10^{-4}
Ni	Acid	10^{-5}
Ag	Acid	10^{-5}
W	Acid	10^{-5}
Au	Acid	10^{-6}
Fe	Acid	10^{-6}
Mo	Acid	10^{-7}
Ta	Acid	10^{-7}
Sn	Acid	10^{-8}
Al	Acid	10^{-10}
Cd	Acid	10^{-12}
Hg	Acid	10^{-12}

Table 1.3: Standard state (T = 300 K and 1 atm). Exchange current densities for the oxygen reduction reaction (ORR) on various metal surfaces [12].

Surface	**Electrolyte**	$\mathbf{j_0/A \cdot cm^{-2}}$
Metal Surfaces in Acid Electrolyte		
Pt	Acid	10^{-9}
Pd	Acid	10^{-10}
Ir	Acid	10^{-11}
Rh	Acid	10^{-11}
Au	Acid	10^{-11}
Pt Alloys in PEMFC		
Pt-C	Nafion	$3 \cdot 10^{-9}$
PtMn-C	Nafion	$6 \cdot 10^{-9}$
PtCr-C	Nafion	$9 \cdot 10^{-9}$
PtFe-C	Nafion	$7 \cdot 10^{-9}$
PtCo-C	Nafion	$6 \cdot 10^{-9}$
PtNi-C	Nafion	$5 \cdot 10^{-9}$

The kinetics of the ORR is significantly improved in alkaline pH electrolytes, whereas the kinetics of the HOR, even on Pt catalysts, in alkaline electrolytes is slower than in acid electrolytes[13]. The alkaline polymer membrane fuel cell (APMFC, also referred to as anion exchange membrane fuel cell, AEMFC) is a recent class of fuel cell that operates through the same principle as the alkaline fuel cell (AFC). The operating temperature of APMFCs is below 100 °C, and the difference is attributed to the use of an alkaline solid polymer electrolyte (alkaline anion exchange membrane, AAEM) rather than the aqueous KOH electrolyte in the traditional AFC.

Although the mechanism for the ORR on Pt and other electrocatalysts has been extensively studied, it is still controversial. The scheme presented in Figure 1.7 shows the proposed pathways for the oxygen reduction reaction.

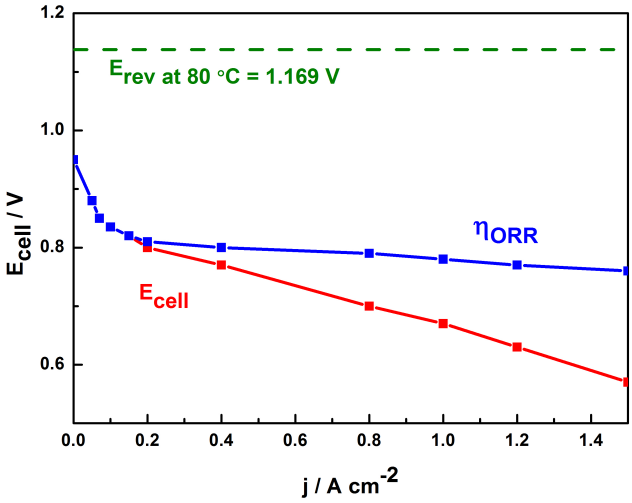

Figure 1.6: Overpotential of a fuel cell; theoretical polarization curve measured at 80 °C (green dashed line), real polarization curve (red line) and contribution of the ORR overpotential to the total η of a PEMFC (blue line).

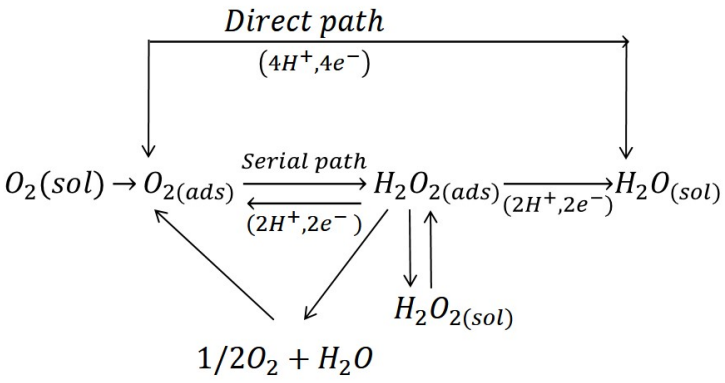

Figure 1.7: Mechanism of the oxygen reduction reaction.

The serial path or two-electron path proceeds through the formation of H_2O_2 as an intermediate species, which can be further reduced to water desorbed in the electrolyte or decomposed to H_2O and O_2. The direct path or four-electron path proceeds through the direct reduction of O_2 to H_2O [14].

The mechanism for the ORR is proposed to be similar in acid and alkaline electrolytes on Pt-based electrocatalysts, which have been the most studied electrocatalysts to date. The first studies on the subject proposed that the rate-determining step (*rds*) on Pt electrodes is the first electron transfer step to the adsorbed molecular O_2 [15]. However, the different ORR activities observed for Pt-based catalysts in acid and alkaline electrolytes requires a further explanation of the possible reaction mechanism in both electrolytes. The pH independence of the redox couple (O_2 /O_2^-) makes the potential for the formation of superoxide (O_2^-) invariable at -0.31 V when the pH changes from 0 to 14. Nevertheless, when the pH changes from 0 to 14, the overall potential of the reaction *via* the four-electron pathway (direct path) is significantly reduced, and the standard reduction reaction potential changes from 1.23 V to 0.40 V (see Figure 1.8). Hence, at pH= 0, the potential for the formation of superoxide (O_2^-) (-0.31 V) is very far from the overall equilibrium potential for the two or four electrons transferred, 1.54 V and 1.01 V, respectively. Consequently, the reaction in acid electrolytes is very slow. Nevertheless, the difference between the potential for the formation of superoxide (-0.31 V) and the standard reduction potential (0.4 V) is strongly reduced in alkaline electrolytes; at pH= 14, this difference is reduced to 0.71 V for the four electrons transferred, producing a lower overpotential in alkaline electrolytes than in acid electrolytes [16 − 18]. This decrease in the overpotential of the ORR is illustrated in the modified Pourbaix diagram in Figure 1.8.

However, some works claim that the faster kinetics of the ORR in alkaline electrolytes is also attributed to the influence of the outer-sphere mechanism. In this case, the oxygen molecule is solvated by the surrounding water molecules, and this solvated O_2 could interact with the surface hydroxyl species (OH_{ads}) *via* a hydrogen bond. This hydrogen bond stabilizes the solvated O_2 in the outer Helmholtz plane (OHP) and promotes an outer-sphere electron transfer to form the superoxide species [17, 19].

In fact, several electrochemical reactions, including the most relevant environmentally friendly energy-related processes such as the hydrogen evolution reaction (HER), the hydrogen oxidation reaction (HOR), the oxygen evolution reaction (OER) and the oxygen reduction reaction (ORR), require the presence of electrocatalysts [20, 21] with the aim of increasing the reaction rate and consequently lower the overpotentials. Electrocatalysts,

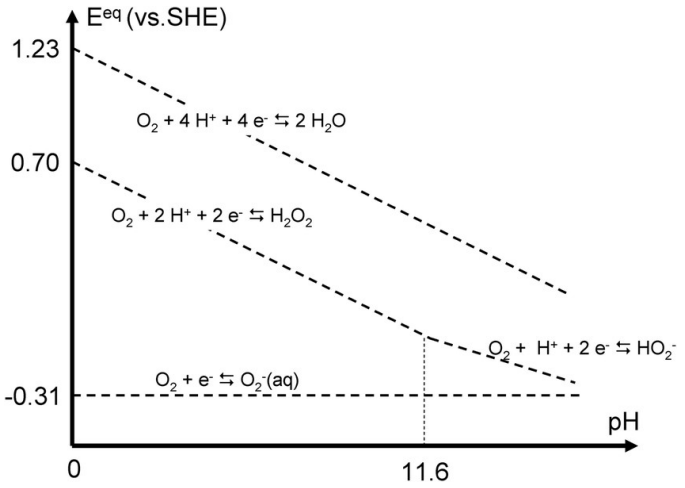

Figure 1.8: Modified Pourbaix diagram.

particularly for the ORR, generally contain high amounts of scarce and expensive platinum group metals (PGM), which are the most active catalysts for low-temperature fuel cells.

1.2 Catalysts for the ORR. Need for replacing Pt-based catalysts by non-precious metal catalysts

Electrochemical devices such as PEMFCs and/or AEMFCs are expected to power environmentally friendly vehicles in the near future. Currently, as mentioned above, the most active catalysts for a PEMFC are based on platinum nanoparticles supported on carbon (Pt/C). However, the Pt loadings are too high, particularly in the cathode side where the ORR occurs [22, 23]. The high cost, the scarcity and the misallocation of Pt cause PEMFC devices to not be economically competitive due to its high price [24], which is also responsible for the slow development of this technology. The amount of Pt used in a typical fuel cell passenger car considering the current technology is *ca.* 10 g_{Pt} [25]. Furthermore, Pt resources on Earth are estimated to be $30000 - 40000$ tons [26]; thus, the 1 billion PEMFC vehicles in service at any moment require the use of 10000 tons of Pt, which is expected to not be sustainable long term and overly expensive.

It is well known that important research has been conducted towards re-

ducing the consumption of Pt for PEMFCs; consequently, the Pt loading in the anode in the actual state-of-the-art has been reduced to 0.05 $mg_{Pt} \cdot cm^{-2}$, which is an acceptable value in economic terms. However, the catalyst loading in the cathode is five times higher than that for the anode [27, 28]. This fact is due to the slow kinetics for the ORR, which is three orders of magnitude lower than that for the HOR even when using Pt-like catalysts [28].

Economic considerations aside, another drawback of Pt is its degradation during operating conditions, and thus, the instability of this material. This is why it is necessary to research new materials that are more durable and that have an activity that is comparable or even higher than that of Pt, particularly for the ORR. In this way, it would be possible to reduce the cost of the devices and to reach the objectives for large-scale production. Numerous attempts have focused on decreasing the Pt loading in the cathode, and the US Department of Energy (DOE) has established a target loading of 0.125 $mg_{Pt} \cdot cm^{-2}$ (both electrodes) for 2020 [29]. There are several ways to reach the set target; the new catalysts should reduce the Pt loading [30], for example, using Pt alloys, in which the best result obtained to date has been reached for Pt_3Ni nanoframes [31] and Mo-Pt_3Ni/C [32] with values of 5.7 $A \cdot mg_{Pt}$ and 6.98 $A \cdot mg_{Pt}$ at 0.9 V in an acid electrolyte, respectively. However, an even better option would be to replace Pt with abundant and non-precious metal materials [33].

The selection of other non-precious metals is dictated by their abundance (Figure 1.9), their cost and their activity for the ORR.

The most active non-precious metal catalysts (NPMCs) reported to date are based on a transition metal inserted in a matrix of N-substituted graphitic carbon, typically referred to as M/N/C [35]. The use of these structures as catalysts for the oxygen reduction reaction is based on the mechanism of biological molecules capable of reducing oxygen molecules, such as oxidases, enzymes or haemoglobin, which are responsible for aerobic respiration in living organisms. The proposed active site is essentially a heme group, as shown in Figure 1.10. The seminal work in the study of this type of structure as a catalyst is based on the work of Jasinski et al., who reported that cobalt phthalocyanine catalysed the ORR in an alkaline electrolyte [36].

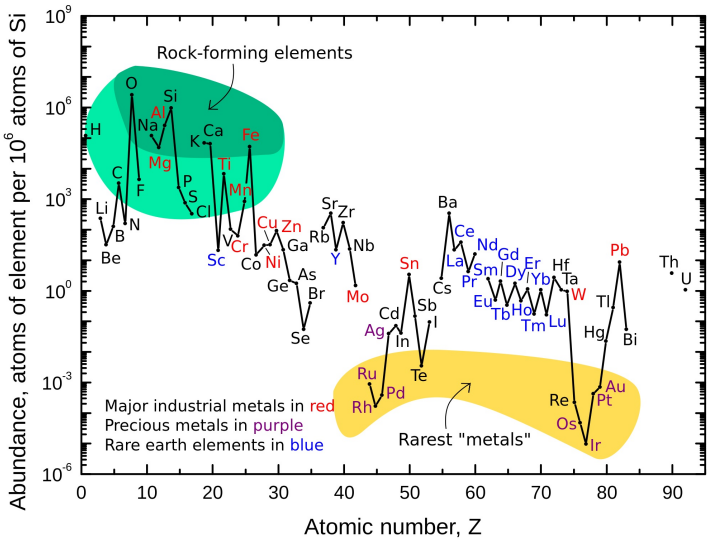

Figure 1.9: Relative abundance of chemical elements in the Earth's upper continental crust [34].

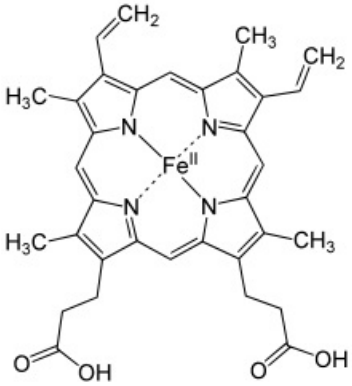

Figure 1.10: Heme group's structure.

1.2.1 Metal-free state-of-the-art catalysts. Nitrogen/carbon-based catalysts

The actual arrangement of the N, M and C atoms at the active sites for the ORR is elusive. The first hypothesis, proposed three decades ago, claimed that N and C atoms are the real active sites of the NPMCs for the ORR [37, 38]. Since then, numerous research efforts have been focused on the development of metal-free oxygen reduction catalysts. Note that although

most works agree that the transition metal should be present during the thermal treatment step to obtain active catalysts for the ORR, whether the transition metal is an indispensable element for the activity of the catalysts or whether it only favours the formation of the active sites is still under debate [39, 40].

In the preparation and study of metal-free catalysts, it is generally assumed that N atoms are the ideal dopants for carbon materials because of their similar atomic size and because they can substitute carbon atoms in the sp^2 network. This dopant can also modify the electrical, mechanical and structural properties of the carbon materials. Moreover, in a graphitic carbon structure, the pyridinic-N dopant acts as an electron donor that increases the n-type conductivity of the carbon [41].

One of the early works on this topic was reported by Lalande et al. in 1997 [42]. This work compared the activity of a carbon black containing only nitrogen atoms with a similar preparation of catalysts that also contained a small amount of iron. Finally, they concluded that nitrogen-carbon materials based on N-doped carbon structures cannot be active for the ORR in acid electrolyte. Although this first approach failed, the possibility of using metal-free catalysts was not discarded by the scientific community.

Further works have demonstrated the possibility of preparing metal-free catalysts that are active for the ORR [43-53]. However, neither the nature of the active site nor any of the parameters likely to form active catalysts has been clarified.

In general, the nitrogen species detected in the carbon structures of this type of catalyst were pyridinic-N, pyrrolic-N, quaternary-N or graphitic-N and oxidized-N. The ratio of the different species varies depending on the precursor and thermal treatment used in the preparation. Although the role of each of these N species is not clear, several research groups have reported that pyridinic-N is the active site responsible for the ORR activity in N-doped carbon materials [48, 49, 54-58]. In this sense, Kundu et al. prepared N-doped CNTs at different temperatures, which showed better ORR activity with higher pyridinic-N contents [55]. In accordance with this concept, Rao et al. also reported a higher catalytic activity for CNTs containing 5.2 at.% of pyridinic-N than CNTs containing 5.7 at.% of graphitic-N [57]. Therefore, these results suggested that pyridinic-N is the most active nitrogen species formed in these types of materials; however, it has not been discounted that

graphitic-N could participate in the activity of N-doped carbon materials. To clarify the different behaviours of these two nitrogen species, N-doped graphene with only pyridinic-N or graphitic-N was prepared [58, 59]. Yasuda et al. reported a selective synthesis method for preparing two types of N-doped catalysts from julolidine and pyridine [58]. This work proposed that pyridinic-N is responsible for the oxygen reduction *via* a four-electron pathway and that graphitic-N is also active and promotes the oxygen reduction through a two-electron mechanism. Regarding the activity of the nitrogen species, some works have proposed that only planar nitrogen structures such as pyridinic and pyrrolic are active for the ORR [45, 48] and that graphitic-N species, which have a 3D structure, show poor activity for the ORR [60-62].

Moreover, the use of different carbons materials in the preparation of metal-free catalysts can have a great impact on the final activity of the prepared materials. Carbon-based materials such as carbon nanotubes and graphene are currently on the rise for applications in electrocatalysis due to their specific properties, such as high electrical conductivity, excellent mechanical flexibility and high thermal/chemical stability [63-65]. The doping of these structures with N atoms has been addressed, revealing that different nitrogen species are anchored in different sites in the carbon matrix. In the case of carbon nanotubes, it was proposed that quaternary-N has a greater ability to substitute carbon atoms in the carbon network, whereas in graphene, pyridinic-N is the most suitable species to be placed in the graphene structure [58, 66].

Given the lack of consensus on what nitrogen species are the most active for the ORR and where they should be located in each of the carbon materials used, several works have been reported regarding the nitrogen species responsible in each of carbon materials used.

Sidik et al. presented a detailed study, both theoretical and experimental [45]. They prepared a Ketjenblack EC-300J doped with nitrogen through a thermal treatment of the carbon in a reactive atmosphere of NH_3 at 900 ^{o}C, reporting an onset potential of 0.51 V *vs.* RHE in an acid electrolyte *via* a two-electron ORR pathway. These authors supported their findings by theoretical calculations, and they found that the most active nitrogen position for the ORR activity in the carbon network is when N atoms are located far from the graphite sheet edges, whereas those that are close to the edges are less active.

Many efforts have been conducted to improve the catalytic ORR activity of metal-free catalysts [43, 44, 46-50, 54]. Superior electrochemical performance for the ORR *via* four electrons was achieved using similar carbon precursors as Ketjenblack in work developed by Subramanian et al. [47]. In this work a series of catalysts were prepared using an acid-treated Ketjenblack as the carbon precursor and various nitrogen-based resins such as melamine formaldehyde (MF), urea formaldehyde (UF), thiourea formaldehyde (TUF), and selenourea formaldehyde (SeUF) as N precursors by a simple addition-condensation reaction. The final catalysts, denoted as SeUF, showed the highest activity in the series, reaching an onset potential of 0.78 V *vs.* RHE in an acid electrolyte. Pyridinic-N is the most abundant N-containing species in the SeUF catalyst, and consequently, its ORR activity is attributed to the presence of pyridinic-N. Moreover, regarding the influence of the different types of nitrogen species on the activity of metal-free catalysts, an extensively review from Dai's group also attributed the improved catalytic performance of the heteroatom-doped carbon nanomaterials to the electron-accepting/donating abilities of the heteroatoms, which results in a net charge on adjacent carbon atoms in the nanocarbon structures, thereby facilitating the O_2 adsorption and charge transfer for the ORR [67]. Supporting this hypothesis, a recent work presented by Guo et al. proposed that only carbon atoms next to pyridinic-N in nitrogen-doped graphitic carbons are responsible for the ORR activity [68]. They suggested that the Lewis basicity in the carbon atoms helps in the initial step of the ORR, the adsorption of O_2 molecules.

Nitrogen-doped CNTs have also been reported by Gong et al. as highly active catalysts that are capable of reducing oxygen *via* a four-electron pathway, showing even higher activity than a commercial Pt-based catalyst (C2-20, 20% platinum on Vulcan XC-72R; E-TEK) in alkaline electrolytes [43]. This catalyst, denoted as VA-NCNT, is formed by vertically aligned N-containing carbon nanotubes produced by the pyrolysis of iron(II) phthalocyanine followed by the complete removal of the iron atoms in the catalyst by electrochemical purification.

Only the presence of pyridinic-N and pyrrolic-N species was detected. The work by Gong et al. encouraged the use of carbon nanotubes as a matrix for the N-doped catalysts. Their findings related to the N-doping of CNTs were supported by Hu et al., who reported density functional theory

(DFT) calculations on the interaction of O_2 molecules with the active sites present in N-doped CNTs (N/CNTs) [69]. The results obtained by these authors indicated that N-doping facilitated the adsorption of O_2 on carbon nanotubes. Changing the diameter and length of N/CNT can influence the bond length of O_2 and the binding energy between O_2 and N/CNT. Moreover, the use of carbon nanotube catalysts in an acid electrolyte by Yu et al. resulted in an active catalyst with a nitrogen content of 3.6 at.% N and an onset potential of *ca.* 0.6 V *vs.* RHE. Additionally, it exhibited excellent durability after two days under continuous cycling between 0.4 V and 1.0 V [48].

In view of the works discussed in the literature, part of this thesis addresses the effect of N-doping in different carbon nanotube structures. Catalyst preparation consists of creating defects in the CNTs using a physical method in a planetary ball mill and the subsequent incorporation of N atoms on such sites [70]. The results revealed high electrochemical activity for the ORR in an acid electrolyte and that the structural modification of CNTs promotes the incorporation of N. Similar N contents (4 at.%) and distributions of the different species as in other works [43, 48] were obtained.

The use of other carbon structures as the carbon matrix, such as graphene, was also reported by Qu et al. [54] with a similar activity as the VA-NCNTs [43]. The durability of both catalysts, prepared using CNTs or graphene, showed better results than for commercial Pt/C 20 % in an alkaline electrolyte. By using a graphene matrix for the preparation of metal-free catalysts, Yang et al. presented a systematic study on the influence of the thermal treatment temperature on the ratio of nitrogen species formed [51]. They observed that the amount of nitrogen incorporated in the C structure decreased with the thermal treatment temperature due to a decrease in the pyridinic-N contribution. They identified 800 ^{o}C as the optimal temperature for the thermal treatment for obtaining N/C catalysts with the best ORR performance, with a total nitrogen content of 10 at.%.

The metal impurities resulting from the synthesis process of the carbon materials, such as in the growth of CNTs and in the use of the modified Hummer's method for the synthesis of graphene materials [71, 72], must be taken into account when preparing metal-free catalysts. These impurities remain encapsulated within several layers of carbon material, which makes their complete removal difficult. The presence of such metal impuri-

ties can promote the graphitization of carbon during the thermal treatment performed for the formation of N-doped catalysts to improve the conductivity of the catalysts [73]. Moreover, the presence of residual metals, particularly Fe residue, has been demonstrated to be beneficial for the ORR [74]. This effect should be considered in the preparation and characterization of metal-free catalysts, such as in the work presented by Gong et al. [43]. Accordingly, this effect has been addressed in the study of N-doped CNTs developed in this thesis. The study on the effect of this residual iron has been conducted by poisoning the residual iron species in the final catalyst with NaSCN.

The use of templates for preparing other carbon structures with ordered pores has recently emerged. For example, Liang et al. recently reported a metal-free catalyst based on a N-doped carbon material with a meso-/microporous structure prepared by the polymerization of o-phenylenediamine in the presence of silica colloid (denoted as meso/micro-PoPD) [46]. The catalyst meso/micro-PoPD exhibits the highest ORR activity in alkaline media among all metal-free N-doped carbon catalysts reported to date. The ORR activity reached a half-wave potential of 0.85 V *vs.* RHE with a loading of 0.1 mg·cm^{-2} catalyst. The preparation of this catalyst is based on the polymerization of a nitrogen-enriched aromatic precursor within a silica colloid template, followed by pyrolysis of the N-rich composite under an inert atmosphere of Ar. Subsequently, removal of the silica template was performed, followed by an activation process through a thermal treatment under a reactive atmosphere of NH_3. The final catalyst was a nitrogen-rich meso/microporous carbon material, whose nitrogen species are primarily graphitic-N. According to this work and in contradiction to previous works, the amount of graphitic-N appears to be more relevant for the activity of the catalysts, at least in this type of meso/microporous ordered carbon structures.

A different approach for increasing the activity of metal-free catalysts for the ORR consists of using heteroatoms other than N, such as B, P or S, during the synthesis of N/carbon catalysts. An extensive study on the influence of the heteroatoms on the activity for the ORR was developed by Jiao et al [75]. This work combined the use of ORR activity predicted by DFT calculations with experimental ORR activity data of a graphene material doped with N, B, P, S or O. According to this work, the most active catalyst was formed by N-doped graphene heteroatoms, although the doping of graphene with the other heteroatoms also showed catalytic activity

(see Figure 1.11).

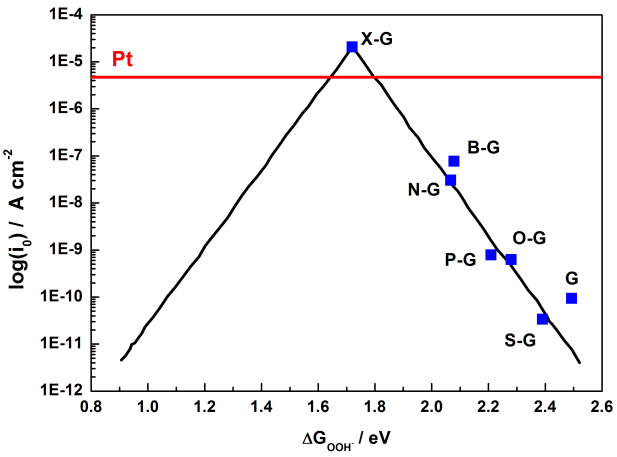

Figure 1.11: Volcano plot for the calculations of the most probable active heteroatoms in a graphene layer reported by Jiao et al. [75].

A different approach explores the preparation of metal-free ORR catalysts based on N-doped carbon structures modified with a second heteroatom as a way to improve their performance. In this sense, it has been reported that the addition of B to N-doped carbon structures enhances the performance of the catalysts in alkaline media [76, 77]. In this line of research, a recent work of Zhang et al. reported a P and N co-doped catalyst with superior performance for the ORR [78]. This catalyst leads to a half-wave potential of 0.85 V and an onset potential of 0.94 V *vs.* RHE with a catalyst loading of 450 $\mu g \cdot cm^{-2}$ in an alkaline electrolyte. The catalyst was prepared by the polymerization of aniline in the presence of phytic acid, obtaining a PANI hydrogel with a mesoporous structure.

The use of other heteroatoms such as only S atoms as a dopant in metal-free catalysts does not appear too promising under the volcano activity presented by Jiao et al. [75]. However, it has been reported that the presence of S promotes the incorporation of higher amounts of N into the carbon sp^2 network, particularly in the pyridinic form of N [79]. In contrast, other works reported that the amount of N actually incorporated into the final catalyst actually decreases after co-doping with S [80, 81]. Regardless, most reports agree that the ORR activity in alkaline media of the S/N co-doped

catalysts significantly increases with respect to the N-doped catalysts, irrespective of the actual amount of N in the final catalyst. In the studies supporting the promotional effect of S on the ORR activity, there is a lack of consensus on the role of S. Some studies suggest that the promotional effect for the ORR of heteroatoms such S arises from the modification of the electronic density of the carbon atoms induced by the presence of vicinal S (or other) atoms [81]. Other reports suggest that the promotional effect for the ORR of S co-doping is due to the higher amount of N incorporated in the final catalyst when S-precursors are used during the synthesis of the electrocatalysts. At this point the results reported about the effect of the S co-doping in metal-free catalysts are contradictory, the works above mentioned put forward either a promotional effect of the S in the N incorporation and as a consequence in the ORR activity or a decreasing in the N amount incorporated to the final material.

In an attempt to shed some light on the influence of S as a bifunctional dopant in nitrogen-containing catalysts, one of the works presented in this thesis addresses this effect by using a S and N precursor that contains both S and N heteroatoms within its structure [82]. The presence of S has a strong influence on the total amount of N incorporated, but in this case, it has no visible effect on the distribution of the N species, agreeing with the work by Nie et al. [79]. The observed amounts of N and S species range between 0.14 and 0.38 at.% for N and between 0.10 and 0.30 at.% for S, and these values are consistent with previous reports [79].

Although the number of papers addressing S/N/C-based catalysts for the ORR is high, only very few of them have studied the influence of S on the ORR in acid media with S/N/C catalysts. Recently, Shi et al. reported that co-doping CNTs with S and N results in a strong promotion of the ORR activity in alkaline media, but the effect is only moderate in acid electrolytes [83]. Slightly higher ORR activity values are discussed in this thesis (half-wave potential of 0.62 V and onset potential of 0.81 V *vs.* RHE) than in the work presented by Shi et al. [83] in acid media. In an alkaline electrolyte, the co-doping has a stronger influence on the ORR activity. Results comparable to the work of Shi et al. (half-wave potential of *ca.* 0.85 V and onset potential of *ca.* 0.92 V *vs.* RHE) were obtained in this thesis (half-wave potential of 0.81 V and onset potential of 0.92 V *vs.* RHE). Both results are close to the best catalyst reported Zhang et al. [78] based on a P and N co-doped

catalyst in an alkaline electrolyte.

In summary, the most suitable candidates for replacing Pt catalysts with metal-free catalysts in an alkaline electrolyte should be based on N/C composites or on the co-doping of carbon with N and other heteroatoms such as P and S. The use of highly graphitized carbon structures such as CNTs imparts the catalysts with high ORR activity and excellent stability. Additionally, the use of ordered porous structures as templates for preparing N/C catalysts is a promising route for the preparation of metal-free catalysts, and by using this method, the N-doped catalyst with the highest activity has been reported. The use of metal-free catalysts in acid media is far more challenging, and it has not been as extensively studied.

1.2.2 Metal/nitrogen/carbon state-of-the-art catalysts

Although the ORR activity of metal-free catalysts has been extensively demonstrated, particularly in alkaline electrolytes (this is discussed in section 1.2.1), even better results, closer to the ORR activity of Pt-based catalysts, have been reported for the metal-containing catalysts known as non-precious metal catalysts (NPMCs).

Studies on this class of catalysts began in 1964, when it was first reported that cobalt (Co) phthalocyanine was active for the ORR in alkaline media [36]. Since then, numerous research works have been presented in this field. Most studies about NPMCs for the ORR are based on transition metals, mainly iron or cobalt, incorporated into a carbonaceous matrix, in which some C atoms are replaced by N atoms. Although the precise nature of the active sites for the ORR in these catalyst is still elusive, most works agree that the active site is formed by a metallic atom (Co or Fe) bonded/coordinated to several nitrogen atoms within a carbon matrix, which are generally termed M/N/C [35, 84].

In addition to the lack of a well-defined and well-characterized structure of the active site in NPMCs and the presumed low density of them, no suitable methods have been described for the identification and quantification of the number of active sites for the ORR in NPMCs. This feature impedes a rational design of these catalysts. A key feature for increasing the activity of these catalysts (and any catalyst in heterogeneous catalysis) is to have a material with a high surface area, thereby increasing the dispersion of the

active sites. In addition to having a sufficient number of accessible active sites, these sites must show a very high stability under the harsh operating conditions of a fuel cell, *i.e.*, highly corrosive environment due to high potentials and the presence of oxidizing agents such as oxygen and H_2O_2.

In general, the preparation of M/N/C catalysts is inspired by the elemental composition of the heme group (see Figure 1.10) and consists on an intimate mixture (either in a solid state or in solution) of a carbon source (matrix/support), a nitrogen source and a transition-metal precursor followed by one (or several) thermal treatment under inert or reactive atmospheres.

Promising results according to the M/N/C structures of the catalysts for Fe/nitrogen/carbon and Co/nitrogen/carbon catalysts have been reported, showing ORR performances (in terms of activity and/or durability) close to those of platinum-based catalysts [85-91].

Due to the wide range of possible combinations of precursors and synthesis methods and the lack of any criteria when choosing them, the selection of the metal, nitrogen and carbon sources is a critical issue for the synthesis and final catalytic properties of M/N/C-based catalysts. Several studies, both theoretical and experimental, regarding the most suitable non-precious metal have been conducted to clarify this important matter [35, 84, 86, 88, 92-97]. An extensive work developed by Jaouen et al. studied the possible reaction mechanisms for the ORR of non-precious metal catalysts in different metal-containing catalysts on M/N/C with M=Cr, Mn, Fe, Co, Ni, or Cu [95]. This work discussed the possibility of an oxygen reduction *via* four-electron or two-electron pathways. The authors concluded that the role of the metal is related to its actual loadings in the final material. Thus, at low catalyst loadings ($\approx 96\mu g \cdot cm^{-2}$), the most active catalysts are based on Co, whereas at high catalyst loadings ($\approx 960\mu g \cdot cm^{-2}$), the most active catalysts are the Fe-based ones. The mechanism followed by the NPMCs studied by Jaouen and co-workers consists of a four-electron pathway for all metals studied at high catalyst loadings, whereas at low catalyst loadings, only the Fe- and Cu-based catalysts follow the four-electron pathway. However, this statement has to be taken carefully due to the great heterogeneity of NPMCs described in the literature, and it cannot be directly extrapolated to all catalysts. In fact, a previous work showed that another Fe/N/C catalyst catalyses the electroreduction of O_2 to H_2O_2 at loadings below $800\mu g \cdot cm^{-2}$ [98], indicat-

ing that the occurrence of the four-electron or two-electron pathway depends on the loading of the catalyst.

In general, the most active NPMCs are based on Fe [86-89, 91, 99]. The mechanism and rate-determining step (*rds*) proposed for the ORR with Fe-based catalysts is similar to the well-known mechanism that occurs in heme/copper oxidases:

- The direct four-electron pathway is based on the following sequence:

$$Fe^{II} \overset{O_2}{\rightarrow} Fe^{III} - OO \overset{e^- + H^+}{\rightarrow} Fe^{III} - OOH \overset{H^+}{\rightarrow} {}^{\bullet +}Fe^{IV} = O + H_2O$$

$${}^{\bullet +}Fe^{IV} = O \overset{e^-}{\rightarrow} Fe^{IV} = O \overset{e^- + H^+}{\rightarrow} Fe^{III} - OH \overset{e^- + H^+}{\rightarrow} Fe^{II} + H_2O$$

The O_2 molecule binds to the iron and forms the oxygenated species. The loss of an electron and protonation of the $Fe^{III} - OO$ species occurs, followed by a further protonation and the cleavage of the O-O bond, resulting in the formation of an oxo-ferryl radical cation and H_2O. Several electron reduction and protonation processes starting from the oxo-ferryl radical give the initial state Fe^{II} and a second H_2O molecule. $Fe^{III} - OOH$ is a branching point where the cycle either continues to the oxo-ferryl radical cation (${}^{\bullet +}Fe^{IV} = O$) or releases H_2O_2 (giving the two-electron pathway). Therefore, the *rds* appears to be the formation of the oxo-ferryl radical cation or a similar transition state [95].

If in the branching point the $Fe^{III} - OOH$ releases H_2O_2 prior to the formation of the oxo-ferryl radical cation (${}^{\bullet +}Fe^{IV} = O$), then the reaction mechanism continues *via* the two-electron pathway.

- The serial pathway through to the two-electron pathway is based on the following sequence from the branching point [95, 100]:

$$Fe^{III} \overset{H_2O_2}{\rightarrow} Fe^{III}HOOH \rightarrow Fe^{III}OH(OH) \rightarrow Fe^{IV}O(H)(OH) \rightarrow {}^{\bullet +}Fe^{IV} = O + H_2O$$

$${}^{\bullet +}Fe^{IV} = O \overset{H_2O_2}{\rightarrow} {}^{\bullet +}Fe^{IV} = O(HOOH) \rightarrow Fe^{IV}OH(HOO^{\bullet})$$

$$Fe^{IV}OH(H^{\bullet})(O^{\bullet}O^{\bullet}) \rightarrow Fe^{III}OH_2(O_2) \rightarrow Fe^{III} + H_2O_2 + O_2$$

In this case, the reaction starts with the Fe^{III} form. At the beginning, one molecule of water is displaced by a molecule of H_2O_2, forming the $Fe^{III}HOOH$ species. In the second step, the O-O bonding is weakened, leading to the protonation of the terminal OH group and the formation of Fe^{IV} cations. The formation of the intermediate species, $Fe^{III}OH(OH)$, has the highest energy barrier; therefore, it is the limiting step of the overall reaction. The proton from the iron-bound OH group is transferred to the O-H radical, and one electron from the FeN_4 macrocycle is transferred to the radical. A water molecule is released, and the oxo-ferryl radical cation ($\bullet^+Fe^{IV} = O$) is formed. The last species reacts with a second H_2O_2 molecule and finally gives a second H_2O molecule, O_2 and the initial iron state Fe^{III}. All steps after the formation of the oxo-ferryl radical cation ($\bullet^+Fe^{IV} = O$) are predicted to be thermodynamically favourable.

In summary, similar rate-determining steps (*rds*) are identified in both mechanisms, either the direct oxygen reduction reaction or the oxygen reduction through H_2O_2 formation, consisting of the weakening and cleavage of the O-O bond.

As previously mentioned, the best ORR performance reported to date has been achieved using Fe-based catalysts. Nevertheless, the reason for why this metal is more susceptible to form more active catalysts is unknown. Different studies on the influence of the metal in the preparation of NPMCs have been published [37, 92-95, 101, 102], leading to scattered conclusions. For instance, it has been reported that the ORR performance of N_4-phthalocyanines coordinated to different metal atoms in alkaline media follows the sequence Fe > Co > Ni > Cu = Mn [101]. Other studies in which the NMPCs were obtained using metal salts, such as hydroxides or acetates, also reported higher activity for the catalysts based on Fe and Co compared to those based on other transition metals such as Cr, Mn, Ni or V [93, 94]. Conversely, other works claim that the highest activity for the ORR is obtained using a Cr salt as the transition metal precursor [102]. In this line, theoretical calculations using density functional theory (DFT) performed by Calle-Vallejo et al. have identified activity trends in the ORR with NPMC based on transition metals coordinated to four pyridinic-N atoms within a graphene structure [92]. They found a volcano-type relationship (see Figure 1.12) between the transition metal and their catalytic performance for the ORR. Mn was found on the top of the volcano, showing the highest activity

in the ORR, followed by Co and Fe, which also presented significant activities in this reaction.

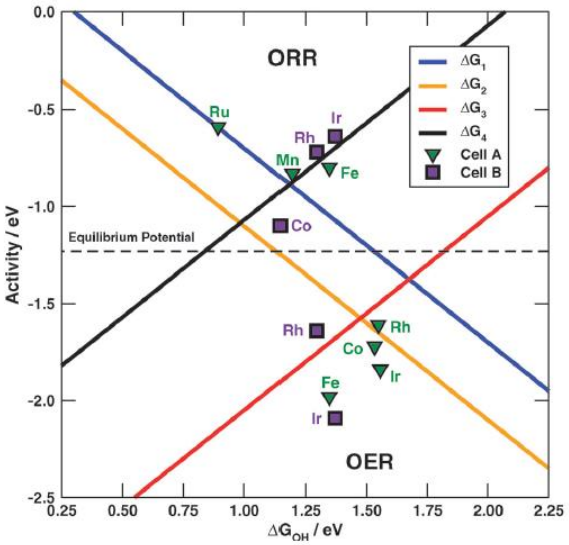

Figure 1.12: Volcano-type relationship between transition metals and their catalytic performance for the ORR reported by Calle-Vallejo et al. [92].

The conflicting results concerning the best metal for the ORR inspired a chapter of this thesis. A study on the influence of transition metals in NPMCs has been performed based on M/N/C catalysts for the ORR activity in acidic media, with the metals studied being Fe, Co and Mn [103]. Different NPMCs were prepared with similar N and transition metal loadings. This study established an activity sequence of Fe $>$ Co $>$ Mn, consistent with most experimental works on this topic, in which Fe-based catalysts are the most active for the ORR.

The study of the different steps for preparing the catalysts showed that their activity in acidic media begins only after the catalysts are subjected to a pyrolysis treatment, leading to the formation of graphitic-N. However, pyridine-N species are also present in all cases to a greater extent.

A careful inspection of several catalysts obtained according to different schemes (diverse metal, N, and C precursors) was made by Jaouen et al. in 2008 [84]. The results showed that the use of Fe metal results in more active catalysts with an ORR mass activity in a rotating disk electrode (RDE) of 18 A·g^{-1} at 0.8 V in acidic media. The characterization of this material

showed a nitrogen content of *ca.* 3 at.% and just 0.7 at.% of Fe.

The use of carbonaceous materials with a high surface area of micropores appears to be an important feature for obtaining high mass activity for the ORR, suggesting that micropores (width $\leq$ 2 nm) host most of the catalytic sites [104]. The formation of these microporous active site structures is promoted to occur during the partial gasification of the precursors and carbon matrix when subjected to fast heat treatment in NH_3. The final NPMC obtained using this protocol presents good activity for the ORR but low stability. The mass loss at which maximum activity is reached (30 to 50 wt.%) corresponds to the largest microporous surface area for the carbon [35, 105].

The incorporation of N and Fe precursors into the porous network of the carbon matrix is a key issue. In this regard, a very successful preparation an Fe/N/C catalyst was reported by Lefèvre et al. [85]. They prepared an Fe/N/C catalyst by using a ball milling synthesis method that elevated the catalytic activity of an Fe-based NPMC by a factor of $>$ 35 relative to the previous best reported activity for Fe-based catalysts. The use of a ball milling forced the introduction of a pore filling material, such as 1,10-phenanthroline, and iron acetate as a metal precursor into the micropores of the carbon support, keeping the structure of the carbon.

The U.S. Department of Energy (DOE) had set a 2010 target of 130 $A{\cdot}cm^{-3}$ of the ORR activity for NMPCs [29]. This target was almost reached in the work of Lefèvre et al., reporting the best results so far with a volumetric activity of *ca.* 20 $A{\cdot}cm^{-3}$ measured and 99 $A{\cdot}cm^{-3}$ (429 $A{\cdot}g^{-1}$) extrapolated at reference conditions in a PEM fuel cell (at 0.8 V iR-free cell voltage, at 80 °C, and at O_2 and H_2 absolute pressures of 1 bar). However, the ORR activity decays very fast at high current densities due to mass transport problems, which is attributed to the location of the active sites within the microporous network of the carbon matrix. However, the actual target proposed by the U.S. Department of Energy (DOE) for 2020 has been increased to 300 $A{\cdot}cm^{-3}$, thus the activity of this type of catalysts should be improved.

The previous best reported Fe-based catalyst reached an ORR activity of 8 $A{\cdot}cm^{-3}$ measured and 19 $A{\cdot}cm^{-3}$ extrapolated at 0.8 V at reference conditions in a PEMFC [106]. This catalyst was prepared by the polymerization of nitroaniline and its mixture with iron chloride and a carbon source

under an inert atmosphere.

Other very active and highly durable Fe-PANI/C and FeCo-PANI/C catalysts were reported by Wu et al. [88]. These catalysts showed a half-wave potential of *ca.* 0.8 V *vs.* RHE and a loss on the current density of only 3% for the catalyst FeCo-PANI/C after a 700 h fuel cell performance test at a constant voltage of 0.4 V. In this case, their preparation derived from the polymerization of aniline, iron(III) chloride and cobalt(II) nitrate using Ketjenblack EC 300J as a carbon support.

All these preparations consist of one or two heat treatments of the M/N/C composites to create the actual active site for the oxygen reduction reaction, followed by an acid-leaching step between the heat treatments to remove the non-stable metal phases.

The synthesis of PANI-based catalysts by Wu et al. identified 900 ^{o}C as the optimum temperature for the heat treatment under an inert atmosphere of N_2 [88]. Conversely, the preparation of the most active catalyst reported by Lefèvre et al. consists of the use of two sequential heat treatments under Ar and NH_3 at 1050 ^{o}C and 950 ^{o}C, respectively [85]. This work concluded that micropores formed during the second heat treatment in NH_3 host the catalytic active sites. Therefore, these results imply that it is not necessary to use microporous carbon sources to obtain active NMPCs because microporosity can be developed during the thermal treatment.

Following synthesis procedures similar to those mentioned above, numerous approaches have been conducted using different precursors of nitrogen, transition metals and carbon supports [35, 88, 89, 91, 97]. In general, the synthesis of this type of catalysts cannot be standardized, depending on the precursors used, the optimum temperature of the thermal treatment and the use of one or two inert and/or reactive treatments vary to obtain highly active ORR catalysts.

Wang et al. reported a catalyst with high ORR activity (11.5 $A{\cdot}g^{-1}$ at 0.8 V *vs.* RHE) and low H_2O_2 yield ($< 1\%$) measured in an acid electrolyte [91] based on Fe and the use of poly-m phenylenediamine (PmPDA) as the nitrogen precursor. The choice of PmPDA for the synthesis of the catalyst is based on its higher nitrogen content and higher thermostability than PANI. Moreover, the PmPDA-FeN_x/C catalyst showed a maximum power density of *ca.* 350 $mW{\cdot}cm^{-2}$ in a PEMFC, which is higher than the values obtained for the FeCo-PANI/C catalyst [88] and other highly active ORR catalysts

based on carbon nanotube-graphene-based complexes (4.4 A·g^{-1} at 0.8 V) [107].

In this line of highly active catalysts, Zelenay's group reported a composite catalyst prepared using iron acetate, cyanamide and oxidized carbon powder with the highest ORR activity in alkaline media reported to date [89]. After the heat treatment at 950 °C in an inert atmosphere, the precursors are transformed into a carbon nanotube (CNT)/carbon nanoparticle (CNP) composite with N and Fe atoms present in its structure (N-Fe-CNT/CNP). Remarkably, the half-wave potential of *ca.* 0.93 V *vs.* RHE obtained in an alkaline electrolyte for the catalyst labelled as N-Fe-CNT/CNP (with a loading of 1 mg·cm^{-2}) even exceeded the activity reported for the 20 wt.% Pt/C catalyst (half-wave potential *ca.* 0.91 V *vs.* RHE). Furthermore, the stability of this catalyst is outstanding, and the performance of the N-Fe-CNT/CNP catalyst is actually improved after 5000 consecutive cycles between 0.6 V and 1.0 V in an O_2-saturated electrolyte, showing a volumetric activity after cycling of 4.8 A·cm^{-3} at 0.9 V *vs.* RHE. Comparable activity results and excellent durability in an alkaline electrolyte were achieved in the work presented in this thesis, reaching a mass activity of 3.1 A·g^{-1} (1.28 A·cm^{-3}, assuming an effective catalyst density of 0.4 g·cm^{-3}) at 0.9 V and a half-wave potential of 0.83 V with a loading of 0.6 mg·cm^{-2} [108]. This work reported exactly the same activity of the Fe/N/G catalyst after 3000 consecutive cycles in the potential range of 0.4 V to 1.4 V in an O_2-saturated electrolyte.

Therefore, it appears that the activity and more importantly the stability of Fe/N/C-based catalysts for the ORR may be improved by the use of more graphitic carbon matrix structures, such as graphene-like or carbon nanotubes [89, 107, 109]. However, it has recently been reported that direct ball milling of a mixture of carbon-supported M-N macrocyclic complexes, such as iron(II) phthalocyanine, provides significantly better results in terms of activity, using high area carbon black rather than graphene nanosheets [110]. In light of the widely differing views on the most suitable carbon source that should be used to obtain the most active and durable catalyst in similar preparation approaches, this thesis work explores the effect of the carbon matrix on the synthesis and catalytic performance of Fe/N/C catalysts [108]. This study consists of using different types of carbon (graphite nanoplates, multi-walled carbon nanotubes or active carbon) for the preparation of the

catalysts.

A further approach for the preparation of NPMCs is the so-called nanocasting method, which consists of using templates to obtain NPMCs with well-ordered porous structures [111]. In general, for this preparation, different silica structures may be used as templates for this approach. Thus far, ordered mesoporous silica such as SBA-15, amorphous silica or silica colloid and montmorillonite (MMT, a layered clay with 2D open channels) have been employed as templates. Liang et al. prepared different NPMCs by the nanocasting method using SBA-15, silica colloid and MMT as templates [90]. The most active mesoporous catalyst obtained in this work was prepared using vitamin B12 as the Co and N precursors and silica colloid as the template (V12/silica colloid). The V12/silica colloid exhibited high ORR activity with a half-wave potential of 0.79 V *vs.* RHE measured in an acid electrolyte. The high ORR performance is strongly associated with its high N and Co contents (9.5 at.% N and 1.4 at.% Co) and thus its high density of active sites. Note that the same preparation was created by polymerizing polyaniline (PANI) over silica colloid using aniline and $FeCl_3$ as precursors (PANI-Fe/Silica colloid), obtaining very similar results to those obtained using the V12/silica colloid catalyst (onset potential of 0.83 V and half-wave potential of 0.73 V *vs.* RHE) and high N and Fe content (8.8 at.% N and 1.5 at.% Fe). The activity of the family of NPMCs prepared *via* the nanocasting method using templates was improved by Adzic's group, using a simple nanocasting of a Co and Fe porphyrins with a SBA-15 template (FeCo-OMPC), followed by a pyrolysis of the mixture after which the template was removed [87]. The characterization of the final catalyst indicated that the contents of Fe, Co and N in the FeCo-OMPC were 2.5, 2.3 and 5.4 wt.%, respectively. The obtained catalyst showed half-wave and onset potentials of 0.85 V and 1 V *vs.* RHE in acid electrolyte, respectively. Single fuel cell tests with this catalyst also showed an outstanding performance, displaying a power density value of *ca.* 700 $mW \cdot cm^{-2}$.

Given the plethora of precursors used thus far for the preparation of these catalysts, Atanassov's group raised 3 considerations to be taken into account to select the nitrogen and carbon precursors using a nanocasting synthesis [99]. The precursor should be i) carbon rich, ii) nitrogen rich and iii) thermally stable for the formation of nitrogen centres at high temperatures. Following these considerations, they synthesized a NPMC using iron

nitrate and carbendazim as the Fe and N-C precursors, respectively, with a silica Cab-O-Sil template. The obtained material presented a high ORR activity with a current density of 120 $mA \cdot cm^{-2}$ at 0.8 V in the MEA test and an excellent durability after 10000 cycles in an O_2-saturated acid electrolyte in the rotating ring disk electrode (RRDE) (loss of activity of 6%) [99].

A novel and promising research line for the synthesis of NPMCs involves the use of metal-organic frameworks (MOFs). MOF are hybrid crystalline porous materials constructed from metal-containing nodes (also known as secondary building units or SBUs) and organic linkers [112]. In addition to the applications of pristine MOFs, there is a growing trend of using MOFs as sacrificial templates for the synthesis of carbon and nanomaterials for electrochemical applications [86, 113]. Zeolitic imidazolate frameworks (ZIFs) are a subclass of MOFs with coordination polymers composed of N-containing ligands (*e.g.*, imidazole and its derivatives) and metal ions (mostly Zn and Co) with a tetrahedral coordination mode [114]. Ma and co-workers reported the first approach for the synthesis of Co-ZIF-based catalysts for the ORR, showing very promising results [115]. However, the high content of cobalt in the Co-based ZIF, approximately ten times greater than the optimum metallic content reported for the Me-N-C catalysts, opens up the possibility for significant improvements in these types of materials. On the other hand, the textural properties of these materials (high specific surface area and microporosity) cope with the aprioristic requirements for designing very active electrocatalysts for the ORR [104]. It is well established that high iron or cobalt contents in the precursors lead to the formation of graphitized structures during the heat treatment and that the number of active sites is low in the graphitized structures [116, 117]. The activity of ZIF-based catalysts was further improved by Dodelet's group by using a Zn-ZIF (ZIF-8) combined with Fe(II) acetate and phenanthroline followed by two consecutive pyrolysis steps in Ar and in NH_3. The obtained catalyst presented a remarkable power density of *ca.* 900 $mW \cdot cm^{-2}$ and 1120 $A \cdot g^{-1}$ (extrapolated) when measured in a PEMFC [86]. Other approaches based upon two consecutive pyrolysis steps in Ar and then in NH_3 of a mixture of an Fe imidazolate framework and Zn-ZIF (ZIF-8) were reported by Liu's group [118]. Both approaches render catalysts with very high initial power performance, but their durability noticeably decreased in the first hours of operation. Conversely, Dodelet's group prepared similar catalysts only under Ar, resulting in more durable

catalysts, although their initial activity is lower [86]. The loss of activity for catalysts subjected to a single pyrolysis treatment after 100 h of operation at 0.5 V is *ca.* 25 %, whereas for the catalysts subjected to two thermal treatments, the loss is *ca.* 80 %, thus confirming the general "unwritten" trend that the higher the activity is, the lower the stability is.

A less explored approach to prepare NPMCs using a porous organic polymer (POP) as a precursor was presented by Liu's group [119]. This method consists of preparing an iron-polyporphyrin activated under a nitrogen heat treatment at 1000 °C, resulting in a highly active catalyst for the ORR. Tests using proton-exchange membrane fuel cells achieved very high measured volumetric and mass activities of 20.2 A·cm^{-3} and 39.4 A·g^{-1} at 0.8 V, respectively, and a maximum peak power density of 730 mW·cm^{-2}.

In summary, the methods used for preparing M/N/C catalysts can be divided in five groups (see Figure 1.13): i) chemical methods, which include the polymerization or the impregnation of the precursors over the carbon matrix or even into the silica templates, among others; ii) mechano-chemical methods, which in principle consists of a physical mixture of the precursors generating high energy in the process, for example, by using a planetary ball mill; iii) nanocasting methods, which consists on the use of silica templates to obtain NPMCs with well-ordered porous structures; iv) the use of the metal-organic frameworks (MOFs) to create highly active micropores structures; and v) the formation of M/N/C catalysts from porous organic polymers (POPs) as precursors.

The most significant results for the best Fe/N/C catalysts reported are compared in Table 1.4.

Table 1.4: Comparison of PEMFC performance at 80 °C.

Catalyst	**iR-corrected**	**Current density (I_d) at 0.8 V / mA·cm^{-2}**
Fe-Phen-C [85]	Yes	170
Fe-Phen-ZIF-8 [86]	No	200
PANI-FeCo-C [88]	Yes	100
FeCo-OMPC [87]	Yes	90
Fe-CBDZ [99]	No	120
PmPDA-FeN_x-C [91]	Yes	90
$Fe_{0.5}$-950 [120]	Yes	110

It is well documented that the activity of the NPMCs is higher in alkaline electrolytes than in acidic ones. However, there is a lack of systematic studies

Figure 1.13: Synthesis methods for the preparation of M/N/C catalysts.

that explore the influence of anion and cation adsorption for the ORR with Fe-based electrocatalysts, contrary to the numerous studies on the subject for Pt-based electrocatalysts [121-123]. This is why a systematic study has been developed in this thesis to investigate the effect of anion and cation binding onto Fe/N/C catalysts in different acidic and basic electrolytes [124]. The effect of the sulfates from the acid leaching was also addressed by studying the nature of the interaction between the adsorbed sulfates and the catalyst through DRIFT spectra recorded at different temperatures.

The range of N-containing promoters used for the preparation of Fe/N/C is immense. In most cases, N- and C-containing molecules are used both as the N- and C- sources, thus avoiding the use of additional C-precursors. As mentioned above, it has been proposed that the use of nitrogen sources with high decomposition temperatures results in superior catalysts for the ORR [99]. Most attempts have been directed at the use of N molecules with high N/C ratios such that the amount of N in the final material is increased. However, conflicting results about the N/C ratio in the final catalyst have been reported. It is well accepted that a high N/C ratio is necessary to obtain a highly active catalyst for the ORR, although depending on the preparation, the range of nitrogen content is from *ca.* 3 to 9 at.% [84, 86, 87, 89-91, 99]. Therefore, in the absence of studies that explore the influence of the relative amounts of the N and C precursors used during the synthesis of Fe/N/C catalysts, the work developed in this thesis addresses the influence

of the N/C ratio in the final Fe/N/C catalysts on the ORR activity in an alkaline electrolyte [125]. In this work, a series of Fe/N-modified graphene composites with different N/C ratios were prepared. The best activity results were obtained with 2.6 at.% of N, a similar N content to the value reported by Zelenay and co-workers for the most active NPMC in an alkaline electrolyte [89].

1.2.3 Nature of active site in non-precious-metal catalysts

Although considerable progress has been made in recent years regarding the activity of NPMCs, the identification of the catalytically active sites for the oxygen reduction reaction in metal-nitrogen-doped carbon materials remains elusive. The most accepted hypothesis is that the active site is composed of a metal ion bonded to several nitrogen atoms, which are covalently integrated within a carbon matrix. The study of the active sites for NPMCs has been focused on the Fe-based catalysts due to their higher activities reported to date. Such active sites are generally labelled as FeN_4/C or FeN_xC_y [35, 84]. Using *in situ* Mössbauer spectroscopy, Bouwkamp-Wijnoltz et al. studied the evolution of the Fe-N_4 moiety formed in the iron porphyrins, and they showed that it is stable up to temperatures of 700 °C [126]. Moreover, it was only at 800 °C when a partial destruction of these moieties was observed. These results should not be extrapolated to any Fe/N/C catalysts because, according to the literature, the optimal temperature for the formation of the active sites depends on the synthesis method and precursors used. Therefore, it appears that the active sites formed in other catalysts could be different from those of the iron porphyrins studied by Bouwkamp-Wijnoltz and co-workers, or perhaps the structure surrounding the active site could influence the final activity in different ways.

On the other hand, some works reported that excessively high temperature results in lower activity due to decomposition of the active sites [99, 127, 128]; however, a weight loss of $30 - 50$ % of the initial material is necessary during the gasification process using NH_3 gas to reach the maximum activity for the ORR [35, 85, 129].

Dodelet and co-workers conducted time-of-flight secondary ion mass spectrometry (ToF SIMS) studies with Fe/N/C-based catalysts. They proposed that the metal is the heart of the most ORR-active catalytic sites [130, 131].

Those works proposed the simultaneous presence of two moieties of FeN_x-like species as catalytic sites, namely, FeN_2/C and FeN_4/C sites, and that their relative abundance depends mostly on the precursor used for the preparation of the catalyst. They followed the variation of $FeN_xC_y^+$ ions in pyrolysed catalysts using ToF SIMS. This work concluded that FeN_2/C is more active than FeN_4/C in acidic media based on the observation that the ORR activity increases as the FeN_2/C relative abundance increase. Over the past years, the use of advanced characterization techniques such as X-ray absorption and Mössbauer spectroscopies have allowed a more fine identification of the structure of the active sites to be achieved. These spectroscopic techniques are very sensitive to the immediate structural and chemical neighbourhoods of the Fe atom. In particular, ^{57}Fe Mössbauer can discriminate between various Fe sites with similar structures but in different oxidation and/or spin states. Thus, using Mössbauer spectroscopy, Kramm et al. identified different FeN_x-like species in Fe/N/C catalysts prepared by the impregnation of carbon black with iron acetate followed by a heat treatment in NH_3. Among all iron species identified, only FeN_4/C and N-FeN_{2+2}/C structures, particularly in its composite version with a nearby basic protonable nitrogen N-$FeN_{2+2}\cdots N_{prot}/C$, are active for the ORR [127]. The possibility of basic sites working as catalytic sites for the ORR has also recently been reported by Guo et al.[68]. This work in N-doped carbon materials proposed that the carbon atoms next to the pyridinic-N are active sites with Lewis basicity, promoting the adsorption of O_2 molecules.

The fine analysis of the structure of one of the most active catalysts reported in the literature (Fe-PANI-C catalyst) was conducted by Ferrandon et al. [96]. In their work, the formation of iron carbide after a second thermal treatment due to a combination of the high temperature and the high iron loading was detected. According to this work, the formation of more iron carbide results in fewer FeN_4 sites, and consequently, lower ORR activity was recorded.

FeN_4/C-based species were also identified as active for the ORR in a catalyst prepared according to the protocol used to synthesize the Fe/N/C catalyst by Dodelet's group in 2009 [85]. Specifically, the most active species is also the N-$FeN_{2+2}\cdots NH^+$ ensemble as proposed by Kramm et al. [127]. In addition, the effect of the second treatment in NH_3 was also addressed. They concluded that all catalysts heat treated in NH_3 during their synthesis have

larger porosity than those heat treated only in Ar. Therefore, they proposed that the largest fraction of active sites of the Ar+NH_3 catalysts is located at the surface of the catalysts, where they are fully accessible to O_2 and H^+. By contrast, most of the active sites of the catalysts only pyrolysed in Ar are located inside the catalytic material; therefore, they are less accessible for the ORR than the previous ones [132].

A recent study investigated the FePhen@MOF-ArNH_3 catalyst, whose preparation consists of the synthesis of the MOF structure containing iron and nitrogen atoms. The synthesis consists of a mixture of the corresponding precursors for the formation of the MOF (in this case, ZIF-8), 1,10-phenanthroline and iron(II) acetate. Finally, the dried powder was subjected to two heat treatments in Ar and NH_3 at 1050 °C. They did not detect the presence Fe-N_x moieties using techniques such as ^{57}Fe Mössbauer spectroscopy and *in situ* synchrotron XAS, and thus, they proposed that in the absence of Fe-N_x ensembles, the majority of the ORR activity resulted from the N-doped carbon structure [133]. The iron species in this catalyst consist of Fe/Fe_xC nanoparticles located in the subsurface of the N-doped carbon. These authors proposed that the presence of this species results in a synergistic effect on the N-doped carbon surrounding Fe/Fe_xC, which allows for the stabilization of the peroxide intermediate and enables the full four-electron reduction from oxygen to water, giving highly active catalysts for ORR measured in electrochemical cell (onset potential of 0.93 V and half-wave potential of 0.77 V **vs**. RHE in acid electrolyte). This hypothesis about the activity of the Fe/Fe_xC nanoparticles instead of Fe-N_x ensembles is contradictory to the previous results reported by Ferrandon et al. [96] in which catalysts the active sites have been proposed as the FeN_4 sites.

The use of advanced characterization techniques, such as *in situ* extended X-ray absorption fine structure (EXAFS) and X-ray absorption near edge structure (XANES) techniques, combined with theoretical studies have managed to clarify the structure of the active sites at different pHs. DFT studies and EXAFS characterization revealed that FeN_x-C sites are forming the active sites, particularly the Fe-N_4 centres (often also defined as Fe-N_{2+2}) [134, 135]. At any pH, the FeN_x-C site is involved in the ORR initiation process of O_2 adsorption on the Fe^{2+}-N_4 site (see mechanism pathway in Figure 1.14). At alkaline pH, the oxygen reduction occurs *via* a four-electron pathway on the FeN_x-C centres, and an optimal stabilization of the peroxide anion

(HO_2^-) intermediate occurs on the metal-nitrogen coordinated sites [17, 126, 134-136]. In contrast, in an acidic electrolyte, a bifunctional mechanism was proposed by Olson et al. [137] and more recently corroborated by Mukerjee's group [135, 138]. In this case, the first O_2 adsorption and consequent formation of the H_2O_2 intermediate occur in the FeN_4C_{10} active sites (more favoured coordination environment, see Figure 1.14). The initiation of the oxygen reduction to hydrogen peroxide molecular intermediate occurs in the Fe^{2+}-N_4 active sites. However, the poor stabilization of hydrogen peroxide implies a need for secondary active centres, in this case, Fe_{NPs}/C, adjacent to Fe^{2+}-N_4 active sites to complete the four-electron process [135].

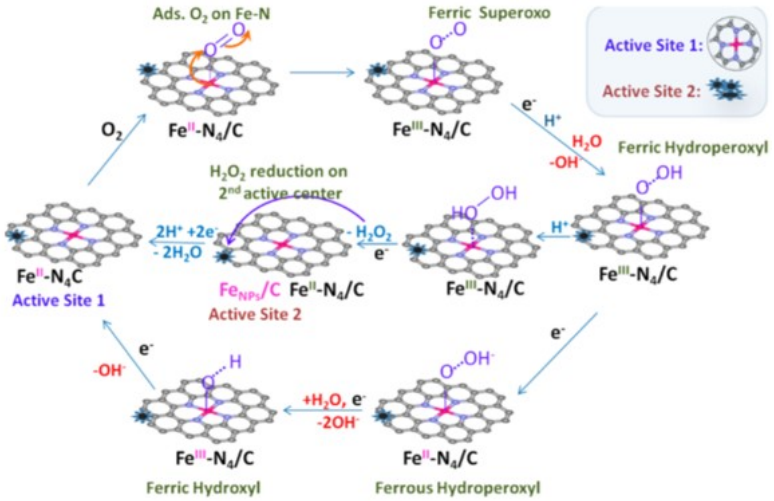

Figure 1.14: Proposed ORR mechanistic pathways on Fe-N_4/C and adjacent Fe_{NPs}/C in acidic (H^+) and alkaline ($H_2O/^-OH$) electrolytes [135].

DFT calculations presented by Holby et al. open the possibility of the formation of a clustered FeN_3 structure (Fe_2N_5) as being responsible for the ORR activity in M/N/C catalysts [139]. These bimetallic FeN_3 sites facilitate cleavage of the O_2 bond. They also concluded that the presence of these bimetallic sites avoids the formation of H_2O_2 intermediates, in other words, avoids the ORR occurring *via* the two-electron pathway.

A recent work by Jaouen's group identified another possible active site with an FeN_4C_{12} core structure similar to that proposed by Mukerjee's group (see Figure 1.15) [120]. This hypothesis of Jaouen's group has been supported by an excellent agreement between theoretical and experimental results. X-

ray absorption spectra and density functional theory calculations including a dispersion term (DFT-D) consistently indicated that the FeN_4C_{12} moieties are the most probable species responsible for the ORR activity on the Fe/N/C catalyst. This work also investigated the reasons why different ORR activity is observed in Fe/N/C catalysts prepared by varying the iron loadings and the thermal treatments, although identical FeN_4C_{12} moieties were identified in all cases. Catalysts subjected to NH_3-thermal treatments exhibit a considerably higher ORR activity than Ar-treated ones. The authors proposed that the use of a NH_3 atmosphere during the thermal treatment favoured the formation of nitrogen groups with a much higher basicity, which enhances the intrinsic ORR activity of FeN_4C_{12} moieties through chemical or electronic effects.

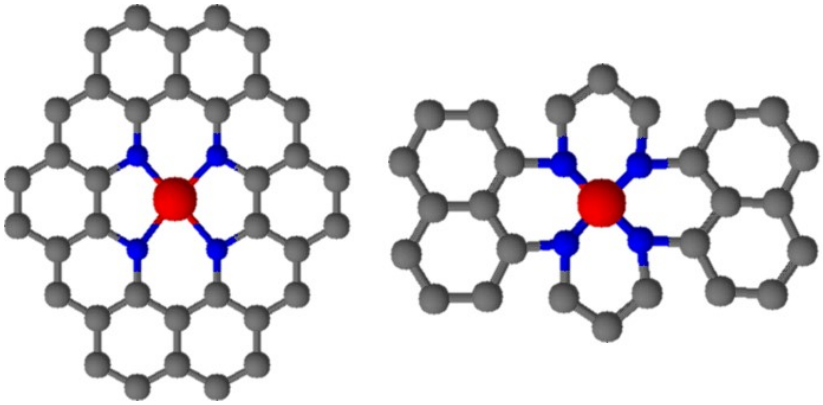

Figure 1.15: Structure of two proposed FeN_4 moieties in graphene sheets (FeN_4C_{10} and FeN_4C_{12} moieties, left and right, respectively).

In summary, different structures of the active sites for the ORR in Fe/N/C catalysts have been proposed, such as the FeN_4 moieties (including N-FeN_{2+2}, FeN_4C_{10} and FeN_4C_{12}), FeN_2, Fe_{NP}/C, Fe/Fe_xC (promoting the activity of the subjacent N-doped carbon atoms) and even bimetallic Fe_2N_5 sites. Furthermore the Fe-containing active sites, carbon atoms next to the pyridinic-N have been proposed as active sites with Lewis basicity. However, these proposed active sites have not yet been clearly identified and/or quantified experimentally.

Moreover, the reaction mechanisms that occur at the different structures proposed as active sites have not been clarified. Hence, the four- *vs.* two-electron selectivity and the possibility of the existence of one or two active

sites are considered.

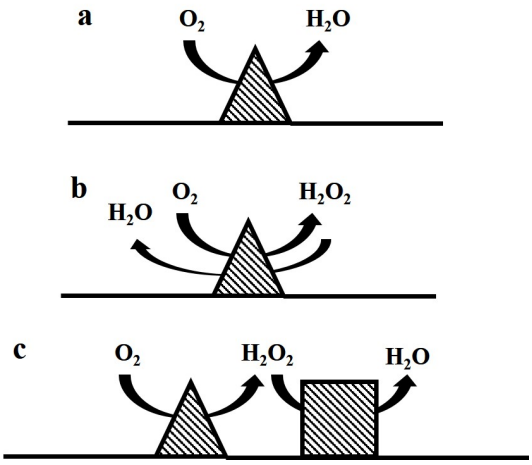

Figure 1.16: Mechanisms for the oxygen reduction reaction. a) Single site direct $4e^-$ mechanism b) Single site consequential $2e^- + 2e^-$ mechanism c) Bifunctional consequential $2e^- + 2e^-$ mechanism.

The four-electron pathway shown in Figure 1.16a occurs in a single active site, which is most likely an FeN_4 moiety proposed as the most likely formed active site. The other possible mechanism shown in Figure 1.16b and Figure 1.16c occurs *via* a peroxide intermediate formation in the ORR. In Figure 1.16b, the peroxide intermediate can be desorbed from the active site and further readsorbed in the same site (possible mechanism inside micropores, where the formation of peroxide is not detected). In Figure 1.16c, the peroxide intermediate interacts with another site that promotes the reduction of peroxide to the final ORR product, as in the mechanism proposed by Mukerjee's group in acidic media (see Figure 1.14).

However, the lack of a specific method to measure the number of active sites, such as CO-stripping in Pt-based catalysts [140, 141], hinders the proper identification and quantification of the active sites formed in NPMCs. In this sense, some approaches using CN^-, SCN^- anions or even CO as probe molecules for the Fe-active sites have been explored with unsuccessful results [3, 91, 142, 143]. It has been observed that the use of SCN^- and CN^-, in acidic and alkaline electrolytes, respectively, acts as an inhibitor of the ORR activity for the Fe-based catalysts, and thus, these ions are assumed to interact with at least some of the Fe active sites present in NPMCs. Nevertheless,

how is the interaction between the probe molecules (SCN^- and CN^-) and the Fe-active sites has not yet been demonstrated. Therefore, it has not been possible identify and quantify the Fe species.

Interestingly, no deactivation of the performance of the Fe-based ORR catalysts was observed in the presence of CO at room temperature. Nevertheless, Strasser and co-workers recently reported that the use of CO pulse chemisorption/desorption at low temperature (193 K) along with temperature-programmed desorption (TPD) are successful tools for quantifying the surface adsorption sites of M/N/C catalysts [144]. The analysis of a Fe/N/C catalyst by Mössbauer spectroscopy confirms the presence of FeN_4 ensembles in the catalyst. Moreover, the use of CO pulse chemisorption/desorption at low temperature offers an insight into the possibility of quantifying the active site density and intrinsic TOF activity descriptors in this Fe/N/C catalyst. For the sake of comparison, the same study with CO molecules was conducted using both metal-free N-C and Fe/N/C catalysts. In this study, CO molecules were not adsorbed in the metal-free catalyst; therefore, the authors assumed that the CO adsorption occurs in the metal active site. Moreover, the amount of CO adsorbed increases with ORR activity, allowing a relation to be established between the amount of active sites and the intrinsic TOF activity descriptors.

The increased knowledge obtained over the past years regarding the nature of the active sites for the ORR in Fe/N/C catalysts shows the potential for designing catalysts with improved ORR performances.

1.2.4 Durability of non-precious-metal catalysts

Another important drawback for the widespread utilization of fuel cells is the durability of the catalysts, irrespective of whether they are based on Pt or NPMCs. Both families of catalysts use carbon materials as supports or matrices in the final structure of the active sites. Carbon corrosion has been a major research topic as one of the major sources of performance loss in Pt/C PEMFCs, although Pt dissolution is also an important degradation mechanism in fuel cells [145-148]. The collapse of the structure of carbon supports after operation conditions may reduce the porosity of the catalyst, producing mass transport limitations, as shown by Schulenburg et al. [149].

Rapid carbon corrosion Eq. 1.16 occurs during the operation of fuel

cells, particularly at high potentials. A fuel cell can reach high potentials of up to 1.6 V during start-up/shutdown and up to 1.4 V for the transient fuel starvation and more moderate potentials when it works at *open circuit voltage* (OCV), commonly 0.9 V or during operating potential at 0.6 V to 1.0 V. The corrosion of the carbon is mainly produced by transient events that polarize either the anode or the cathode at high electric potentials [150, 151]. While complete fuel starvation is a rare incident, the build-up of a H_2/air front at the anode systematically occurs during start-up and shutdown [152, 153].

$$C + 2H_2O \rightarrow CO_2 + 4H^+ + 4e^- \text{ at } 0.4 \text{ V} \tag{1.16}$$

Although the degradation of Pt/C-based catalysts has been extensively studied, the degradation mechanism of NPMCs is still a relatively unexplored field. Important questions about the effect of high-voltage transients on NPMCs include whether the degradation of the $Fe/N_x/C_y$ active sites precedes or follows the carbon corrosion process and whether the degradation rate of NPMCs is faster than that of Pt/C catalysts subjected to identical start-up/shutdown protocols. In addition, start-up/shutdown cycling protocols may be used as an interesting means of identifying the active sites in NPMCs catalysts through a reverse strategy. By degrading a catalyst to different extents, a wide range of ORR activities may be obtained, and a post mortem characterisation by spectroscopic techniques or even using *in situ* investigations of degradation by identical location transmission electron microscopy (IL-TEM) can be compared to the unused catalyst [153, 154].

On the other hand, the use of more graphitized carbon materials such as activated carbon, carbon nanotubes or graphene results in more stable catalysts than the ones prepared from carbon black [97, 109, 155]. This is because graphene and CNTs are more resistant towards oxidation than carbon black and even than activated carbon.

The durability of NPMCs for the ORR has been recently addressed. Zelenay's group compared the use of different carbon sources (carbon black, activated carbon and CNTs) for the synthesis of Fe-PANI/C-based catalysts [97]. They showed that multi-walled carbon nanotube (MWNT)-supported catalysts have higher resistance towards degradation for more than 500 h at a cell voltage of 0.4 V, generating a current density of 0.3 $A{\cdot}cm^{-2}$ in a

PEM fuel cell. The same group reported the highest ORR performance for N-Fe-CNT/CNP in an alkaline electrolyte, showing an exceptional durability and even enhancing the activity (50 mV higher at half-wave potential) of the catalyst after 5000 cycles in the potential range of 0.6 V to 1.0 V in an O_2-saturated electrolyte [89]. In general, the durability of NPMCs in alkaline electrolytes is higher than that of Pt/C-based catalysts, even when the catalysts are subjected to severe degradation tests, simulating the start-up/shutdown operating range up to at least 1.4 V. Along this line, Sahraie et al. reported a NPMC prepared from ionic liquids as precursors with an excellent durability up to 1.3 V in a N_2-saturated alkaline medium [156]. Along the same line, one of the works presented in this thesis has observed high durability of Fe/N/C catalysts based on graphene (graphene nanoplates) or on multi-walled carbon nanotubes (MWCNTs), even when they are subjected to high potentials up to 1.4 V during 3000 cycles in O_2-saturated alkaline media in a RDE [108]. The stability of these Fe/N-based catalysts in alkaline electrolytes is higher than that of the benchmark Pt/C (40 wt.%) under the same measurement conditions.

Goellner et al. recently reported an extensive study on the degradation of an Fe/N/C catalyst to evaluate whether the degradation of the NPMCs primarily resulted from carbon corrosion, as in the Pt/C-based catalyst, or from the dissolution of the contained metal [153]. The study investigated the changes induced by high-voltage transients in the ORR activity, morphology and spectroscopic response of the catalyst, applying step potential cycles at 0.9 V and 1.4 V with 3 s at each step in a N_2-saturated acidic electrolyte. The degradation was strongly enhanced at high temperature, which is correlated with an increased carbon-corrosion rate and the destruction of the FeN_x-based active sites. They proposed that the Fe/N/C initially contains two types of FeN_x active sites, ones hosted in the micropores and the others in the defect sites. The oxidation of carbon produces several morphological changes at the surface of the catalyst, and Fe ions may be solvated and removed by water, most likely as Fe^{II} (see Figure 1.17).

To assess whether the higher stability of Fe/N/Graphene nanoplates catalyst reported in this thesis is related to a better resistance against corrosion, the evolution of the catalyst with the applied potential (from 0.6 V to 1.4 V *vs.* RHE) was studied using *in situ* electrochemical infrared spectroscopy (EC-SPAIRS). Carbon stability can be monitored by following the evolution

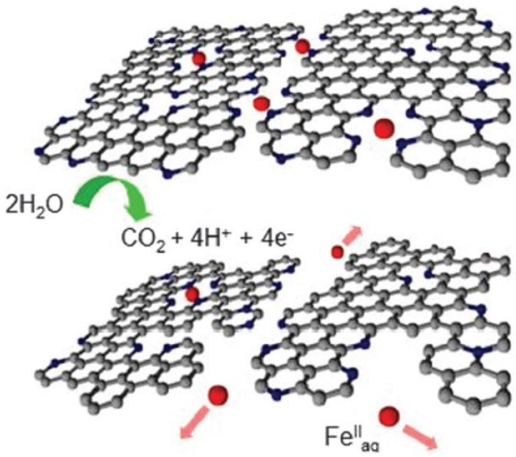

Figure 1.17: Scheme of the degradation mechanism of the catalyst caused by the carbon corrosion [153].

of evolved CO_2 (or carbonates in alkaline electrolyte). The spectra recorded for the Fe/N/graphene nanoplate catalyst are featureless, and infrared bands indicative of the formation of carbonates or other oxidized species are not observed [108].

1.3 Scope of the research

This thesis has investigated different Pt-free electrocatalysts for the ORR, mainly non-precious-metal catalysts based on iron and metal-free catalysts based on carbon materials doped with heteroatoms such as nitrogen and sulfur. The study of the electrocatalysts consists of exploring different synthesis methods used for their preparation, as well as an extensive structural and electrochemical characterization of the prepared materials. The main objectives pursued in this work are as follows:

- Study the structure and activity of metal-free catalysts for the ORR in N-doped carbon electrocatalysts and evaluate the effect of the co-doping of N and S heteroatoms.
- Preparing highly active NPMCs by using different synthesis methods, both chemical and mechanochemical methods. Furthermore, study the influences of different transitions metals, carbon matrices and nitrogen

contents on the structure and activity of the catalysts.

- Study the behaviour of NPMCs at different pHs. Evaluate the effect of the counter ion and the possible mechanisms for the different activities observed in acidic and alkaline electrolytes.
- Attempt to clarify the nature of the active sites formed in the Fe/N/C catalysts and establish a possible correlation between structure and activity of the NPMCs.
- Study the durability of the catalysts and the possible causes of the degradation experienced after long periods of operation.

1.4 References

[1] J. Andrews, B. Shabani, The role of hydrogen in a global sustainable energy strategy, Wiley Interdisciplinary Reviews: Energy and Environment, 3 (2014) 474-489.

[2] I.E. Agency, Energy and Climate Change. World Energy Outlook Special Report, 2015.

[3] M.S. Thorum, J.M. Hankett, A.A. Gewirth, Poisoning the Oxygen Reduction Reaction on Carbon-Supported Fe and Cu Electrocatalysts: Evidence for Metal-Centered Activity, The Journal of Physical Chemistry Letters, 2 (2011) 295-298.

[4] U. Eberle, B. Müller, R. von Helmolt, Fuel cell electric vehicles and hydrogen infrastructure: status 2012, Energy & environmental science, 5 (2012) 8780-8798.

[5] I.E. Agency, IEA Energy Technology Essentials - Hydrogen Production and Distribution, (2007).

[6] J. Larminie, A. Dicks, Fuel Cell System Explained, 2003.

[7] L.J.M.J. Blomen, M.N. Mugerwa, Fuel Cell Systems, Springer Science and Business Media, LLC, New York, 1993.

[8] K. Mauritz, R. Moore, State of Understanding of Nafion, Chemical reviews, 104 (2004) 4535-4586.

[9] V. Ramani, Fuel cells, The Electrochemical Society interface, 15 (2006) 41-44.

[10] A.J. Bard, L.R. Faulkner, Electrochemical methods : fundamentals and applications, John Wiley & Sons2001.

[11] H.A. Gasteiger, J. Garche, Fuel Cells, Handbook of Heterogeneous Catalysis, Wiley-VCH Verlag GmbH & Co. KGaA2008.

[12] R.P. O'Hayre, S.-W. Cha, W. Colella, F.B. Prinz, Fuel Cell. Fundamentals, John Wiley & Sons, New Jersey, 2006.

[13] O. Deavin, S. Murphy, A. Ong, S. Poynton, R. Zeng, H. Herman, J. Var-

coe, Anion-exchange membranes for alkaline polymer electrolyte fuel cells: comparison of pendent benzyltrimethylammonium- and benzylmethylimidazolium-head-groups, Energy & environmental science, 5 (2012) 8584-8597.

[14] M. N.M., R.J. P.N., Surface studies of model fuel cell electrocatalysts, Surface Science Reports, 45 (2002) 117-229.

[15] D.B. Sepa, M.V. Vojnovic, L.M. Vracar, A. Damjanovic, Different views regarding the kinetics and mechanisms of oxygen reduction at Pt and Pd electrodes, Electrochimica Acta, 32 (1987) 129-134.

[16] B.B. Blizanac, P.N. Ross, N.M. Markovic, Oxygen electroreduction on Ag(1 1 1): The pH effect, Electrochimica Acta, 52 (2007) 2264-2271.

[17] N. Ramaswamy, S. Mukerjee, Fundamental Mechanistic Understanding of Electrocatalysis of Oxygen Reduction on Pt and Non-Pt Surfaces: Acid versus Alkaline Media, Advances in Physical Chemistry, 2012 (2012) 1-17.

[18] P. Rodriguez, M.T.M. Koper, Electrocatalysis on gold, PCCP. Physical chemistry chemical physics, 16 (2014) 13583-13594.

[19] N. Ramaswamy, S. Mukerjee, Influence of Inner- and Outer-Sphere Electron Transfer Mechanisms during Electrocatalysis of Oxygen Reduction in Alkaline Media, The Journal of Physical Chemistry C, 115 (2011) 18015-18026.

[20] C.C.L. McCrory, S. Jung, I.M. Ferrer, S.M. Chatman, J.C. Peters, T.F. Jaramillo, Benchmarking Hydrogen Evolving Reaction and Oxygen Evolving Reaction Electrocatalysts for Solar Water Splitting Devices, J. Am. Chem. Soc. , 137 (2015) 4347-4357.

[21] I. Katsounaros, S. Cherevko, A.R. Zeradjanin, K.J.J. Mayrhofer, Oxygen Electrochemistry as a Cornerstone for Sustainable Energy Conversion, Angew. Chem. Int. Ed. , 53 (2014) 102-121.

[22] W. Liu, D. Zuckerbrod, In Situ Detection of Hydrogen Peroxide in PEM Fuel Cells, Journal of the Electrochemical Society, 152 (2005) A1165-A1170.

[23] H.A. Gasteiger, N.M. Marković, Just a Dream-or Future Reality?, Science, 324 (2009) 48-49.

[24] W. Liu, M. Crum, Effective Testing Matrix for Studying Membrane

Durability in PEM Fuel Cells: Part I. Chemical Durability, ECS transactions, 3 (2006) 531-540.

[25] M.M. Bomgardner, Making Fuel Cell Vehicles An [Almost] Affordable Reality, Chemical & Engineering News, 92 (2014) 17-20.

[26] R.G. Cawthorn, The Platinum Group Element Deposits of the Bushveld Complex in South Africa, Platinum Metals Review, 54 (2010) 205-215.

[27] M. Debe, U.S. Department of Energy Hydrogen and Fuel Cells Program 2011 Annual Merit Review Proceedings, 2011.

[28] H. Gasteiger, S. Kocha, B. Sompalli, F. Wagner, Activity benchmarks and requirements for Pt, Pt-alloy, and non-Pt oxygen reduction catalysts for PEMFCs, Applied catalysis. B, Environmental, 56 (2005) 9-35.

[29] U.S. Department of Energy, Multi-Year Research, Development and Demonstration Plan.Technical Plan-Fuel cells, 2012.

[30] I.E.L. Stephens, A.S. Bondarenko, U. Gronbjerg, J. Rossmeisl, I. Chorkendorff, Understanding the electrocatalysis of oxygen reduction on platinum and its alloys, Energy & Environmental Science, 5 (2012) 6744-6762.

[31] C. Chen, Y. Kang, Z. Huo, Z. Zhu, W. Huang, H.L. Xin, J.D. Snyder, D. Li, J.A. Herron, M. Mavrikakis, M. Chi, K.L. More, Y. Li, N.M. Markovic, G.A. Somorjai, P. Yang, V.R. Stamenkovic, Highly Crystalline Multimetallic Nanoframes with Three-Dimensional Electrocatalytic Surfaces, Science, 343 (2014) 1339-1343.

[32] X. Huang, Z. Zhao, L. Cao, Y. Chen, E. Zhu, Z. Lin, M. Li, A. Yan, A. Zettl, Y.M. Wang, X. Duan, T. Mueller, Y. Huang, High-performance transition metal-doped Pt3Ni octahedra for oxygen reduction reaction, Science, 348 (2015) 1230-1234.

[33] M.S. Faber, S. Jin, Earth-abundant inorganic electrocatalysts and their nanostructures for energy conversion applications, Energy & Environmental Science, 7 (2014) 3519-3542.

[34] G.B. Haxel, J.B. Hedrick, G.J. Orris, Rare Earth Elements-Critical Resources for High Technology, in: P.H. Stauffer, J.W.H. II (Eds.), 2002.

[35] F. Jaouen, E. Proietti, M. Lefèvre, R. Chenitz, J.-P. Dodelet, G. Wu,

H. Chung, C. Johnston, P. Zelenay, Recent advances in non-precious metal catalysis for oxygen-reduction reaction in polymer electrolyte fuel cells, Energy & Environmental Science, 4 (2011) 114-130.

[36] R. Jasinski, A New Fuel Cell Cathode Catalyst, Nature, 201 (1964) 1212-1213.

[37] K. Wiesener, N4-chelates as electrocatalyst for cathodic oxygen reduction, Electrochimica Acta, 31 (1986) 1073-1078.

[38] R. Franke, D. Ohms, K. Wiesener, Investigation of the influence of thermal treatment on the properties of carbon materials modified by N4-chelates for the reduction of oxygen in acidic media, Journal of Electroanalytical Chemistry, 260 (1989) 63-73.

[39] P.H. Matter, E. Wang, M. Arias, E.J. Biddinger, U.S. Ozkan, Oxygen reduction reaction catalysts prepared from acetonitrile pyrolysis over alumina-supported metal particles, Journal of Physical Chemistry B, 110 (2006) 18374-18384.

[40] V. Nallathambi, J.W. Lee, S.P. Kumaraguru, G. Wu, B.N. Popov, Development of high performance carbon composite catalyst for oxygen reduction reaction in PEM Proton Exchange Membrane fuel cells, Journal of Power Sources, 183 (2008) 34-42.

[41] M. Terrones, P.M. Ajayan, F. Banhart, X. Blase, D.L. Carroll, J.C. Charlier, R. Czerw, B. Foley, N. Grobert, R. Kamalakaran, P. Kohler-Redlich, M. Rühle, T. Seeger, H. Terrones, N-doping and coalescence of carbon nanotubes: synthesis and electronic properties, Appl Phys A, 74 (2002) 355-361.

[42] G. Lalande, R. Côté, D. Guay, J.P. Dodelet, L.T. Weng, P. Bertrand, Is nitrogen important in the formulation of Fe-based catalysts for oxygen reduction in solid polymer fuel cells?, Electrochimica Acta, 42 (1997) 1379-1388.

[43] K. Gong, F. Du, Z. Xia, M. Durstock, L. Dai, Nitrogen-Doped Carbon Nanotube Arrays with High Electrocatalytic Activity for Oxygen Reduction, Science, 323 (2009) 760-764.

[44] C. Choi, S. Park, S. Woo, Heteroatom doped carbons prepared by the pyrolysis of bio-derived amino acids as highly active catalysts for oxygen

electro-reduction reactions, Green chemistry, 13 (2011) 406-412.

[45] R.A. Sidik, A.B. Anderson, N.P. Subramanian, S.P. Kumaraguru, B.N. Popov, O2 Reduction on Graphite and Nitrogen-Doped Graphite:? Experiment and Theory, The Journal of Physical Chemistry B, 110 (2006) 1787-1793.

[46] H.-W. Liang, X. Zhuang, S. Brüller, X. Feng, K. Müllen, Hierarchically porous carbons with optimized nitrogen doping as highly active electrocatalysts for oxygen reduction, Nat Commun, 5 (2014).

[47] N.P. Subramanian, X. Li, V. Nallathambi, S.P. Kumaraguru, H. Colon-Mercado, G. Wu, J.-W. Lee, B.N. Popov, Nitrogen-modified carbon-based catalysts for oxygen reduction reaction in polymer electrolyte membrane fuel cells, Journal of Power Sources, 188 (2009) 38-44.

[48] D. Yu, Q. Zhang, L. Dai, Highly Efficient Metal-Free Growth of Nitrogen-Doped Single-Walled Carbon Nanotubes on Plasma-Etched Substrates for Oxygen Reduction, Journal of the American Chemical Society, 132 (2010) 15127-15129.

[49] K.A. Kurak, A.B. Anderson, Nitrogen-Treated Graphite and Oxygen Electroreduction on Pyridinic Edge Sites, The Journal of Physical Chemistry C, 113 (2009) 6730-6734.

[50] Y. Zheng, Y. Jiao, J. Chen, J. Liu, J. Liang, A. Du, W. Zhang, Z. Zhu, S. Smith, M. Jaroniec, G.Q. Lu, S. Qiao, Nanoporous Graphitic-C3N4@Carbon Metal-Free Electrocatalysts for Highly Efficient Oxygen Reduction, Journal of the American Chemical Society, 133 (2011) 20116-20119.

[51] S. Yang, X. Feng, X. Wang, K. Müllen, Graphene-Based Carbon Nitride Nanosheets as Efficient Metal-Free Electrocatalysts for Oxygen Reduction Reactions, Angewandte Chemie International Edition, 50 (2011) 5339-5343.

[52] Y. Tang, B.L. Allen, D.R. Kauffman, A. Star, Electrocatalytic Activity of Nitrogen-Doped Carbon Nanotube Cups, Journal of the American Chemical Society, 131 (2009) 13200-13201.

[53] R. Liu, D. Wu, X. Feng, K. Müllen, Nitrogen-Doped Ordered Mesoporous Graphitic Arrays with High Electrocatalytic Activity for Oxygen Reduction, Angewandte Chemie International Edition, 49 (2010) 2565-2569.

[54] L. Qu, Y. Liu, J.-B. Baek, L. Dai, Nitrogen-Doped Graphene as Efficient Metal-Free Electrocatalyst for Oxygen Reduction in Fuel Cells, ACS Nano, 4 (2010) 1321-1326.

[55] S. Kundu, T. Nagaiah, W. Xia, Y. Wang, S. Van Dommele, J. Bitter, M. Santa, G. Grundmeier, M. Bron, W. Schuhmann, M. Muhler, Electrocatalytic Activity and Stability of Nitrogen-Containing Carbon Nanotubes in the Oxygen Reduction Reaction, The journal of physical chemistry. C, 113 (2009) 14302- 14310.

[56] H. Li, W. Kang, L. Wang, Q. Yue, S. Xu, H. Wang, J. Liu, Synthesis of three-dimensional flowerlike nitrogen-doped carbons by a copyrolysis route and the effect of nitrogen species on the electrocatalytic activity in oxygen reduction reaction, Carbon, 54 (2013) 249-257.

[57] C. Rao, C. Cabrera, Y. Ishikawa, In Search of the Active Site in Nitrogen-Doped Carbon Nanotube Electrodes for the Oxygen Reduction Reaction, The journal of physical chemistry letters, 1 (2010) 2622-2627.

[58] S. Yasuda, L. Yu, J. Kim, K. Murakoshi, Selective nitrogen doping in graphene for oxygen reduction reactions, Chemical communications (London. 1996), 49 (2013) 9627-9629.

[59] L. Lai, J.R. Potts, D. Zhan, L. Wang, C.K. Poh, C. Tang, H. Gong, Z. Shen, J. Lin, R.S. Ruoff, Exploration of the active center structure of nitrogen-doped graphene-based catalysts for oxygen reduction reaction, Energy & Environmental Science, 5 (2012) 7936-7942.

[60] X. Wang, Y. Liu, D. Zhu, L. Zhang, H. Ma, N. Yao, B. Zhang, Controllable Growth, Structure, and Low Field Emission of Well-Aligned CNx Nanotubes, The Journal of Physical Chemistry B, 106 (2002) 2186-2190.

[61] J. Casanovas, J.M. Ricart, J. Rubio, F. Illas, J.M. Jiménez-Mateos, Origin of the Large N 1s Binding Energy in X-ray Photoelectron Spectra of Calcined Carbonaceous Materials, Journal of the American Chemical Society, 118 (1996) 8071-8076.

[62] S. Kuroki, Y. Nabae, M. Chokai, M.-a. Kakimoto, S. Miyata, Oxygen reduction activity of pyrolyzed polypyrroles studied by 15N solid-state NMR and XPS with principal component analysis, Carbon, 50 (2012) 153-162.

[63] M. Liu, R. Zhang, W. Chen, Graphene-Supported Nanoelectrocatalysts for Fuel Cells: Synthesis, Properties, and Applications, Chemical Reviews, 114 (2014) 5117-5160.

[64] K. Parvez, S. Yang, Y. Hernandez, A. Winter, A. Turchanin, X. Feng, K. Müllen, Nitrogen-Doped Graphene and Its Iron-Based Composite As Efficient Electrocatalysts for Oxygen Reduction Reaction, ACS nano, 6 (2012) 9541-9550.

[65] M.S. Dresselhaus, G. Dresselhaus, J.C. Charlier, E. Hernandez, Electronic, thermal and mechanical properties of carbon nanotubes, Philosophical transactions - Royal Society. Mathematical, Physical and engineering sciences, 362 (2004) 2065-2098.

[66] L.G. Bulusheva, A.V. Okotrub, I.A. Kinloch, I.P. Asanov, A.G. Kurenya, A.G. Kudashov, X. Chen, H. Song, Effect of nitrogen doping on Raman spectra of multi-walled carbon nanotubes, Physica status solidi. B, Basic research, 245 (2008) 1971-1974.

[67] L. Dai, Y. Xue, L. Qu, H.-J. Choi, J.-B. Baek, Metal-Free Catalysts for Oxygen Reduction Reaction, Chemical reviews, 115 (2015) 4823-4892.

[68] D. Guo, R. Shibuya, C. Akiba, S. Saji, T. Kondo, J. Nakamura, Active sites of nitrogen-doped carbon materials for oxygen reduction reaction clarified using model catalysts, Science, 351 (2016) 361-365.

[69] X. Hu, Y. Wu, H. Li, Z. Zhang, Adsorption and Activation of O2 on Nitrogen-Doped Carbon Nanotubes, The Journal of Physical Chemistry C, 114 (2010) 9603-9607.

[70] C. Domínguez, F.J. Pérez-Alonso, M. Abdel Salam, S.A. Al-Thabaiti, A.Y. Obaid, A.A. Alshehri, J.L. Gómez de la Fuente, J.L.G. Fierro, S. Rojas, On the relationship between N content, textural properties and catalytic performance for the oxygen reduction reaction of N/CNT, Applied Catalysis B: Environmental, 162 (2015) 420-429.

[71] M. Terrones, Carbon nanotubes: synthesis and properties, electronic devices and other emerging applications, International materials reviews, 49 (2004) 325-377.

[72] M. Yu, Y. Huang, C. Li, Y. Zeng, W. Wang, Y. Li, P. Fang, X. Lu, Y.

Tong, Building Three-Dimensional Graphene Frameworks for Energy Storage and Catalysis, Advanced Functional Materials, 25 (2015) 324-330.

[73] F.J. Maldonado Hódar, F.J. Maldonado-Hódar, C. Moreno Castilla, J. Rivera Utrilla, Y. Hanzawa, Y. Yamada, Catalytic Graphitization of Carbon Aerogels by Transition Metals, Langmuir, 16 (2000) 4367-4373.

[74] J. Masa, A. Zhao, W. Xia, Z. Sun, B. Mei, M. Muhler, W. Schuhmann, Trace metal residues promote the activity of supposedly metal-free nitrogen-modified carbon catalysts for the oxygen reduction reaction, Electrochemistry communications, 34 (2013) 113-116.

[75] Y. Jiao, Y. Zheng, M. Jaroniec, S.Z. Qiao, Origin of the Electrocatalytic Oxygen Reduction Activity of Graphene-Based Catalysts: A Roadmap to Achieve the Best Performance, Journal of the American Chemical Society, 136 (2014) 4394-4403.

[76] S. Wang?, E. Iyyamperumal?, A. Roy, Y. Xue, D. Yu, L. Dai, Vertically Aligned BCN Nanotubes as Efficient Metal-Free Electrocatalysts for the Oxygen Reduction Reaction: A Synergetic Effect by Co-Doping with Boron and Nitrogen, Angewandte Chemie International Edition, 50 (2011) 11756-11760.

[77] Y. Xue, D. Yu, L. Dai, R. Wang, D. Li, A. Roy, F. Lu, H. Chen, Y. Liu, J. Qu, Three-dimensional B,N-doped graphene foam as a metal-free catalyst for oxygen reduction reaction, Physical Chemistry Chemical Physics, 15 (2013) 12220-12226.

[78] J. Zhang, Z. Zhao, Z. Xia, L. Dai, A metal-free bifunctional electrocatalyst for oxygen reduction and oxygen evolution reactions, Nat Nano, 10 (2015) 444-452.

[79] R. Nie, X. Bo, C. Luhana, A. Nsabimana, L. Guo, Simultaneous formation of nitrogen and sulfur-doped carbon nanotubes-mesoporous carbon and its electrocatalytic activity for oxygen reduction reaction, International Journal of Hydrogen Energy, 39 (2014) 12597-12603.

[80] D. Singh, J. Tian, K. Mamtani, J. King, J.T. Miller, U.S. Ozkan, A comparison of N-containing carbon nanostructures (CNx) and N-coordinated iron-carbon catalysts (FeNC) for the oxygen reduction reaction in acidic

media, Journal of Catalysis, 317 (2014) 30-43.

[81] J. Liang, Y. Jiao, M. Jaroniec, S.Z. Qiao, Sulfur and nitrogen dual-doped mesoporous graphene electrocatalyst for oxygen reduction with synergistically enhanced performance, Angewandte Chemie, 51 (2012) 11496-11500.

[82] C. Domínguez, F. Pérez Alonso, S. Al Thabaiti, S. Basahel, A. Obaid, A. Alyoubi, J.L. Gómez de la Fuente, S. Rojas, Effect of N and S co-doping of multiwalled carbon nanotubes for the oxygen reduction, Electrochimica Acta, 157 (2015) 158-165.

[83] Q. Shi, F. Peng, S. Liao, H. Wang, H. Yu, Z. Liu, B. Zhang, D. Su, Sulfur and nitrogen co-doped carbon nanotubes for enhancing electrochemical oxygen reduction activity in acidic and alkaline media, Journal of Materials Chemistry A, 1 (2013) 14853.

[84] F. Jaouen, J. Herranz, M. Lefevre, J.P. Dodelet, U.I. Kramm, I. Herrmann, P. Bogdanoff, J. Maruyama, T. Nagaoka, A. Garsuch, J.R. Dahn, T. Olson, S. Pylypenko, P. Atanassov, E.A. Ustinov, Cross-laboratory experimental study of non-noble-metal electrocatalysts for the oxygen reduction reaction, ACS applied materials & interfaces, 1 (2009) 1623-1639.

[85] M. Lefevre, E. Proietti, F. Jaouen, J.P. Dodelet, Iron-based catalysts with improved oxygen reduction activity in polymer electrolyte fuel cells, Science, 324 (2009) 71-74.

[86] E. Proietti, F. Jaouen, M. Lefèvre, N. Larouche, J. Tian, J. Herranz, J.-P. Dodelet, Iron-based cathode catalyst with enhanced power density in polymer electrolyte membrane fuel cells, Nature Communications, 2 (2011) 416.

[87] J.Y. Cheon, T. Kim, Y. Choi, H.Y. Jeong, M.G. Kim, Y.J. Sa, J. Kim, Z. Lee, T.H. Yang, K. Kwon, O. Terasaki, G.G. Park, R.R. Adzic, S.H. Joo, Ordered mesoporous porphyrinic carbons with very high electrocatalytic activity for the oxygen reduction reaction, Scientific Reports, 3 (2013) 2715.

[88] G. Wu, K.L. More, C.M. Johnston, P. Zelenay, High-performance electrocatalysts for oxygen reduction derived from polyaniline, iron, and cobalt, Science, 332 (2011) 443-447.

[89] H. Chung, J. Won, P. Zelenay, Active and stable carbon nanotube/-

nanoparticle composite electrocatalyst for oxygen reduction, Nature Communications, 4 (2013) 1922.

[90] H.W. Liang, W. Wei, Z.S. Wu, X. Feng, K. Müllen, Mesoporous metal-nitrogen-doped carbon electrocatalysts for highly efficient oxygen reduction reaction, Journal of the American Chemical Society, 135 (2013) 16002-16005.

[91] G.-P. Wu, J. Yang, D. Wang, R. Xu, K. Amine, C.-X. Lu, A novel route for preparing mesoporous carbon aerogels using inorganic templates under ambient drying, Materials Letters, 115 (2014) 1-4.

[92] F. Calle Vallejo, J. Martínez, J. Rossmeisl, Density functional studies of functionalized graphitic materials with late transition metals for oxygen reduction reactions, Physical Chemistry Chemical Physics, 13 (2011) 15639-15643.

[93] P. He, M. Lefèvre, G. Faubert, J.P. Dodelet, Oxygen reduction catalysts for polymer electrolyte fuel cells from the pyrolysis of various transition metal acetates adsorbed on 3,4,9,10-perylenetetracarboxylic dianhydride, Journal of New Materials for Electrochemical Systems, 2 (1999) 243-251.

[94] R. Yang, K. Stevens, J.R. Dahn, Investigation of Activity of Sputtered Transition-Metal (TM)-C-N (TM = V, Cr, Mn, Co, Ni) Catalysts for Oxygen Reduction Reaction, Journal of The Electrochemical Society, 155 (2008) B79-B91.

[95] F. Jaouen, J.-P. Dodelet, O2 Reduction Mechanism on Non-Noble Metal Catalysts for PEM Fuel Cells. Part I: Experimental Rates of O2 Electroreduction, H2O2 Electroreduction, and H2O2 Disproportionation, The Journal of Physical Chemistry C, 113 (2009) 15422-15432.

[96] M. Ferrandon, A.J. Kropf, D.J. Myers, K. Artyushkova, U. Kramm, P. Bogdanoff, G. Wu, C.M. Johnston, P. Zelenay, Multitechnique Characterization of a Polyaniline-Iron-Carbon Oxygen Reduction Catalyst, The Journal of Physical Chemistry C, 116 (2012) 16001-16013.

[97] G. Wu, K.L. More, P. Xu, H.L. Wang, M. Ferrandon, A.J. Kropf, D.J. Myers, S. Ma, C.M. Johnston, P. Zelenay, A carbon-nanotube-supported graphene-rich non-precious metal oxygen reduction catalyst with enhanced performance durability, Chemical communications, 49 (2013) 3291-3293.

[98] A. Bonakdarpour, M. Lefevre, R. Yang, F. Jaouen, T. Dahn, J.-P. Dodelet, J.R. Dahn, Impact of Loading in RRDE Experiments on Fe-N-C Catalysts: Two- or Four-Electron Oxygen Reduction?, Electrochemical and Solid-State Letters, 11 (2008) B105-B108.

[99] A. Serov, K. Artyushkova, P. Atanassov, Fe-N-C Oxygen Reduction Fuel Cell Catalyst Derived from Carbendazim: Synthesis, Structure, and Reactivity, Advanced Energy Materials, 4 (2014).

[100] W. Sicking, H.-G. Korth, G. Jansen, H. de Groot, R. Sustmann, Hydrogen Peroxide Decomposition by a Non-Heme Iron(III) Catalase Mimic: A DFT Study, Chemistry - A European Journal, 13 (2007) 4230-4245.

[101] K. Wiesener, D. Ohms, V. Neumann, R. Franke, N4 macrocycles as electrocatalysts for the cathodic reduction of oxygen, Materials Chemistry and Physics, 22 (1989) 457-475.

[102] R. Côté, G. Lalande, G. Faubert, D. Guay, J.P. Dodelet, G. Dénès, Non-noble metal-based catalysts for the reduction of oxygen in polymer electrolyte fuel cells, Journal of New Materials for Electrochemical Systems, 1 (1998) 7-16.

[103] C. Domínguez, F.J. Pérez-Alonso, M. Abdel Salam, J.L. Gómez de la Fuente, S.A. Al-Thabaiti, S.N. Basahel, M.A. Peña, J.L.G. Fierro, S. Rojas, Effect of transition metal (M: Fe, Co or Mn) for the oxygen reduction reaction with non-precious metal catalysts in acid medium, International Journal of Hydrogen Energy, 39 (2014) 5309-5318.

[104] F. Jaouen, M. Lefèvre, J.-P. Dodelet, M. Cai, Heat-Treated Fe/N/C Catalysts for O2Electroreduction: Are Active Sites Hosted in Micropores?, The Journal of Physical Chemistry B, 110 (2006) 5553-5558.

[105] Z. Chen, D. Higgins, A. Yu, L. Zhang, J. Zhang, A review on non-precious metal electrocatalysts for PEM fuel cells, Energy & Environmental Science, 4 (2011) 3167-3192.

[106] T.E. Wood, Z. Tan, A.K. Schmoeckel, D. O'Neill, R. Atanasoski, Non-precious metal oxygen reduction catalyst for PEM fuel cells based on nitroaniline precursor, Journal of Power Sources, 178 (2008) 510-516.

[107] Y. Li, W. Zhou, H. Wang, L. Xie, Y. Liang, F. Wei, J.-C. Idrobo, S.J.

Pennycook, H. Dai, An oxygen reduction electrocatalyst based on carbon nanotube-graphene complexes, Nat Nano, 7 (2012) 394-400.

[108] C. Domínguez, F.J. Pérez-Alonso, M.A. Salam, S.A. Al-Thabaiti, M.A. Peña, F.J. García-García, L. Barrio, S. Rojas, Repercussion of the carbon matrix for the activity and stability of Fe/N/C electrocatalysts for the oxygen reduction reaction, Applied Catalysis B: Environmental, 183 (2016) 185-196.

[109] G. Wu, P. Zelenay, Nanostructured Nonprecious Metal Catalysts for Oxygen Reduction Reaction, Accounts of Chemical Research, 46 (2013) 1878-1889.

[110] S. Zhang, H. Zhang, X. Hua, S. Chen, Tailoring molecular architectures of Fe phthalocyanine on nanocarbon supports for high oxygen reduction performance, Journal of Materials Chemistry A, 3 (2015) 10013-10019.

[111] A.H. Lu, F. Schüth, Nanocasting: A Versatile Strategy for Creating Nanostructured Porous Materials, Advanced materials, 18 (2006) 1793-1805.

[112] W. Lu, Z. Wei, Z.-Y. Gu, T.-F. Liu, J. Park, J. Park, J. Tian, M. Zhang, Q. Zhang, T. Gentle Iii, M. Bosch, H.-C. Zhou, Tuning the structure and function of metal-organic frameworks via linker design, Chemical Society Reviews, 43 (2014) 5561-5593.

[113] A. Morozan, F. Jaouen, Metal organic frameworks for electrochemical applications, Energy & Environmental Science, 5 (2012) 9269-9290.

[114] K.S. Park, Z. Ni, A.P. Cote, J.Y. Choi, R. Huang, F.J. Uribe-Romo, H.K. Chae, M. O'Keeffe, O.M. Yaghi, Exceptional chemical and thermal stability of zeolitic imidazolate frameworks, Proceedings of the National Academy of Sciences of the United States of America, 103 (2006) 10186-10191.

[115] S. Ma, G. Goenaga, A. Call, D.-J. Liu, Cobalt Imidazolate Framework as Precursor for Oxygen Reduction Reaction Electrocatalysts, Chemistry - A European Journal, 17 (2011) 2063-2067. [116] U.I. Kramm, I. Herrmann-Geppert, S. Fiechter, G. Zehl, I. Zizak, I. Dorbandt, D. Schmeißer, P. Bogdanoff, Effect of iron-carbide formation on the number of active sites in Fe-N-C catalysts for the oxygen reduction reaction in acidic media, Journal of Materials Chemistry A, 2 (2014) 2663.

[117] M. Lefèvre, J.P. Dodelet, Recent Advances in Non-Precious Metal Electrocatalysts for Oxygen Reduction in PEM Fuel Cells, ECS Transactions, 45 (2012) 35-44.

[118] D. Zhao, J.-L. Shui, C. Chen, X. Chen, B.M. Reprogle, D. Wang, D.-J. Liu, Iron imidazolate framework as precursor for electrocatalysts in polymer electrolyte membrane fuel cells, Chemical Science, 3 (2012) 3200-3205.

[119] S. Yuan, J.-L. Shui, L. Grabstanowicz, C. Chen, S. Commet, B. Reprogle, T. Xu, L. Yu, D.-J. Liu, A Highly Active and Support-Free Oxygen Reduction Catalyst Prepared from Ultrahigh-Surface-Area Porous Polyporphyrin, Angewandte Chemie (International ed.), 52 (2013) 8349-8353.

[120] A. Zitolo, V. Goellner, V. Armel, M.-T. Sougrati, T. Mineva, L. Stievano, E. Fonda, F. Jaouen, Identification of catalytic sites for oxygen reduction in iron- and nitrogen-doped graphene materials, Nature Materials, 14 (2015) 937-942.

[121] N. Markovic, Kinetics of oxygen reduction on Pt(hkl) electrodes: Implications for the crystallite size effect with supported Pt electrocatalysts, Journal of the Electrochemical Society, 144 (1997) 1591-1597.

[122] J. Spendelow, A. Wieckowski, Electrocatalysis of oxygen reduction and small alcohol oxidation in alkaline media, PCCP. Physical chemistry chemical physics, 9 (2007) 2654-2675.

[123] D. Strmcnik, K. Kodama, D. van der Vliet, J. Greeley, V.R. Stamenkovic, N.M. Markovi?, The role of non-covalent interactions in electrocatalytic fuel-cell reactions on platinum, Nature chemistry, 1 (2009) 466-472.

[124] C. Domínguez, F.J. Pérez-Alonso, J.L. Gómez de la Fuente, S.A. Al-Thabaiti, S.N. Basahel, A.O. Alyoubi, A.A. Alshehri, M.A. Peña, S. Rojas, Influence of the electrolyte for the oxygen reduction reaction with Fe/N/C and Fe/N/CNT electrocatalysts, Journal of Power Sources, 271 (2014) 87-96.

[125] C. Dominguez, F.J. Perez-Alonso, M.A. Salam, S.A. Al-Thabaiti, M.A. Pena, L. Barrio, S. Rojas, Effect of the N content of Fe/N/graphene catalysts for the oxygen reduction reaction in alkaline media, Journal of Materials Chemistry A, 3 (2015) 24487-24494.

[126] A.L. Bouwkamp Wijnoltz, A.L. Bouwkamp-Wijnoltz, W. Visscher,

J.A.R. van Veen, E. Boellaard, A.M. van der Kraan, S.C. Tang, On Active-Site Heterogeneity in Pyrolyzed Carbon-Supported Iron Porphyrin Catalysts for the Electrochemical Reduction of Oxygen: An In Situ Mössbauer Study, The journal of physical chemistry. B, 106 (2002) 12993-13001.

[127] U.I. Kramm, J. Herranz, N. Larouche, T.M. Arruda, M. Lefevre, F. Jaouen, P. Bogdanoff, S. Fiechter, I. Abs-Wurmbach, S. Mukerjee, J.P. Dodelet, Structure of the catalytic sites in Fe/N/C-catalysts for O2-reduction in PEM fuel cells, Physical Chemistry Chemical Physics, 14 (2012) 11673-11688.

[128] J. Tian, A. Morozan, M.T. Sougrati, M. Lefèvre, R. Chenitz, J.-P. Dodelet, D. Jones, F. Jaouen, Optimized Synthesis of Fe/N/C Cathode Catalysts for PEM Fuel Cells: A Matter of Iron-Ligand Coordination Strength, Angewandte Chemie International Edition, 52 (2013) 6867-6870.

[129] J. Herranz, F. Jaouen, M. Lefèvre, U.I. Kramm, E. Proietti, J.-P. Dodelet, P. Bogdanoff, S. Fiechter, I. Abs-Wurmbach, P. Bertrand, T.M. Arruda, S. Mukerjee, Unveiling N-Protonation and Anion-Binding Effects on Fe/N/C Catalysts for O2 Reduction in Proton-Exchange-Membrane Fuel Cells, The Journal of Physical Chemistry C, 115 (2011) 16087-16097.

[130] M. Lefèvre, J.P. Dodelet, P. Bertrand, O2 Reduction in PEM Fuel Cells: Activity and Active Site Structural Information for Catalysts Obtained by the Pyrolysis at High Temperature of Fe Precursors, The Journal of Physical Chemistry B, 104 (2000) 11238-11247.

[131] M. Lefèvre, J.P. Dodelet, P. Bertrand, Molecular Oxygen Reduction in PEM Fuel Cells:? Evidence for the Simultaneous Presence of Two Active Sites in Fe-Based Catalysts, The Journal of Physical Chemistry B, 106 (2002) 8705-8713.

[132] U.I. Kramm, M. Lefèvre, N. Larouche, D. Schmeisser, J.-P. Dodelet, Correlations between Mass Activity and Physicochemical Properties of Fe/N/C Catalysts for the ORR in PEM Fuel Cell via 57Fe Mössbauer Spectroscopy and Other Techniques, Journal of the American Chemical Society, 136 (2014) 978-985.

[133] K. Strickland, E. Miner, Q. Jia, U. Tylus, N. Ramaswamy, W. Liang, M.-T. Sougrati, F. Jaouen, S. Mukerjee, Highly active oxygen reduction

non-platinum group metal electrocatalyst without direct metal-nitrogen coordination, Nature Communications, 6 (2015) 7343.

[134] S. Kattel, P. Atanassov, B. Kiefer, A density functional theory study of oxygen reduction reaction on non-PGM Fe-Nx-C electrocatalysts, Physical Chemistry Chemical Physics, 16 (2014) 13800-13806.

[135] U. Tylus, Q. Jia, K. Strickland, N. Ramaswamy, A. Serov, P. Atanassov, S. Mukerjee, Elucidating Oxygen Reduction Active Sites in Pyrolyzed Metal-Nitrogen Coordinated Non-Precious-Metal Electrocatalyst Systems, The Journal of Physical Chemistry C, 118 (2014) 8999-9008.

[136] C.E. Szakacs, M. Lefevre, U.I. Kramm, J.-P. Dodelet, F. Vidal, A density functional theory study of catalytic sites for oxygen reduction in Fe/N/C catalysts used in H2/O2 fuel cells, Physical Chemistry Chemical Physics, 16 (2014) 13654-13661.

[137] T.S. Olson, S. Pylypenko, J.E. Fulghum, P. Atanassov, Bifunctional Oxygen Reduction Reaction Mechanism on Non-Platinum Catalysts Derived from Pyrolyzed Porphyrins, Journal of The Electrochemical Society, 157 (2010) B54-B63.

[138] N. Ramaswamy, U. Tylus, Q. Jia, S. Mukerjee, Activity Descriptor Identification for Oxygen Reduction on Nonprecious Electrocatalysts: Linking Surface Science to Coordination Chemistry, Journal of the American Chemical Society, 135 (2013) 15443-15449.

[139] E.F. Holby, G. Wu, P. Zelenay, C.D. Taylor, Structure of Fe-Nx-C Defects in Oxygen Reduction Reaction Catalysts from First-Principles Modeling, The Journal of Physical Chemistry C, 118 (2014) 14388-14393.

[140] H.A. Gasteiger, CO electrooxidation on well-characterized Pt-Ru alloys, Journal of physical chemistry, 98 (1994) 617-625.

[141] M. Watanabe, Electrocatalysis by ad-atoms. Part III. Enhancement of the oxidation of carbon monoxide on platinum by ruthenium ad-atoms, Journal of electroanalytical chemistry, 60 (1975) 275-283.

[142] I.T. Bae, D.A. Scherson, In situ X-ray absorption of a carbon monoxide-iron porphyrin adduct adsorbed on high-area carbon in an aqueous electrolyte, The journal of physical chemistry. B, 102 (1998) 2519-2522.

[143] L. Birry, J. Zagal, J.-P. Dodelet, Does CO poison Fe-based catalysts for ORR?, Electrochemistry communications, 12 (2010) 628-631.

[144] N.R. Sahraie, U.I. Kramm, J. Steinberg, Y. Zhang, A. Thomas, T. Reier, J.-P. Paraknowitsch, P. Strasser, Quantifying the density and utilization of active sites in non-precious metal oxygen electroreduction catalysts, Nat Commun, 6 (2015).

[145] K.J.J. Mayrhofer, J.C. Meier, S.J. Ashton, G.K.H. Wiberg, F. Kraus, M. Hanzlik, M. Arenz, Fuel cell catalyst degradation on the nanoscale, Electrochemistry Communications, 10 (2008) 1144-1147.

[146] S. Maass, F. Finsterwalder, G. Frank, R. Hartmann, C. Merten, Carbon support oxidation in PEM fuel cell cathodes, Journal of Power Sources, 176 (2008) 444-451.

[147] K.H. Kangasniemi, D.A. Condit, T.D. Jarvi, Characterization of Vulcan Electrochemically Oxidized under Simulated PEM Fuel Cell Conditions, Journal of The Electrochemical Society, 151 (2004) E125-E132.

[148] N. Linse, L. Gubler, G.G. Scherer, A. Wokaun, The effect of platinum on carbon corrosion behavior in polymer electrolyte fuel cells, Electrochimica Acta, 56 (2011) 7541-7549.

[149] H. Schulenburg, B. Schwanitz, N. Linse, G.G. Scherer, A. Wokaun, J. Krbanjevic, R. Grothausmann, I. Manke, 3D Imaging of Catalyst Support Corrosion in Polymer Electrolyte Fuel Cells, The Journal of Physical Chemistry C, 115 (2011) 14236-14243.

[150] J.P. Meyers, R.M. Darling, Model of Carbon Corrosion in PEM Fuel Cells, Journal of The Electrochemical Society, 153 (2006) A1432-A1442.

[151] C.A. Reiser, L. Bregoli, T.W. Patterson, J.S. Yi, J.D. Yang, M.L. Perry, T.D. Jarvi, A Reverse-Current Decay Mechanism for Fuel Cells, Electrochemical and Solid-State Letters, 8 (2005) A273-A276.

[152] A. Oyarce, E. Zakrisson, M. Ivity, C. Lagergren, A.B. Ofstad, A. Bodén, G. Lindbergh, Comparing shut-down strategies for proton exchange membrane fuel cells, Journal of Power Sources, 254 (2014) 232-240.

[153] V. Goellner, C. Baldizzone, A. Schuppert, M. Sougrati, K. Mayrhofer,

F. Jaouen, Degradation of Fe/N/C catalysts upon high polarization in acid medium, PCCP. Physical chemistry chemical physics, 16 (2014) 18454-18462.

[154] J.C. Meier, I. Katsounaros, C. Galeano, H.J. Bongard, A.A. Topalov, A. Kostka, A. Karschin, F. Schuth, K.J.J. Mayrhofer, Stability investigations of electrocatalysts on the nanoscale, Energy & Environmental Science, 5 (2012) 9319-9330.

[155] P. Yu, W. Gu, R. Makharia, F. Wagner, H.A. Gasteiger, The Impact of Carbon Stability on PEM Fuel Cell Startup and Shutdown Voltage Degradation, ECS transactions, 3 (2006) 797-809.

[156] N. Ranjbar Sahraie, J.P. Paraknowitsch, C. Göbel, A. Thomas, P. Strasser, Noble-Metal-Free Electrocatalysts with Enhanced ORR Performance by Task-Specific Functionalization of Carbon using Ionic Liquid Precursor Systems, Journal of the American Chemical Society, 136 (2014) 14486-14497.

Chapter 2

Experimental methods

This chapter describes the synthetic methods used for the preparation of the electrocatalysts reported in this thesis and the mechano-chemical, textural and electrochemical characterization techniques used for the study of such electrocatalysts.

2.1 Synthesis of catalysts

In general, the preparation of Pt-free catalysts, both metal-free and non-precious metal catalysts, comprises three sequential steps. i) The first step is the intimate mixture of the nitrogen and/or metal precursors with a carbon source. The mixing can be carried out by using different methods such as impregnation or mechano-chemical methods. ii) Next, the composite formed is subjected to one or several thermal treatments under inert or reactive atmosphere in order to create the active phases for the oxygen reduction reaction studied. iii) Finally, the catalyst is subjected to an acid-leaching process to remove the unstable phases in acid medium.

2.1.1 Impregnation method

The impregnation method was carried out according to the procedure reported by Liu et al. [1], consisting on four steps: i) deposition of a nitrogen rich polymer over a carbon source, ii) impregnation of a metallic precursor over a previously treated carbon, iii) thermal treatment of the composite and iv) acid leaching. The purpose of the first step is to enhance the number of nitrogen atoms that can be incorporated to the carbon matrix.

(i) An aqueous solution of urea (CH_4N_2O, PANREAC PRS, 1.2 g of urea in 80 mL of distilled water) was mixed with the carbon source (C:urea molar ratio of 2 : 1) and sonicated during 30 min. Next, formaldehyde ($C_3H_4N_4O_3$ Aldrich, 37 wt.%) was added to the solution to a final urea:formaldehyde molar ratio of 2 : 1. The temperature was raised up to 50 ^{o}C in a continuous stirring. The initial solution pH value of 6 was increased to 10 (adding some drops of a NaOH solution) once the temperature of the solution reached 50 ^{o}C and the solution was kept under stirring for 90 min. Next, the temperature was raised up to 75 ^{o}C under continuous stirring for 30 min. Then, the pH was set to 2.5 and the conditions of temperature and stirring were kept for 1 h. Finally, the solvent was evaporated in a rotary evaporator and dried at 70 ^{o}C for 12 h.

(ii) The metal phthalocyanine of the corresponding metal (Fe, Co or Mn) was dissolved using tetrahydrofuran (THF, FLUKA ACS $\geq 99,5\%$). The metal content used was of 20 wt.%. The previously treated carbon was also dispersed in THF. Afterwards, both dispersions were mixed and heated up to 75 ^{o}C under stirring for 2 h. Finally, the solvent was evaporated in a rotary evaporator and dried at 70 ^{o}C for 12 h.

(iii) The sample obtained was subjected to a thermal treatment in a quartz tube at 800 ^{o}C under an inert atmosphere of N_2 (25 mL·min^{-1}) for 1 h.

(iv) The catalyst obtained from the previous step was leached in an acid solution of 0.5 M H_2SO_4 (H_2SO_4, PANREAC 96 % QP) at 60 ^{o}C for 2 h. The solid obtained was washed with distilled H_2O and recovered by centrifugation at 2500 rpm for 10 min until the pH of the supernatant water was of *ca.* 6.5. Then, the solid was dried at 70 ^{o}C for 12 h. In this step the unstable metallic phases in acid solution are removed.

2.1.2 Mechano-chemical method

Two different mechano-chemical synthesis methods using a ballmilling method were conducted in this thesis:

(i) In this first preparation, multiwalled carbon nanotubes were used as the carbon matrix (CNTs, SUNANO; purity > 90 %, Syn Nanotech

Co Ltd) and urea (CH_4N_2O, PANREAC PRS) or thiourea (CH_4N_2S, Sigma-Aldrich ACS reagent, 99 %) was used as the N and N/S precursors. Previous to further treatments, CNTs were subjected to an acid leaching with HNO_3 20 % v/v at 110 °C for 5 h to eliminate possible residues from the synthesis of CNTs. CNTs were ballmilled in a planetary ballmill (PM100, Retsch) for different periods of time from 0 to 150 h at 350 rpm in a 50 mL stain steel vessel, with the aim to generate an increasing number of defects and/or edges in the CNTs, thereby increasing materials' ability to incorporate other heteroatoms. Then, urea or thiourea and previously treated CNTs (molar ratio CNTs:urea or CNTs:thiourea 2 : 1) were intimately mixed by ballmilling for 24 h. After that, samples were subjected to a thermal treatment in a quartz reactor at 800 °C in a N_2 flow for 1 h.

(ii) The second preparation consists in a first step where 0.75 g of the desired carbon matrix, either active carbon, (Norit GSX 94017-7), multiwalled carbon nanotubes (CNTs) (Nanocyl NC 7000) or graphite nanoplates (XG-Sciences Graphene nanoplates C750) and 0.0027 g of the N precursor, (1, 4, 8, 11-tetraazacyclo-tetradecane, Aldrich 98 %) were ballmilled. The ballmilling was carried out in a 50 mL stain steel vessel under room conditions, at 350 rpm during 4 h and employing a planetary ballmill (PM100, Retsch). The N/C composite obtained was mixed with the same amount than in the previous step (0.75 g) of the carbon precursor and urea (CH_4N_2O, PANREAC PRS) using an atomic ratio of C/N of 5.5 in a ballmilling at 350 rpm during 4 h in a 50 mL stain steel vessel. In a following step the appropriate amount of iron (II) phthalocyanine (Sigma-Aldrich, 90 %) to obtain a Fe concentration of *ca.* 1.4 wt.% in the catalyst, was added to the N/C composite obtained after the two ball milling steps described above. This mixture was ballmilled again during 10 h at 350 rpm in a 50 mL stain steel vessel. The solid obtained was thermally treated in a quartz tubular reactor at 800 °C for 1 h under an inert atmosphere of N_2 or under a reactive atmosphere of NH_3/N_2. In some cases, aliquots of the catalysts were subjected to acid-leaching; for this purpose samples were treated in 0.5 M H_2SO_4 (PANREAC 96 % QP) at 60 °C for 2 h to eliminate non-stable phases in acid electrolyte. The solid obtained was washed with distilled H_2O by centrifugation at 2500 rpm for 10

min until the pH of the supernatant water was of *ca.* 6.5 and dried at 70 °C for 12 h. Some of the samples which were subjected to the acid-leaching were thermally treated again at 350 °C under N_2 for 1 h to remove adsorbed sulfates.

2.2 Characterization techniques

2.2.1 Elemental analysis

2.2.1.1 Analysis of the C,H, N and S contents

The elemental analysis technique allows to determine the content of carbon, hydrogen, nitrogen and sulphur for a broad range of compounds, both organic and inorganic compounds, irrespectively of their state of aggregation (solid or liquid).

The technique is based on the total oxidation of the sample by a complete and instantaneous combustion, obtaining products of the combustion such as CO_2, H_2O, N_2 and SO_2 that are dragged by the carrier gas (He) to the specific of CO_2, H_2O and SO_2 infrared cells detectors. Afterwards, these gases are removed to evaluate the N_2 by differential thermal conductivity [2].

Samples were measured in an elemental analyser LECO CHNS-932 that has a balance AD-4 Perkin-Elmer (resolution of 0.1 μg and weight range of 1000 mg) and a microbalance MX5 Mettler Toledo (resolution of 0.1 μg and weight range of 5.1 g).

2.2.1.2 Inductively coupled plasma mass spectrometry (ICP-MS)

The inductively plasma mass spectrometry is based on the principles of vaporization, dissociation and ionization of the chemical elements when these elements are held in a high temperature plasma. The produced ions can be separated by the ratio mass/charge in a high resolution mass spectrometer.

The equipment is formed by (see Figure 2.1):

(i) Sample injection system. The sample in the liquid state is moved through an Ar flow to the plasma.

(ii) Inductively coupled plasma. The plasma is reached when an oscillating

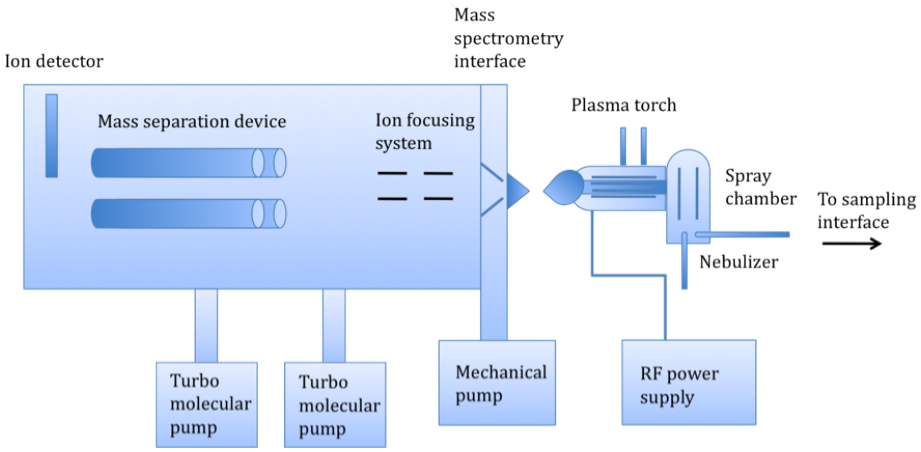

Figure 2.1: Inductively coupled plasma mass spectrometry (ICP-MS) scheme.

magnetic field, induced by a high frequency current, acts under an Ar flow. The confined plasma in the magnetic field is known as plasma torch, reaching temperatures up to 8000 K. Under these conditions the atoms from the samples are ionized.

(iii) Plasma sample interface. The ions are conducted to the chamber of the mass spectrometer, at room temperature and under ultra-high vacuum. The interface is formed by two consecutive cones made of Ni that contains small holes through which the ions from the center of the plasma are filtered.

(iv) Mass spectrometer. The ions are separated in the mass spectrometer according to their mass/charge ratio. The analysers can be a quadrupole that have slow resolution for ions that have similar mass/charge ratio or an analyser of double focused sector that has better resolution.

The measurements of the Fe content in the catalysts described in this thesis were carried out in an ICP-MS Perkin-Elmer Elan 6000. The samples were previously dissolved in a mixture of HNO_3 (3 ml, PANREAC 65 %), HCl (2 ml, PANREAC 37 %), HF (3 ml, PANREAC 48 %) and H_3PO_4 (3 ml, PANREAC 85 %) at 473 ^{o}C and 60 bar of pressure in a microwave digester Multiwave 3000 Anton Paar.

2.2.2 Textural properties characterization

2.2.2.1 Physical adsorption of N_2. BET measurements

The physisorption of gases is the most usual technique to determine the specific surface area and the pore distribution in porous solids. The N_2 is one of the most used gases. The technique is based on the adsorption-desorption of N_2 at 77 K, its boiling point.

A gas in contact with the surface of a solid material produces equilibrium between both the adsorbed molecules and the molecules in gas phase; this equilibrium is dependent on the gas pressure and the temperature. The ratio between the amount of adsorbed gas into the solid material at different partial pressures of adsorbate (P/P_0, where P_0 is the pressure of saturation of N_2 at 77 K) at constant temperature ($T_{boiling} = 77$ K) records the adsorption isotherm.

The specific surface area is determined by the BET (Bruenauer-Emmett-Teller) method [3]. This method consists in calculating the volume of the monolayer of the adsorbate and the specific surface BET (S_{BET}) which is obtained from the following equation:

$$S_{BET} = \left(\frac{V_m}{M \cdot g}\right) N_A \cdot \sigma \tag{2.1}$$

where V_m is the volume of the monolayer, M is the molar volume of the adsorbate, g is the mass of the adsorbent used, N_A is the Avogradro's number ($6.023 \cdot 10^{23}$ molecules·mol^{-1}) and σ is the area occupied by the molecule of the adsorbate on the monolayer. Using liquid N_2, the value for σ is 0.162 nm^2. The value of V_m is obtained from the experimental adsorption data adjusted to the BET isotherm:

$$\frac{P}{V_{ads} \cdot (P_0 - P)} = \frac{1}{V_m \cdot C} + \frac{C-1}{V_m \cdot C} \cdot \frac{P}{P_0} \tag{2.2}$$

where P is the partial pressure of the adsorbed gas, P_0 is the vapor pressure of the gas at the temperature at which the adsorption takes place, V_m is the volume of the adsorbed gas where the monolayer is formed, C is a constant value dependent on the condensation and the adsorption heat of the adsorbate and V_{ads} is the volume of the adsorbed gas at the pressure P.

The BET surface area and N_2 adsorption-desorption isotherms of the

samples were obtained in a Tri-Star Micromeritics equipment. The samples were previously degassed at 140 °C for 12 h in a vacuum system to remove the solid and/ or liquid pollutants in the pores or in the surface of the samples.

2.2.2.2 Transmission electron microscopy (TEM)

The technique provides topographical images of the samples at nanometric scale, allowing the study of the shapes, distribution and location of the specific compounds, such as metallic particles over amorphous or polycrystalline substrates.

The transmission electron microscopy (TEM) is based on the interaction of a high energy electron beam ($200 - 400$ KV), produced by a thermionic emission source (filament of W or LaB_6) or the field emission gun (FEG), with a very thin layer of sample (thickness $\approx 0.1 - 0.5$ μm) at high vacuum conditions. When the beam strikes on the sample, two different processes take place: elastic process, where the incident electrons are dispersed without loss of energy, and inelastic process, where the electrons give a part of their energy to the internal electrons. The interaction of the electrons with the magnetic fields make possible that the electrons can be manipulated by the electromagnets and the magnetic lenses. When the electrons go through the sample, they can pass through the sample without any interaction (direct beam) or can be dispersed for the sample in a similar way than in the X-ray diffraction. The dispersed electrons provide information about the structure of the sample and they are recombined by the lenses of the projector forming the image [4].

Samples were studied using an electronic microscopy JEOL 2000FX. The equipment has an accelerating potential of 200 kV, a maximum resolution of 0.35 nm and has also a probe for analysing the energy-dispersive X-ray (EDX). Samples were previously prepared by their dispersion and homogenization in an isopropyl solution.

2.2.3 Structural characterization

2.2.3.1 X-ray diffraction (XRD)

The X-ray diffraction allows the study of the crystalline structures present in the samples. The technique is very useful for monitoring the structural

changes, identifying and measuring the particle size of the crystalline phases. It has been used for the identification of the crystalline phases formed in the synthesis of the catalysts and in some cases for measuring the particle size applying the Debye-Scherrer equation.

The X-ray diffraction consist in radiating the sample with a monochromatic X-ray beam, using anodes of Mo (λ = 0.709 Å) or Cu (λ = 0.709 Å). The interaction between the X-ray beam and the electrons of the analysed material gives rise to a dispersion phenomenon. Diffraction phenomena appear when the constructive interferences are produced by X-rays scattered at specific angles of incidence (θ) from each set of lattice planes in a sample (see Figure 2.2). The technique is based on that the solid compounds are formed by crystalline particles whose atoms constitute periodic three-dimensional networks. The networks act as diffraction grids for the monochromatic beam, with a wave length in the same order of magnitude than the distance between the different atoms. Under the same conditions, according to the Bragg's law (Eq. 2.3) [5], each crystalline compound gives an unique diffractrogram considered as the "fingerprint" for each ordered solid. In a mixing of compounds, each one produces its own diffractrogram irrespectively to the other compounds, so the technique is a reliable identification of the mixture.

$$n\lambda = 2dsin\theta \tag{2.3}$$

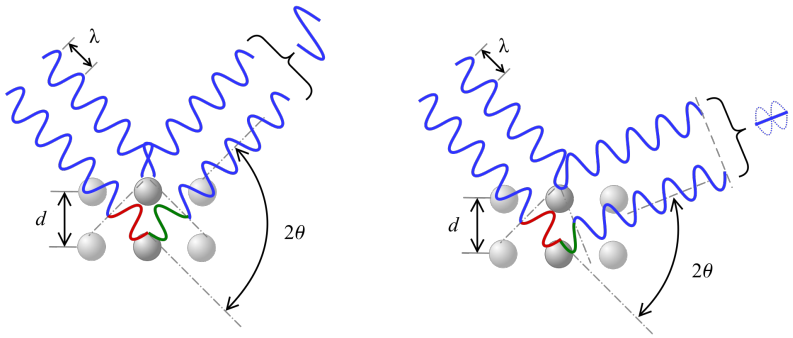

Figure 2.2: Interaction of a X-ray beam with a crystal, a constructive interference according to the Bragg's law (left) and a destructive interference (right).

The heterogeneous catalysts are usually formed by several microcrystalline phases; this is why they are often analysed by the conventional powder method [6]. The average crystal size (d) in the powder sample can be obtained from the Debye-Scherrer equation:

$$d = \frac{K \cdot \lambda}{B \cdot cos\theta} \tag{2.4}$$

where K is the shape factor of the crystal ($0.7 - 1.7$ nm), λ is the wavelength of the radiation employed (Cu-K$_\alpha$ = 0.15418 nm), B is the full width at half (rad), θ is the angular position of maximum diffraction peak (rad) and d is the average crystal size (nm).

The equation establishes that the narrow diffraction peaks correspond to big and crystalline particles, while the broadened peaks correspond to small and amorphous particles. According to the mathematic treatment of the equation only the crystal size influences the width of the diffraction line. Nevertheless, there are more agents that influence the width of the lines such as instrumental factors (misalignment of the diffraction pattern, no X-ray source monochromatic, etc.) and agents that are caused by the non-ideal crystals (stresses and crystal deformations)[7]. Moreover, the diffraction lines may experience displacements due to the appearance of solid solutions producing the replacement of one of the original atoms in the crystalline network by other different size atom. This fact produces changes in the network parameters, in the interplanar distances (d_{hkl}), and in the angular position for the maximum diffraction (θ).

The samples were analysed by the conventional method in a thin powder. The samples were compacted over a steel support, so that the surface of the sample has to be the most smooth and homogeneous as possible to avoid additional extinctions to the crystalline phases. The measurements were carried out in a vertical SEIFERT diffractometer 300P, using a secondary graphitic monochromator hiring Cu-K$_{alpha}$ radiation (λ = 0.15418 nm, average value between Cu-K$_{\alpha 1}$ and Cu-K$_{\alpha 2}$). The operation conditions in the source were of 40 KV and 40 mA. The diffractrograms were recorded in a range of Bragg's angles (2θ) between 20^o and 90^o, the accumulation time was of 20 s and the step size of 0.04^o. Data were analysed using the RayfleX (version 2.25) software.

2.2.3.2 Raman spectroscopy

The Raman spectroscopy is based on the interaction between the incident photon and the molecule under study, producing the excitation of the molecule. This technique provides information about the structural properties of the studied material.

Relaxation of the excited molecule can occur in two ways. The molecule can back to the initial energetic state, releasing an amount of energy equal to that absorbed. This phenomenon is known as elastic or Rayleigh scattering. On the other hand, the molecule can back to a different energetic state; in this case an energy exchange occurs, producing an inelastic scattering characteristic of the Raman effect. If the final energy state of the molecule is higher than the initial state, the released energy is lower than the absorbed energy therefore the wavelength increases and the radiation frequency decreases. This process produces a Raman scattering known as Stokes. However if the final state of the molecule corresponds with a lower energetic level than the initial one, the released energy is higher than the absorbed energy, producing a lower wavelength and higher radiation frequency. This Raman scattering is called anti-Stokes [8],(see Figure 2.3).

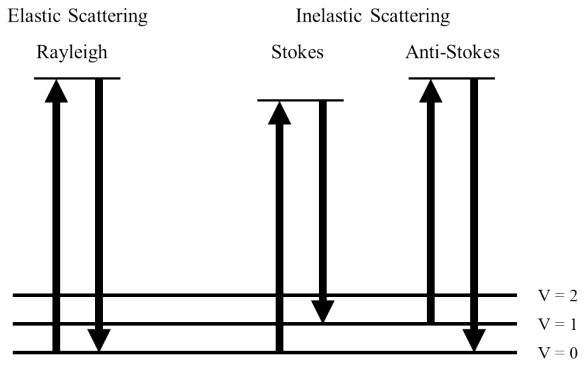

Figure 2.3: Transitions between energy levels.

The Stokes scattering are more likely to occur at lower temperatures than anti-Stokes. This is why the Stokes band has higher intensity than anti-Stokes band and the ratio of both intensities corresponds to the temperature of the sample. The Stokes region has an identical reflection in the anti-Stokes region but due to the high intensity of the Stokes region, the Raman studies

are performed in this region.

Transitions between energy states correspond to the transitions between vibrational states. Thus, both infrared spectroscopy (IR) and Raman spectroscopy are based on transitions in vibrational states of the molecule. In the case of IR spectroscopy, it is studied the absorption of IR beam as a function of the frequency.

Furthermore for Raman spectroscopy, the laser beam (ultraviolet, visible, near infrared or infrared) strikes the sample and the phenomenon of study, it is the dispersed light, whose frequency changes respect to the excitant line. So Raman spectroscopy measures the vibrational frequencies like a shift between the energy of the incident beam and the scattered one.

The samples were analysed in powder at room temperature. Raman spectra were recorded in air using a single monochromator Renishaw system 1000 equipped with a thermoelectrically cooled CCD detector and holographic super-Notch filter. The samples were excited with the 532 nm Ar line. The instrument is internally calibrated with a silicon reference at 520 cm^{-1} and gives a peak position resolution of 1 cm^{-1}, the spectrum acquisition time was 10 s and 5 spectra were acquired to ensure an optimal signal to noise ratio.

2.2.3.3 Diffuse reflectance infrared Fourier transform spectroscopy (DRIFTS)

The diffuse reflectance infrared Fourier transform spectroscopy is a particular type of infrared spectroscopy (IR), used for the study of opaque materials and difficult to compact.

In general, the infrared spectroscopy studies the interaction of the matter with the photons in a specific region of the electromagnetic spectrum, this region includes the wave lengths between 2.5 and 25 μm, or expressed in wave numbers between 4000 and 400 cm^{-1}. In this region of the spectrum some energetic transitions take place producing the bond vibrations of the molecules. The plotting of the IR intensity *vs.* the wave number lets the identification of the functional groups by comparing the recorded spectrum with the data base spectra.

In measurements by using the DRIFT cell, the sample is added to the holder, the configuration of the cell allows gas flow through the sample. The

hermetic closure (domo) has two windows for the entrance and exit of the IR radiation. The incident radiation is absorbed, refracted and reflected by the sample and finally it is recorded by the spectrometer passing through several mirrors.

Infrared spectra (DRIFT) were obtained with a Jasco FTIR-6300A spectrometer equipped with an MCT detector. The spectra were recorded with a resolution of 4 cm^{-1} and an accumulation of 256 scans. Samples were finely ground and placed into a ceramic crucible in the DRIT chamber. First, 25 mL min^{-1} of pure He was flowed through the chamber at 200 °C for 1 h to remove physisorbed H_2O. The temperature was set at 25 °C and DRIFT spectra were recorded for each sample and used as reference spectra. Then, samples were subjected to a thermal treatment in He at 500 °C for 1 h (heating rate 10 °C min^{-1}). Then, the temperature was decreased to 25 °C under He and DRIFT spectra for each sample were recorded.

2.2.3.4 X-ray photoelectron spectroscopy (XPS)

The X-ray photoelectron spectroscopy is a technique of electron spectroscopy for chemical analysis (ESCA) used to study the surface of the electrocatalysts. XPS spectra provide information about the oxidation state and relative abundance of the surface elements (semi-qualitative analysis).

The technique is based on the photoelectric effect (Figure 2.4), discovered by H. Hertz in 1887 and widely explained by Einstein in 1905. The effect consist in the emission of electrons from the internal energy levels of the atoms produced by the irradiation of the sample with a high energy X-ray beam (h?). The kinetic energy of the electrons is related with their binding energy, and this binding energy is characteristic of the elements present in the sample, and the interactions between them [9].

The radiation used for the photoexcitation of the electrons from the internal levels requires monochromatic and high energy of X-ray photons. The X-ray photons from the excitation source give the energy to the internal electrons in the atom and these electrons are pull out to the atom. A hemispherical detector collects the emitted electrons and records their energy for the photoelectronic emission spectrum. The radiation can penetrate in the sample from 1 to 10 μm and the pull out electrons produce inelastic collisions that disperse the energy of the electrons. Therefore, only the electrons,

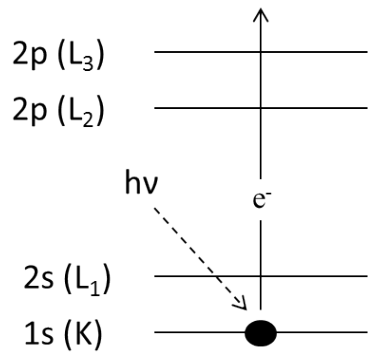

Figure 2.4: Photoelectric effect.

whose free paths are between 0.5 and 4 nm, achieve the detector, so that the photoelectronic spectroscopy is a superficial technique of the last layers in the atoms.

The binding energy of the emitted electrons can be calculated by the difference between the energy of the incident X-ray photons and the kinetic energy of the emitted electrons, corrected by two parameters:

$$BE = h \cdot v - E_c - \phi_s - C \tag{2.5}$$

where BE is the binding energy of the emitted electron, $h \cdot v$ is the excited energy, E_c is the kinetic energy of the emitted electron, ϕ_s represents the work function of the spectrometer, which is the average loss energy in the spectrometer, and C is the loading effect.

The emission of electrons causes that the sample is positively charged during the measurement. This effect is minimized in conductive samples through the grounding of the sample holder, but in non-conductive samples this effect is maximized because it is not possible to recover their neutrality through the grounding. On this last case, the electrons are attracted by the positive potential of the sample, the peaks in the spectrum move to a higher binding energy and their kinetic energy is reduced in a value C known as loading effect. The solution to this problem requires the use of an internal pattern to calibrate the binding energy (BE), the most used pattern is the peak corresponding to C $1s$ ($BE = 284.6$ eV).

The binding energy of the internal electrons is characteristic of each atom.

Therefore, the technique identifies the atomic species in the surface of the material, except to the hydrogen and helium atoms.

The binding energy of the emitted electron from an orbital depends on the atomic number, the oxidation state and the environment of the chemical element. This means that the binding energy depends on the electronic density of the atom in the compound. The shifting of the binding energy in the studied level respect to the binding energy of the pattern due to the interactions is labelled as chemical shifting. The chemical shifting shows the increment of the binding energies as the oxidation state increase. The binding energies for the elements in different compounds are recorded in a database [10].

The intensity and the area under the photoelectronic spectrum are proportional to the number of atoms in each element. The proportionality factor is known as the sensitivity factor, S. This factor depends on the instrumental factors and the cross section of the typical electronic levels of each element.

The equipment used in the analysis is a SPECS GmbH spectrometer with a system UHV provided with an energy analyser PHOIBOS 150 9MCD. X-ray emission source is a non-monochromatic anode Mg (K_α = 1253.6 eV) operating at 200 W and 12 kV. The working pressure in the analysis chamber is around $5 \cdot 10^{-8}$ Torr.

2.2.3.5 X-ray absorption techniques

X-ray absorption spectroscopy (XAS) is a bulk characterization technique useful to study and identify the oxidation state of elements, the concentration, the atomic distance, the coordination number, the local geometry and surface reactivity of the compounds under study that can be liquids, solids or gases.

A special feature of XAS is the requirement of syncrothron radiation sources which provide intense and tuneable X-ray beams. The technique is based on the absorption of the X-rays by the matter whose energy is converted into the kinetic energy of the photoelectrons. When an X-ray strikes an atom, one of the core electrons is either excited to a higher energy unoccupied state and this transition is studied by XAS.

The amount of energy absorbed by matter is usually estimated by a transmission method, but can also be estimated by measuring secondary

phenomena, such as photoelectrons, Auger electrons, secondary electrons, fluorescent X-rays, thermal radiation and drain electric currents. XAS spectra are typically plotted as mass absorption coefficients of matter against the incident X-ray energy or wavelength, In those spectra, we find different edges at particular X-ray energies. These absorption edges correspond to X-ray photon with enough energy to excite a core electron. When X-rays of energies are close to electron binding energies, the electron is excited and features known as absorption edges are observed. The nomenclature of the edge depends upon the core electron which is excited: the principal quantum numbers $n = 1, 2$, and 3, correspond to the K-, L-, and M-edges, respectively. For instance, excitation of a $1s$ electron occurs at the K-edge, while excitation of a $2s$ or $2p$ electron occurs at an L-edge. This is shown in Figure 2.5 [11, 12].

The mass absorption coefficient is the sum of two effects: photoelectric absorption and X-rays scattering. The photoelectric absorption is the ionization of an inner-shell electron. Therefore, the absorption coefficient due to the photoelectric part can be calculated by the photoionization cross-section. The scattering part is due to the Rayleigh (coherent) and Compton (inelastic) X-ray scattering. Moreover, X-ray absorption spectra are often taken as if they represent only the photoelectric absorption effect, although the experimental spectra contain both effects. The absorption edge is not exactly the same as the electron binding energy, because the absorption edge energy corresponds to the excitation of core electrons into the lowest unoccupied molecular orbital (LUMO) in the molecular orbital picture, or Rydberg state in the atomic orbital picture [11].

The X-ray absorption spectra of condensed matter near the threshold energy have fine structures, X-Ray Absorption Fine Structure (XAFS). Fine structures are sometimes observable at energies less than the threshold energy, and they are called the pre-edge structure. These fine structures are called X-Ray Absorption Near Edge Structure, XANES. The absorption fine structure will extend up to 1000 eV above the threshold energy, and thus it is called Extended X-Ray Absorption Fine Structure EXAFS [11].

The basic XAFS advantages are [12]:

(i) Selectivity in the chemical-element type, which enables one to acquire information on the local environment of each element of the material

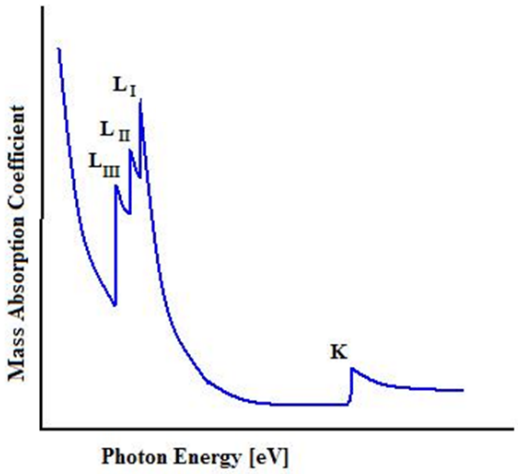

Figure 2.5: Mass absorption coefficient against photon energy.

under investigation.

(ii) Sensitivity to the partial densities of vacant states near the Fermi level.

(iii) High density sensitivity ($10 - 100$ particles per mole) and relatively short times (from milliseconds to tens of minutes) for detecting experimental spectra when synchrotron radiation is used.

(iv) A small required sample volume (usually, an amount less than 30 mg·cm^{-2} is enough).

Extended X-ray absorption fine structure (EXAFS)

The extended X-ray absorption fine structure (EXAFS) is the fine structure in the X-ray absorption coefficient starting somewhat past an absorption edge and extending typically 1000 eV further.

EXAFS only appears when atoms are in a condensed state. The photon is completely absorbed and kicks out a core photoelectron from the absorbing atom, leaving behind a core hole. This excited atom with a core hole may produce further excitations but in order to simplify the picture, this probability is ignored. This photoelectron will be ejected with energy equal to the energy of the incoming photon less its binding energy, when it is in the core. This photoelectron will interact with the surrounding atoms. Assuming that

all absorbed energy of the photon is used for the excitation of the single core electron, the kinetic energy of the excited photoelectron is given by the difference between the photon energy and the electron's binding energy in the atom [13].

The final-state photoelectron is modified to first order by a single scattering from each surrounding atom. The energy of the photoelectron must be treated as a wave whose wavelength λ is given by the Broglie relation:

$$\lambda = \frac{h}{p} \tag{2.6}$$

where p is the momentum of the photoelectron and h is the Planck's constant. In EXAFS regime p can be determined by the free electron ratio:

$$\frac{p^2}{2 \cdot m} = h \cdot v - E_0 \tag{2.7}$$

where the X-ray photon frequency v has an energy hv and E_0 is the energy of the photoelectron.

The interaction of an isolated atom with the surrounding atoms can be represented as in Figure 2.6. The surrounding atoms will scatter the outgoing waves as indicated by the dashed lines. The final state is the superposition of the outgoing and scattered waves. The absorption of the X-rays is given by the initial and the final states. The initial state is the electron in the atomic core and the final state is this electron excited to the escaping photoelectron.

The backscattered waves will add or subtracted from the outgoing wave at the center depending on their relative phase. The total amplitude of the electron wave function will be enhanced or reduced, respectively, thus modifying the probability of absorption of the X-ray. As the photoelectron energy varies, its wavelength varies as indicated in Eqs. 2.5 and 2.6. Thus the variation of the fine structure in EXAFS is a direct consequence of the of photoelectron's wave nature. The variation of the backscattering strength as a function of the photoelectron's energy depends on the type of atom doing the backscattering. These variations are represented as oscillations in the EXAFS spectrum.

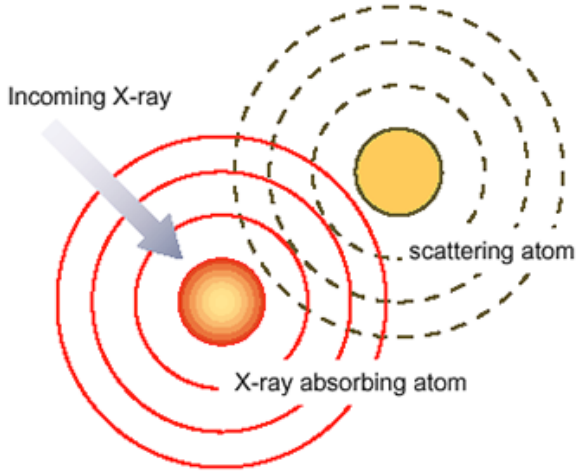

Figure 2.6: Schema of the photoelectron wave. The solid lines indicate the outgoing portion, and the dashed lines indicate portions of the scattered wave from the surrounding atoms.

X-ray absorption near edge structure (XANES)

The X-ray absorption near-edge structure (XANES) is determined by the local density of vacant states in an absorbing atom, as well as by multiple-scattering effects, *i.e.* scattering of an excited photoelectron on several atoms. The XANES spectrum covers the range between the threshold and the point at which the extended X-ray absorption fine (EXAFS) begins [12].

XANES is associated with the excitation process of a core electron to bound and quasi-bound states, since the excitation process involves multielectron and multiscattering effects. The multiscattering of the excited electron confers sensitivity to the details of the spatial arrangement of atoms neighboring the absorbing one, not only their radial distance but also their orientations relative to one other, bond angles, and so on. A practical point worthy of note is that XANES structures are usually more stronger than the EXAFS oscillations, and this may make XANES particularly useful in dilute systems [13].

XAFS data of the samples studied during this thesis were acquired at the CLAESS beamline of the ALBA Synchrotron facility with the help of ALBA's staff. The Fe K absorption edge (7112 eV) was calibrated with the help of a Fe foil. A Si (111) double crystal monochromator working in

continuous mode was used for the energy scans. EXAFS spectra are the result of the merging of at least 6 scans. Analysis of the EXAFS spectra was performed with the software VIPER for Windows. In the spectra of the absorption coefficient μ, a linear fit was made to the pre-edge region in order to normalize the signal. A smooth atomic background μ_0 was evaluated using a smoothing cubic spline [14].

2.2.3.6 Thermogravimetric analysis (TGA)

The thermogravimetric analysis is used to study the stability of solids under controlled temperature and atmosphere by recording mass loss or gain as a function of the temperature.

The thermogram recorded provides us information about the thermal stability and the temperature at which the changes in the mass of the sample take place. The necessary equipment consists on an electronic balance, an oven controlled by a programmer, a temperature sensor, an inlet gas system and a data acquisition system.

The measurements were carried out in a Melter Toledo, TGA/SDTA 851e, with a balance whose resolution is 1 μg. It comprises a cylindrical microvan with a heating maximum of temperature of 1100 ^{o}C in 5 minutes; the precision at the maximum temperature is $\pm$0.25 ^{o}C.

2.3 Electrochemical characterization

The electrochemical techniques include a set of techniques that allow the study of the electrochemical reactions at the interphase between the electrocatalyst and the electrolyte. In general, it implies the measurement of either the electrode potential or the current that passes through the electrode as a result of the application of potential or current programs to the electrode. The electrochemical experiments are controlled by potentiostats/galvanostats which are electronic devices that modulate the working potential of the working electrode with respect to a reference electrode by adjusting the current in an auxiliary or counter electrode [15].

2.3.1 Cyclic voltammetry

The cyclic voltammetry (CV) is based on the application of a potential to the working electrode from an initial value E_i, to a predetermined limit E_l, where the direction of the scan is reversed, until a final potential E_f (Figure 2.7). The applied potential and the current recorded in the electrode are simultaneously registered. The final potential can be different from the initial potential and the sweep rate ($V \cdot s^{-1}$) can be also modified. The experiments record the current flowing through the working electrode as a function of the potential.

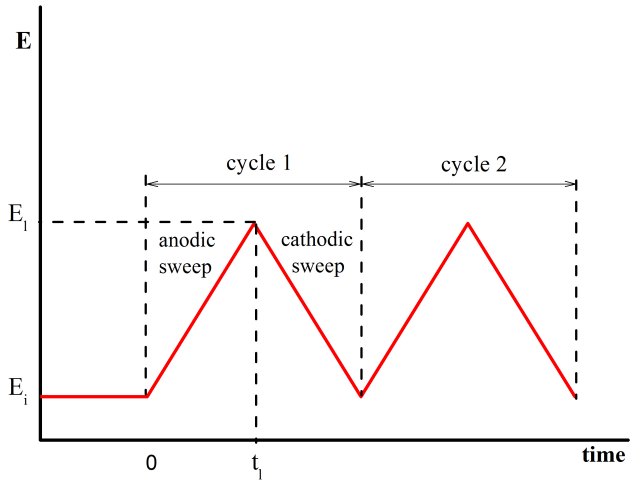

Figure 2.7: E/t profile of a typical potential program applied in a CV experiment.

The plot of the current density in the working electrode *vs.* the applied potential is known as cyclic voltammogram (CV). As standard criteria, the current has positive values for the anodic sweep (oxidation process) and negative values for the cathodic sweep (reduction process). Typically, the most common values evaluated in a CV (Figure 2.8) are the peak currents (anodic peak current i_{pa} and cathodic peak current i_{pc}) and the distance between the potential corresponding to the anodic and cathodic peaks (E_{pa} and E_{pc}), respectively. The distance between the peak potentials, ΔE_p,

gives us an estimation of the reversibility of the electrochemically process studied. The maximum potential in order to consider a reversible reaction is $\Delta E_p = 59/n$ mV at 25 °C [16].

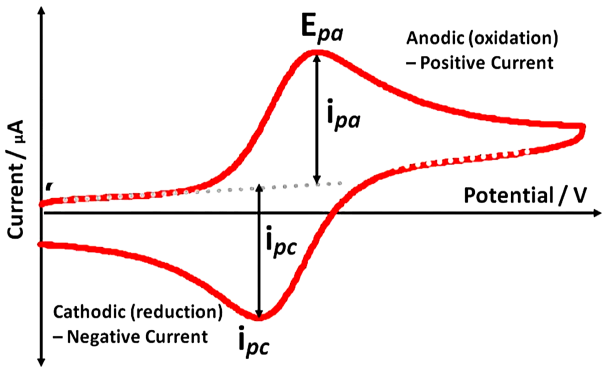

Figure 2.8: Cyclic Voltammetry for the redox couple of ferricyanide to ferrocyanide.

The currents recorded in electrochemical processes, including cyclic voltammetry, may come from Faradaic processes or they may be associated with charge and discharge process of the electrical double layer in the surface of the electrode. The Faradaic processes are governed by the Faraday's law, which establishes that the extension of a chemical reaction in the electrode is proportional to the current that passes through the electrode [17]. The change of sweep rate in a CV experiment has a strong influence on the kind of processes that take place in the surface of the electrode. Thus, an increase in the sweep rate decreases the influence of the mass transport process and show more clearly charge transfer processes and capacitive responses.

Due to the simplicity of this technique and the high amount of information that can be extracted, the cyclic voltammetry has become one of the most popular electrochemical techniques. The extremely sensitivity of the response in a cyclic voltammetry to the superficial structure of the electrode, makes the cyclic voltammetry becomes in the "fingerprint" of the electrode surface.

In this thesis, the cyclic voltammetry was used to evaluate the performance of the electrocatalysts towards the oxygen reduction reaction. The electrochemical cell used for the voltammetric experiments was made of Pyrex, the working electrode (WE) was a glassy carbon of 5 mm of diameter

on which the electrocatalyts under study was deposited, the reference electrode (RE) was a home-made reversible hydrogen electrode and the counter electrode (CE) was either a carbon rod or a gold wire.

2.3.2 Cyclic voltammetry using rotating disk electrode (RDE) and rotating ring disk electrode (RRDE)

There are some techniques in which the electrode is moved relative to the electrolyte. The techniques that involve a convective mass transport both the reactive and the products of the electrochemical reaction are known as hydrodynamic techniques. Therefore, the cyclic voltammetry under these conditions is known as hydrodynamic cyclic voltammetry. The use of this kind of techniques enhances the speed at which the steady state is reached because it minimizes the limitations of the mass transport.

A rotating disk electrode (RDE) comprises a disk made of a conductive material embedded in an insulating one and directly attached to an engine by a shaft. In this type of electrodes, the hydrodynamic equations and the equation of the diffusion-convection have been solved in the steady state. The electrode is rotated with a determined frequency N ($rev \cdot s^{-1}$), expressed as angular rate ω (s^{-1}), where $\omega = 2 \cdot \pi \cdot N$. The rotation drags horizontally out the solution from the disk in a radial direction, producing and upward axial flow (see Figure 2.9 scheme) to replenish the solution at the surface.

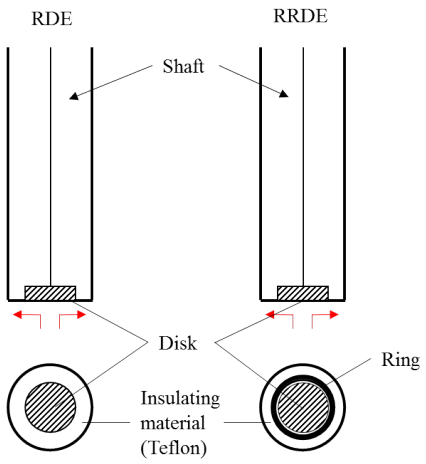

Figure 2.9: Rotating disk electrode (RDE) and rotating ring disk electrode (RRDE) configurations.

In a typical RDE experiments, the cyclic voltammograms are recorded at a selected rotation rate, reaching a steady current known as limit current characteristic to the actual rotation rate. According to the Levich's equation the limit current can be defined as:

$$i_{lim} = 0.62 \cdot n \cdot F \cdot A \cdot D^{2/3} \cdot v^{-1/6} \cdot C^* \cdot \omega^{1/2} \tag{2.8}$$

where i_{lim} is the limit current, n is the number of transferred electrons, F is the Faraday constant, A is the geometric area of the electrode, D is the diffusion coefficient of the electroactive specie, v is the cinematic viscosity, C^* is the concentration of the electroactive specie in the bulk and ω is the rotation rate.

The typical profile recorded for the ORR with a RDE is shown in Figure 2.10. Three regions can be observed: *i)* the pure kinetically controlled region, *ii)* the region controlled by a mixed kinetic-difussional control and *iii)* the region governed by diffusion phenomena. In the case of diffusion region, the ORR limiting current varies with the rotation rate applied to the working electrode.

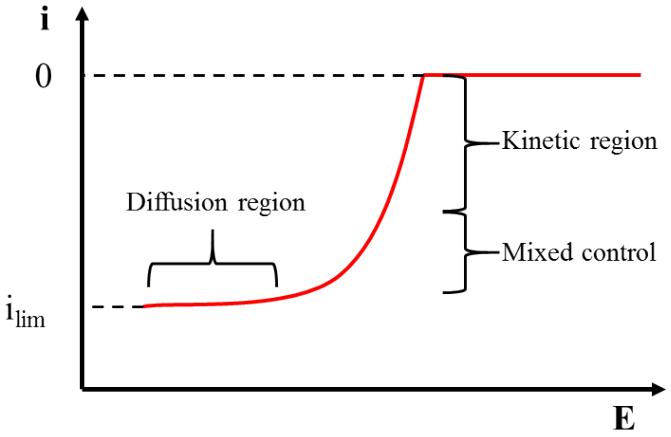

Figure 2.10: Cyclic voltammetry for the oxygen reduction reaction (ORR).

According to the Koutecky-Levich equation, the total current i for the ORR contains contributions from the diffusional and kinetic currents:

$$\frac{1}{i} = \frac{1}{i_k} + \frac{1}{i_{lim}} \tag{2.9}$$

where i_{lim} is the limiting current controlled by mass transport and i_k is the kinetic current governed by the kinetics of ORR on the electrocatalyst under study.

The combination of Eq. 2.8 and Eq. 2.9 establishes a direct relationship between $\frac{1}{i}$ and $\omega^{1/2}$ (Eq. 2.11), being the intercept in the abscise axes the reverse to the kinetic current i_k and the slope proportional to the number of electrons transferred.

$$B = 0.62 \cdot n \cdot F \cdot A \cdot D^{2/3} \cdot v^{-1/6} \cdot C^* \tag{2.10}$$

$$\frac{1}{i} = \frac{1}{i_k} + \frac{1}{B \cdot \omega^{1/2}} \tag{2.11}$$

Based on this equation, the number of electrons transferred during the ORR can be determined at atmospheric pressure and at temperature of 298 K by assuming that the O_2 concentration in the solution (C^*) is $1.1 \cdot 10^{-3}$ M, the diffusion coefficient of the O_2 (D) is $1.9 \cdot 10^{-5}$ $cm^2 \cdot s^{-1}$ and the cinematic viscosity (v) is $1.009 \cdot 10^{-2}$ $cm^2 \cdot s^{-1}$ [18] . Moreover, the kinetic current i_k can be calculated from Eq. 2.9. For the calculation of i_k during ORR it is necessary to substrate the capacitive current from the total current density recorded in the experiment in order to obtain the pure ORR Faradaic current density. Thus, the ORR Faradic current density during the anodic scan, i_F, is obtained by subtracting total current density from capacitive current i_{cap} which is obtained from the cyclic voltammogram in Argon-saturated electrolyte so that $i_F = i_{TOT} - i_{cap}$, defined as negative for a reduction reaction. From i_F it is possible to calculate the current if O_2 diffusion is infinitely fast, it is the kinetic current i_k. The relationship between the i_k and i_F is established by the Koutecky-Levich equation described above [19]:

$$i_k = \frac{-i_F \cdot i_{lim}}{i_F - i_{lim}} \tag{2.12}$$

i_k is defined as < 0 for the reduction. It is also convenient to report catalyst activity as the mass activity defined by:

$$i_M = \frac{-i_k}{m_{cat}} \tag{2.13}$$

where the i_k is expressed in A and the m_{cat} is the mass loading of the

catalyst on the working electrode in g [19].

The rotating ring disk electrode (RRDE) (Figure 2.9) utilizes a metal (usually Pt) ring surrounding the working electrode, with an insulating gap separating them. The ring electrode is used to detect products formed at the disk during the experiment. The RRDE requires the use of a bi-potentiostat to control separately the potential of the disk and the potential of the ring. In the case of the ORR measurements carried out in this work, the RRDE was used to detect the amount of H_2O_2 produced during the ORR, keeping the potential of the ring at 1.2 V.

The RDE and RRDE experiments were performed in an electrochemical cell, using and Autolab PGSTAT 302N bi-potentiostat and a rotation control provided by Pine Instruments.

2.3.3 In-situ Fourier transform infrared spectroscopy coupled to electrochemical cell

The infrared spectroscopy (IRS) is based on the absorption of photons in the infrared range ($\nu = 14300 - 10$ cm^{-1}) of electromagnetic spectrum, that produces a migration between two different vibrational levels in a non-excited molecule [20]. The molecules absorb specific frequencies that are characteristic of their structure allowing the identification of the corresponding chemical specie. The most common studied region is the medium infrared region ($\nu = 4000 - 400$ cm^{-1}).

The Fourier transform infrared spectroscopy (FTIR) is based on the double beam Michelson's interferometer, which divides the radiation in two beams. The beams are again recombined after different wavelength ways. The interference between both beams produces oscillations in the intensity of the emerging beam that is recorded in the detector, obtaining a spectrum after the application of the Fourier transform.

The infrared spectroscopy is a technique used in electrochemistry to examine the electrode-electrolyte interface at the molecular level. This technique is sensitive to the functional groups in a molecule, it means, structural fragments with characteristic chemical properties. It can be used to study species adsorbed at the electrode surface and species in the thin layer of the solution adjacent to the electrode, giving information on the species present at the interface and on the absorption site. The use of a modified electro-

chemical cell coupled to the infrared spectroscopy is known as EC-FTIR. These kinds of experiments are studied using the specular reflectance due to it is not possible to measure the phenomena of transmission because the studied material is deposited on an opaque surface. The measured signal is the difference between the reflectance spectres recorded at different potentials. So we have a reference spectrum to a specific potential (R_{ref}) and collect spectra at different potentials (R_i) as the electrochemical reaction occurs.

The actual spectrometers are able to acquire a hundred of spectra in a few seconds, allowing take a spectrum with a good signal to noise ratio at resolutions $4 - 16$ cm^{-1}. The sweep potential should be slow enough so that spectra corresponding to the interest phenomena that occur at different potentials can be collected.

The FTIR spectra carried out in this thesis, were recorded in a range of $1000-3000$ cm^{-1} at a resolution of 8 cm^{-1} in a Bruker IFS 66vs spectrometer with an angle of incidence of 65^{o} with a methacrylate cell comprising a CaF_2 prism in the bottom. The reference electrode (RE) is a reversible hydrogen electrode (RHE) and the counter electrode (CE) is a gold wire. The working electrode (WE) is a gold disk with a 7 mm of diameter where the catalysts is dropped. The WE is pressed against the CaF_2 prism, creating a thin layer of electrolyte ($\approx 1\mu m$) between the electrode and the CaF_2. The scan rate used is 1 mV·s^{-1} and the FTIR are recorded on a continuous basis during the measurement (≈each 50 mV) (Figure 2.11).

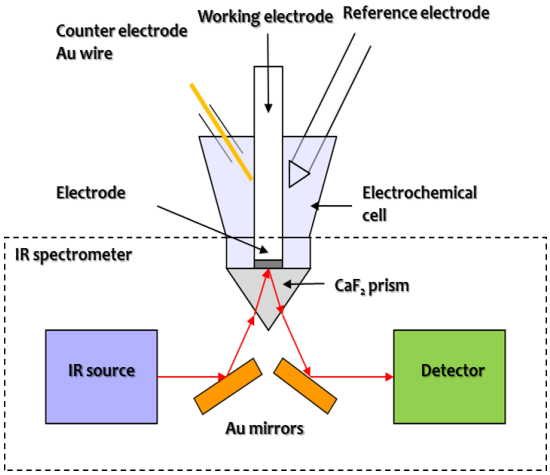

Figure 2.11: Scheme of an electrochemical cell acopled to Fourier transform infrared spectroscopy.

2.4 References

[1] G. Liu, X. Li, J.-W. Lee, B. Popov, A review of the development of nitrogen-modified carbon-based catalysts for oxygen reduction at USC, Catalysis Science & Technology, 1 (2011) 207-217.

[2] F.L. Holmes, Elementary analysis and the origin of physiological chamistry, Isis, 54 (1963) 50-58.

[3] S. Brunauer, On a theory of the van der Waals adsorption of gases, Journal of the American Chemical Society, 62 (1940) 1723-1732.

[4] M. Faraldos, C. Goberna, Técnicas de Análisis y Caracterización de materiales, Consejo Superior de Investigaciones Científicas-CSIC, Madrid, 2012.

[5] R. Jenkins, R.L. Snyder, Introduction to X-Ray Powder Difractometry, John Wiley & Sons Inc., New York, 1996.

[6] G. Perego, Characterization of heterogeneous catalysts by X-ray diffraction techniques, Catalysis today, 41 (1998) 251-259.

[7] B.E. Warre, X-ray diffraction, Addison-Wesley, Reading, 1969.

[8] J.R. Ferraro, C.W. Brown, K. Nakamoto, Introductory Raman Spectroscopy: Second Edition, 2003.

[9] C.D. Wagner, W.M. Riggs, J.F. Davis, J.F. Moulder, Handbook of X-Ray Photoelectron Spectroscopy, Perkin Elmer Corp., Minesota, 1978.

[10] C.D. Wagner, W.M. Riggs, J.F. Davis, J.F. Moulder, G.E. Muilenberg, Perkin Elmer Corp.1978.

[11] J. Kawai, Absorption Techniques in X-ray Spectrometry, in: R.A. Meyers (Ed.) Encyclopedia of Analytical Chamistry, John Wiley & Sons Ltd, Chichester, 2000, pp. 13288-13315.

[12] Z. Li, E. Dervishi, V. Saini, L. Zheng, W. Yan, S. Wei, Y. Xu, A. Biris, X-ray Absorption Fine Structure Techniques, Particulate science and technology, 28 (2010) 95-131.

[13] D.C. Koningsberger, R. Prins, X-ray absorption: principles, applications, techniques of EXAFS, SEXAFS and XANES, John Wiley & sons,

Inc.1988.

[14] K.V. Klementev, Deconvolution problems in x-ray absorption fine structure spectroscopy, Journal of physics. D, Applied physics, 34 (2001) 2241-2247.

[15] A. Hickling, Studies in electrode polarisation. Part IV.-The automatic control of the potential of a working electrode, Transactions of the Faraday Society, 38 (1942) 27-33.

[16] A.J. Bard, L.R. Faulkner, Electrochemical Methods. Fundamentals and Applications, John Wiley & Sons, Inc.2001.

[17] J.J. Van Benschoten, Cyclic voltammetry experiment, Journal of Chemical Education, 60 (1983) 772-776.

[18] J. Qiao, Effect of KOH concentration on the oxygen reduction kinetics catalyzed by heat-treated co-pyridine/C electrocatalysts, International Journal of Electrochemical Science, 8 (2013) 1189-1208.

[19] F. Jaouen, J. Herranz, M. Lefevre, J.P. Dodelet, U.I. Kramm, I. Herrmann, P. Bogdanoff, J. Maruyama, T. Nagaoka, A. Garsuch, J.R. Dahn, T. Olson, S. Pylypenko, P. Atanassov, E.A. Ustinov, Cross-laboratory experimental study of non-noble-metal electrocatalysts for the oxygen reduction reaction, ACS applied materials & interfaces, 1 (2009) 1623-1639.

[20] K. Nakamoto, Infrarred and Raman Spectra of Inorganic and Coordination Compounds, John Wiley & Sons inc.1997.

Chapter 3

Publications

The publications include in this thesis are:

(I) **C. Domínguez**; F.J. Pérez-Alonso; M. Abdel Salam; J.L. Gómez de la Fuente; S.A. Al-Thabaiti; S.N. Basahel; M.A. Peña; J.L.G. Fierro; S. Rojas. Effect of transition metal (M: Fe, Co or Mn) for the oxygen reduction reaction with non-precious metal catalysts in acid medium. Int. J. Hydrogen Energy. 39, pp.5309-5318.2014.
DOI:10.1016/j.ijhydene.2013.12.078.

(II) **C. Domínguez**; F.J. Pérez-Alonso; J.L. Gómez De La Fuente; S.A. Al-Thabaiti; S.N. Basahel; A.O. Alyoubi; A.A. Alshehri; M.A. Peña; S. Rojas. Influence of the electrolyte for the oxygen reduction reaction with Fe/N/C and Fe/N/CNT electrocatalysts. J. Power Sources. 271, pp. 87 - 96. 2014.
DOI: 10.1016/j.jpowsour.2014.07.173.

(III) **C. Domínguez**; F.J. Pérez-Alonso; M. Abdel Salam; S.A. Al-Thabaiti; A.Y. Obaid; A.A. Alshehri; J.L. Gómez de la Fuente; J.L.G. Fierro; S. Rojas. On the relationship between N content, textural properties and catalytic performance for the oxygen reduction reaction of N/CNT. Appl. Catal. B: Environ. 162, pp. 420-429. 2015.
DOI: 10.1016/j.apcatb.2014.07.002.

(IV) **C. Domínguez**, F.J. Pérez-Alonso, S.A. Al-Thabaiti, S.N. Basahel, A.Y. Obaid, A.O. Alyoubi, J.L. Gómez De La Fuente, S. Rojas. Effect of N and S co-doping of multiwalled carbon nanotubes for the oxygen

reduction. Electrochimica Acta. 157, pp. 158-165. 2015.
DOI:10.1016/j.electacta.2015.01.031.

(V) **C. Domínguez**; F.J. Pérez-Alonso; M. Abdel Salam; S.A. Al-Thabaiti, M.A. Peña, L. Barrio, S. Rojas. Effect of the N content of Fe/N/-Graphene catalysts for the oxygen reduction reaction in alkaline media. J. Mat. Chem. A 3, pp. 24487-24494. 2015.
DOI: 10.1039/c5ta04355g.

(VI) **C. Domínguez**; F.J. Pérez-Alonso; M. Abdel Salam; S.A. Al-Thabaiti, M.A. Peña, F.J. García-García, L. Barrio, S. Rojas. Repercussion of the carbon matrix for the activity and stability of Fe/N/C electrocatalysts for the oxygen reduction reaction. Appl. Catal. B: Environ. 183, pp. 185-196. 2016.
DOI:10.1016/j.apcatb.2015.10.043.

INTERNATIONAL JOURNAL OF HYDROGEN ENERGY 39 (2014) 5309–5318

Available online at www.sciencedirect.com

ScienceDirect

journal homepage: www.elsevier.com/locate/he

Effect of transition metal (M: Fe, Co or Mn) for the oxygen reduction reaction with non-precious metal catalysts in acid medium

C. Domínguez [a], F.J. Pérez-Alonso [a], M. Abdel Salam [b], J.L. Gómez de la Fuente [a], S.A. Al-Thabaiti [b], S.N. Basahel [b], M.A. Peña [a], J.L.G. Fierro [a], S. Rojas [a,*]

[a] Grupo de Energía y Química Sostenibles (EQS), Instituto de Catálisis y Petroleoquímica, CSIC, C/ Marie Curie, 2, L10, 28049 Madrid, Spain

[b] Chemistry Department, Faculty of Science, King Abdulaziz University, P.O. Box 80200, Jeddah 21589, Saudi Arabia

ARTICLE INFO

Article history:
Received 16 September 2013
Received in revised form
3 December 2013
Accepted 8 December 2013
Available online 2 January 2014

Keywords:
Non-precious metal catalysts
Oxygen reduction reaction
Mn
Co
Fe
N

ABSTRACT

The effect of the metal for the oxygen reduction reaction (ORR) in acid medium with non-precious metal catalysts has been investigated. A series of non-precious metal catalysts with typical formulation M/N/C with M being Mn, Co or Fe have been prepared by incorporating N onto an active carbon matrix by means of thermal treatments under inert atmospheres. The N-containing active carbons were further treated with the M-containing precursors based upon Mn, Co or Fe phthalocyanines and thermally treated under inert atmosphere. The performance for the ORR in acid medium of all of the catalysts has been evaluated by means of electrochemical techniques. The activity, both in terms of onset potential for the ORR and maximum current density at representative potentials between 900 and 700 mV follows the trend Fe > Co > Mn. In addition, the performance of the Fe-based catalysts obtained during the different stages of the catalyst preparation has been also evaluated. The catalysts obtained after the pyrolysis step are the only ones showing measurable rates for the ORR. Although the amount of N and Fe incorporated onto the carbon matrix decreases the pyrolysis treatment, this treatment leads to the formation of the real active sites for the ORR irrespectively of the nature of the transition metal.

1. Introduction

Proton exchange membrane fuel cells (PEMFCs) are very efficient devices for the conversion of the chemical energy stored in molecules such as H_2 or alcohols into electricity [1]. In particular, PEMFCs are expected to be widely implemented in the transportation sector and in portable devices because of their low operating temperature which enables fast start-up. Although the performance of the current state-of-the-art Pt-based PEMFCs has improved significantly and mass activities of ca. 0.3 mA mg^{-1}_{Pt} have been reported, they do not yet reach the target of 0.44 mA mg^{-1}_{Pt} at 0.9 V for 2017 recommended by the United States Department of Energy (DOE) [2,3]. The low

* *Corresponding author*. Tel.: +34 91 585 4632; fax: +34 653 858 987.
E-mail address: srojas@icp.csic.es (S. Rojas).

0360-3199/$ – see front matter
http://dx.doi.org/10.1016/j.ijhydene.2013.12.078

efficiency of Pt/C electrocatalysts for the oxygen reduction reaction (ORR) is amongst the most significant obstacles preventing the widespread utilisation of PEMFCs. At the practical level, this issue is overcome by using higher Pt loadings on the cathode electrode resulting in very high prices per kW. A more advanced approach implies the use of bimetallic M-Pt-based catalysts; typically carbon supported PtCo or PtCoNi with different stoichiometry and morphologies which in some cases produce mass activities in the order, or even higher, than DOE's 2017 requirements [3]. However, issues related with catalyst's durability, in particular Pt degradation in the cathode, along with features such as noble metal scarcity and high price must be also considered for the designing of efficient ORR electrocatalysts. In fact, large-scale applications would only be possible when non-expensive and long term technologies are available. With this scenario in mind, non-precious metal catalysts (NPMCs) become suitable candidates for replacing Pt and Pt-alloys as the cathode electrode of PEMFCs. This is because they are less expensive and more abundant than noble metals [4] and their lower kinetics for the ORR, as compared to Pt electrodes, can be compensated by using higher amounts of catalysts without severe economic repercussions.

Since 1964, when Jasinski observed that cobalt phthalocyanine catalysed the ORR [5], numerous attempts to designing very active NPMCs for the ORR have been reported [4,6]. The most active NPMCs for the ORR reported hitherto are based upon Fe or Co metals coordinated with N-atoms incorporated within a graphite network. In general, these catalysts are prepared by thermal treatments under inert atmospheres (usually referred to as pyrolysis) of a mixture containing a carbon support, ideally with high degree of microporosity, a nitrogen source such as polyaniline (PANI) [7], phenanthroline (Phen) [8] and a transition-metal precursor. First, the different components are mixed by physicochemical methods such as wet impregnation or by means of mechanical processes such as ball milling or a combination of both techniques. It has been identified also that the thermal treatment step plays a key role in the formation of the active sites. Different reaction atmospheres (N_2, Ar, and NH_3) are usually employed at temperatures between 800 and 1050 °C [9,10]. After the thermal treatment, the solids are usually treated in liquid acid medium and thermally treated again to obtain the final active NPMC usually denoted as M/N/C. Although a wide range of M/N/C ratios are produced, the most typical N content ranges between 2.5 and 5 at.% whereas metal loadings vary from 0.3–1, 0.15–0.75 and 0.48 at.% for Fe, Co and Cu have been reported depending on the metal precursor [4,11]. The mass activities of these catalysts in acid medium varies with their formulation and mass activity values of around 18, 1 and 0.6 A g^{-1} have been reported for Fe, Co and Cu-based NPMCs, respectively [4].

Remarkably, it has been observed also that rather different synthetic routes lead to electrocatalysts with virtually identical catalytic properties suggesting that different types of active sites endowed with similar catalytic performances for the ORR can exist [4]. Although the actual nature of the active sites remains elusive, most works on NPMC for the ORR suggest that it consists of N-coordinated Fe or Co moieties incorporated within the carbon network, *i.e.*, Fe/N/C or Co/N/C [4]. Some recent studies goes further and suggest that graphene-coordinated FeN_4 and CoN_4 or FeN and CoN_2 moieties are the actual active sites in NPMCs [12–14]. In general, there is a strong consensus in that transition metals must be present during the pyrolysis step in order to obtain active catalysts for the ORR; however it is still under debate whether the transition metal is necessary only to create the active site or it is also part of it [15–17]. The first hypothesis, proposed three decades ago, suggests that N and C atoms are the real active site for the ORR with NMPCs [18,19]. On the other hand, most recent studies agree in that the transition metal is actually an active component of the active site for the ORR, at least in acid medium. Whichever the case, the choice of the transition metal would affect the activity of the NMPCs for the ORR. For instance, it has been reported that the ORR performance in alkaline medium of N_4-phthalocyanines coordinated to different metal atoms follows the sequence Fe > Co > Ni > Cu = Mn [20]. Other studies in which the ORR electrocatalysts were obtained from pyrolysis of transition metal salts such as hydroxidesor acetates, also report a higher activity of the catalysts based on Fe and Co as compared to those based on other transition metals such as Cr, Mn, Ni or V [21,22]. On the other hand, other studies claim that the highest activity for the ORR is obtained by using Cr salt as the transition metal source [23]. Finally, recent theoretical calculations using Density Functional Theory (DFT) by Calle-Vallejo et al. have identified activity trends in the ORR with NPMC based on a transition metals coordinated to 4 pyridinic-N atoms within a graphene structure [24]. They found a volcano-type relationship between the transition metal and their catalytic performance for the ORR. Mn is found at the top of the cure showing the highest activity in the ORR followed by Co and Fe which also presented significant activities in this reaction.

The conflicting results concerning the nature of the transition metal for the ORR could be explained by the different synthetic routes, materials including transition metal- and N-precursors, final compositions and reaction medium studied. In this work we study the influence of transition metal (Fe, Co or Mn) in NPMC based upon M/N/C for the ORR in acid medium. We have prepared different NPMC with similar N and transition metal loadings using activated carbon as support, a polymeric N-rich resin and the corresponding metal phthalocyanine. In addition, the evolution of the nature of the Fe-based samples has been carefully characterized during the different steps of their preparation. Furthermore, their performances for the ORR in acid medium have been also evaluated.

2. Experimental

2.1. Synthesis of NPMCs

A series of NPMC containing Fe, Co or Mn as the transition metal and a matrix of N-modified active carbon have been prepared by a protocol comprising the following steps: *i*) Deposition of a N-rich polymer on active carbon; *ii*) impregnation of the corresponding metal phthalocyanine on the N-polymer/active carbon composite; *iii*) pyrolysis at 800 °C in

nitrogen atmosphere and *iv*) acid leaching to remove non-stable phases. A detailed description of each step is as follows. The aim of the first step is to incorporate a large amount of N atoms within the carbon network of the active carbon. In particular, a N-rich compound, urea (CH_4N_2O, PANREAC PRS) was dissolved in distilled water and mixed with the active carbon (AC) (Norit GSX 94017-7) in a molar ratio of AC/Urea = 2. The mixture was sonicated for 30 min to obtain a homogeneous dispersion. Then, it was mixed with a formaldehyde (Fluka, puriss p.a. ACS) aqueous solution (urea:formaldehyde molar ratio of 2:1). The temperature of the mixture was increased to 50 °C while stirring. The initial pH of the reaction mixture was adjusted to 6 and once the reaction temperature reached 50 °C it was increased to 10. These temperature and pH conditions were kept for 90 min under stirring. Then, the reaction temperature was increased to 75 °C initiating thus the polymerization reaction between urea and formaldehyde. After 30 min, the pH was set at 2.5 by addition of required amount of H_2SO_4 solution 0.5 M leading to the condensation of urea–formaldehyde polymer on the active carbon. Once the polymer was deposited on the active carbon, the solvent was eliminated in a rotary evaporator and the sample dried at 70 °C for 12 h.

In the step *ii*) the appropriate amount of metal precursor (Fe-, Co- or Mn-phthalocyanine) to obtain a 20 wt.% metal in the final catalyst was dissolved in tetrahydrofuran (THF: FLUKA purism ACS pa ≥99.5%). The solution was added to a dispersion of the N-rich polymer/active carbon composite in THF and heated to 75 °C with stirring. After 2 h THF was removed in a rotary evaporator and the solid obtained was dried in air for 12 h at 70 °C. In order to incorporate the N atoms into the graphite network of the active carbon, the solid was subjected to a pyrolysis treatment (step *iii*) in a quartz tubular reactor at 800 °C during 1 h under an inert atmosphere of 25 mL min^{-1} of N_2. In order to eliminate non-stable phases in acid electrolyte the sample recovered after the pyrolysis step was treated in a 0.5 M H_2SO_4 solution (PANREAC QP) at 60 °C for 2 h and recovered by centrifugation several times until the recovered waters have a pH value of around 6.5; step *iv*. Finally, the catalyst obtained was dried at 70 °C during 12 h.

Table 1 collates the nomenclature and the synthetic protocols (identification of the steps for the synthesis of the catalysts studied in this work). As shown in the table, Fe-based samples have been recovered after each individual step of the synthesis of the NPMC and used as catalysts for the ORR. The performance of the Fe precursor (FePhC) has been studied for comparison.

Table 1 – Nomenclature of the catalysts obtained after different synthetic routes.

Metal precursor	Steps to obtain the catalyst	Nomenclature
Co-phthalocyanine	i, ii, iii and iv	Co/N/C-800-L
Mn-phthalocyanine	i, ii, iii and iv	Mn/N/C-800-L
Fe-phthalocyanine	i, ii, iii and iv	Fe/N/C-800-L
Fe-phthalocyanine	i, ii and iii	Fe/N/C-800
Fe-phthalocyanine	i and ii	Fe/N/C
Fe-phthalocyanine	–	FePhC

2.2. Structural characterization of the NPMCs

The temperature for the thermal treatments and the thermal stability of the different samples was determined from thermogravimetric analysis (TGA) recorded in N_2 from room temperature to 1373 K with a Mettler-Toledo TGA/sDTA 851e. X-ray diffractograms were collected on a Seifert 3000 powder diffractometer operating with Cu Kα radiation ($\lambda = 0.15418$ nm) generated at 40 kV and 40 mA. Scans were recorded at 0.02°/s for 2θ values between 10° and 90°.

X-ray photoelectron spectra (XPS) of the samples were acquired with a VG Escalab 200R spectrometer fitted with an Mg Kα ($h\upsilon = 1253.6$ eV) 120 W X-ray source. The energy regions of the photoelectrons of interest were scanned until an acceptable signal-to-noise ratio was achieved. Intensities were estimated by calculating the integral of each peak, determined by subtraction of the Shirley-type background and fitting of the experimental curve to a combination of Lorentzian and Gaussian lines of variable proportions. Accurate binding energies were determined by setting the C 1s peak at 284.6 eV.

Carbon, nitrogen ad hydrogen contents of the samples were measured with an elemental analyser (LECO CHNS-932).

Textural properties were evaluated by means of N_2 adsorption–desorption isotherms recorded at liquid N_2 temperature with a Micromeritics ASAP 2000 apparatus. Samples were degassed at 150 °C under vacuum for 24 h. Specific areas were calculated by applying the BET equation within the relative pressure range $P/P^0 = 0.05–0.30$.

2.3. Electrochemical characterization

The electrochemical experiments were performed with a computer controlled Autolab Pgstat 302N potentiostat/galvanostat. A standard three-compartment glass cell and a rotating disk electrode (RDE) (Pine research Instruments) were used for all electrochemical experiments. The counter electrode was a graphite rod and the reference electrode was an Ag/AgCl electrode (Methrom Switzerland). In this manuscript potentials are quoted with respect to the RHE.

A glassy carbon electrode with a thin film of the electrocatalyst under study was used as the working electrode. For the thin film preparation, samples were dispersed ultrasonically for 10 min in a mixture of Millipore Milli Q water and Nafion (5 wt.%) to a final ratio of 98 vol.% and 2 vol.%, respectively. The final concentration of the electrocatalyst in the suspension was 6 mg_{cat} L^{-1}. A volume of 20 μL of the suspension was pipetted onto a previously polished glassy carbon tip of the RDE.

Previous to the electrochemical testing, the working electrode was electrochemically cleaned by potential cycling from 0 to 1.1 V *vs.* RHE during 50 consecutive cycles in Ar-saturated 0.1 M $HClO_4$ electrolyte. Cyclic voltammograms (CVs) between 0 and 1.0 V at 10 mV s^{-1} in N_2-saturated 0.1 M $HClO_4$ were recorded.

The ORR polarization curves were collected by means of the RDE technique between 0 and 1 V at 10 mV s^{-1} and 1600 rpm in O_2-saturated 0.1 M $HClO_4$ electrolyte. The Faradaic current density (j_F mA cm^{-2}) was obtained by subtracting the current obtained during the anodic sweep scan in the O_2-saturated electrolyte from the capacitive current obtained

in the potential sweep recorded in Ar-saturated O_2-free electrolyte under the same experimental conditions. The ORR kinetic current i_k (A) was calculated by considering the relationship between i_k and i_F as established by the Koutecky–Levich equation ($i_k = -i_F \cdot i_{lim}/(i_F - i_{lim})$) where i_k is the kinetic current defined as <0 for reduction reactions and i_{im} is the limiting current and geometric area of the electrode. Finally, the ORR mass activity is defined by $i_M = -i_k/m_{cat}$ where m_{cat} is the catalyst loading expressed in g [6].

3. Results and discussion

Fig. 1 shows the weight loss of Fe/N/C, Co/N/C and Mn/N/C samples, *i.e.*, those recovered after step *ii* with the increasing temperature recorded in N_2 atmosphere. This analysis simulates the environment of the pyrolysis (step *iii*) processes and allows setting the pyrolysis temperature. As observed in Fig. 1, all samples display a similar weight loss pattern, especially within the lower temperature range. A first weight loss is observed at temperatures lower than 200 °C as a result of the loss of physisorbed water. A second weight loss is observed starting at ca. 450 °C for Fe/N/C, Co/N/C and Mn/N/C stabilizing at ca. 650 °C. Noticeably, both weight losses overlap in the case of the Mn/N/C but are well differentiated for the Fe- and Co-samples. Less significant weight loss process are recorded at higher temperatures for the three samples up to 1000 °C. As a consequence, the pyrolysis temperature for step *iii* was set at 800 °C. Taking into account the high stability of active carbon in the inter atmosphere of the TGA, the weight loss recorded for all samples should account to the decomposition of the N- and transition metal precursors, this is, of the metal-phthalocyanines and N-polymeric resin.

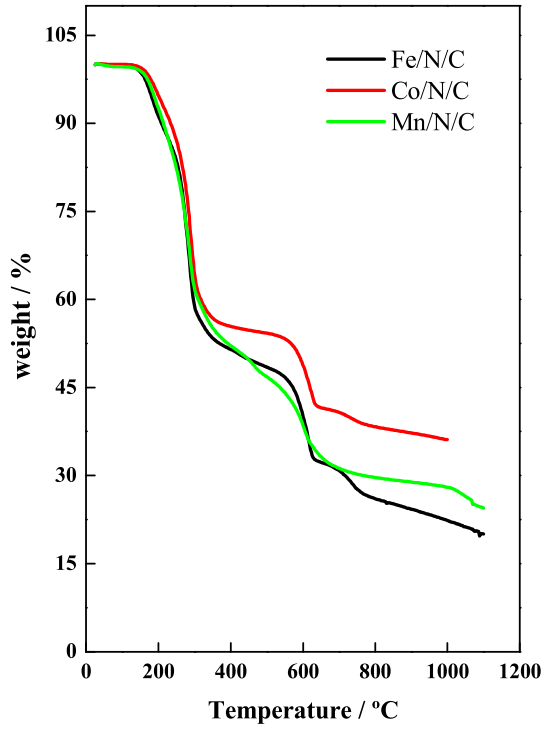

Fig. 1 – TGA profiles of Fe/N/C, Co/N/C and Mn/N/C recorded in N_2 atmosphere.

Consequently, the material recovered after the thermal treatment should contain the initial active carbon plus the N and metal (Fe, Co or Mn) actually incorporated onto the active carbon. In all cases the amount of sample obtained is of ca. 30 wt.% by weight of the initial material. However, the TGA profiles in Fig. 1 suggest that a higher amount of metal and/or N have been incorporated on Co/N/C than on Mn/N/C one.

The atomic compositions of C, H and N actually incorporated in the different samples have been determined by elemental analysis. The results are shown in Table 2.

The results obtained for the Fe-based samples clearly show how the amount of N actually incorporated in each sample decreases after each one of the different synthetic steps during the preparation of the final material. This trend sustains the hypothesis that the N-containing precursors (Fe phthalocyanine and urea-formaldehyde polymer) are the ones that actually decompose and get loss during the pyrolysis step and as a consequence less N than expected becomes incorporated onto the carbon network in the final catalysts. Furthermore, the similar amount of N in samples Fe/N/C-800-L (4.7 wt.%) and Fe/N/C-800 (4.9 wt.%) suggests that the N actually incorporated onto the carbon network after the pyrolysis process is very stable in acid media.

Table 2 also shows that the amount of N actually incorporated in the final catalysts varies with the metal and it decreases in the sequence Co/N/C-800-L > Mn/N/C-800-L > Fe/N/C-800-L in good agreement with the results derived from the thermogravimetric analyses.

The surface composition of the different samples has been studied by means of XPS. Fe 2p, Co 2p, Mn 2p, C 1s, N 1s and O 1s core-level regions were recorded and analysed in order to estimate the relative surface abundance of these elements and with the aim to identify the different N, C and Co, Mn and Fe species presented at the surface of the samples and their evolution during the different thermal and chemical treatments. The evolution of the N 1s core-level spectra of the Fe-based samples collected at different stages of their synthesis (see Table 1) have been recorded and are shown in Fig. 2a. Fig. 2b shows the N 1s core-level spectra of Co/N/C-800-L, Mn/N/C-800-L and Fe/N/C-800-L. Fig. 2a shows N1s core-level spectra of the Fe-based samples depicting the evolution of the N species during the course of the synthetic procedure from Fe phthalocyanine precursor (FePhC) to Fe/N/C, i.e., the composite obtained after steps i) and ii) and finally to the samples obtained after the pyrolysis step (Fe/N/C-800) and acid washing (Fe/N/C-800-L). First, the spectra of the Fe precursor (see Fig. 2a), Fe-phthalocyanine (FePhC), records a single peak centred at 398.6 eV and assigned to pyridinic-N,

Table 2 – C, H and N contents (expressed as wt.%) of the samples.

Sample	wt.% C	wt.% H	wt.% N
FePhC	63.8	3.0	18.5
Fe/N/C	54.8	3.8	23.4
Fe/N/C-800	77.4	1.1	4.9
Fe/N/C-800-L	75.4	1.4	4.7
Co/N/C-800-L	74.1	1.3	7.8
Mn/N/C-800-L	70.0	1.3	5.9

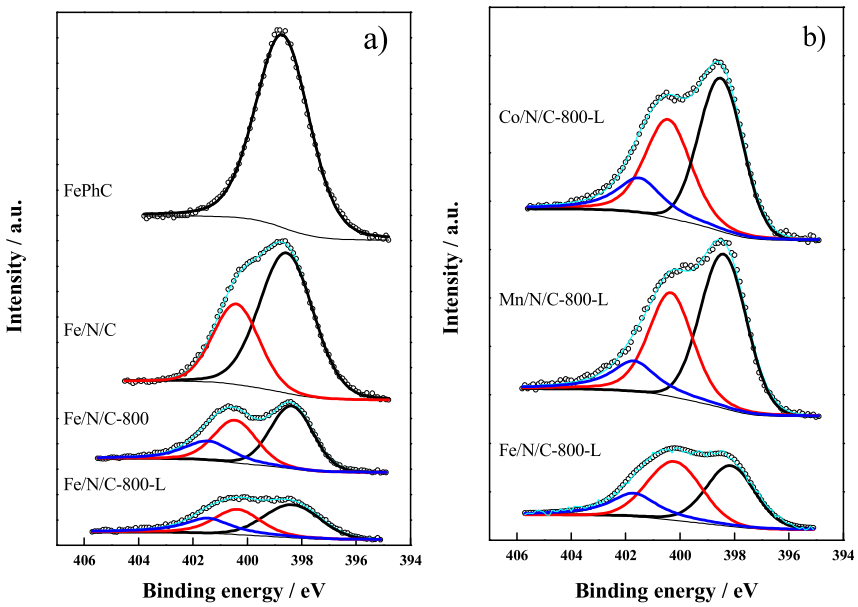

Fig. 2 – a) N 1s core-level region of the Fe-containing samples recorded during the different stages of their preparation. b) N 1s core-level regions in samples Co/N/C-800-L, Mn/N/C-800-L and Fe/N/C-800-L. Open circles (recorded spectra), cyan (fitted spectra), black, red and blue peaks correspond to the fitted components ascribed to pyridinic-, pyrrolyc- and graphitic-N species, respectively. (For interpretation of the references to colour in this figure legend, the reader is referred to the web version of this article.)

i.e., N bound to two C-atoms, identified by a black peak in Fig. 2a. The formation of the Fe/N/C composite by means of the chemical treatments described above (see steps *i* and *ii*) results in the appearance of a second N species with peak maxima at ca. 400.4 eV (red peak in Fig. 2a) and ascribed to pyrrolic-N. Remarkably, the pyrolysis step (step *iii*) results in a significant decrease of the intensity of the pyridinic-N and pyrrolic-N peaks in the spectrum of Fe/N/C-800 (see Fig. 2a and Table 3) along with the appearance of a further N species, usually referred to as graphitic-N characterized by a peak at higher binding energies >401 eV [6,25] and identified in blue in Fig. 2a. These three N-species remain visible in the spectra of the sample recovered after treatment in 0.5 M H_2SO_4 (Fe/N/C-800-L); i.e., step *iv*. The N-species detected in Co/N/C-800-L and Mn/N/C-800-L are similar to those observed in the spectra of Fe/N/C/-800-L as shown in Fig. 2b. A closer inspection of Fig. 2b, however, reveals that the relative amount of the N-species varies with each sample.

The relative abundance of surface N and M (Fe, Co or Mn) species has been determined also from the XPS analysis. As observed in Table 3, the N/C ratio decreases after the pyrolysis process for Fe-based samples in good agreement with the elemental analysis results shown above. By contrary, the N/C ratio remains constant after acid treatment (step *iv*) and Fe/N/C-800-L sample presents similar amount of surface N than Fe/N/C-800 indicating that the N incorporated onto the active carbon is stable in acid medium. This trend is also in good agreement with the data obtained by elemental analysis. On the other hand, the Fe/C ratio decreases dramatically from 0.007 to 0.002 after acid washing which is a clear indication that most of Fe phases formed after the pyrolysis step are not stable in acid media confirming previous results [26].

On the other hand, the amount of N actually incorporated onto the final catalysts varies with the metal precursor. Thus the N/C atomic ratio of the final catalysts decreases in the sequence Co/N/C-800-L > Mn/N/C-800-L > Fe/N/C-800-L. The Co-based catalyst exhibits the highest amount of N in the series; both at the catalyst surface (XPS analysis) and in the bulk (elemental analysis). Remarkably, the M/C surface atomic ratio follows the same trend as that of the N/C ratio, this is, the amount of Co in Co/N/C-800-L is greater than that of Mn in Mn/N/C-800-L which in greater than that of Fe in Fe/N/C-800-

Table 3 – N/C, O/C and M/C (M = Fe, Co and Mn) surface atomic ratios derived from XPS analysis of different samples studied.

Sample	$N_{pyridinic}$	$N_{pirrolyc}$	$N_{graphitic}$	N/C	N/M	M/C
FePhC	1.0	n.d.	n.d.	0.10	12.1	0.010
Fe/N/C	0.7	0.3	n.d.	0.10	18.8	0.006
Fe/N/C-800	0.5	0.3	0.2	0.05	6.40	0.007
Fe/N/C-800-L	0.4	0.4	0.2	0.04	21.90	0.002
Co/N/C-800-L	0.5	0.3	0.2	0.08	17.01	0.005
Mn/N/C-800-L	0.5	0.4	0.1	0.07	16.90	0.004

L. These results suggest that a direct relationship between the amount of N in the active carbon and the amount of metal incorporated into the catalysts might exist. This in turn could be indicative of the formation of MN_x moieties. The N/M ratio obtained by XPS is much higher than the theoretical value of $x = 4$ suggesting also the presence of metal-free N-surface species.

Table 3 also shows the contributions of the different individual N species identified by XPS to the total surface N. As stated above, the spectra of Co/N/C-800-L, Mn/N/C-800-L and Fe/N/C-800-L contain three different types of species of nitrogen usually referred as to pyridinic, pyrrolic and graphitic [6,25]. Although pyridinic-N is the most abundant species in all catalysts its relative abundance is lower in Fe/N/C-800-L than in the Co and Mn-based catalysts. It should be also noted that Mn/N/C-800-L exhibits the lower amount of graphitic-N in the series.

The Fe 2p, Co 2p and Mn 2p core-level spectra Fe/N/C-800-L, Co/N/C-800-L and Mn/N/C-800-L were also recorded (not shown). The presence Co^{2+} and Mn^{2+} and Fe^{2+} and Fe^{3+} has been identified; the relative abundance of Co, Mn and Fe is reported in Table 3.

Fig. 3a shows the X-ray diffractograms of the different Fe-based samples from the Fe phthalocyanine precursor to the final catalyst. The X-ray diffractogram of active carbon is also included for comparison. The diffraction lines detected in each diffractogram have been assigned to crystalline structure in agreement with the JPCDS cards as indicated in each figure. As shown in Fig. 3a, the diffractogram of the Fe precursor, FePhC, displays the characteristic set of reflections of both phthalocyanine and Fe-phthalocyanine phases. These set of reflections are also observed in the diffractogram of Fe/N/C although a significant peak broadening is observed indicating a loss of crystallinity during its incorporation onto the urea–formaldehyde–modified AC (steps *i* and *ii*). Remarkably, the reflections corresponding to the phthalocyanine and the Fe phthalocyanine disappear altogether after the pyrolysis step (*iii*). In fact, the diffractogram of Fe/N/C-800 shows the characteristic reflections of the cementite (Fe_3C) phase along with the characteristic peaks of the graphitic structure of the AC. Finally, the diffractogram of Fe/N/C-800-L exhibits only two broad peaks centred at ca. 23° and 45° corresponding to the graphitic structure along with a faint peak probably indicating the presence of Fe_3C. The evolution of the crystalline phases during the synthesis of the Fe-based catalysts agrees well with the results described above. Fe-phthalocyanine is successfully deposited onto the urea–formaldehyde–AC support. During the pyrolysis treatment, the polymer and the phthalocyanine are removed from the solid and N and Fe become incorporated on Fe/N/C-800.

The presence of diffraction lines ascribed to Fe_3C clearly shows that not all of the Fe atoms become coordinated with N ones. Remarkably, most of such N-free Fe phases are removed during the acid leaching and are not observed in the diffractogram of the final catalysts Fe/N/C-800-L.

Fig. 3b displays the diffractograms of Fe/N/C-800-L, Co/N/C-800-L and Mn/N/C-800-L. All samples show intense diffraction peaks at 23° and 45° assigned to graphitic carbon as it was mentioned previously. In addition, Fe/N/C-800-L displays faint Fe_3C reflections as stated above. Such carbide phase are not observed in the diffractograms of Co or Mn counterparts but instead reflections corresponding to metallic Co and Mn_3O_4 are observed in the diffractograms of Co/N/C-800-L and Mn/N/C-800-L, respectively. As for the Fe-based catalyst, the absence of diffraction lines of phthalocyanine in the diffractogram of these latter samples indicates that such phases have been removed during the pyrolysis step.

The N_2 adsorption/desorption isotherms of all samples under study (not shown here) can be assigned to type I isotherms characteristic of microporous solids and in general

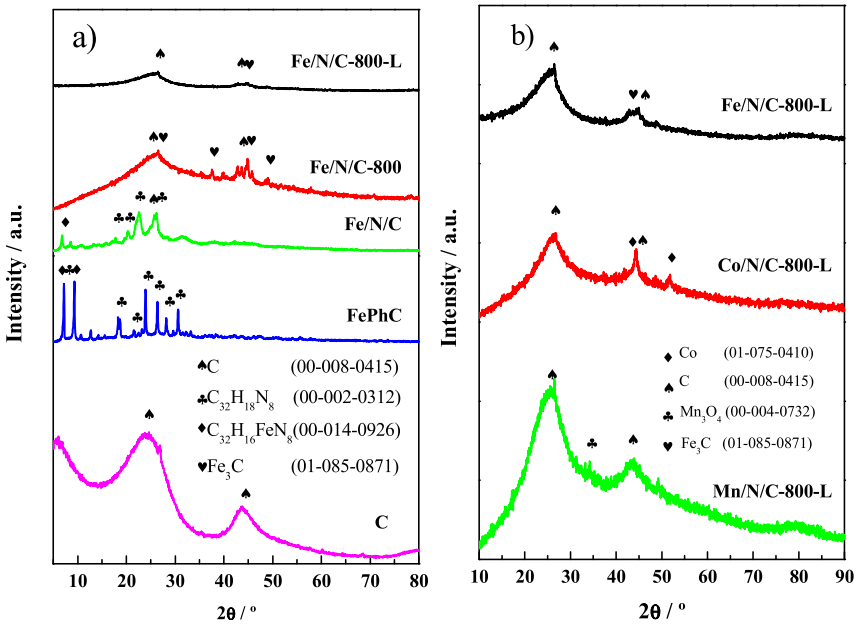

Fig. 3 – a) Evolution of the XRD profiles of the Fe-based samples during the synthesis of the final catalysts. b) XRD profiles of Co/N/C-800-L, Mn/N/C-800-L and Fe/N/C-800-L catalysts. The diffractogram of C is shown in a for comparison. For the assignment of the diffraction peaks the reader is referred to the symbol codes shown in the insets of a and b.

they show the same textural properties as pristine activated carbon. Fig. 4 shows the BET specific surface area of all samples studied. The BET area of the as received active carbon is of 850 $m^2\ g^{-1}$. This value decreases significantly during the preparation of the different catalysts as shown in Fig. 4. Thus, the incorporation of the urea–formaldehyde and of the metal precursor results in a significant reduction of the specific surface area to 21.4 $m^2\ g^{-1}$ for Fe/N/C probably due to the blockage of the active carbon micropores. The BET values increase slightly after the pyrolysis step. For instance, the BET area of Fe/N/C-800 increases up to ca. 225 $m^2\ g^{-1}$. This observation goes in line with previous reports that suggest the removal of the organic phase (urea–formaldehyde and phthalocyanine in our case) during the thermal treatment lead to the increasing of the specific surface area of the material. Noticeably, the BET surface area the electrocatalysts obtained after the acid treatment in 0.5 M H_2SO_4 decreased significantly shown values of 112, 66 and 17 $m^2\ g^{-1}$ for Fe/N/C-800-L, Co/N/C-800-L and Mn/N/C-800-L, respectively.

Fig. 5a depicts the cyclic voltammograms of the Fe-based samples recorded at 10 mV s^{-1} in Ar-saturated 0.1 M $HClO_4$. The shape of cyclic voltammograms subjected to the pyrolysis step (Fe/N/C-800 and Fe/N/C-800-L) show a square wave response typical of potential independent capacitive response [6]. These electrocatalysts also displayed significantly higher current response values than FePhC and Fe/N/C. This is because of the lower surface specific areas of the two latter samples (see Fig. 4). In addition, the voltammograms of Fe/N/C-800-L and Fe/N/C-800 show a distinct redox wave with peak maxima E_{pa} of 0.7 V and 0.8 V, respectively possibly related to the pair Fe (II)/Fe (III).

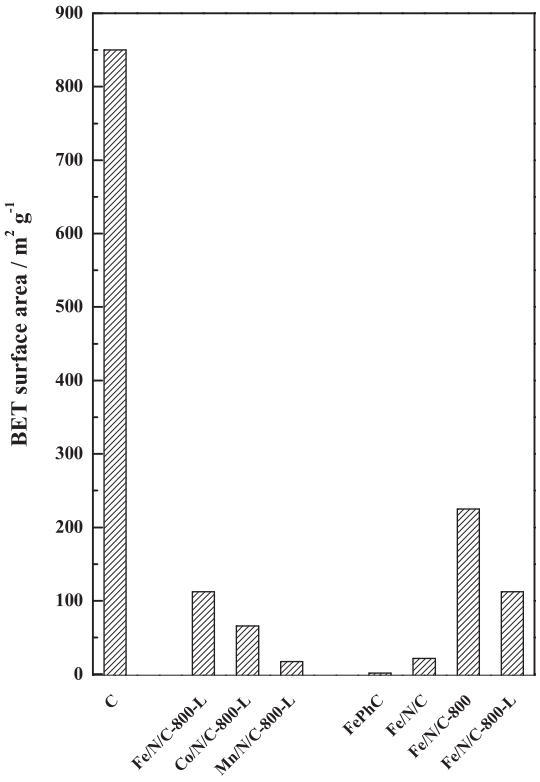

Fig. 4 – BET specific surface areas of the samples under study.

Fig. 5b shows the ORR polarization curves of the Fe-based samples recorded during the anodic sweep in O_2 saturated 0.1 M $HClO_4$ electrolyte at 10 mV s^{-1} and 1600 rpm after subtraction of the corresponding capacitive currents. Noticeably, the samples recovered after the pyrolysis step, Fe/N/C-800 and Fe/N/C-800-L are the only ones that show net oxygen reduction currents, in good agreement with previous results [4]. In principle, the lack of activity for the ORR of FePhC and Fe/N/C cannot be justified by the characterization results. As shown above, these samples contain similar or even higher amount of Fe and N than the samples recovered after the pyrolysis step (see Tables 2 and 3). However, a careful inspection of the XPS results reveals that only the samples subjected to the pyrolysis treatment present graphitic-N within their structure.

Although not shown, FePhC and Fe/N/C exhibit a good ORR activity during the first cycles of the ORR recorded in O_2-saturated acidic electrolyte, but it decreases steadily with the number of cycles probably due to demetalation in acid medium of the iron phthalocyanine until reaching the stable *i*/*E* response show in Fig. 5b [27,28].

It is also important to highlight that the ORR activity of Fe/N/C-800 is higher than that of Fe/N/C-800-L. This observation clearly shows that the treatment in acid medium result in the loss of species, probably Fe-containing ones, which are active for the ORR but are not stable in acid medium so they become loss during the leaching in 0.5 M H_2SO_4. It should be remarked at this point that the treatment in acid medium was conducted using a 5 times more concentrated acid solution than that of the electrolyte. It is plausible to presume that some species which show activity for the ORR would have been removed under such strong acid treatment that might remain stable in the electrolyte used for the ORR measurements. Moreover, it has been also reported that the adsorption of sulphates results in the loss of the ORR activity of NPMCs due to the blockage of the active sites [26].

Fig. 6a shows the cyclic voltammograms of Fe/N/C-800-L, Co/N/C-800-L and Mn/N/C-800-L recorded in Ar-saturated 0.1 M $HClO_4$ at 10 mV s^{-1}. All voltammograms show square shaped response typical of potential independent capacitive solids. Total current values are, however, characteristic of each sample and follow the decreasing trend: Fe/N/C-800-L > Co/N/C-800-L > Mn/N/C-800-L. Interestingly, this trend is the same than that of the BET specific surface area of these samples which is a clear indication that a direct relationship between the capacitive current response of a solid and its BET area exists.

Fig. 6b shows ORR polarization curves obtained with Fe/N/C-800-L, Co/N/C-800-L and Mn/N/C-800-L in O_2 saturated 0.1 M $HClO_4$ electrolytes. For an accurate comparison of the catalytic performances of these samples, the curves have been recorded during anodic sweep after subtraction of their capacitive current.

Clearly, the ORR performance of Fe/N/C-800-L is superior to that of Co/N/C-800-L and Mn/N/C-800-L ORR throughout the whole polarization range. Moreover, Mn/N/C-800-L records the lower ORR activity in the series.

This ORR activity pattern seems to be directly related with the capacitance values of each sample recorded under inert atmosphere, see Fig. 6a. Surprisingly, this activity trend is not in line with the total amount of surface N or metal in the

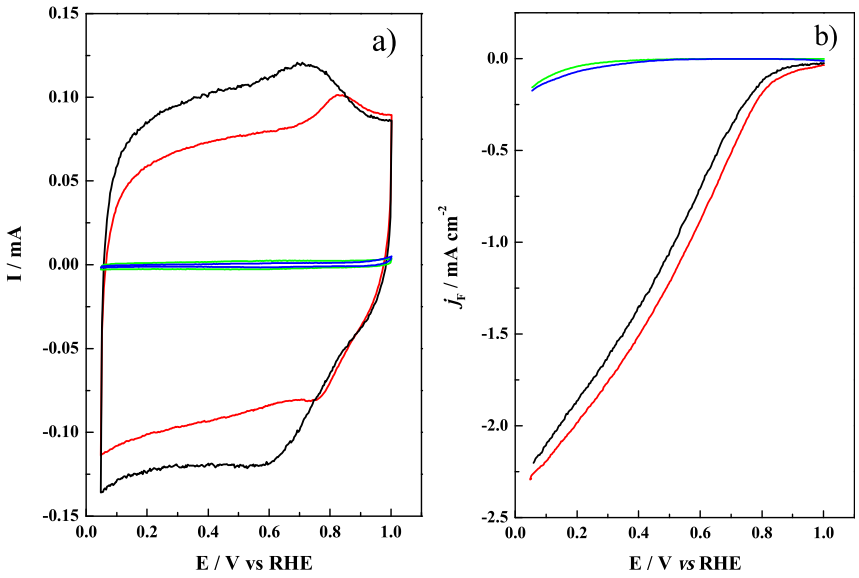

Fig. 5 – a) Cyclic voltammograms of Fe/N/C-800-L (black line), Fe/N/C-800 (red line), Fe/N/C (green line) and FePhC (blue line) recorded in Ar saturated 0.1 M $HClO_4$ at 10 mV s^{-1}. In all cases the catalyst loading is 0.6 mg cm^{-2}. b) Faradaic current density (j_F) of the Fe-based electrocatalysts corresponding to different synthesis steps recorded during the positive going sweep in O_2 saturated 0.1 M $HClO_4$ at 10 mV s^{-1} and 1600 rpm. Sample loading 0.6 mg cm^{-2}. (For interpretation of the references to colour in this figure legend, the reader is referred to the web version of this article.)

catalysts (see Table 3). In fact, the amount of such surface species (N and metal) in Fe/N/C-800-L is the lowest in the series. On the other hand, the amount of graphitic-N in Mn/N/C-800-L is almost half the value of samples Fe/N/C-800-L and Co/N/C-800-L giving a further indication of the importance of the development of graphitic-N for the ORR.

When dealing with NPMCs there is no experimental way to determine neither the number of active sites of each catalysts nor their real surface area which would enable to determine specific catalytic properties of each samples. As a consequence, the mass activity of the catalyst is taken as a way to evaluate the intrinsic catalytic activity of NPMCs. We have therefore compared the mass activity (i_M) of each catalyst in order to determine more accurately their performances for the ORR. Fig. 7 displays the variation of i_M during the ORR Fe/N/C-800-L, Co/N/C-800-L and Mn/N/C-800-L in the kinetically

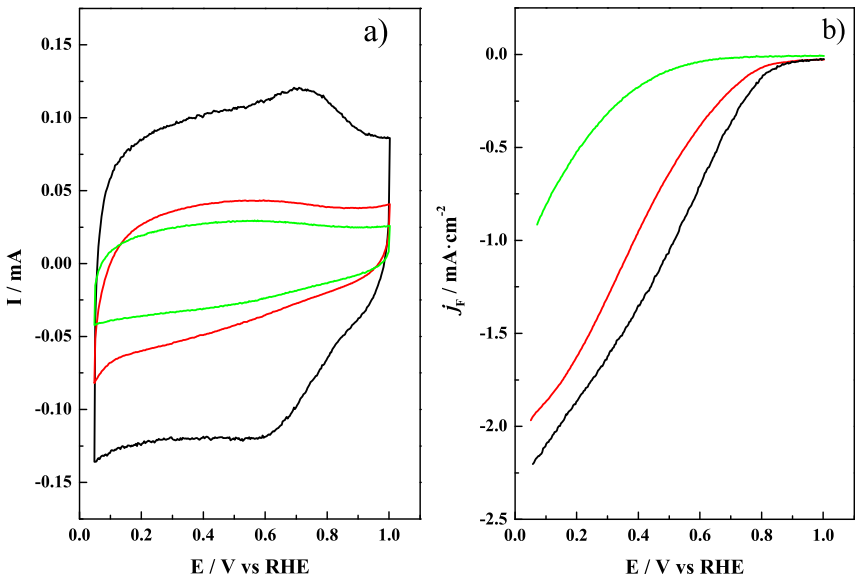

Fig. 6 – a) Cyclic voltammograms of Fe/N/C-800-L (black line), Co/N/C-800-L (red line) and Mn/N/C-800-L (green line) recorded in 0.1 M $HClO_4$ at 10 mV·s^{-1} and 1600 rpm. Sample loading 0.6 mg·cm^{-2}. b) Faradaic current density (j_F) of Fe/N/C-800-L (black line), Co/N/C-800-L (red line) and Mn/N/C-800-L (black line) recorded during the positive going sweep in oxygen saturated 0.1 M $HClO_4$ at 10 mV s^{-1} and 1600 rpm. Sample loading 0.6 mg cm^{-2}. (For interpretation of the references to colour in this figure legend, the reader is referred to the web version of this article.)

controlled potential region. Fe/N/C-800-L and Co/N/C-800-L show the highest performance for the ORR in all polarization range whilst mass activity of Mn/N/C-800-L is rather poor. Thus, Fe/N/C-800-L exhibits i_M of 0.22 A g^{-1} at 0.8 V whereas Co/N/C-800-L records a value of 0.12 A g^{-1} at the same potential. Again, this ORR trend does not correlate with the amount of exposed N or metal atoms deduced from the XPS analysis.

The results obtained are consistent with previous work in the literature. Thus according Jaouen et al. [4,6] the most active NPMC catalysts for the ORR are based upon Fe. However, recent theoretical DFT studies contradict this results and suggest that Mn-based NPMCs should display higher ORR activity than Fe- and Co-based catalysts [24]. This conflicting result might arise from the theoretical assumption that the active sites for the ORR are based upon MN_4 sites. Our characterization results suggest that these sites have not been formed, at least exclusively, in our M/N/C-800-L catalysts. Besides, we have evaluated the ORR in acid medium and it is well admitted that the ORR performances could be modified severely with the pH of the electrolyte.

There is a strong consensus in that the ORR active sites in NMPC based upon active carbon materials is located within the micropores and it probably consists of MN_x moieties [8,10]. If this statement is true, then the ORR activity should correlate with the exposed concentration of metal and nitrogen. Noticeably, and in good line with the characterization results shown in Table 2, Co/N/C-800-L and Mn/N/C-800-L contain more N and transition metal atoms within their structure than Fe/N/C-800-L. However, the ORR performance of the latter is superior to that of the Co- and Mn-based catalysts (see Figs. 6 and 7). If we assume that the nature of transition metal has no influence whatsoever for the ORR activity of the catalyst, then the ORR performance of NPMCs would be dominated by total metal loading. However, our results clearly show that the performance of Fe/N/C-800-L for the ORR is far superior to that of Co/N/C-800-L and Mn/N/C-800-L, despite of the lower M/C and N/C ratios in this sample. This observation highlights the importance of the nature of the active site for the ORR with NPMCs.

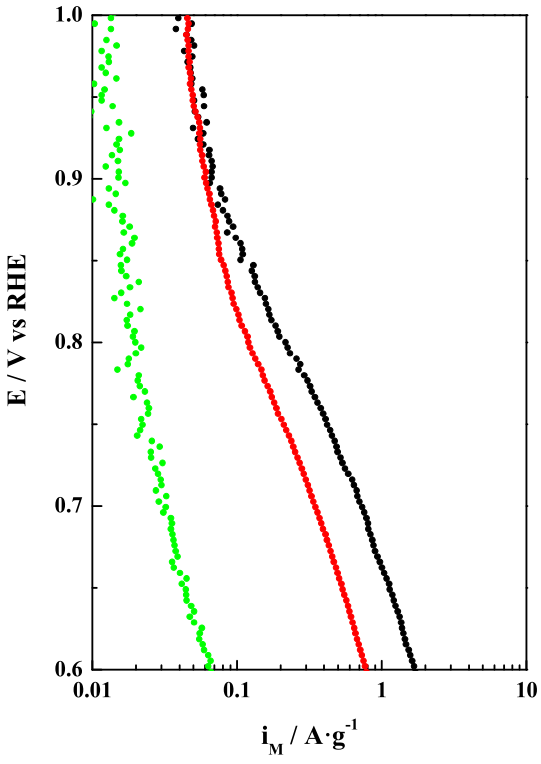

Fig. 7 – Mass activities (i_M) of Fe/N/C-800-L, Co/N/C-800-L and Mn/N/C-800-L recorded in oxygen saturated 0.1 M $HClO_4$ at 10 mV s^{-1}, 1600 rpm. Catalyst loading 0.6 mg cm^{-2}.

Although as discussed above mass activity is a useful and accurate way to determine and compare the performance of NPMCs for the ORR. A more rigorous comparison, at least from the catalysis point of view, should take into account features as the number of accessible active sites or at least catalyst's surface area. It is well admitted that materials with higher surface areas lead to a better dispersion of the active sites. We have normalized the ORR by the surface area of the N exposed sites obtained by multiplying the BET surface area by the content of surface N as determined by XPS analyses [29]. After this normalization, Fe/N/C-800-L still remains the most active catalyst in the series showing a current density of 0.050 A $m^{-2}{}_N$ at 0.8 V. Under the same reaction conditions Co/N/C-800-L and Mn/N/C-800-L record lower current density values of 0.23 and 0.18 A $m^{-2}{}_N$, respectively. These results also show that the activity of these M/N/C-800-L catalysts for the ORR is not directly related to the total amount of exposed N.

In view of these results and assuming that the nature of the species of N surface is similar in all M/N/C-800-L catalysts, it is clear that the transition metal has a strong influence in the ORR in acid medium. Fe seems to promote the formation of either more active sites or/and a higher amount of such active sites for the ORR as compared to Co or Mn.

Although the nature of active sites still remains elusive, the distinct performance for the ORR of the NPMCs studied in this work can only be ascribed to the nature of the transition metal.

Summarizing, NPMCs only exhibit high and stable catalytic activity for the ORR after pyrolysis step. During this process, the active sites for the ORR are created, probably with the involvement of graphitic-N species. The choice of the transition metal is also crucial to obtain highly active catalysts for the ORR. Our results indicate that Fe leads to more active catalysts than Co and Mn for the ORR.

4. Conclusions

The effect of the transition metal for the synthesis and performance of non-precious metal catalysts for the ORR in acid medium has been studied. NPMCs based upon Fe, Co and Mn deposited on N-modified active carbon have been prepared by following a 4-step synthetic protocol which involves physicochemical, thermal and acid treatments using the same metallic (M-phthalocyanines) and N precursors. The effect of each of these steps in the nature and catalytic performance of the Fe-based catalysts has been studied. Active and stable NPMCs for the ORR are only successfully created after the pyrolysis treatment which leads to the incorporation of the

transition metal along with the creation of graphitic-N groups. Fe-based NPMCs render more active catalysts for the ORR than Co and Mn ones despite the total amount of surface exposed metal and N is not the higher in the series. Our results indicate that the activity of NPMCs is dominated by the nature of the transition metal, and that Fe renders more active catalysts than Co and Mn.

Acknowledgements

This project was funded by the Deanship of Scientific Research (DSR), King Abdulaziz University, Jeddah, under grant number (D-006-432). The authors, therefore, acknowledge with thanks DSR technical and financial support. Economic support from projects ENE2010-15381 from the Spanish Ministry of Science and Innovation and Project 201080E116 from the CSIC is also acknowledged.

REFERENCES

[1] Gasteiger HA, Kocha SS, Sompalli B, Wagner FT. Activity benchmarks and requirements for Pt, Pt-alloy, and non-Pt oxygen reduction catalysts for PEMFCs. Appl Catal B Environ 2005;56:9–35.
[2] Rabis A, Rodriguez P, Schmidt TJ. Electrocatalysis for polymer electrolyte fuel cells: recent achievements and future challenges. ACS Catal 2012;2:864–90.
[3] Debe MK. Electrocatalyst approaches and challenges for automotive fuel cells. Nature 2012;486:43–51.
[4] Jaouen F, Proietti E, Lefèvre M, Chenitz R, Dodelet JP, Wu G, et al. Recent advances in non-precious metal catalysis for oxygen-reduction reaction in polymer electrolyte fuel cells. Energy Environ Sci 2011;4:114–30.
[5] Jasinski R. A new fuel cell cathode catalyst. Nature 1964;201:1212–3.
[6] Jaouen F, Herranz J, Lefèvre M, Dodelet JP, Kramm UI, Herrmann I, et al. Cross-laboratory experimental study of non-noble-metal electrocatalysts for the oxygen reduction reaction. ACS Appl Mater Interfaces 2009;1:1623–39.
[7] Wu G, More KL, Johnston CM, Zelenay P. High-performance electrocatalysts for oxygen reduction derived from polyaniline, iron, and cobalt. Science 2011;332:443–7.
[8] Proietti E, Jaouen F, Lefèvre M, Larouche N, Tian J, Herranz J, et al. Iron-based cathode catalyst with enhanced power density in polymer electrolyte membrane fuel cells. Nat Commun 2011;2.
[9] Ramaswamy N, Mukerjee S. Fundamental mechanistic understanding of electrocatalysis of oxygen reduction on Pt and non-Pt surfaces: acid versus alkaline media. Adv Phys Chem 2012;2012:1–17.
[10] Lefèvre M, Proietti E, Jaouen F, Dodelet JP. Iron-based catalysts with improved oxygen reduction activity in polymer electrolyte fuel cells. Science 2009;324:71–4.
[11] Ferrandon M, Kropf AJ, Myers DJ, Artyushkova K, Kramm U, Bogdanoff P, et al. Multitechnique characterization of a polyaniline–iron–carbon oxygen reduction catalyst. J Phys Chem C 2012;116:16001–13.
[12] Bouwkamp-Wijnoltz AL, Visscher W, Van Veen JAR, Boellaard E, Van der Kraan AM, Tang SC. On active-site heterogeneity in pyrolyzed carbon-supported iron porphyrin catalysts for the electrochemical reduction of oxygen: an in situ mössbauer study. J Phys Chem B 2002;106:12993–3001.
[13] Lefèvre M, Dodelet JP, Bertrand P. Molecular oxygen reduction in PEM fuel cell conditions: ToF-SIMS analysis of Co-based electrocatalysts. J Phys Chem B 2005;109:16718–24.
[14] Koslowski UI, Abs-Wurmbach I, Fiechter S, Bogdanoff P. Nature of the catalytic centers of porphyrin-based electrocatalysts for the ORR: a correlation of kinetic current density with the site density of Fe-N4 centers. J Phys Chem C 2008;112:15356–66.
[15] Matter PH, Ozkan US. Non-metal catalysts for dioxygen reduction in an acidic electrolyte. Catal Lett 2006;109:115–23.
[16] Matter PH, Wang E, Arias M, Biddinger EJ, Ozkan US. Oxygen reduction reaction catalysts prepared from acetonitrile pyrolysis over alumina-supported metal particles. J Phys Chem B 2006;110:18374–84.
[17] Nallathambi V, Lee JW, Kumaraguru SP, Wu G, Popov BN. Development of high performance carbon composite catalyst for oxygen reduction reaction in PEM proton exchange membrane fuel cells. J Power Sources 2008;183:34–42.
[18] Franke R, Ohms D, Wiesener K. Investigation of the influence of thermal treatment on the properties of carbon materials modified by N4-chelates for the reduction of oxygen in acidic media. J Electroanal Chem 1989;260:63–73.
[19] Wiesener K. N4-chelates as electrocatalyst for cathodic oxygen reduction. Electrochim Acta 1986;31:1073–8.
[20] Wiesener K, Ohms D, Neumann V, Franke R. N4 macrocycles as electrocatalysts for the cathodic reduction of oxygen. Mater Chem Phys 1989;22:457–75.
[21] He P, Lefèvre M, Faubert G, Dodelet JP. Oxygen reduction catalysts for polymer electrolyte fuel cells from the pyrolysis of various transition metal acetates adsorbed on 3,4,9,10-perylenetetracarboxylic dianhydride. J New Mater Electrochem Syst 1999;2:243–51.
[22] Yang R, Stevens K, Dahn JR. Investigation of activity of sputtered transition-metal (TM)–C–N (TM = V, Cr, Mn, Co, Ni) catalysts for oxygen reduction reaction. J Electrochem Soc 2008;155:B79–91.
[23] Côté R, Lalande G, Faubert G, Guay D, Dodelet JP, Dénès G. Non-noble metal-based catalysts for the reduction of oxygen in polymer electrolyte fuel cells. J New Mater Electrochem Syst 1998;1:7–16.
[24] Calle-Vallejo F, Martínez JI, Rossmeisl J. Density functional studies of functionalized graphitic materials with late transition metals for oxygen reduction reactions. Phys Chem Chem Phys 2011;13:15639–43.
[25] Oh HS, Oh JG, Lee WH, Kim HJ, Kim H. The influence of the structural properties of carbon on the oxygen reduction reaction of nitrogen modified carbon based catalysts. Int J Hydrogen Energy 2011;36:8181–6.
[26] Herranz J, Jaouen F, Lefèvre M, Kramm UI, Proietti E, Dodelet JP, et al. Unveiling N-protonation and anion-binding effects on Fe/N/C catalysts for O_2 reduction in proton-exchange-membrane fuel cells. J Phys Chem C 2011;115:16087–97.
[27] Li W, Yu A, Higgins DC, Llanos BG, Chen Z. Biologically inspired highly durable iron phthalocyanine catalysts for oxygen reduction reaction in polymer electrolyte membrane fuel cells. J Am Chem Soc 2010;132:17056–8.
[28] Baranton S, Coutanceau C, Roux C, Hahn F, Léger JM. Oxygen reduction reaction in acid medium at iron phthalocyanine dispersed on high surface area carbon substrate: tolerance to methanol, stability and kinetics. J Electroanal Chem 2005;577:223–34.
[29] Pérez-Alonso FJ, Salam MA, Herranz T, Gómez de la Fuente JL, Al-Thabaiti SA, Basahel SN, et al. Effect of carbon nanotube diameter for the synthesis of Fe/N/multiwall carbon nanotubes and repercussions for the oxygen reduction reaction. J Power Sources 2013;240:494–502.

Journal of Power Sources 271 (2014) 87–96

Contents lists available at ScienceDirect

Journal of Power Sources

journal homepage: www.elsevier.com/locate/jpowsour

Influence of the electrolyte for the oxygen reduction reaction with Fe/N/C and Fe/N/CNT electrocatalysts

Carlota Domínguez [a], Francisco J. Pérez-Alonso [a, *], José L. Gómez de la Fuente [a], Shaeel A. Al-Thabaiti [b], Sulaiman N. Basahel [b], Abdurrahman O. Alyoubi [b], Abdulmohsen A. Alshehri [b], Miguel A. Peña [a], Sergio Rojas [a, *]

[a] Grupo de Energía y Química Sostenibles (EQS), Instituto de Catálisis y Petroleoquímica, CSIC, C/ Marie Curie, 2, L10, 28049 Madrid, Spain
[b] Chemistry Department, Faculty of Science, King Abdulaziz University, P.O. Box 80200, Jeddah 21589, Saudi Arabia

HIGHLIGHTS

- The performance of NPMCs for the ORR is affected by the pH.
- The nature of the electrolyte is not critical when ORR are measured at constant pH.
- Sulfates seem to adsorb more strongly on NPMCs than other anions.

GRAPHICAL ABSTRACT

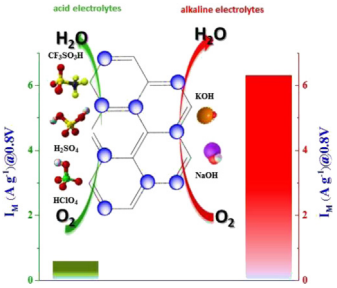

ARTICLE INFO

Article history:
Received 10 April 2014
Received in revised form
4 July 2014
Accepted 27 July 2014
Available online 2 August 2014

Keywords:
NPMC
Electrolyte
ORR
CNT
DRIFT
Fe

ABSTRACT

The behavior of Fe-based non-precious metal catalysts (NPMCs) in different electrolytes and the repercussion for the oxygen reduction reaction (ORR) has been studied. For this matter, a series of Fe-based NPMC electrocatalysts have been prepared from different carbon sources, carbon black and multiwalled carbon nanotubes. The catalysts have been subjected to chemical treatments in 0.5 M H_2SO_4 and thoroughly characterized. Their performance for the ORR in different electrolytes *e.g.* $HClO_4$, H_2SO_4, CF_3SO_3H, KOH and NaOH has been studied. Higher ORR rates have been recorded in the alkaline electrolytes as compared to the acid ones. Remarkably, the effect of the electrolyte is almost negligible when measured at a given pH value; *i.e.*, the ORR performance is not affected by the nature of the anion when measured in acid electrolytes or the cation when measured in alkaline electrolytes. On the other hand, the activity of NPMCs for the ORR decreases remarkably after treatment of the catalysts in 0.5 M H_2SO_4. This effect accounts to both the removal of active sites for the ORR during acid treatment and to the blockage of active sites due to the presence of adsorbed sulfates.

1. Introduction

Proton exchange membrane fuel cells (PEMFCs) have the potential to reduce today's society's dependence on fossil fuels and as a consequence they are expected to be widely implemented in the transportation sector and in portable devices. However, several economic and technological challenges are yet to be resolved. In

* Corresponding authors.
E-mail addresses: fperez@icp.csic.es (F.J. Pérez-Alonso), srojas@icp.csic.es (S. Rojas).

http://dx.doi.org/10.1016/j.jpowsour.2014.07.173
0378-7753/

particular, it is necessary to decrease the high loadings of Pt which are used in the state-of-the-art cathodes in order overcome the sluggish kinetics of the oxygen reduction reaction (ORR) resulting in very expensive PEMFCs. [1] In addition, features such as noble metal scarcity and Pt degradation in the cathode must be also considered for the designing of efficient ORR electrocatalysts. The design of alternative electrocatalysts with a significant reduction of Pt on their formulation [2] or even better, based upon non-expensive materials [3–6] is still a major challenge to implement real large-scale applications based on PEMFCs.

Non-precious metal catalysts (NPMCs) are strong candidates for replacing Pt in the cathode of PEMFCs. Although NPMCs with comparable ORR kinetic currents to the benchmark Pt/C have been reported recently [3,7–10], high-current-density performance and durability in acid media has to be improved significantly before NPMCs cathodes can replace Pt-based ones. In recent years numerous studies have been devoted to identify the nature of the active sites for the ORR within NPMCs [11–15], however, studies about the relationships between NPMCs and the reaction media, *i.e.*, the electrolyte are scarce. However, it is well-known that the nature of the electrolyte plays a key role in the performance of Pt-based catalysts for the ORR.

Seminal investigations with NPMCs for the ORR were inspired by nature and based on N_4-macrocycles of abundant elements such as cobalt and iron [16–20]. In this type of compounds, oxygen adsorption readily occurs at ambient temperature onto an iron center coordinated by four surrounding nitrogen functional groups [21]. However, these N_4-macrocycles coordinated to a metal center record no stable activity for the ORR in acidic media because the metal-N_x active site is destroyed by demetalation [17,18,22]. In this sense, it is well known that in order to obtain NMPCs with stable activity for the ORR in acid electrolytes a pyrolysis step above 600 °C in the presence of a nitrogen precursor, a transition metal precursor and a carbon matrix is necessary.

Graphene-coordinated FeN_4 and CoN_4 or FeN and CoN_2 moieties been proposed as the actual active sites in NPMCs [23–25]. Recently, Kramm et al. [12,13] studied the nature of the active sites for the ORR of Fe/N/C catalysts by using ^{57}Fe Mössbauer spectroscopy. They identified five different iron species and assigned the active site solely to an individual Fe(II) species within a FeN_4 arrangement with their ferrous ions both in a low or high spin. The same group reported that the N-surface groups which are part of this active site can bind anions such as sulfates from the electrolyte or HSO_3^- from Nafion membrane hence decreasing the measured turnover frequency for the ORR of the active sites [26]. These results clearly illustrate the importance that chemical changes on the catalyst surface may have for the ORR activity of NPMCs. It also shows that the understanding of the interrelations between the electrolyte and the NPMCs, in particular of the adsorption processes of the electrolyte onto NPMC surface, is paramount for the understanding of the catalytic performance for the ORR and consequently for the design of more active and robust NPMCs.

The effects of anion and cation adsorption for the ORR with Pt-based electrocatalysts are well documented [27–29]. In general, the presence of strongly adsorbed anions in the electrolytes such as H_2SO_4 or H_3PO_4 results in the appearance of high overpotentials for the ORR. This effect is not observed, however, when the ORR is measured in non-adsorbing electrolytes such as $HClO_4$, CF_3SO_3H or alkaline electrolytes. The observed decline of the ORR activity is related to strong anion adsorption of such electrolytes at the surface of Pt which impedes the adsorption of oxygen molecules onto the active sites. It is also well documented that the ORR performance of Pt/C is affected by the nature of the cation and decreasing in the order KOH > NaOH > LiOH [29]. This effect has been ascribed to non-covalent interaction between surface oxygenated species on Pt and the cation which results in the blocking of the active sites. However, studies for the effect of cation for the ORR with NPMCs are scarce. A recent study [30] shows that the cation influence for the ORR with perovskite catalysts ($LaMn_2O_{3+\delta}$) has both the same trend and order of magnitude than with Pt/C. However, the observed cation effect for the ORR is much smaller with a perovskite catalyst such as $Ba_{0.5}Sr_{0.5}Co_{0.8}Fe_{0.2}O_{3-\delta}$, and in fact it is only observed when comparing the catalytic performance in KOH and LiOH.

This work aims to investigate the effect of anion and cation binding onto Fe/N/C catalysts in different acid and basic electrolytes and the repercussions for the ORR. In addition, the effect of the strong adsorption of sulfates at the catalyst surface during the acid treatment used for the preparation of Fe/N/C and Fe/N/CNT has been also studied. Fe/N/C electrocatalysts have been synthesized by ball milling of a mixture of active carbon or carbon nanotubes, urea and Fe-phthalocyanine. Finally, the active sites have been created by pyrolysis at 800 °C under N_2 atmosphere. An aliquot of the obtained solid was treated in 0.5 M H_2SO_4 to removing the acid-soluble phases. The ORR of all catalysts before and after acid washing was evaluated by electrochemical means using an RDE (Rotating disk electrode) in the different electrolytes described above.

2. Experimental

2.1. Synthesis of Fe/N/C and Fe/N/CNT catalysts

The Fe/N/C catalysts studied in this work were prepared as follows. In a first step 5.5 g of the carbon matrix, either active carbon, (Norit GSX 94017-7) or multiwalled carbon nanotubes (CNTs) (Nanocyl NC 7000) and 0.2 g of the N precursor, 1,4,8,11-Tetraazacyclotetradecane (Aldrich 98%), were ballmilled, under room conditions, employing a planetary ballmill (PM100, Retsch), at 350 rpm during 4 h in a 50 mL WC vessel. The N/C composite obtained was mixed with 5.5 g of the carbon precursor (active carbon or CNTs) and 9.9 g of Urea (CH_4N_2O, PANREAC PRS) and ballmilled at 350 rpm during 4 h in a 50 mL WC vessel. In a following step the appropriate amount of iron phthalocyanine (Aldrich) to obtain a Fe concentration of 1.6 wt.% in the catalyst before pyrolysis, was added to 7.5 g of the N/C composite obtained after the two ball milling steps described above. This mixture was ballmilled again during 10 h at 350 rpm in a 50 mL WC vessel. The solid obtained was thermally treated (pyrolised) in a quartz tubular reactor at 800 °C for 1 h in an inert atmosphere of 25 mL min^{-1} of N_2. The resulting NPMCs were labeled as Fe/N/C or Fe/N/CNT where C and CNT denote whether the catalysts have been synthesized with active carbon or CNT, respectively. Aliquots of both catalysts were subjected to an acid-leaching, for this purpose samples were treated in 0.5 M H_2SO_4 (PANREAC QP) at 60 °C for 2 h to eliminate non-stable phases in acid electrolyte. The solid obtained was washed with distilled H_2O by centrifugation at 2500 rpm for 10 min until the pH of the recovered water was of ca. 6.5 and dried at 70 °C for 12 h. The NPMCs obtained acid leaching are labeled as L-Fe/N/C and L-Fe/N/CNT where L-prefix denote the acid treated catalysts.

2.2. Structural characterization

X-ray diffractograms were collected on a Seifert 3000 powder diffractometer operating with CuKα radiation (λ = 0.15418 nm) generated at 40 kV and 40 mA. Scans were recorded at 0.02°/s for 2θ values between 10° and 90°.

X-ray photoelectron spectra (XPS) of selected core-level elements were acquired with a VG Escalab 200R spectrometer fitted with an MgKα (hυ = 1253.6 eV) 120 W X-ray source. The energy

regions of the photoelectrons of interest were scanned until an acceptable signal-to-noise ratio was achieved. Intensities were estimated by calculating the integral of each peak, determined by subtraction of the Shirley-type background and fitting of the experimental curve to a combination of Lorentzian and Gaussian lines of variable proportions. Accurate binding energies (±0.2 eV) were determined by referencing to the C 1s peak at 284.6 eV.

Carbon, nitrogen, hydrogen and sulfur contents of the samples were measured with an elemental analyzer (LECO CHNS-932).

Infrared spectra (DRIFT) were obtained with a Jasco FTIR-6300A spectrometer equipped with an MCT detector. The spectra were recorded with a resolution of 4 cm^{-1} and an accumulation of 256 scans. Fe/N/C and L-Fe/N/C were finely ground and placed into a ceramic crucible in the DRIT chamber. In a first step, 25 mL min^{-1} of pure He was flowed through the chamber at 200 °C for 1 h to remove physisorbed H_2O. The temperature was set at 25 °C and DRIFT spectra were recorded for each sample and used as reference spectra. Then, Fe/N/C and L-Fe/N/C samples were subjected to a thermal treatment in He at 500 °C K for 1 h (heating rate 10 °C min^{-1}). Then, the temperature was decreased to 25 °C under He and DRIFT spectra for each sample were recorded.

Textural properties were evaluated by N_2 adsorption–desorption isotherms of the samples recorded at liquid N_2 temperature with a Micromeritics ASAP 2000 apparatus. Samples were degassed at 140 °C under vacuum for 24 h. Specific areas were calculated by applying the BET method within the relative pressure range $P/P^0 = 0.05–0.30$.

2.3. Electrochemical characterization

The electrochemical experiments were performed by using a computer controlled Autolab Pgstat 302N potentiostat/galvanostat.

A standard three-compartment glass cell and a rotating disk electrode (RDE) (Pine research Instruments) were used for all electrochemical experiments. The counter electrode was a graphite rod and the reference electrode was a Reversible Hydrogen Electrode (RHE). All potentials in this manuscript are referred to the RHE.

A glassy carbon electrode with a thin film of the electrocatalyst under study was used as the working electrode. For the thin film preparation of the Fe/N/C series the catalysts were dispersed ultrasonically in a mixture of Millipore Milli Q® water, and Nafion (5 wt.%) with a final ratio of 98 vol.% and 2 vol.%, respectively. For the Fe/N/CNT series the ink were prepared using a mixture of isopropanol, Millipore Milli Q® water and Nafion (5 wt.%) with a final ratio of 19.6 vol.%, 78.5 vol.% and 1.9 vol.%, respectively. The final concentration of the electrocatalyst in the suspension was 6 mg_{cat} mL^{-1}. A volume of 20 μL of the suspension was pipetted onto the previously polished glassy carbon tip (0.196 cm^2) of the RDE.

Previous to the electrochemical testing, the working electrode was electrochemically cleaned by potential cycling from 0 to 1.1 V for 50 cycles in Ar-saturated 0.1 M of the electrolyte used: CF_3SO_3H, H_2SO_4, $HClO_4$, KOH or NaOH, until stable voltammograms are obtained (Fig. S1). Cyclic voltammograms (CVs) were recorded between 0 and 1.0 V at 10 mV s^{-1} in Ar-saturated 0.1 M of the electrolyte used: CF_3SO_3H, H_2SO_4, $HClO_4$, KOH or NaOH.

The ORR polarization curves were collected by means of the RDE technique by recording a series of cyclic voltammograms between 0 V and 1 V at 10 mV s^{-1} and 1600 rpm in O_2-saturated in 0.1 M of the electrolyte used: CF_3SO_3H, H_2SO_4, $HClO_4$, KOH or NaOH. The Faradaic current density (j_F in mA cm^{-2}) was obtained by subtracting the current obtained during the anodic sweep scan in the O_2-saturated electrolyte from the capacitive current obtained in the potential sweep recorded in Ar-saturated O_2-free electrolyte under the same experimental conditions. The ORR kinetic current (i_k) was calculated by using the relationship between i_k and i_F as established by the Koutecky–Levich equation ($i_k = -i_F \cdot i_{lim}/(i_F - i_{lim})$) where i_K is the kinetic current defined as < 0 for reduction reactions and i_{lim} is the limiting current. Finally, the ORR mass activity is defined by $i_M = -i_K/m_{cat}$ where m_{cat} is the catalyst loading expressed in grams [31].

3. Results and discussion

3.1. Physicochemical characterization

Fig. 1 shows the diffractograms of Fe/N/C and L-Fe/N/C. Both diffractograms display a set of reflections characteristic of the Fe_3C phase along with a strong reflection of the (002) planes of graphite at $2\theta \approx 25°$. In addition, the diffractogram of Fe/N/C presents small diffractions peaks of Fe_3O_4 which are not observed in the diffractogram of L-Fe/N/C indicating that phase has been leached during the acid treatment in 0.5 M H_2SO_4. This observation is predictable due to the high solubility of Fe oxide and carbide phases in acid media. On the other hand, the diffraction peaks of the Fe_3C phase, although less intense, are still observed in the diffractogram of L-Fe/N/C suggesting that the Fe_3C is not completely removed during acid treatment even though this phase is also highly soluble in acid media such as 0.5 M H_2SO_4. In view of these results, it is plausible to assume that Fe_3C is encapsulated or strongly bound within the carbon matrix of L-Fe/N/C.

C, H, N and S contents (wt.%) have been determined by elemental analysis (see Table 1). The results obtained indicate that all of the N incorporated (around 4 wt.%) onto the carbon matrix after the pyrolysis process is stable after acid treatment confirming previous results [32]. As observed in Table 1, L-Fe/N/C contains a significant amount of S of 0.9 wt.%, much greater than S detected in Fe/N/C. The presence of S in the acid treated sample clearly indicates that sulfate anions remain adsorbed on the catalyst after the 0.5 M H_2SO_4 treatment.

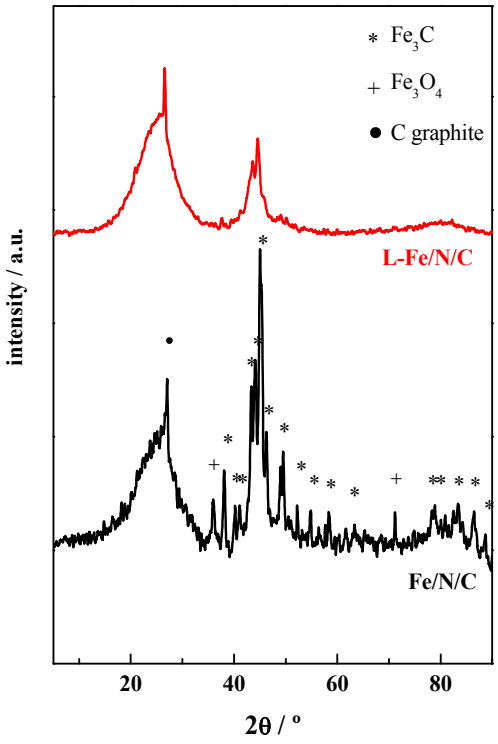

Fig. 1. X-ray diffraction patterns for L–Fe/N/C and Fe/N/C.

Table 1
C, H, N and S wt.% contents of the catalysts under study determined from elemental analysis. Specific surface areas determined form the BET method.

Catalyst	C wt.%	H wt.%	N wt.%	S wt.%	BET area/m^2g^{-1}
Fe/N/C	75.9	1.2	3.9	0.20	238.8
L–Fe/N/C	76.1	1.2	3.9	0.90	159.7
L–Fe/N/C-350	70.0	1.4	3.7	0.32	
Fe/N/CNT	84.8	0.5	2.5	0.01	160.6
L–Fe/N/CNT	87.2	0.5	2.6	0.28	145.1
L–Fe/N/CNT-350	86.2	0.5	2.6	0.16	

The Fe 2p, S 2p, C 1s, N 1s and O 1s core-level region spectra of Fe/N/C and L-Fe/N/C were recorded in order to estimate the relative surface abundance of these elements and to identify their nature, see Table 2. The N 1s and Fe 2p core-level spectra of Fe/N/C and L-Fe/N/C are shown in Fig. 2. The N 1s spectra comprise three components with peak maxima at 398.5, 400.1 and 401–401.5 eV. The peak at 398.5 eV corresponds to pyridinic forms of nitrogen (pyridinic-N), whereas the peak at 400.1 eV is assigned to pyrrolic nitrogen (pyrrolic-N) or/and to nitrogen in pyridones (pyridone-N). The N species at the highest binding energy of 401–401.5 eV are usually ascribed to quaternary nitrogen (graphitic-N) defined as relatively more positively charged nitrogen than pyridinic-N, and being part of a larger aromatic structure including protonated pyridinic-N and nitrogen atoms replacing carbon atoms in graphene structures [31,33,34].

As observed in Fig. 2 and in Table 2, the contribution of pyrrolic-N (and/or pyridone-N) to the total N-species increases at the expenses of the other N-species after the acid treatment in 0.5 M H_2SO_4. However, and in good agreement with the data recorded from elemental analyses (see Table 1), the total N_{at}/C_{at} surface atomic ratio remains stable after the acid treatment. On the other hand, the Fe_{at}/C_{at} surface atomic ratio decreases from 0.005 in Fe/N/C to 0.002 in L-Fe/N/C, confirming that a significant fraction of the Fe-containing phases have been removed during the acid treatment in 0.5 M H_2SO_4. Two distinct Fe species with peak maxima at 710.5 and 707.1 eV ascribed to Fe^{2+}/Fe^{3+} and Fe^0 species, respectively [35,36] can be observed in the Fe $2p_{3/2}$ core-level spectrum of Fe/N/C. This observation is in good agreement with the XRD analysis showing the coexistence of Fe_3O_4 and Fe_3C phases in Fe/N/C. The spectrum of L-Fe/N/C, however, contains a single less intense peak with maximum at around 710.5 eV indicative of the presence of Fe oxidized species. The decreasing of the intensity of the Fe 2p XPS indicates that a significant fraction of Fe species are removed during the acid treatment. This observation is also supported by the XRD data shown above which also show that previous to the acid treatment, Fe_3O_4 and Fe_3C crystal phases are present in Fe/N/C but only weak peaks of the latter species are observed in the diffractogram for L-Fe/N/C. The position of the Fe 2p core-level peak at ca. 710.5 eV for L-Fe/N/C along with the presence of a satellite line at ca. 715.5 eV is indicative of the presence of Fe^{2+} species. As a consequence, the Fe species remaining in L-Fe/N/C can be assigned to Fe/N*x* species, probably FeN_4 and/or FeN_{2+2}, which have been proposed as the active sites for the ORR reaction [37,38].

Table 2
N/C, S/C and Fe/C surface atomic ratios derived from XPS analysis of Fe/N/C and L–Fe/N/C samples.

Sample	Pyridinic-N	Pyrrolic-N	Quaternary-N	N/C	Fe/C	S/C
Fe/N/C	0.50	0.15	0.35	0.041	0.0050	–
L–Fe/N/C	0.43	0.25	0.32	0.042	0.0020	0.002
L–Fe/N/C-350	0.46	0.22	0.32	0.047	0.0025	–
Fe/N/CNT	0.55	0.28	0.12	0.026	0.0020	–
L–Fe/N/CNT	0.46	0.32	0.18	0.024	0.0010	0.001
L–Fe/N/CNT-350	0.49	0.39	0.09	0.021	0.0011	0.0007

The lack of XPS peaks for Fe-reduced species in the spectra of L-Fe/N/C indicates the removal of the fraction of the Fe_3C phase located at the surface of the catalyst during the acid treatment. However, since Fe_3C crystallites are clearly detected by XRD is reasonable to assume that a fraction of such phase is not soluble in acid media probably because it remains encapsulated within the carbon matrix and as a consequence it cannot be detected by a surface-sensitive technique such as XPS.

The S 2p core-level spectrum of L-Fe/N/C (Fig. 2c) shows a single component with peak maximum at 168.5 eV ascribed to sulfate (SO_4^{2-}) species. This observation is in line with the elemental analysis results which show that the amount of S-containing species increases after acid treatment with 0.5 M H_2SO_4. It has been recently reported that the ORR activity of NPMCs is severely affected by the presence of adsorbed sulfate species which bind to protonated pyridinic nitrogen which is proposed to be part of the active site for the ORR [26]. The importance of the electrolyte for the performance of NPMCs for the ORR, which is in fact widely recognized for Pt-based electrocatalysts [27–29], has not been thoroughly studied hitherto. In the next section the influence of the electrolyte (nature of anion and pH) for the performance of NPMCs for the ORR will be described.

3.2. Effect of the electrolyte for the ORR performance of Fe/N/C and L-Fe/N/C

Fig. 3 shows the cyclic voltammograms for Fe/N/C and L-Fe/N/C recorded at 10 mV s^{-1} in Ar saturated 0.1 M solutions of the electrolyte under study, namely $HClO_4$, H_2SO_4, CF_3SO_3H, KOH and NaOH. Fe/N/C and L-Fe/N/C record similar voltammograms in all acid electrolytes displaying a square wave profile typical of potential-independent capacitive responses [31] along with two peaks ascribed to the Fe^{2+}/Fe^{3+} redox couple. The anodic peak (Ep_a) appears at ca. 0.65 V in the voltammograms recorded with L-Fe/N/C regardless of the nature of the acid electrolyte. By contrary, the Ep_a varies with the nature of the acid electrolyte in the voltammograms for Fe/N/C. Thus, when measured in CF_3SO_3H or $HClO_4$ the Ep_a appears at ca. 0.79 V, shifting to less positive potential values of ca. 0.65 V when measured in H_2SO_4. It should be noted that this latter Ep_a value is the same as those recorded for the H_2SO_4-treated catalyst, L-Fe/N/C, in all of the acid electrolytes. These results suggest that the shifting towards less positive values of the Ep_a of the Fe^{2+}/Fe^{3+} pair in the voltammogram for Fe/N/C recorded in 0.1 M H_2SO_4 as compared to the other acid electrolytes, is due to the presence of sulfates on the surface of Fe/N/C resulting in the stabilization of the Fe^{3+} species, *i.e.*, facilitating the oxidation of Fe^{2+} and hence shifting the Ep_a to less positive values. This behavior suggests that sulfate anions adsorb more strongly on Fe/N/C than perchlorate or triflate anions.

On the other hand, both Fe/N/C and L-Fe/N/C exhibit similar cyclic voltammograms when recorded in the alkaline electrolytes. The voltammograms display a square wave profile, wider at the more negative potentials, typical of capacitive responses. Noticeably, the Fe^{2+}/Fe^{3+} redox pair is not observed in the voltammograms recorded in alkaline media (not even if the potential window is extended to more anodic and/or cathodic potentials).

Fig. 4 shows the ORR polarization curves of Fe/N/C and L-Fe/N/C after subtraction of their corresponding capacitive currents recorded in the electrolyte under study. Irrespective of the catalyst and the electrolyte, the polarization curves exhibit a mixed kinetic-diffusion controlled region and a diffusion limiting current region. Clearly, both Fe/N/C and L-Fe/N/C exhibit superior performances for the ORR in the alkaline electrolytes. Remarkably, the performance of both electrocatalysts varies significantly with the pH but it is not severely affected with the actual nature of the electrolyte; this is,

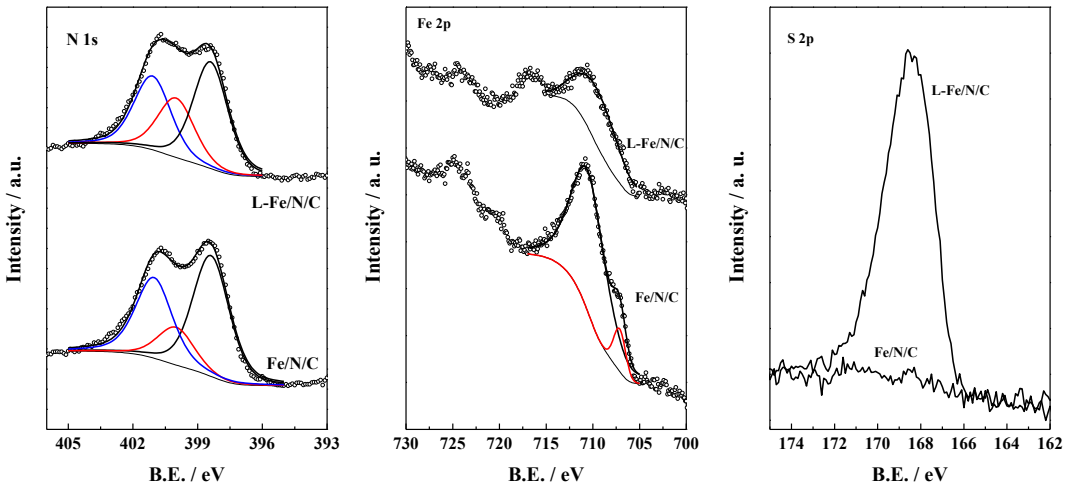

Fig. 2. XP spectra of the N 1s, Fe 2p and S 2p core-levels of Fe/N/C and L–Fe/N/C. The peaks for pyridinic-N, pyrrolic-N and quaternary-N in the N 1s core-level region spectrum are shown in black, red and blue, respectively. Fe^{2+}/Fe^{3+} and Fe^{0} components in the Fe 2p core-level region spectrum are shown in black and red, respectively. (For interpretation of the references to colour in this figure legend, the reader is referred to the web version of this article.)

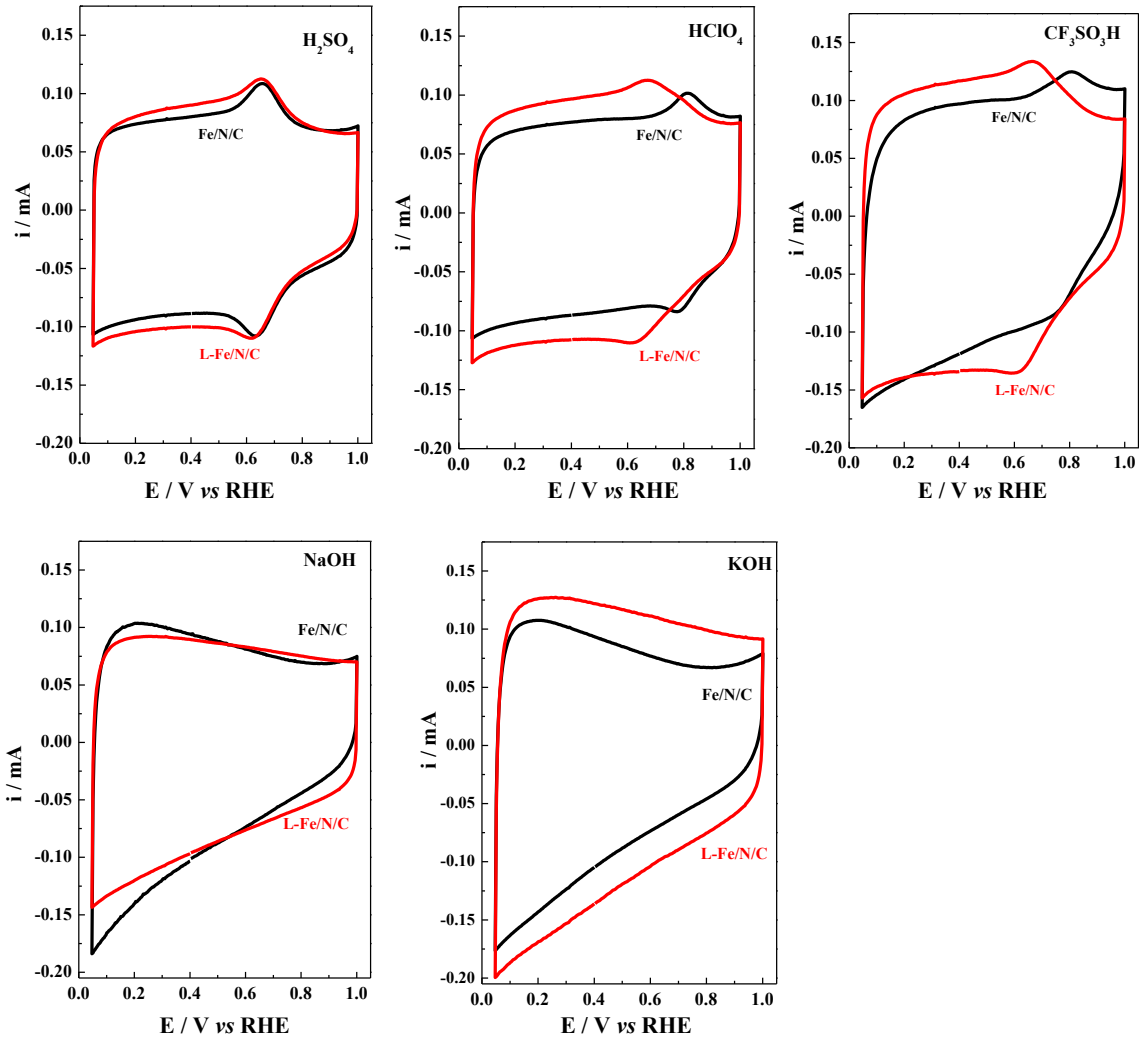

Fig. 3. Cyclic voltammograms for Fe/N/C (black lines) and L–Fe/N/C (red lines) recorded at 10 mV s^{-1} in 0.1 M of H_2SO_4, $HClO_4$, CF_3SO_3H, NaOH and KOH. Catalyst loading 0.6 mg cm^{-2}. (For interpretation of the references to colour in this figure legend, the reader is referred to the web version of this article.)

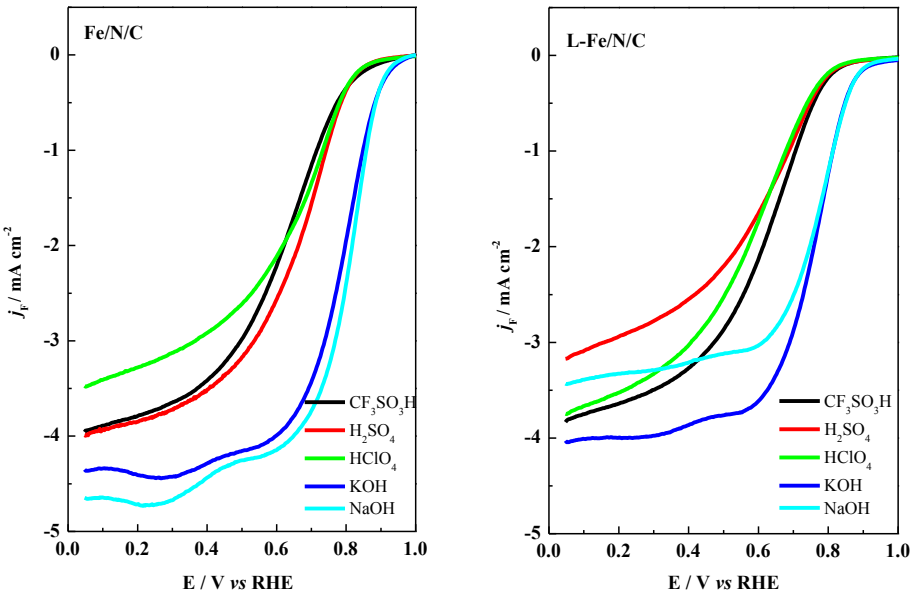

Fig. 4. Faradaic current densities (j_F) of Fe/N/C and L–Fe/N/C recorded during the positive going sweep in O_2 saturated 0.1 M electrolyte (as indicated in the legend) at 10 mVs^{-1}, 1600 rpm. Electrocatalyst loading 0.6 mg cm^{-2}.

similar performances are recorded in all alkaline electrolytes and in all acidic electrolytes. In addition, the current densities for Fe/N/C are higher than those recorded with L-Fe/N/C when measured in the same electrolytes.

Fig. 5 shows the mass transport corrected mass activities (i_M) of Fe/N/C and L-Fe/N/C in the kinetically controlled region which confirm the trends observed in the ORR polarization curves. The ORR performance varies with the pH and significantly higher ORR rates are recorded in alkaline electrolytes. However, the ORR kinetics is not severely affected by the nature of the anion (acid electrolytes) or the cations (alkaline electrolytes) and similar ORR rates have been recorded in all of the acid electrolytes and in all of the alkaline ones. As for the acid media, the ORR performance in CF_3SO_3H record a slightly different slope than that in H_2SO_4 and $HClO_4$ displaying higher i_M at low overpotentials and lower i_M at high overpotentials.

A previous study of Mukerjee et al. [39] reports that the higher activity of Fe/N/C catalysts for the ORR in alkaline media can be ascribed to the promotion of the direct molecular O_2 adsorption on the Fe^{2+} active site *vs* the outer-sphere mechanism (which follows the $2e^-$ pathway) which usually predominates for the ORR in alkaline media. This is because the OH^- species adsorbed at Fe^{2+} behave as a labile ligand hence being easily displaced by O_2. Ross et col. [40,41] studied the effect of pH in the ORR with noble metals and concluded that since the rate determining step (the transfer of one electron to $O_{2,ad}$ to $\cdot O_{2,ad}^-$) is a pH independent process, the

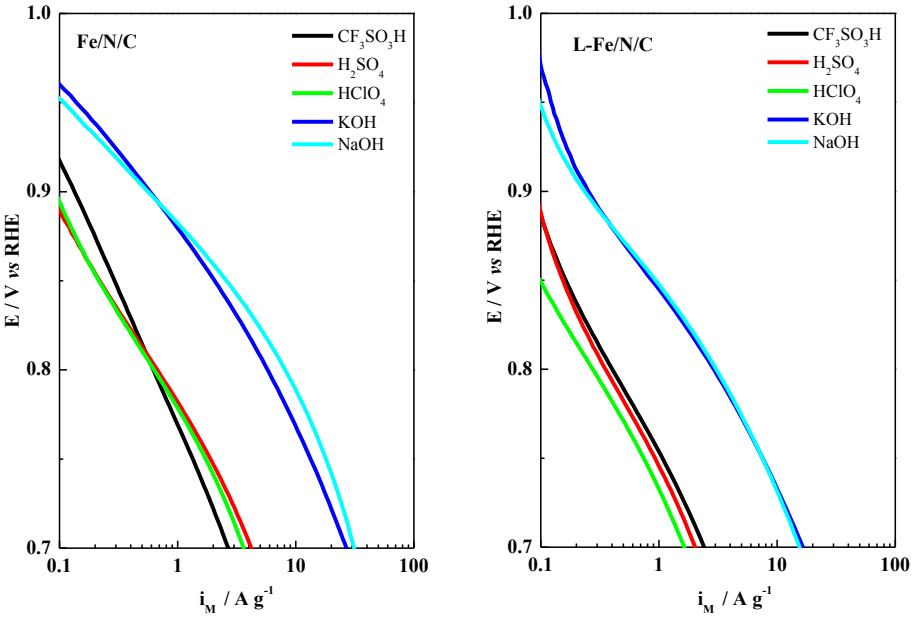

Fig. 5. Diffusion corrected mass activities (i_M) of Fe/N/C and L–Fe/N/C in O_2 saturated 0.1 M electrolyte at 10 mV s^{-1}, 1600 rpm. Sample loading 0.6 mg cm^{-2}.

reversible potential for the ORR should be pH independent as well. However, if the overall process is taken into account, by considering the involvement of H^+, then the overpotential becomes pH dependent decreasing with the increasing pH value.

Summarizing, our results clearly show that when measured at a given pH value, either acid or alkaline, the performance of Fe/N/C for the ORR is not severely influenced by the nature of electrolyte. The almost negligible effect of the cation or anion counterions for the ORR indicates that $CF_3SO_3^-$, ClO_4^- and SO_4^{2-} from the acid electrolytes or Na^+ and K^+ from the alkaline ones do not compete for the active sites with O_2 during the ORR or all cation or anion counterions compete in the same way. On the other hand, the observed shifting of the peaks for the Fe^{2+}/Fe^{3+} redox couple to more negative potentials in the cyclic voltammograms recorded in H_2SO_4 as compared to those recorded in $HClO_4$ or CF_3SO_3H see Fig. 3 indicate that sulfate anions adsorb more strongly than perchlorate or triflate ones on Fe/N/C. It has been suggested that a correlation between catalytic activity for the ORR and the potential of the M^{2+}/M^{3+} redox pair of metal N_4-macrocycles exists and that the more positive the Ep, the higher the catalytic activity for the ORR [42]. However, we have found no evidence for such a correlation between the Ep_a of the Fe^{2+}/Fe^{3+} and the performance for the ORR with the NPMCs reported in this manuscript. It should be noted that the actual nature of the NPMCs reported in this work, based upon the incorporation of Fe into N/C composites, is not the same than that of N_4-macrocyles reported in reference 42. In addition, a closer inspection of the blank voltammograms shown in Fig. 3 reveals that the amount of the Fe species responsible for the Fe^{2+}/Fe^{3+} pair is similar in both Fe/N/C and L-Fe/N/C. This observation is remarkable since the total amount of Fe in the latter sample is significantly lower than that in Fe/N/C (see Table 2) due to the dissolution of Fe species during the treatment in 0.5 M H_2SO_4. These conflicting observations suggest that the iron species responsible for the Fe^{2+}/Fe^{3+}pair (which appear to react with sulfates) might not actually be part of the active centers for the ORR.

3.3. Effect of sulfates for the ORR

As shown in Table 3, L-Fe/N/C exhibits between 37% and 47% lower i_M for the ORR at 0.8 V than Fe/N/C when measured in the acid electrolytes and between 50% and 60% lower activities when measured in alkaline media. One obvious reason for the lower ORR activity of L-Fe/N/C is the dissolution of a fraction of the Fe species during 0.5 M H_2SO_4 treatment. As shown in Table 2, the amount of Fe in L-Fe/N/C is around 60% lower than on Fe/N/C; however, it should be noted that not all of the Fe species within Fe/N/C are active for the ORR. A further cause for the observed decreasing ORR activity could be the blockage of the active sites by adsorbed sulfates. In fact, both XPS and chemical analyses indicate that S-containing species, more specifically sulfates as deduced from the peak at 168.5 eV characteristic of SO_4^{2-} species, see Fig. 2c, remain on L-Fe/N/C after the 0.5 M H_2SO_4 treatment. The presence of such sulfate species results in a severe decreasing of the BET area of Fe/N/C from 239 m^2g^{-1} to 160 m^2g^{-1} recorded for L-Fe/N/C, as shown in Table 1. As shown in Fig. 6, the decreasing of the BET area is mainly due to the blockage of the micropores; it should be noted that the active sites for the ORR are proposed to be hosted in micropores [8,9].

Table 3
Mass activities at 0.8 V for Fe/N/C and L–Fe/N/C samples in O_2 saturated 0.1 M of different electrolytes studied at 10 mV s^{-1}, 1600 rpm. Sample loading 0.6 mg cm^{-2}.

Electrolyte	i_M at 0.8 V/A g^{-1}	
	Fe/N/C	L–Fe/N/C
CF_3SO_3H	0.60	0.38
H_2SO_4	0.63	0.34
$HClO_4$	0.59	0.31
KOH	5.50	2.70
NaOH	7.70	2.90

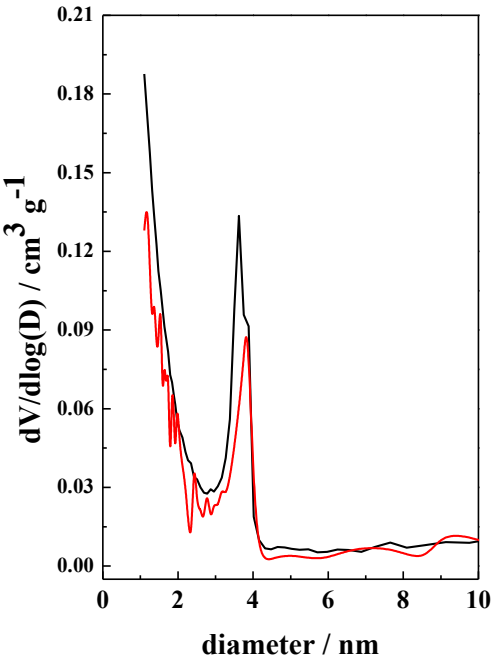

Fig. 6. Pore size distribution profiles for L–Fe/N/C (red line) and Fe/N/C (black line) samples. (For interpretation of the references to colour in this figure legend, the reader is referred to the web version of this article.)

In principle two hypotheses for the negative impact of adsorbed sulfates for the ORR can be proposed. On the one hand, sulfates would be adsorbed onto the micropores without forming chemical bonds and they simply hindering the access of O_2 into the active sites. On the other hand, actual chemical bonds between the sulfates and Fe or H bonded to N could be formed resulting in the poisoning of the active sites. The shifting of the E_{pc} and E_{pa} in the voltammograms for L-Fe/N/C (see Fig. 4) suggests that sulfates species could be interacting with Fe species. Moreover, the results shown in Table 2 show that the Fe/S surface atomic ratio is close to 1 for L-Fe/N/C suggesting a relationship exist between the amount of Fe on the catalysts and the amount of adsorbed sulfates. The question arises as to why L-Fe/N/C records visible activity for the ORR if all Fe sites are bonded to sulfates.

To elucidate the nature of the interaction between the adsorbed sulfates and the catalyst, DRIFT spectra for L-Fe/N/C were recorded at different temperatures. As shown in the Supplementary information section, and in good agreement with previous reports [26], it is possible to remove sulfates by subjecting L–Fe/N/C to thermal treatments under inert atmosphere. In order to remove sulfates, L–Fe/N/C was treated at 500 °C under N_2 within the DRIFT chamber and the DRIFT spectrum was collected at 20 °C. For the sake of comparison, DRIFT spectra were also recorded for Fe/N/C under the same protocol. The DRIFT spectra for L-Fe/N/C and Fe/N/C shown in Fig. 7 were obtained at 20 °C after subjecting the catalysts to a thermal treatment at 500 °C under N_2 (at 10° min^{-1}) during 30 min followed by subtraction of a reference spectrum recorded at 20 °C; as a consequence negative going bands indicate of the disappearance of adsorbed species. The spectrum for L-Fe/N/C depicts a broad

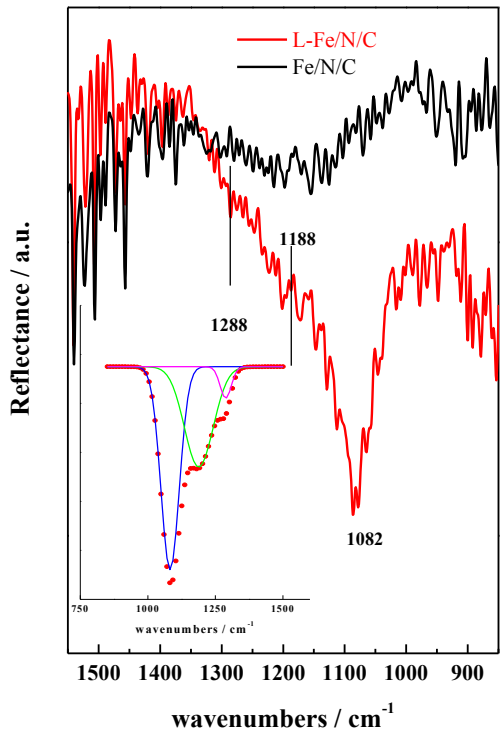

Fig. 7. DRIFT spectra recorded at room temperature of samples Fe/N/C and L–Fe/N/C after treatment in He at 500 °C during 1 h obtained after subtraction of spectra collected at 25 °C. The inset figure is the deconvolution of the band between 850 $cm^{-1}$and 1550 cm^{-1} of L–Fe/N/C.

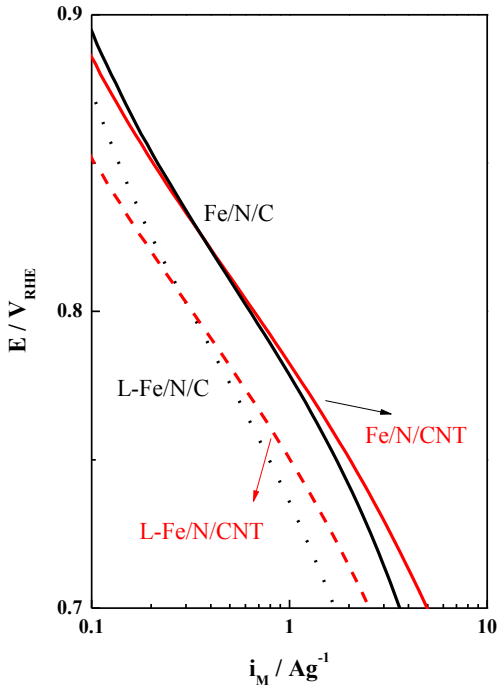

Fig. 8. Mass activities (i_M) for the ORR with Fe/N/C (black line), L–Fe/N/C (black dotted line), Fe/N/CNT (red line) and L–Fe/N/CNT (red dotted line) in O_2 saturated 0.1 M $HClO_4$ at 10 mV s^{-1}, 1600 rpm. Sample loading 0.6 mg cm^{-2}. (For interpretation of the references to colour in this figure legend, the reader is referred to the web version of this article.)

negative-going asymmetric band with maximum at around 1082 cm^{-1} tailing to higher frequencies showing two shoulders at ca. 1188 and 1288 cm^{-1}; the position of the peak maxima and the relative intensity of the less intense peaks is clearly observed after baseline correction and spectral fitting with Gaussian curves as shown in the inset to Fig. 7. This broad band, assigned to adsorbed sulfates is not observed in the spectrum of Fe/N/C. The results shown in Table 2 show that the Fe/S surface atomic ratio Fe/N/C is close to 1 for L–Fe/N/CNT suggesting that sulfates might be interacting with Fe species. In fact, the FTIR spectra for $FeSO_4 \cdot 7H_2O$ exhibit a very intense band at 1083 cm^{-1}. However, the FTIR spectra for $(NH_4)_2SO_4$ records a very strong band at 1078 cm^{-1}, so the assignment of the band at 1082 cm^{-1} is not straightforward. Besides, it should be taken into account that the spectra shown in Fig. 7 are for sulfates adsorbed on a solid, so FTIR spectra showing different bands, or more likely, shifting in the frequency of the characteristic bands can be obtained. The relationship between the symmetry of sulfate species forming chemical bonds with species located at the surface of a solid and their infrared spectra has been studied previously [43,44]. The presence of a single broad peak at around 1080 cm^{-1} is indicative of the presence of outer-sphere complexes of sulfates which retain their water of hydration and form no surface chemical bonds displaying a spectrum similar to aqueous sulfate. On the other hand, a metal-sulfate chemical bond, either monodentate or bidentate, results in a lower symmetry of sulfate characterized by an active band at 975 cm^{-1} and three or two different bands above 1000 cm^{--1} depending on whether the complex is bidentate or monodentate, respectively. The most intense band in the DRIFT spectra shown in Fig. 7 at 1082 cm^{-1} indicates the presence of non-bonded sulfates. Moreover, the lack of the band at 975 cm^{-1} suggests that sulfates are not bonded to metal centers. On the other hand, the bands at 1188 and 1288 cm^{-1} are indicative of the presence of metal-sulfate bonds.

The presence of sulfates adsorbed on Fe/N/C catalysts after H_2SO_4 treatment and their negative effect for the ORR has been observed by Herranz et al. [26] They proposed that sulfates react with –NH groups vicinal to FeN_x sites, rather than with Fe, resulting in a decreasing of the turnover of frequency (TOF) for the ORR. This proposal explains the lack of bands at 975 cm^{-1} in our DRIFT spectra which are indicative of sulfate bonding to Fe and justify the lower activity of L-Fe/N/C for the ORR. However, the implication of the presence of non-bonded sulfates for the ORR, if any, is not clear. In order to get a better understanding of the interaction between sulfates and the actives sites for the ORR we have prepared similar NPMCs based upon multiwalled carbon nanotubes so that the effect of microporosity can be neglected.

3.4. Synthesis and ORR performance of Fe/N/CNT and L-N/CNT

Fe/N/CNT and L-Fe/N/CNT have been synthesized by using a non-porous carbonaceous support, multiwalled carbon nanotubes (CNT), and following the same protocols as described above for the synthesis of Fe/N/C and L-Fe/N/C. In line with the results obtained for Fe/N/C series, Fe oxides and Fe_3C phases are observed in Fe/N/CNT and L-Fe/N/CNT (X-ray diffractograms are shown in Fig. S2). Also, three different N species (pyridinic, pyrrolic and quaternary) are observed by XPS (see Fig. S3). The main difference between both series of catalysts is that the amounts of N and Fe in Fe/N/CNT are ca. 33% lower than those in Fe/N/C (see Tables 1 and 2 for further details). Similar to Fe/N/C, acid treatment in 0.5 M H_2SO_4 of Fe/N/CNT leads to a significant decreasing of the Fe content by dissolution of the soluble Fe species along with the appearance of adsorbed sulfates (see XPS in Fig. S3). As shown in Table 1, the amount of

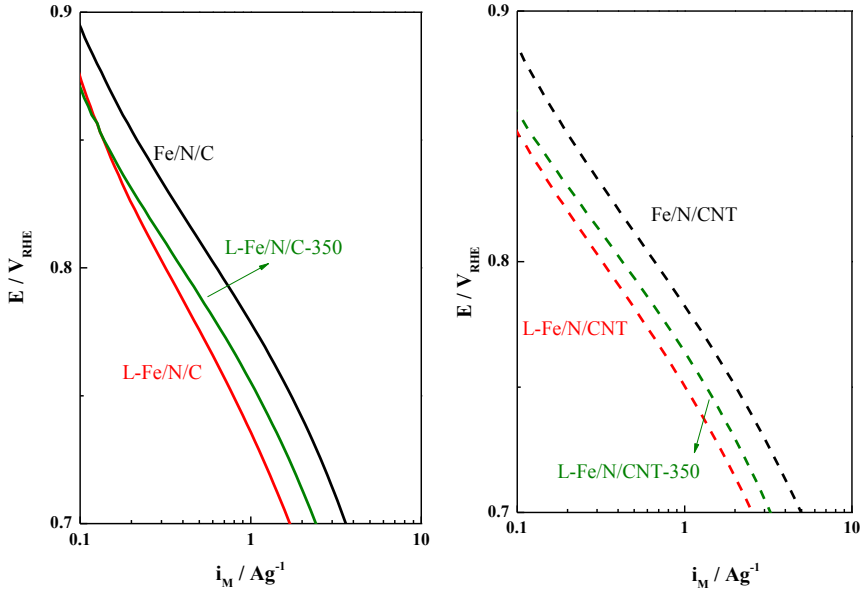

Fig. 9. Mass activities (i_M) of Fe/N/C, L–Fe/N/C and L–Fe/N/C-350 (left panel) and Fe/N/CNT, L–Fe/N/CNT and L–Fe/N/CNT-350 (right panel) in O_2 saturated 0.1 M $HClO_4$ at 10 mV s^{-1}, 1600 rpm. Sample loading 0.6 mg cm^{-2}.

S remaining on L-Fe/N/CNT is significantly lower than that recorded for L-Fe/N/C. However, and in good agreement with the results described above for L-Fe/N/C, the Fe/S surface atomic ratio for Fe/N/CNT is close to 1 (see Table 2), suggesting that a relation between the amount of Fe and the amount of adsorbed sulfates also exists when CNTs are used as the carbon source.

The cyclic voltammograms for Fe/N/CNT and L-Fe/CNT follow the same trend as those observed for Fe/N/C, *i.e.*, the presence of adsorbed sulfates leads to a shifting of the redox peaks to lower potentials (see Fig. S5). Finally, the BET area value of the CNT-based catalysts is smaller than that of the C-ones, but it is invariant after H_2SO_4 treatment.

As shown in Fig. 8, and despite of the lower amount of Fe and N, Fe/N/CNT records a similar mass activity (i_M) for the ORR than Fe/N/C. Moreover, the loss of ORR activity recorded with L–Fe/N/CNT is similar to that observed for L–Fe/N/C.

As stated above, the loss of ORR performance is due to both the removal of acid soluble Fe species and the presence of sulfates onto the actives sites. In order to remove adsorbed sulfates, L–Fe/N/C and L–Fe/N/CNT were subjected to thermal treatments at 350 °C under N_2 for 1 h and the solid obtained were labeled as L–Fe/N/C-350 and L-Fe/N/CNT-350, respectively. This temperature was set after the thermal gravimetric analysis shown in Fig. S4. Clearly, the amount of sulfates decreases after the thermal treatment, and in fact, sulfates are not detected in the surface of neither L–Fe/N/C-350 nor L–Fe/N/CNT-350 by XPS (see Table 2). As shown in Fig. 9, the ORR mass activity of L–Fe/N/C-350 and L–Fe/N/CNT-350 increases after the thermal treatment but the complete recovery of the ORR performance is not achieved. This is a clear indication that the loss of activity is also due to the dissolution of a fraction of the Fe species during treatment in 0.5 M H_2SO_4. Remarkably, the recovered activity is very similar for both catalysts.

The results shown in this section clearly show adsorbed sulfates on NPMCs have a negative impact for the ORR. Moreover, the nature of the interaction between adsorbed sulfates and the catalyst is not affected by the nature of the carbon source used for the preparation of the catalyst. As a consequence, similar ORR activity losses are recorded with NMPCs prepared with active carbon or with carbon nanotubes.

4. Conclusions

The performance of Fe/N/C for the ORR is severely affected by the pH of the electrolyte. Higher ORR activities are recorded in alkaline electrolytes as compared to acidic ones. However, the effect of the counterion, *i.e.*, of the anion or cations when measured under acidic or alkaline electrolytes, respectively, is almost negligible. On the other hand, if during the synthesis of Fe/N/C or Fe/N/CNT acid treatments are used, anions such as sulfates will become adsorbed onto the active sites resulting in a severe decrease of the ORR performance. The observed negative impact of the presence of sulfates for the ORR for both Fe/N/C and Fe/N/CNT indicates that sulfates remain bonded to the active sites rather than simply blocking the access of O_2 into the active sites.

Acknowledgments

This project was funded by the Deanship of Scientific Research (DSR), King Abdulaziz University, Jeddah, under grant number (D-006-432). The authors, therefore, acknowledge with thanks DSR technical and financial support. Economic support from projects ENE2010-15381 from the Spanish Ministry of Science and Innovation and Project 201080E116 from the CSIC is also acknowledged.

Appendix A. Supplementary data

Supplementary data related to this article can be found at http://dx.doi.org/10.1016/j.jpowsour.2014.07.173.

References

[1] H.A. Gasteiger, S.S. Kocha, B. Sompalli, F.T. Wagner, Appl. Catal. B 56 (2005) 9–35.
[2] I.E.L. Stephens, A.S. Bondarenko, U. Grønbjerg, J. Rossmeisl, I. Chorkendorff, Energy Environ. Sci. 5 (2012) 6744–6762.
[3] F. Jaouen, E. Proietti, M. Lefèvre, R. Chenitz, J.P. Dodelet, G. Wu, H.T. Chung, C.M. Johnston, P. Zelenay, Energy Environ. Sci. 4 (2011) 114–130.
[4] Y. Feng, T. He, N. Alonso-Vante, Chem. Mater. 20 (2008) 26–28.
[5] E. Vayner, R.A. Sidik, A.B. Anderson, B.N. Popov, J. Phys. Chem. C 111 (2007) 10508–10513.

[6] H. Zhong, H. Zhang, G. Liu, Y. Liang, J. Hu, B. Yi, Electrochem. Commun. 8 (2006) 707–712.
[7] G. Wu, K.L. More, C.M. Johnston, P. Zelenay, Science 332 (2011) 443–447.
[8] M. Lefèvre, E. Proietti, F. Jaouen, J.P. Dodelet, Science 324 (2009) 71–74.
[9] E. Proietti, F. Jaouen, M. Lefèvre, N. Larouche, J. Tian, J. Herranz, J.P. Dodelet, Nat. Commun. 2 (2011).
[10] G. Wu, P. Zelenay, Acc. Chem. Res. 46 (2013) 1878–1889.
[11] M. Ferrandon, A.J. Kropf, D.J. Myers, K. Artyushkova, U. Kramm, P. Bogdanoff, G. Wu, C.M. Johnston, P. Zelenay, J. Phys. Chem. C 116 (2012) 16001–16013.
[12] U.I. Kramm, J. Herranz, N. Larouche, T.M. Arruda, M. Lefèvre, F. Jaouen, P. Bogdanoff, S. Fiechter, I. Abs-Wurmbach, S. Mukerjee, J.P. Dodelet, Phys. Chem. Chem. Phys. 14 (2012) 11673–11688.
[13] U.I. Kramm, M. Lefèvre, N. Larouche, D. Schmeisser, J.-P. Dodelet, J. Am. Chem. Soc. 136 (2013) 978–985.
[14] S. Yasuda, L. Yu, J. Kim, K. Murakoshi, Chem. Commun. 49 (2013) 9627–9629.
[15] C. Domínguez, F.J. Pérez-Alonso, M. Abdel Salam, J.L. Gómez de la Fuente, S.A. Al-Thabaiti, S.N. Basahel, M.A. Peña, J.L.G. Fierro, S. Rojas, Int. J. Hydrogen Energy 39 (2014) 5309–5318.
[16] R. Jasinski, Nature 201 (1964) 1212–1213.
[17] S. Baranton, C. Coutanceau, C. Roux, F. Hahn, J.M. Léger, J. Electroanal. Chem. 577 (2005) 223–234.
[18] A.A. Tanaka, C. Fierro, D. Scherson, E.B. Yeager, J. Phys. Chem. 91 (1987) 3799–3807.
[19] A. van der Putten, A. Elzing, W. Visscher, E. Barendrecht, J. Electroanal. Chem. Interfacial Electrochem. 221 (1987) 95–104.
[20] J.H. Zagal, Coord. Chem. Rev. 119 (1992) 89–136.
[21] A.J.B. Alberts, J. Lewis, M. Raff, K. Roberts, P. Walter, Molecular Biology of the Cell, New York, 2002.
[22] H. Meier, U. Tschirwitz, E. Zimmerhackl, W. Albrecht, G. Zeitler, J. Phys. Chem. 81 (1977) 712–718.
[23] A.L. Bouwkamp-Wijnoltz, W. Visscher, J.A.R. Van Veen, E. Boellaard, A.M. Van der Kraan, S.C. Tang, J. Phys. Chem. B 106 (2002) 12993–13001.
[24] M. Lefevre, J.P. Dodelet, P. Bertrand, J. Phys. Chem. B 109 (2005) 16718–16724.
[25] U.I. Koslowski, I. Abs-Wurmbach, S. Fiechter, P. Bogdanoff, J. Phys. Chem. C 112 (2008) 15356–15366.
[26] J. Herranz, F. Jaouen, M. Lefèvre, U.I. Kramm, E. Proietti, J.P. Dodelet, P. Bogdanoff, S. Fiechter, I. Abs-Wurmbach, P. Bertrand, T.M. Arruda, S. Mukerjee, J. Phys. Chem. C 115 (2011) 16087–16097.
[27] N. Markovic, H. Gasteiger, P.N. Ross, J. Electrochem. Soc. 144 (1997) 1591–1597.
[28] J.S. Spendelow, A. Wieckowski, Phys. Chem. Chem. Phys. 9 (2007) 2654–2675.
[29] D. Strmcnik, K. Kodama, D. van der Vliet, J. Greeley, V.R. Stamenkovic, N.M. Marković, Nat. Chem. 1 (2009) 466–472.
[30] J. Suntivich, E.E. Perry, H.A. Gasteiger, Y. Shao-Horn, Electrocatalysis 4 (2013) 49–55.
[31] F. Jaouen, J. Herranz, M. Lefèvre, J.P. Dodelet, U.I. Kramm, I. Herrmann, P. Bogdanoff, J. Maruyama, T. Nagaoka, A. Garsuch, J.R. Dahn, T. Olson, S. Pylypenko, P. Atanassov, E.A. Ustinov, ACS Appl. Mater. Interfaces 1 (2009) 1623–1639.
[32] F.J. Pérez-Alonso, M.A. Salam, T. Herranz, J.L. Gómez De La Fuente, S.A. Al-Thabaiti, S.N. Basahel, M.A. Peña, J.L.G. Fierro, S. Rojas, J. Power Sources 240 (2013) 494–502.
[33] J.R. Pels, F. Kapteijn, J.A. Moulijn, Q. Zhu, K.M. Thomas, Carbon 33 (1995) 1641–1653.
[34] H.S. Oh, J.G. Oh, W.H. Lee, H.J. Kim, H. Kim, Int. J. Hydrogen Energy 36 (2011) 8181–8186.
[35] F. Bonnet, F. Ropital, P. Lecour, D. Espinat, Y. Huiban, L. Gengembre, Y. Berthier, P. Marcus, Surf. Interface Anal 34 (2002) 418–422.
[36] C.S. Kuivila, J.B. Butt, P.C. Stair, Appl. Surf. Sci. 32 (1988) 99–121.
[37] H.R. Byon, J. Suntivich, E.J. Crumlin, Y. Shao-Horn, Phys. Chem. Chem. Phys. 13 (2011) 21437–21445.
[38] J. Yang, D.J. Liu, N.N. Kariuki, L.X. Chen, Chem. Commun. (2008) 329–331.
[39] N. Ramaswamy, S. Mukerjee, Adv.Phys. Chem. 2012 (2012).
[40] B.B. Blizanac, P.N. Ross, N.M. Markovic, Electrochimica Acta 52 (2007) 2264–2271.
[41] P.N. Ross, Why Is Pt So Unique. A Chemical Physics Approach, https://www1.eere.energy.gov/hydrogenandfuelcells/pdfs/phil_ross.pdf.
[42] J. Masa, K. Ozoemena, W. Schuhmann, J.H. Zagal, J. Porphyrins Phthalocyanines 16 (2012) 761–784.
[43] D. Peak, R.G. Ford, D.L. Sparks, J.Colloid Interface Sci. 218 (1999) 289–299.
[44] K. Nakamoto, Infrared and Raman Spectra of Inorganic and Coordination Compounds, New York, 1986.

Supplementary Materials

Stability of the non-acid treated electrodes during ORR in acid media

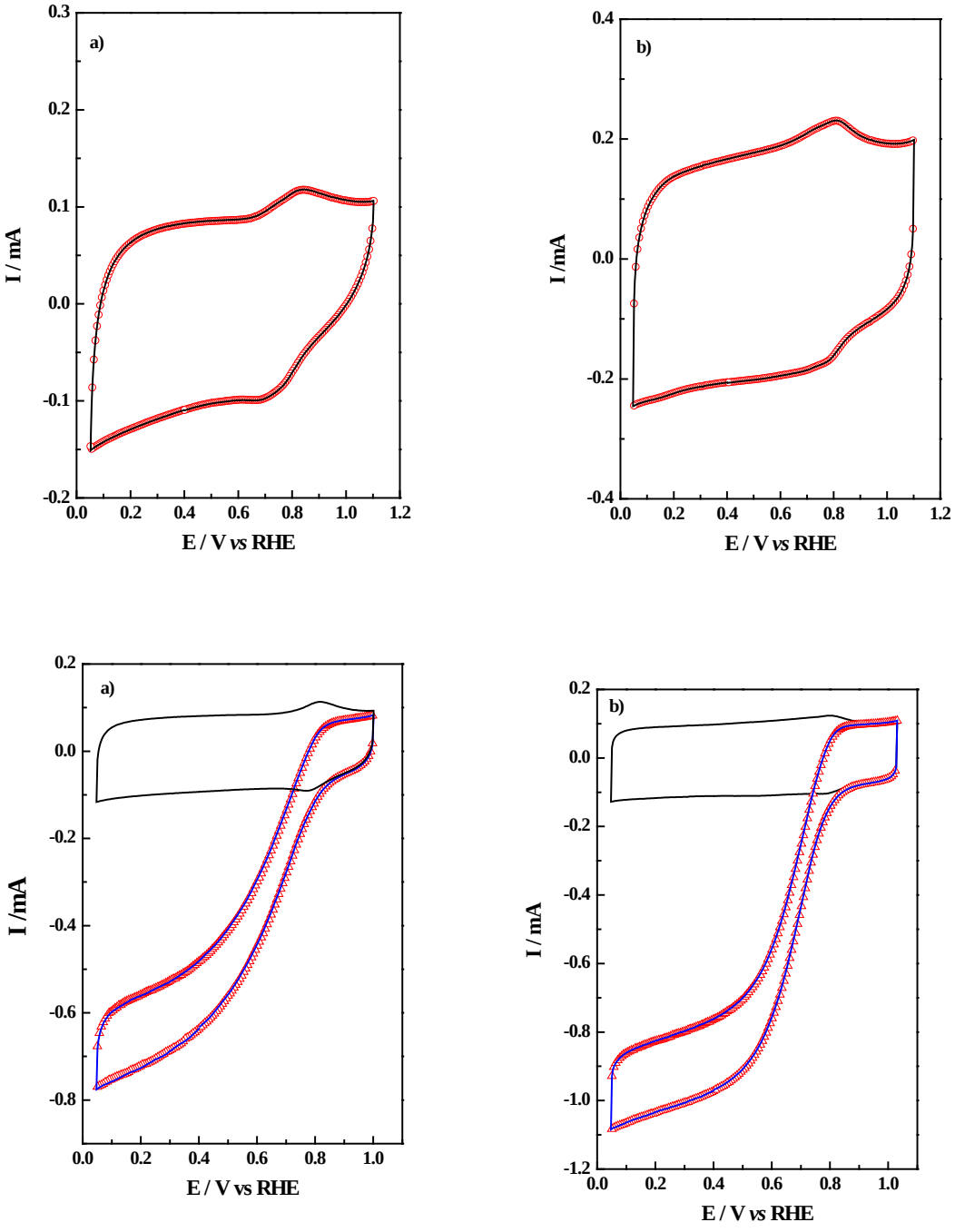

Figure S1. Upper panel: 30th (black line) and 50th (red open circles) cyclic voltammograms recorded in Ar-purged 0.1 M $HClO_4$ at 50 mVs^{-1} for a) Fe/N/C and b) Fe/N/CNT. Lower pane: 10th (blue line) and 11th (red open triangles) cyclic voltammograms recorded in O_2 saturated 0.1 M $HClO_4$ with Fe/N/C (a) and Fe/N/CNT

(b) at 10 mV s^{-1} and 1600 rpm. The black curves are the cyclic voltammograms in Ar saturated 0.1 M $HClO_4$ recorded immediately after the ORR experiments for each catalyst.

Physicochemical characterization of Fe-based catalysts prepared with CNTs

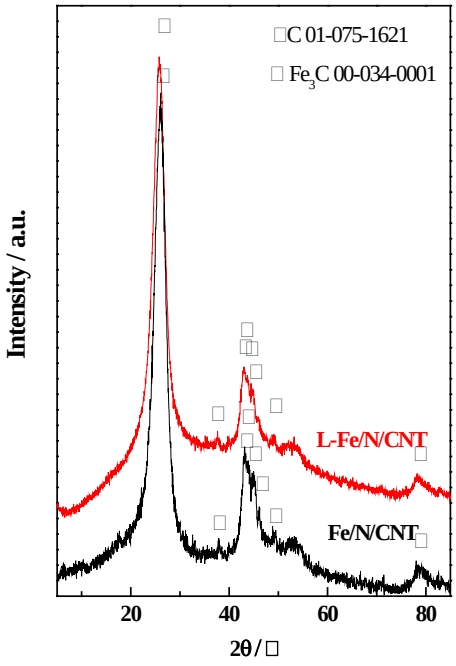

Figure S2. XRD profiles for L-Fe/N/CNT and Fe/N/CNT catalysts.

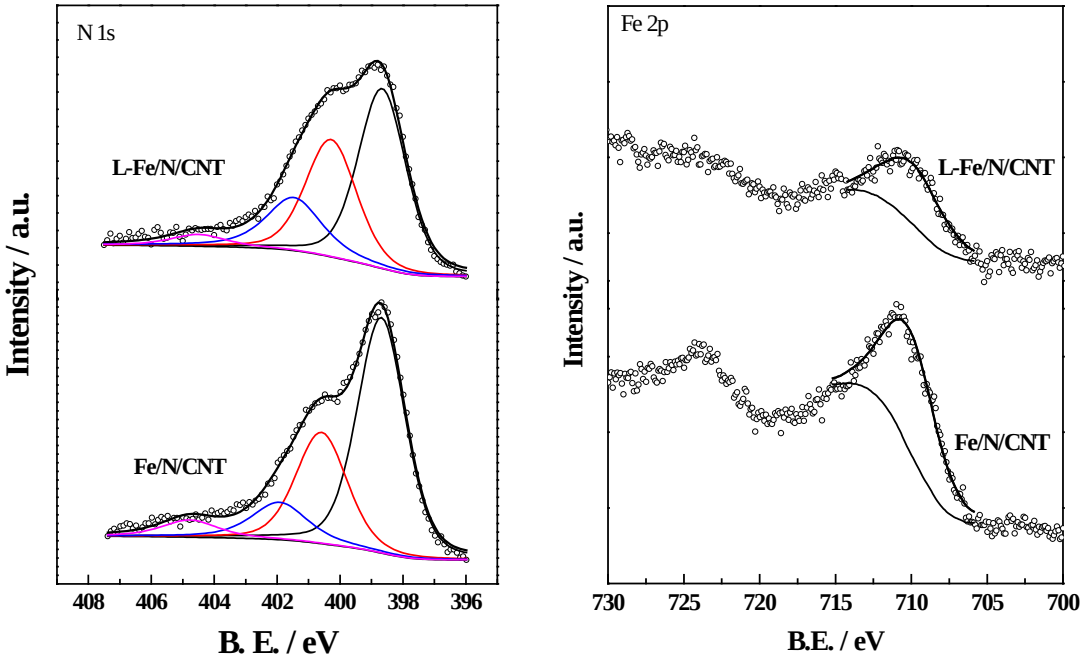

Figure S3. - XP spectra of N 1s and Fe 2p core-levels for Fe/N/CNT and L-Fe/N/CNT. The black, red, blue and magenta peaks in the spectra for the N1s core-level region correspond to pyridinic-N, pyrrolic-N, quaternary-N and oxidized-N, respectively.

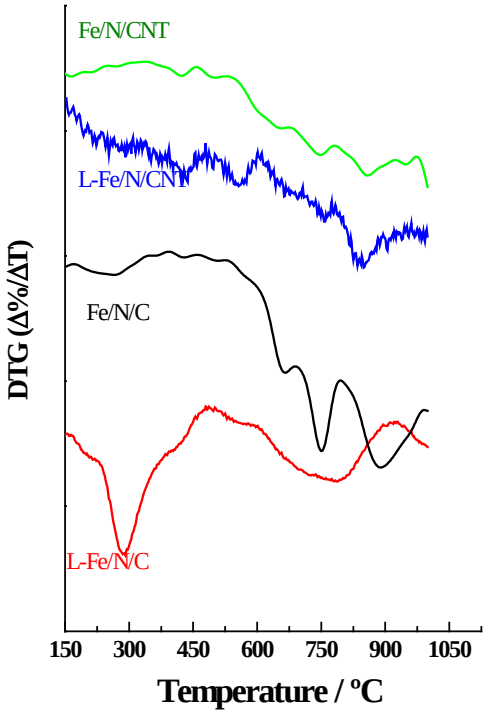

Figure S4. Differential thermogravimetric analyses of Fe/N/C, L-Fe/N/C, Fe/N/CNT and L-Fe/N/CNT recorded in N_2 atmosphere

Differential thermogravimetric analyses (DTA) for Fe/N/C, L-Fe/N/C, Fe/N/CNT and L-Fe/N/CNT recorded under N_2 atmosphere. Both L-Fe/N/C and L-Fe/N/CNT show a peak centered at around 285 ºC which is not observed in the spectrum for Fe/N/C. Previous studies have ascribed this peak to the removal of adsorbed sulfates In line with the XPS and chemical analysis results discussed above, the area of the peak recorded for L-Fe/N/C is greater than that for L-Fe/N/CNT confirming that a higher amount of sulfates remain adsorbed L-Fe/N/C than on L-Fe/N/CNT.

Electrochemical characterization of Fe-based catalysts prepared with CNTs

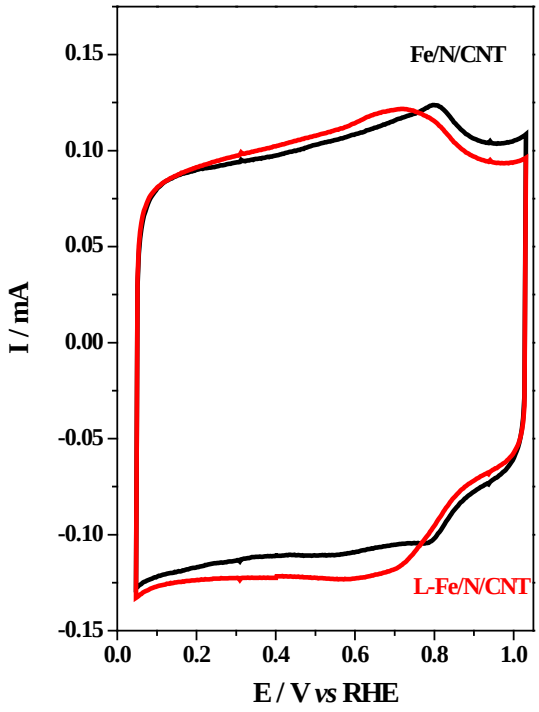

Figure S5. Cyclic voltammograms for Fe/N/CNT (black line) and L-Fe/N/CNT (red line) recorded at 10 mV s^{-1} in 0.1 M of $HClO_4$. Catalyst loading 0.6 mg cm^{-2}.

Applied Catalysis B: Environmental 162 (2015) 420–429

Contents lists available at ScienceDirect

Applied Catalysis B: Environmental

journal homepage: www.elsevier.com/locate/apcatb

On the relationship between N content, textural properties and catalytic performance for the oxygen reduction reaction of N/CNT

Carlota Domínguez[a], Francisco J. Pérez-Alonso[a,*], Mohamed Abdel Salam[b], Shaeel A. Al-Thabaiti[b], Abdullah Y. Obaid[b], Abdulmohsen A. Alshehri[b], José L. Gómez de la Fuente[a], José L.G. Fierro[a], Sergio Rojas[a,*]

[a] Grupo de Energía y Química Sostenibles (EQS), Instituto de Catálisis y Petroleoquímica, CSIC, C/Marie Curie, 2, L10, 28049 Madrid, Spain
[b] Chemistry Department, Faculty of Science, King Abdulaziz University, PO Box 80200, Jeddah 21589, Saudi Arabia

ARTICLE INFO

Article history:
Received 16 April 2014
Received in revised form 27 June 2014
Accepted 1 July 2014
Available online 9 July 2014

Keywords:
ORR
CNTs
Defects
NPMCs
Fuel cells

ABSTRACT

Non-precious metal catalysts for the oxygen reduction reaction (ORR) based upon the incorporation of different amounts of N into the C—C network of multiwalled carbon nanotubes (CNTs) have been prepared by using CNTs and urea as the carbon and nitrogen sources, respectively. First, and with the aim of generating different levels of defects in the carbon network, the CNTs have been subjected to ballmilling during different periods of time between 0 and 150 h. Then, urea was mixed with the treated CNTs, subjected to further ballmilling and pyrolized at 800 °C. The number of defects, and as a consequence, the amount of N incorporated into the CNTs, increases with the duration of the ballmilling time. Moreover, the structure of the CNTs obtained after longer ballmilling times collapses leading to a carbon material with a high degree of microporisity. The performance of the N/CNT for the ORR, in terms of both the onset potential and mass current activity, increases with the amount of N actually incorporated into the CNT. Moreover, the H_2O_2 formation during ORR varies with the morphology of the catalyst. Thus, the formation of H_2O_2 is favored with the electrocatalysts in which the CNT structure is preserved, whereas the total reduction of O_2 to H_2O is favored for the electrocatalysts in which micropores are formed.

1. Introduction

The increasing demand of primary energy, which is mainly coped by increasing the use of fossil fuels, has serious environmental and socioeconomical implications. As a consequence, most countries have embraced strong energy and environmental policies aimed to decreasing their dependence on fossil fuels and to control the level of harmful emissions. In this context, the use of C-decoupled sources of energies has emerged as an alternative to fossil fuels. Among those, H_2 has been recognized as an ideal energy vector since its production and transformation into useful energy can be achieved by fully C-decupled technologies.

It is widely recognized that H_2-feed proton exchange membrane fuel cells (PEMFCs) are the ideal devices to transform chemical energy into electricity. As a consequence, they have been identified as ideal devices for powering transportation vehicles and portable devices. In the current state-of-the-art, both the anode and cathode electrodes of PEMFCs are based upon carbon supported Pt nanosized particles. It is well admitted that Pt is the best catalyst for both hydrogen oxidation and oxygen reduction (ORR) reactions in acid media. However, due to the sluggish kinetics of the ORR, the amount of Pt used on the cathode electrode is too high, of *ca.* 0.5 $mg_{Pt}\,cm^{-2}$ [1] and as a consequence the price of PEMFCs is not yet competitive. Numerous attempts are addressed to decrease Pt loading on the cathode electrode and Department of Energy of US Government (DOE) has established a target loading of 0.15 $mg_{Pt}\,cm^{-2}$ for 2015 [2]. The most successful ones aim to enhance the exposed area by decreasing Pt size and to optimize Pt electronic properties towards oxygen adsorption and reduction by alloying Pt with metals such as Ni and Co. A disruptive approach consists in replacing Pt (or other noble metals for this matter) content altogether by using non-precious metal catalysts (NPMCs) which are less expensive and more abundant than noble metals [3]. As a rule of thumb, NPMCs exhibit lower intrinsic kinetics of for the ORR; however, this feature can be compensated by using higher amounts of NPMC without severe economic repercussions.

* Corresponding authors. Tel.: +34 91 585 4632.
E-mail addresses: fperez@icp.csic.es (F.J. Pérez-Alonso), srojas@icp.csic.es (S. Rojas).

http://dx.doi.org/10.1016/j.apcatb.2014.07.002
0926-3373/

In general, the more active NPMCs are based upon a transition metal inserted within a matrix of N-substituted graphitic carbon, usually referred to as M/N/C [3]. These catalysts are in fact based upon the pioneering work of Jasinski et al. who reported that cobalt phtalocyanine catalyzed the ORR in alkaline medium [4]. Although it is well documented that this type of NPMCs exhibit significant lower activities than Pt/C for the ORR in acid media, current densities as high as 230 A cm^{-3} at 0.8 V have been reported [5]. In general, the preparation of NPMCs comprises the intimate mixture by wet impregnation and/or mechanical process using planetary ball milling of a carbon matrix such as active carbon, carbon nanotubes or graphene or a carbon precursor, a transition metal (M) precursor and a nitrogen source followed by one or several thermal treatments. In order to obtain the active sites for the ORR, thermal treatments must be conducted at of 600 °C or higher either under inert or reactive (NH_3) atmospheres. Previous works have concluded that N atoms from a N-rich polymer precursor are anchored within the carbon matrix leading to the formation of the active sites during the thermal treatment [6,7]. In addition, during this thermal process micropores are generated and as a result higher ORR activities are recorded [8].

The actual arrangement of the N, M and C atoms at the active sites for the ORR is elusive. The first hypothesis proposed three decades ago claimed that N and C atoms are the real active sites of the NPMCs for the ORR [9,10]. More recent studies sustain, however, that the active sites consist of a non-precious metal such as Fe, Co or Mn coordinated to an undetermined number of N atoms inserted onto a carbon matrix [3,11,12]. In this line, a recent study recognized the ORR ability of M/N/C M=Fe, Co and Mn follows the order Fe > Co > Mn [13]. It is worth to remark that although most works coincide in that the transition metal should be present during the thermal treatment step in order to generate active catalysts for the ORR it is still under debate whether the transition metal is an indispensable element of the active site itself or whether it only serves to create the active sites but it is unclear whether it does actually participate in the turnover cycles [14–16].

Several types of carbons and carbon sources have been employed for the synthesis of NPMCs. In general, the most active catalysts for the ORR are obtained when the final catalyst has a large fraction of micropores or when they are created during thermal treatments. On the other hand, a recent study about the durability of NPMCs reports that CNTs render more durable catalysts than carbon blacks [17].

As stated above, N atoms are necessary to create the active site for the ORR. The following N species have been detected upon N incorporation into graphitic structures; pyridinic, pyrrolic, graphitic (or quaternary) and oxidized N. The ratio of these species varies with the N precursor and thermal treatment. The role of the different N species controversial and studies pointing to each one of these N species as the main responsible for the ORR activity exist. Recently, Yasuda et al. have reported that pyridinic N promotes the ORR *via* a four-electron pathway whereas graphitic N promotes the indirect reduction of O_2 *via* a two-electron pathway, *i.e.*, through the formation of H_2O_2 [18], revealing that different nitrogen species are anchored to the carbon matrix differently, in the case of graphene and carbon nanotubes, pyridinic-N is placed at the edge of the graphene planes and CNTs whereas quaternary-N could substitute carbon atoms within graphitic network and the graphene layer and it is also placed at the edge of the carbon source [18,19].

Recently, FeN_4 and FeN_{2+2} ensembles have been identified as the real active sites for the ORR with Fe-based NPMCs [20–23]. Some studies went further and highlighted the importance of the protonation of the N atoms coordinated to the metal atom and/or of N atoms adjacent to the Fe/N sites for the ORR [7,22,23].

Regardless of the actual role of N for the ORR, it appears like the catalytic performance of NPMCs increases with the amount of N onto the catalyst which is in turn related with the amount of defects into carbon nanotubes [24]. The aim of this work is to understand the relationship between the amount of defects of a carbon matrix (CNTs) and the incorporation of N into the carbon network and the repercussions for the ORR in acid medium. In a first step we aimed to generate controllable amounts of defects into CNTs by subjecting CNTs to increasing ballmilling periods. Then, N was incorporated onto the treated CNTs by a further ballmilling step followed by a thermal treatment in N_2. Finally, the performance of the catalysts obtained for the ORR in acid medium was evaluated by electrochemical techniques.

2. Experimental

2.1. Synthesis of NPMCs

A series of NPMC have been synthesized by means of a mechanical method consisting in two sequential ballmilling steps under r.t. conditions, employing a planetary ball mill (PM100, Retsch), followed by a thermal treatment under inert atmosphere. Multiwalled carbon nanotubes were used as the carbon matrix (CNTs, SUNANO; purity > 90%, Syn Nanotech Co Ltd) and urea (CH_4N_2O, PANREAC PRS) was used as the N-precursor. Previous to further treatments, CNTs were subjected to an acid leaching with HNO_3 20% v/v at 110 °C for 5 h to eliminate contaminants [25]. The vessel employed during ballmilling treatment is made of stainless steel; 10 mm diameter stainless steel balls were used. First, the CNTs were ballmilled for different periods of time of 0, 12, 24, 48, 72 or 150 h, with the aim to generate an increasing number of defects and/or edges in the ballmilled CNTs, thereby increasing materials' ability to incorporate heteroatoms such as N or Fe, thus leading to a greater density of active sites. The materials obtained were referred to as CNT-t, where t denotes the time under ballmilling. Then, urea and CNT-t (molar ratio CNT-t:Urea 2:1) were intimately mixed by ballmilling for 24 h. The samples recovered were subjected to a thermal treatment in a quartz tubular reactor at 800 °C (heating ramp of 20 °C min^{-1} under an inert atmosphere of 25 mL min^{-1} N_2 for 1 h). At this temperature, all samples loose *ca.* 70 wt% of their initial mass as shown in Fig. S1 (Supplementary material). The incorporation of the N atoms within the C sp^2 matrix was achieved during this thermal step [6]. The samples recovered after the thermal treatment were labeled as N/CNT-t.

2.2. Physicochemical characterization

Carbon, nitrogen and hydrogen weight contents were measured with an elemental analyser (LECO CHNS-932).

X-ray photoelectron spectra (XPS) were acquired with a VG Escalab 200R spectrometer fitted with an Mg $K\alpha$ ($h\upsilon$ = 1253.6 eV) 120 W X-ray source. The energy regions of the photoelectrons of interest were scanned until an acceptable signal-to-noise ratio was achieved. Intensities were estimated by calculating the integral of each peak after subtraction of the Shirley-type background and fitting of the experimental curve to a combination of Lorentzian and Gaussian lines of variable proportions. Accurate binding energies (±0.2 eV) were determined by setting the most intense C 1s peak at 284.6 eV.

Raman spectra were recorded in air using a single monochromator Renishaw system 1000 equipped with a thermoelectrically cooled CCD detector and holographic super-Notch filter. The samples were excited with the 532 nm Ar line. The instrument is internally calibrated with a silicon reference at 520 cm^{-1} and gives a peak position resolution of 1 cm^{-1}, the spectrum acquisition time

was 10 s and 5 spectra were acquired to ensure an optimal signal to noise ratio.

X-ray diffractograms were collected on a Seifert 3000 powder diffractometer operating with Cu $K\alpha$ radiation ($\lambda = 0.15418$ nm) generated at 40 kV and 40 mA. Scans were recorded at 0.02° s^{-1} for 2θ values between 10° and 90°.

Textural properties were evaluated by N_2 adsorption–desorption isotherms of the samples recorded at liquid N_2 temperature with a Micromeritics ASAP 2000 apparatus. Samples were degassed at 140 °C under vacuum for 24 h. Specific areas were calculated by applying the BET method within the relative pressure range $P/P^0 = 0.05–0.30$.

The transmissions electron microscopy (TEM) images of the samples were collected using a JEOL JEM 2100FX microscope operating at 200 keV, point resolution of 0.31 nm. The specimens for analysis were prepared by dispersing the powdered samples in a mixture of isopropanol and Milli-Q water using an ultrasonic bath. A drop of each resulting suspension was placed on a copper grid covered with a porous carbon film.

The Fe wt.% composition of the solids was determined by inductively coupled plasma emission spectrometry (ICP-OES) using a Perkin-Elmer Optima 3300DV apparatus.

2.3. Electrochemical characterization

The electrochemical experiments were performed with a computer controlled Autolab PGstat 302N potentiostat/galvanostat. A standard three-compartment glass cell and a rotating disk electrode (RDE) (Pine research Instruments) were used for all electrochemical experiments. The counter electrode was a graphite rod and the reference electrode was a homemade RHE electrode.

A glassy carbon electrode with a thin film of the electrocatalyst under study was used as the working electrode. For the thin film preparation, samples were dispersed ultrasonically for 10 min in a mixture of Millipore Milli $Q^{®}$ water, isopropyl alcohol (Aldrich, 99.8%) and Nafion (5 wt%) with a final ratio of 80, 18.8 and 0.2 vol%, respectively. The final concentration of the electrocatalyst in the suspension was of 6 mg_{cat} mL^{-1}. A volume of 20 μL of the suspension was pipetted onto the previously polished glassy carbon tip of the RDE.

Previous to the electrochemical testing, the working electrode was electrochemically cleaned by potential cycling from 0.05 to 1.1 V *vs.* RHE for 50 cycles in Ar-saturated 0.1 M $HClO_4$ electrolyte. Cyclic voltammograms (CVs) were recorded between 0.05 and 1.03 V at 10 mV s^{-1} in Ar-saturated 0.1 M $HClO_4$.

The ORR polarization curves were collected by means of the RDE technique between 0.05 V and 1.03 V at 10 mV s^{-1} and 1600 rpm in O_2-saturated 0.1 M $HClO_4$ electrolyte. The Faradaic current density (j_F mA cm^{-2}) was obtained by subtracting the current obtained during the anodic sweep scan in the O_2-saturated electrolyte from the capacitive current (density) obtained in the potential sweep recorded in Ar-saturated O_2-free electrolyte under the same experimental conditions. The ORR kinetic current (i_k) was calculated from the Kouteky–Levich equation ($i_k = -i_F \times i_{lim}/(i_F - i_{lim})$) where i_K is the kinetic current and i_{lim} is the limiting current. Finally, the ORR mass activity is defined by $i_M = -i_K/m_{cat}$ where m_{cat} is the catalyst loading expressed in *g* [11]. H_2O_2 production were recorded using a rotating ring disk electrode (RRDE) which ring is made of platinum, under the same experimental conditions than that reported above for the RDE experiments, *i.e.*, recording a linear sweep voltammetry scan between 0.05 V and 1.03 V at 10 mV s^{-1} and 1600 rpm in O_2-saturated 0.1 M $HClO_4$ electrolyte while applying a constant ring potential of 1.2 V. The fraction of H_2O_2 produced was calculated according to the next equation:

(1) $X_{H_2O_2} = \frac{2I_R/N}{I_D + I_R/N}$ where I_D is the disk current and I_R is the ring current and using a ring efficiency (N) of 26% [26].

In order to determine the whether Fe impurities are responsible for the ORR activity selected catalysts were poisoned with thiocyanate in order to suppress the activity of the Fe sites. For this matter, selected catalysts were deposited onto the working electrode (see above) and immersed in a 0.01 M solution of NaSCN (Aldrich >99.99%) during 15 min at 1000 rpm. Then, ORR polarization curves were recorded following a protocol identical as that described above.

3. Results and discussion

3.1. Physicochemical characterization of CNT-t and N/CNT-t

The bulk C, H and N contents obtained from elemental analysis are shown in Table 1. The results obtained clearly show that the amount N incorporated into the samples increases with the duration of the ballmilling treatment from 0.66 in N/CNT-0 to 3.94 wt% in N/CNT-150. This results are in line with previous works using other carbon supports (black pearls and carbon black), in which a similar trend was observed [27,28]. However, a careful inspection of the evolution of the N contents with the ballmilling time reveals that the incorporation of N is only moderate for the CNT-t subjected to ballmilling periods between 0 and 48 h but increases dramatically for the CNT-t ballmilled for longer periods of time of 72 and 150 h.

Table 1 also shows that the combined amount of C, H and N is lower than 100% and that it decreases with the increasing ballmilling time indicating that other elements might be incorporated into the samples after ballmilling. In addition to the presence of oxygen and metals used for the synthesis of the CNTs (see Section 3 for N/CNT-0), previous studies have shown that Fe species become incorporated even encapsulated within the carbon matrix during the ballmilling process. This effect will be addressed below. The C 1s, N 1s and O 1s core-level spectra of the different samples were recorded in order to estimate the relative surface abundance of the elements and to identify the nature of the N species and their evolution during ballmilling. The N 1s spectra, show in Fig. 1 have been fitted to four components with peak maxima at 398.5, 400.1, 401–401.5 and 403.4–404 eV, respectively. The FWMH for all N 1s peaks is of around 2. In view of these binding energy values, the N species have been ascribed to pyridinic-N, pyrrolic-N, graphitic-N and N-oxide species, respectively [3,11].

Table 1
C, N and H content determined by elemental analysis and N/C weight ratios.

Sample	Weight content (%)			N/C weight ratio	N/C atomic ratio
	C	H	N		
N/CNT-0	93.91	0.14	0.66	0.007	0.006
N/CNT-12	92.21	0.21	0.84	0.009	0.008
N/CNT-24	90.76	0.26	1.23	0.014	0.012
N/CNT-48	91.11	0.30	1.20	0.013	0.011
N/CNT-72	89.12	0.58	1.75	0.020	0.017
N/CNT-150	84.58	0.97	3.94	0.047	0.040

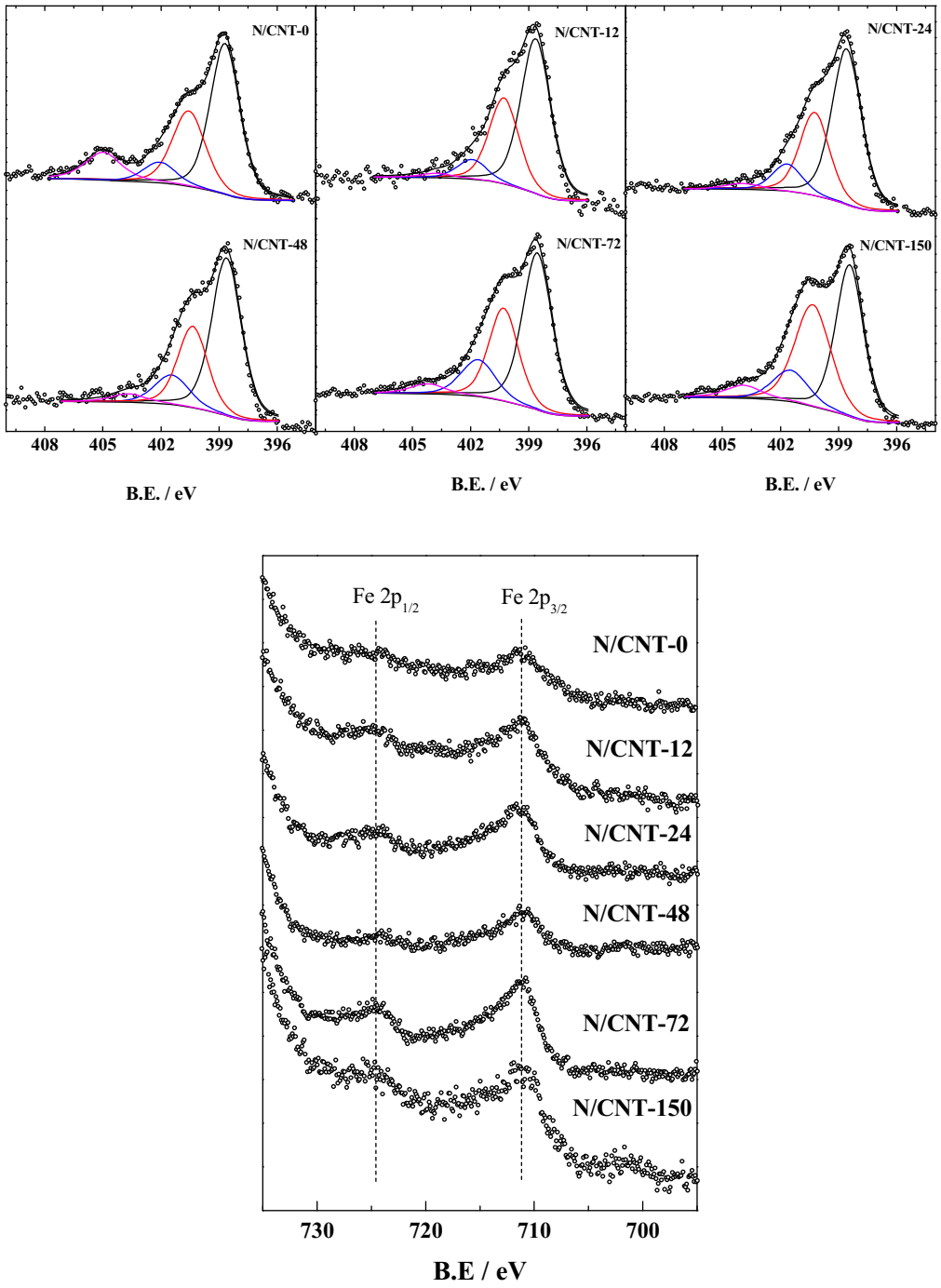

Fig. 1. (a) N 1s core-level spectra of the N/CNT-t samples (black line). Peaks for N-pyridinic, N-pyrrolic, N-quaternary and oxidized N are shown in black, red, blue and magenta. (b) Fe 2p core-level spectra of N/CNT-t samples. (For interpretation of the references to color in this figure legend, the reader is referred to the web version of this article.)

Table 2
Surface abundance of N, Fe and O and distribution of N species.

Sample	Surface atomic ratios			ratio of surface N species			
	N/C	Fe/C	O/C	$N_{pyridinic}$	$N_{pyrrolic}$	$N_{graphitic}$	N_{oxide}
$CNT_{pristine}$	0.003	n.d.	0.052	0.43	0	0.16	0.41
N/CNT-0	0.019	0.0007	0.045	0.51	0.28	0.08	0.13
N/CNT-12	0.010	0.0010	0.042	0.58	0.32	0.07	0.02
N/CNT-24	0.017	0.0010	0.047	0.57	0.30	0.10	0.02
N/CNT-48	0.012	0.0005	0.052	0.55	0.29	0.12	0.04
N/CNT-72	0.019	0.0012	0.062	0.51	0.30	0.14	0.04
N/CNT-150	0.038	0.0018	0.064	0.49	0.34	0.12	0.05

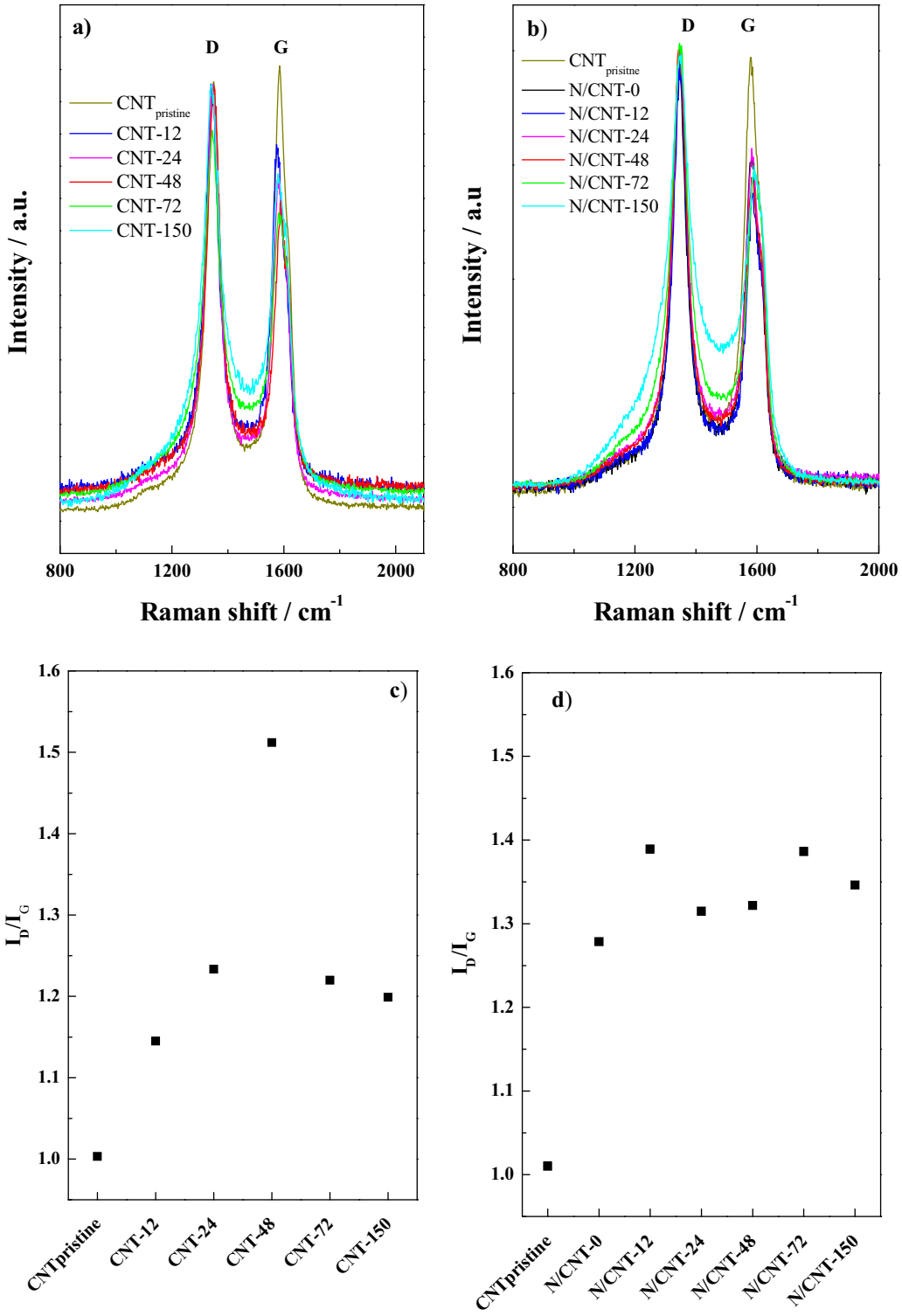

Fig. 2. Evolution of the Raman spectra recorded for (a) the CNTs subjected to different ballmilling times (CNT-t), (b) the final catalysts N/CNT-t. The spectrum of the fresh CNT is included for comparison. Evolution of the I_D/I_G ratio for (c) CNT-t and (d) N/CNT-t.

A careful comparison between the bulk and surface N/C atomic ratios reported, respectively, in Tables 1 and 2 indicate that the N atoms incorporated on the CNTs subjected to a previous ballmilling process, *i.e.*, all CNTs except CNT-0, are preferentially distributed on the surface of the catalyst. It is remarkable a higher surface enrichment of N for sample N/CNT-0 and N/CNT-24.

Four different surface N-species are detected by XPS in all samples, including the fresh CNT (spectrum not shown). Remarkably, the amount of oxidized N (characterized by the peak at the highest binding energy) is of *ca.* 41 at% in the fresh CNT (see Table 2) decreasing significantly for the samples subjected to ballmilling. In the same line, previous works suggest that pyridinic-N has an important role in the ORR activity [18,29] by favouring the so-called four-electron pathway (direct reduction of O_2 to H_2O) as compared to N-graphitic which seems to promote the so called two-electron pathway. According to the results shown in Table 2,

the amount of N-pyridinic in the N/CNT-t ranges between *ca.* 50 at% and 60 at% whereas the amount of N-graphitic is much lower, ranging between 7 at% and 14 at%. The proportion of N-graphitic and N-pyridinc species are not severely affected by the duration of the ballmilling treatment.

The presence of Fe in the N/CNT-t and its evolution with ballmilling time has been monitored by XPS. Fig. 1b shows the Fe 2p core-level region of all samples. The binding energy of the Fe $2p_{3/2}$ peak is centered at *ca.* 711 eV. This binding energy is usually assigned to the presence of Fe^{3+} species although in some cases it has also been assigned to Fe^{2+} or to FeOOH species. The presence of Fe^{3+} usually leads to the observation of a shake-up satellite peak at *ca.* 719.2 eV, which is the fingerprint of the Fe^{3+} species [30]. However, this satellite peak is only observed in the spectrum for N-CNT-12, although due to the low intensity of the signals the presence of Fe^{3+} species is not excluded in the other spectra. As shown in Table 2, the amount of Fe (reported as Fe/C atomic ratio) is similar in all samples and in fact it follows no clear trend with the duration of the ballmilling treatment. Although not shown, the amount of Fe in the pristine CNT (before subjected to ballmilling) is of *ca.* 0.7 wt% as deduced from ICP-OES analysis. Since Fe is not detected by XPS in the fresh CNT it is reasonable to assume that the iron species remain encapsulated within several carbon layers. These results indicate that the incorporation of Fe into the final CNTs is not due only to the ballmilling process from wear steel vessel used during synthesis. The actual amount of Fe in N/CNT-48 was also analyzed by ICP-OES, obtaining a value of 1.27 wt%. The evolution of the structural defects in the CNTs with the ballmilling time was studied by Raman spectroscopy. In general, the Raman spectra of graphitic materials exhibit three characteristic bands at 1580 cm^{-1}, 1351 cm^{-1} and 2700 cm^{-1} which are usually referred to as G, D and 2D bands, respectively [19,31]. The G band is caused by the stretching of the C—C bond in graphitic materials appearing in all sp^2 carbon systems. [32]. On the other hand, both D and 2D bands are related to the degree of disorder of the carbon structure [33]. Therefore, the consequences of the ballmilling time for the creation of defects on the carbon structure of the CNTs can be assessed by recording the evolution of the normalized intensities of the D and G bands (I_D/I_G) bands. Fig. 2a depicts the first order Raman spectra of the CNT-t showing, for all samples, the expected D and G bands. The Raman spectra depicted in Fig. 2a and b shows a decreasing of the G band with the increasing ballmilling time, which is indicative of the loss of crystallinity of the CNTs during the treatment and to the creation of a greater number of defects. In addition, it can be observed how the D band slight broadens with the increasing ballmilling time. This effect could be indicative of the incorporation of N which would increase the structural imperfection of CNTs, specially pyridinic-N and graphitic-N [19]. The evolution of the I_D/I_G bands is shown in Fig. 2c and d; as observed, the ratio of the I_D/I_G bands increases after 12 h of ballmilling and then it remains roughly constant irrespective of the duration of the treatment.

The evolution of the crystallite size of the N/CNT-t has been followed by XRD analysis (Fig. 3). Crystallite size has been measured by applying the Scherrer equation to the most intense 0 0 2 peak at *ca.* 25°. The calculated particle size is of 3.7 ± 0.2 nm for the samples subjected to ballmilling periods $t \leq 48$ h. This value is similar to that calculated for the pristine CNT of 3.8 nm. On the other hand, the catalysts prepared using the CNTs subjected to longer ballmilling periods exhibit smaller crystallites sizes of 2.9 and 1.9 nm for N/CNT-72 and N/CNT-150. These results suggest that a drastic change in the nature of the samples takes place after 72 h of ballmilling.

Table 3 shows the BET surface area, external surface and micropore surface values of all samples studied. The BET values recorded for the CNT-t remain roughly invariable, or exhibit a slight decrease, for the CNTs subjected to ballmilling periods of up to 48 h; *i.e.*

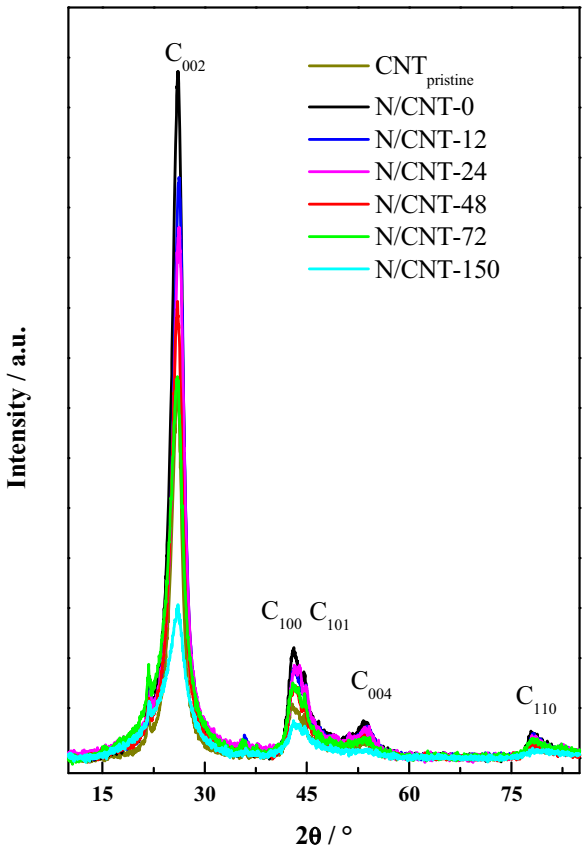

Fig. 3. X-ray diffractograms of the N/CNT-t. The diffractogram of the pristine CNT is shown for comparison. All diffraction peaks are ascribed to hexagonal graphite (pdf no. 01-075-1621).

CNT-12, CNT-24 and CNT-48. However, the BET values of the CNTs subjected to longer ballmilling periods increase significantly from 212 $m^2 g^{-1}$ recorded for the fresh CNT, to 486 and 524 $m^2 g^{-1}$ recorded for CNT-72 and CNT-150, respectively. This significant increasing of the BET area is due to the generation of microporosity during ballmilling. Thus, CNT-72 and CNT-150 record micropore surface areas of 150 and 169 $m^2 g^{-1}$, respectively, as compared to 13 $m^2 g^{-1}$ recorded for the fresh CNT. This is an important feature since it has been reported previously that the real active sites for the ORR in NPMCs are hosted within the micropores of the carbon matrix [6–8].

Table 3
BET area, external surface and micropore surface corresponding to carbon nanotubes samples after ball milling times (CNT-t) and samples after to being mixed with nitrogen precursor and heat treatment (N/CNT-t).

Sample	BET surface area ($m^2 g^{-1}$)	External surface area ($m^2 g^{-1}$)	Micropore surface area ($m^2 g^{-1}$)
$CNT_{pristine}$	212	199	13
CNT-12	218	211	7
CNT-24	208	196	12
CNT-48	209	191	18
CNT-72	486	336	150
CNT-150	524	355	169
N/CNT-0	229	227	3
N/CNT-12	239	235	4
N/CNT-24	237	228	9
N/CNT-48	235	224	12
N/CNT-72	392	283	109
N/CNT-150	483	288	195

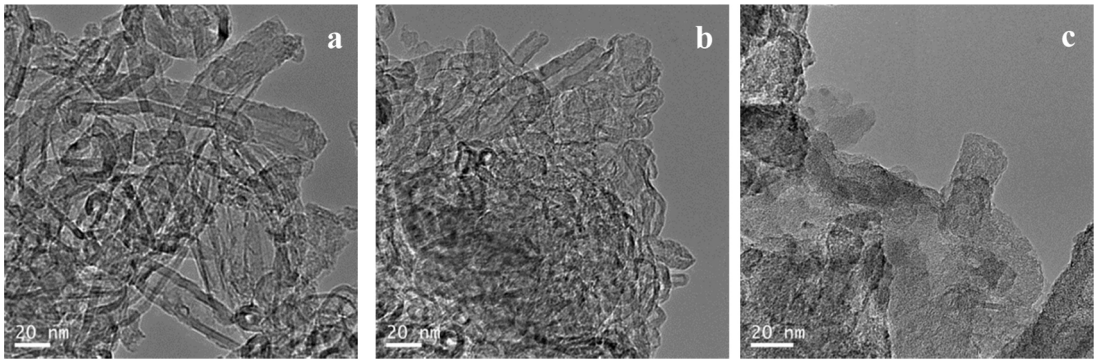

Fig. 4. Selected TEM images of (a) N/CNT-0, (b) N/CNT-48 and (c) N/CNT-150 recorded at the same magnification.

As also shown in Table 3 the BET values recorded after N incorporation increases moderately for the samples without micropores in their structure, CNT-0, CNT-12, CNT-24 and CNT-48, decreasing for the catalysts prepared with CNT-72 and CNT-150. This decreasing account to the lower external and micropore surface area, so if NPMC active sites are effectively form by MN_4, they could be created in both sites (external and micropore surface). Note that N/CNT-150 catalyst increases the area correspond to micropores area after urea mixed and later pyrolysis steps. It is also important to note that external surface area is almost the same for N/CNT-72 and N/CNT-150 catalysts.

The effect of the duration of the ballmilling process for the morphology of the CNT-t has been assessed by recording TEM images of the samples, see Fig. 4.

CNTs are clearly observed in the TEM micrograph of N/CNT-0. Although CNTs are still observed in the image for N/CNT-48 a large fraction of amorphous carbon is also present in this sample. In addition, the CNTs are visible shorter in N/CNT-48. Finally, CNTs are almost absent the micrographs recorded with N/CNT-150 and instead amorphous carbon is the main structure observed in the micrographs.

3.2. Performance of N/CNT-t for the ORR

Fig. 5 shows the cyclic voltammograms (CVs) for all of the N/CNT-t electrocatalysts recorded at 10 mV s^{-1} in 0.1 M of $HClO_4$ in Ar saturated solution. The CVs show a squared wave profile, typical of potential independent capacitive responses [11]. As expected, the capacitive currents increase with the area of the catalysts and N/CNT-72 and N/CNT-150 record the greatest values in the series. In view of the results in Table 3, it appears like the intensity of the capacitive response may be related to external surface area because samples which external areas values are highly similar also present similar capacitive current values (N/CNT-72 and N/CNT-150).

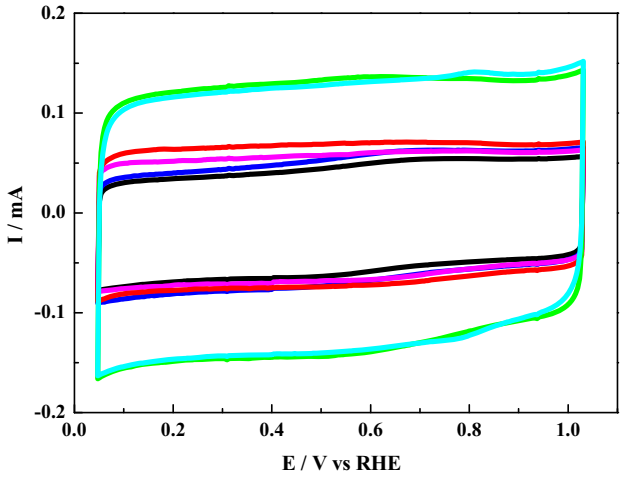

Fig. 5. Cyclic voltammograms for N/CNT-t recorded at 10 mV s^{-1} in 0.1 M $HClO_4$. Catalyst loading 0.6 mg cm^{-2}. N/CNT-0 (black), N/CNT-12 (blue), N/CNT-24 (magenta), N/CNT-48 (red), N/CNT-72 (green) and N/CNT-150 (cyan). (For interpretation of the references to color in this figure legend, the reader is referred to the web version of this article.)

Fig. 6a shows the ORR polarization curves of all N/CNT-t samples recorded during the positive going sweep in O_2 saturated 0.1 M $HClO_4$ electrolyte at 10 mV s^{-1} and 1600 rpm after subtraction of the corresponding capacitive currents. It should be noted that N/CNT-t are the only samples which record measurable activities for the ORR whereas CNT-t are inactive for the ORR. The ORR curves for all N/CNT-t exhibit a mixed kinetic controlled and a diffusion controlled region. A trend for the ORR can be clearly observed and the onset potential for the ORR shifts to more positive values as the amount of N in the catalyst increases. Thus, the onset potentials for N/CNT-0 and N/CNT-150 are of 0.72 and 0.84 V, respectively. These values are the less positive and the more positive in the series and clearly illustrate that the increasing amount of N in the final catalyst results in more active catalysts for the ORR. Not only the onset potential varies with the amount of N in the catalysts, but also higher current densities between 0.6 and 1.0 V are recorded as the amount of N in the catalyst increases, *i.e.*, for the catalysts subjected to longer ballmilling treatments. Fig. 6b displays the normalized mass activities (i_M) (faradaic current values normalized to the mass of catalyst on the electrode) for all catalysts. As expected, the mass activity values increase with the increasing amount of N in the catalyst and N/CNT-150 records the highest mass activity in the series of 0.547 A g^{-1} at 0.8 V.

The results presented so far clearly illustrate that the duration of the ballmilling treatment has strong consequences in the morphology and textural properties of CNTs affecting both the incorporation of N and as a consequence the performance of the final catalysts for the ORR. However, not all of such effects are affected in the same way by ballmilling time. For instance, the morphology of the CNTs is severely affected after ballmilling treatments during 72 h or longer. Whereas CNTs are actually observed by TEM in the CNT-t subjected to ballmilling during $t \leq 48$ h, the structure of the CNTs collapses after 72 h of ballmilling and nanotubes are not observed in the micrographs of CNT-72 and CNT-150. In line with this observation, the BET areas of the CNT-t remain roughly constant for ballmilling times of up to 48 h, increasing swiftly for the CNT-t subjected to 72 and 150 h of ballmilling. The increasing BET areas for these latter samples is due to the generation of a high degree of microporosity after ballmilling periods ≥72 h. As observed by TEM, the formation of micropores is due to the collapse of the structure of the CNTs. On the other hand, the generation of defects in the sp^2 structure of the CNTs, measured as the I_D/I_G ratio, reaches a plateau after 12 h of

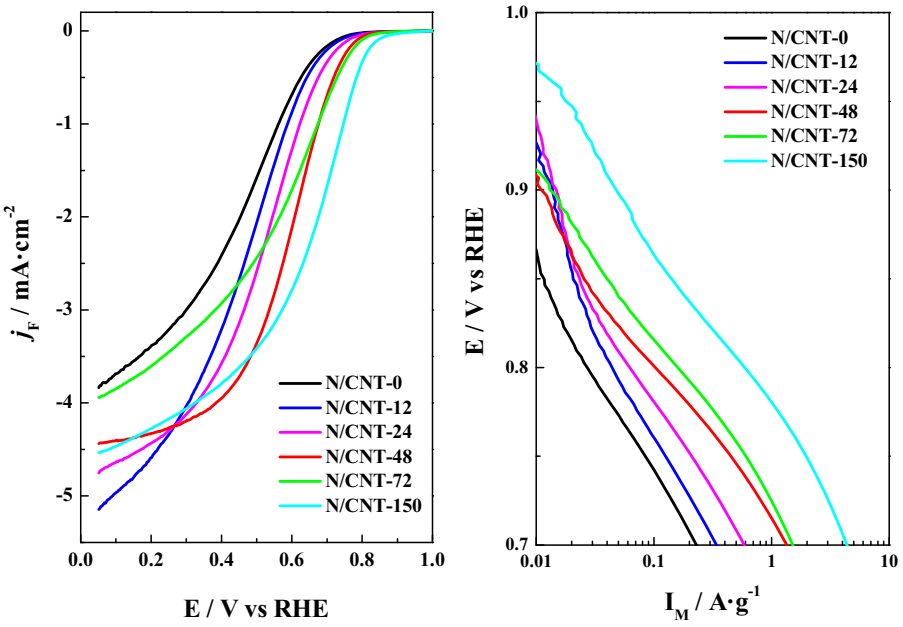

Fig. 6. (a) Faradaic current densities (j_F) and (b) mass activity (i_M) of all N/CNT-t recorded during the positive going sweep in oxygen saturated 0.1 M at 10 mV s^{-1}, 1600 rpm. Catalyst loading 0.6 mg cm^{-2}.

ballmilling. Finally, the incorporation of N increases with the higher ballmilling time of the CNT-t.

Before addressing the effects of the amount of N into the CNTs and of the development of porosity due to the collapse of the structure of the CNTs during ballmilling for the ORR we shall discuss the effect of the presence of residual iron for the ORR. It is well documented that cyanide adsorbs strongly on metals such as Fe or platinum group metals hence suppressing their activity for the ORR [34–36]. Since ORR experiments have been conducted at pH ~ 1, we used thiocyanate rather than cyanide to block the Fe sites. In order adsorb thiocyanate onto the selected catalysts: N/CNT-150, N/CNT-48 or N/CNT-0, the catalyst was deposited onto a rotatory electrode (see Section 2 for the disposition procedure) immersed in a 0.01 M solution of NaSCN in distilled H_2O during 15 min under rotation at 1000 rpm and rinsed Milli-Q water. Fig. 7 shows the performance of N/CNT-150, N/CNT-48 and N/CNT-0 for the ORR before and after thiocyanate adsorption. As observed, the ORR performance of all catalysts is moderately affected by the presence of thiocyanate, recording *ca.* 10–15% lower i_M values after thiocyanate adsorption. This observation indicates that the residual iron species detected by XPS are active for the ORR, but they are not the main responsible for the overall ORR performance of the catalysts. Moreover, Fig. 7 also shows that all catalysts show a similar level of deactivation upon thiocyanate adsorption so the trends in the ORR activity shown in Fig. 6, *i.e.*, increasing i_M for the ORR with the increasing N-content.

As shown in Fig. 8, the mass activity (i_M) for the ORR at 0.8 V goes in parallel with the amount of N in the catalysts. A similar trend can be observed between the i_M and the micropore area, but no such trend between i_M and Fe content can be observed (see Fig. S2 in Supplementary material). The observed increasing of the i_M with the increasing amount of N demonstrates that in order to obtain more active catalysts for the ORR is necessary to designing synthetic strategies which allow incorporating higher amounts of N in the catalysts. However, two regimes for the incorporation of N into CNTs, and as a consequence for the ORR performance, can be observed. First, the incorporation of N increases only moderately for the CNT-t subjected to ballmilling periods ≤48 h. In fact, the amount of N actually incorporated into the CNTs increases linearly with the increasing amount of defects in the CNTs, which increases

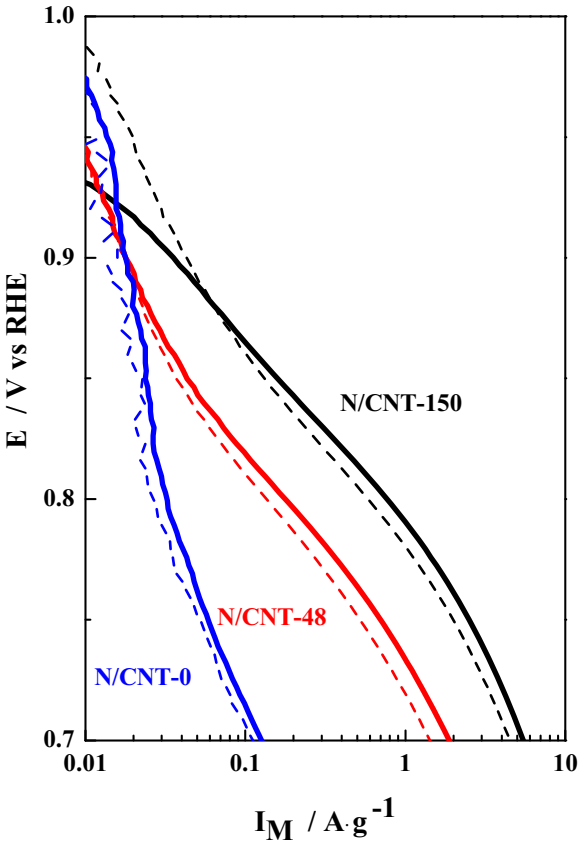

Fig. 7. Mass activity for the ORR recorded with N/CNT-150 (straight black line), N/CTN-48 (straight red line) and N/CNT-0 (straight blue line) in 0.1 M $HClO_4$ at 10 mV s^{-1} and 1600 rpm. Dotted lines are the mass activities recorded with the SCN-doped electrodes under the same reaction conditions. (For interpretation of the references to color in this figure legend, the reader is referred to the web version of this article.)

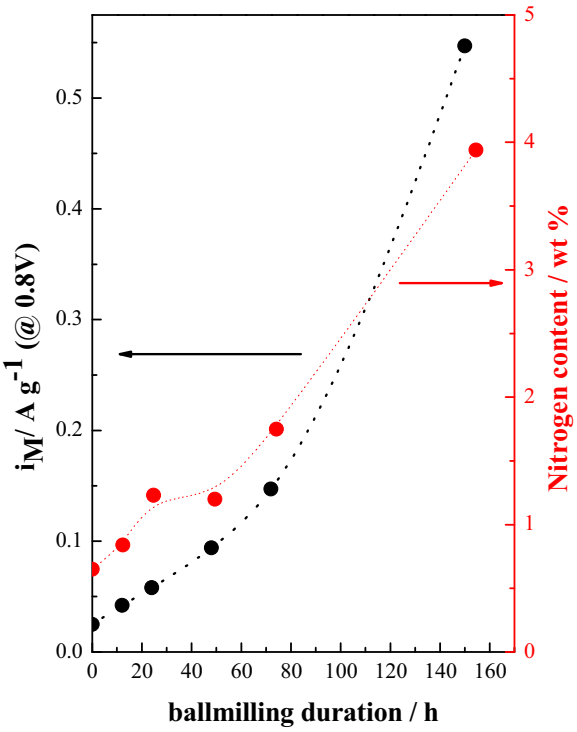

Fig. 8. Evolution of mass activity (i_M) recorded at 0.8 V (black line) and nitrogen content (wt%) (red line) with ballmilling time for N/CNT-t. (For interpretation of the references to color in this figure legend, the reader is referred to the web version of this article.)

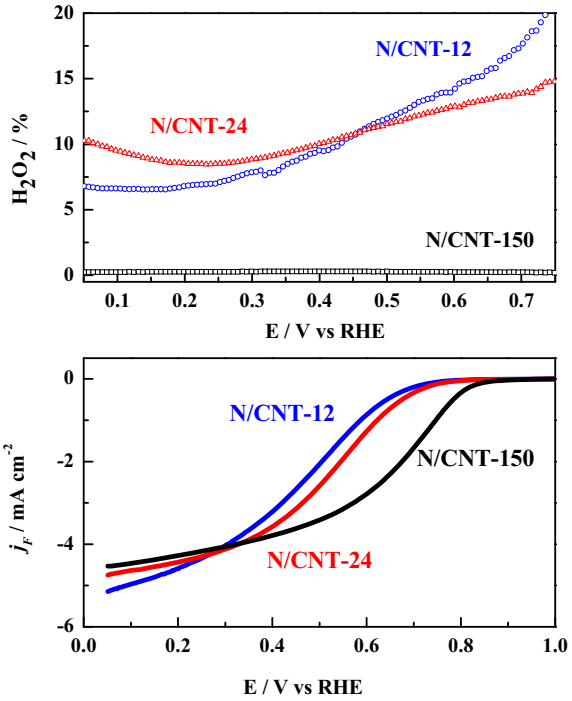

Fig. 9. Lower panel, positive going direction CV at 10 mV s^{-1} in O_2 saturated 0.1 M $HClO_4$ with N/CNT-t t 12 (blue), 24 (red) and 150 (black) h. (0.6 mg cm^{-2}). Upper panel, simultaneously recorded H_2O_2 production (as determined for the ring currents) at 1600 rpm for a ring potential E_R = 1.2 V. (For interpretation of the references to color in this figure legend, the reader is referred to the web version of this article.)

moderately with the ballmilling time. On the other hand, the incorporation of N increases significantly for the CNT-t subjected to longer ballmilling periods of 72 and 150 h and so it does the ORR activity. Remarkably, Raman analyses indicate that the CNTs subjected to longer ballmilling periods contain a similar amount of defects than the ones subjected to treatments between 12 and 48 h suggesting that the present of defects is not the only feature controlling the incorporation of N into carbon based NPMCs. As stated above, the CNTs subjected to longer ballmilling periods exhibit significantly higher BET areas due to the generation of micropores. It is plausible to assume that this increasing of the BET area would result in a higher fraction of sites available for the incorporation of N. As shown in Fig. 8 the performance for the ORR increases with the amount of N in the catalysts. This trend applies to all samples regardless of their textural properties. However, Fig. 8 also shows that the formation of micropores, due to the collapse of the nanotubes' structure, leads to the formation of more active sites for the ORR. As shown in Fig. 8, mass activity of the active sites generated within the micropores is greater than that expected if the amount of N is the only parameter taken into account. This observation goes in line with the proposal that the most active sites for the ORR are hosted within the micropores [8]. Although our results demonstrate that active sites can be also created on carbon supports without micropores it is obvious that the presence of micropores results in more active catalysts for the ORR.

As described above, a careful inspection of Fig. 8 reveals that i_M increases linearly with the content of nitrogen in the CNTs but it appears to increase more rapidly for the samples in which microporosity has been developed, N/CNT-72 and N/CNT-150.

In order to understand the higher mass activity recorded for the electrocatalysts in which micropores have been formed the ORR pathway has been further studied. In principle, it is well accepted that the ORR can proceed *via* a direct reduction of O_2 to H_2O, the so-called 4 electrons pathway, or through the indirect reduction pathway, *i.e.*, through the formation of H_2O_2. The production of H_2O_2 has been determined by recording RRDE experiments with catalysts in which micropores have been develop (N/CNT-150) and with two catalysts in which the CNT structure is intact but with different amounts of N (N/CNT-12 and N/CNT-24). Fig. 9 shows the production of H_2O_2 (%) recorded for N/CNT-12, N/CNT-24 and N/CNT-150.

As observed in Fig. 9, the production of H_2O_2 is different for the sample with micropores within their structure and for the samples without micropores. For the former, N/CNT-150, the production of H_2O_2 is low of *ca.* 1% increasing slightly at less positive potentials. On the contrary, both N/CNT-12 and N/CNT-24 record higher production of H_2O_2, especially at potential values close to 0.75 V. More importantly, the production of H_2O_2 decreases as the potential is sweep to less positive values. It appears like the direct reduction of O_2, the so called 4e$^-$ pathway, is favored in the catalysts with micropores whereas the 2e$^-$ pathway, *i.e.*, O_2 reduction to H_2O_2, is more important in the catalysts without micropores. It has been reported previously that the ORR on pyridinic-N and graphitic-N proceed *via* the 4- and 2-electrons pathways, respectively [18]. As shown in Table 2, the proportion of pyridinic-N and graphitic-N is similar in all of the catalysts reported in this work irrespective of their morphology. Therefore, the higher formation of H_2O_2 recorded with the catalysts in which the CNT structure is preserved cannot be justified by the presence of different chemical species or active sites. A possible explanation to justify the lower formation of H_2O_2 in the catalysts in which the active sites are located within micropores could be due to diffusional effects whereby H_2O_2, which is formed within micropores, readsorbs and reacts easily onto the active sites responsible for the formation of H_2O before leaving the micropores. As a consequence, the amount of H_2O_2 actually detected in the RRDE experiments would be lower than that recorded with catalysts in which the readsorption process is not favored. On the other

hand, the readsorption of H_2O_2 and its further reduction to H_2O is not favored in catalysts with more open morphologies such as those based upon CNTs where once formed, H_2O_2 would reach the solution without further reaction.

4. Conclusions

By subjecting CNTs to ballmilling generates defects in the sp^2 carbon network are created. The number of such defects increases with ballmilling time. However, if the treatment is extended to 72 h or longer periods, the structure of the CNTs collapses and microporous carbon is formed. The incorporation of N into the graphite structure of the carbon obtained increases only moderately with the amount of defects but it increases significantly with the appearance of micropores. The N/CNT catalysts are active for the ORR in acid medium. In fact, the ORR performance of the N/CNT increases with the increasing amount of N in the final catalyst and as a consequence, the catalysts with the greater amount of N, which are those with the higher micropore area, are the most active in the series for the ORR.

Acknowledgements

This project was funded by the Deanship of Scientific Research (DSR), King Abdulaziz University, Jeddah, under grant number (D-006-432). The authors, therefore, acknowledge with thanks DSR technical and financial support. Economic support from Project 201080E116 from the CSIC is also acknowledged.

Appendix A. Supplementary data

Supplementary data associated with this article can be found, in the online version, at http://dx.doi.org/10.1016/j.apcatb.2014.07.002.

References

[1] H.A. Gasteiger, S.S. Kocha, B. Sompalli, F.T. Wagner, Appl. Catal., B: Environ. 56 (2005) 9–35.
[2] J.S. Spendelow, D.C. Papageorgopoulos, Fuel Cells 11 (2011) 775–786.
[3] F. Jaouen, E. Proietti, M. Lefèvre, R. Chenitz, J.P. Dodelet, G. Wu, H.T. Chung, C.M. Johnston, P. Zelenay, Energy Environ. Sci. 4 (2011) 114–130.
[4] R. Jasinski, Nature 201 (1964) 1212–1213.
[5] E. Proietti, F. Jaouen, M. Lefèvre, N. Larouche, J. Tian, J. Herranz, J.-P. Dodelet, Nat. Commun. 2 (2011) 416.
[6] M. Lefevre, E. Proietti, F. Jaouen, J.P. Dodelet, Science 324 (2009) 71–74.
[7] U.I. Kramm, J. Herranz, N. Larouche, T.M. Arruda, M. Lefevre, F. Jaouen, P. Bogdanoff, S. Fiechter, I. Abs-Wurmbach, S. Mukerjee, J.P. Dodelet, Phys. Chem. Chem. Phys. 14 (2012) 11673–11688.
[8] F. Jaouen, M. Lefèvre, J.-P. Dodelet, M. Cai, J. Phys. Chem. B 110 (2006) 5553–5558.
[9] R. Franke, D. Ohms, K. Wiesener, J. Electroanal. Chem. 260 (1989) 63–73.
[10] K. Wiesener, Electrochim. Acta 31 (1986) 1073–1078.
[11] F. Jaouen, J. Herranz, M. Lefevre, J.P. Dodelet, U.I. Kramm, I. Herrmann, P. Bogdanoff, J. Maruyama, T. Nagaoka, A. Garsuch, J.R. Dahn, T. Olson, S. Pylypenko, P. Atanassov, E.A. Ustinov, ACS Appl. Mater. Interfaces 1 (2009) 1623–1639.
[12] G. Wu, K.L. More, C.M. Johnston, P. Zelenay, Science 332 (2011) 443–447.
[13] C. Domínguez, F.J. Pérez-Alonso, M. Abdel Salam, J.L. Gómez de la Fuente, S.A. Al-Thabaiti, S.N. Basahel, M.A. Peña, J.L.G. Fierro, S. Rojas, Int. J. Hydrogen Energy. 39 (2014) 5309–5318.
[14] P.H. Matter, U.S. Ozkan, Catal. Lett. 109 (2006) 115–123.
[15] P.H. Matter, E. Wang, M. Arias, E.J. Biddinger, U.S. Ozkan, J. Phys. Chem. B 110 (2006) 18374–18384.
[16] V. Nallathambi, J.W. Lee, S.P. Kumaraguru, G. Wu, B.N. Popov, J. Power Sources 183 (2008) 34–42.
[17] G. Wu, K.L. More, P. Xu, H.L. Wang, M. Ferrandon, A.J. Kropf, D.J. Myers, S. Ma, C.M. Johnston, P. Zelenay, Chem. Commun. 49 (2013) 3291–3293.
[18] S. Yasuda, L. Yu, J. Kim, K. Murakoshi, Chem. Commun. 49 (2013) 9627–9629 (London, 1996).
[19] L.G. Bulusheva, A.V. Okotrub, I.A. Kinloch, I.P. Asanov, A.G. Kurenya, A.G. Kudashov, X. Chen, H. Song, Phys. Status Solidi B: Basic Res. 245 (2008) 1971–1974.
[20] H.R. Byon, J. Suntivich, E.J. Crumlin, Y. Shao-Horn, Phys. Chem. Chem. Phys. 13 (2011) 21437–21445.
[21] J. Yang, D.J. Liu, N.N. Kariuki, L.X. Chen, Chem. Commun. (2008) 329–331.
[22] U.I. Kramm, J. Herranz, N. Larouche, T.M. Arruda, M. Lefevre, F. Jaouen, P. Bogdanoff, S. Fiechter, I. Abs-Wurmbach, S. Mukerjee, J.-P. Dodelet, Phys. Chem. Chem. Phys. 14 (2012) 11673–11688.
[23] U.I. Kramm, M. Lefèvre, N. Larouche, D. Schmeisser, J.-P. Dodelet, J. Am. Chem. Soc. 136 (2013) 978–985.
[24] F.J. Pérez Alonso, M.A. Salam, T. Herranz, J.L. Gómez de la Fuente, S.A. Al Thabaiti, S.N. Basahel, M.A. Peña, J.L.G. Fierro, S. Rojas, J. Power Sources 240 (2013) 494–502.
[25] J.L.G. de la Fuente, S. Rojas, M.V. Martínez-Huerta, P. Terreros, M.A. Peña, J.L.G. Fierro, Carbon 44 (2006) 1919–1929.
[26] U.A. Paulus, T.J. Schmidt, H.A. Gasteiger, R.J. Behm, J. Electroanal. Chem. 495 (2001) 134–145.
[27] E. Proietti, S.p. Ruggeri, J.-P. Dodelet, J. Electrochem. Soc. 155 (2008) B340.
[28] E. Proietti, J.-P. Dodelet, ECS Trans. 16 (2008) 393–404.
[29] F. Jaouen, S. Marcotte, J.-P. Dodelet, G. Lindbergh, J. Phys. Chem. B 107 (2003) 1376–1386.
[30] T. Herranz, S. Rojas, M. Ojeda, F.J. Pérez-Alonso, P. Terreros, K. Pirota, J.L.G. Fierro, Chem. Mater. 18 (2006) 2364–2375.
[31] G. Compagnini, Carbon 35 (1997) 1793–1797.
[32] M. Dresselhaus, A. Jorio, M. Hofmann, G. Dresselhaus, R. Saito, Nano Lett. 10 (2010) 751–758.
[33] P. Delhaes, M. Couzi, M. Trinquecoste, J. Dentzer, H. Hamidou, C. Vix-Guterl, Carbon 44 (2006) 3005–3013.
[34] Y. Li, W. Zhou, H. Wang, L. Xie, Y. Liang, F. Wei, J.-C. Idrobo, S.J. Pennycook, H. Dai, Nat. Nano 7 (2012) 394–400.
[35] M.S. Thorum, J.M. Hankett, A.A. Gewirth, J. Phys. Chem. Lett. 2 (2011) 295–298.
[36] D. Strmcnik, M. Escudero-Escribano, K. Kodama, R. StamenkovicVojislav, A. Cuesta, N.M. Marković, Nat. Chem. 2 (2010) 880–885.

Supplementary Materials

On the relationship between N content, textural properties and catalytic performance for the oxygen reduction reaction of N/CNT

Carlota Domínguez[1], Francisco J. Pérez-Alonso*[,1], Mohammed A. Salam[2], Shaeel A. Al-Thabaiti[2], Abdullah Y. Obaid[2], Abdulmohsen A. Alshehri[2], José L. Gómez de la Fuente[1] J. L. G. Fierro[1] and Sergio Rojas*[,1]

Thermogravimetic (TG) analysis of the N-modified CNTs collected after different ballmilling periods were recorded with a Mettler Toledo TGA/SDTA 851 apparatus. Typically, 30-40 mg of the sample was heated from 298 to 1373 K at 20 K min^{-1} under a flow of 50 mL min^{-1} of pure N_2.

Figure S1. Thermogravimetric analyses of the N-modified CNTs recorded under a flow of 50 mL min^{-1} of pure N_2 at 20 K min^{-1}. TGA analysis of the fresh CNT (CNTpristine) is shown for comparison

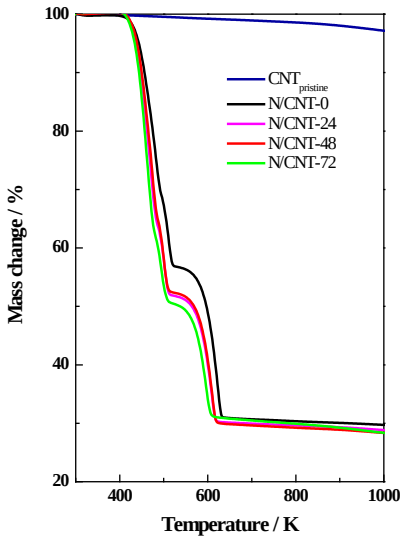

Figure S2. Evolution of mass activity (i_M) recorded at 0.8 V (black lines) and a) Fe content as determined by XPS and b) micropore area (red lines) with ballmilling time for N/CNT-t

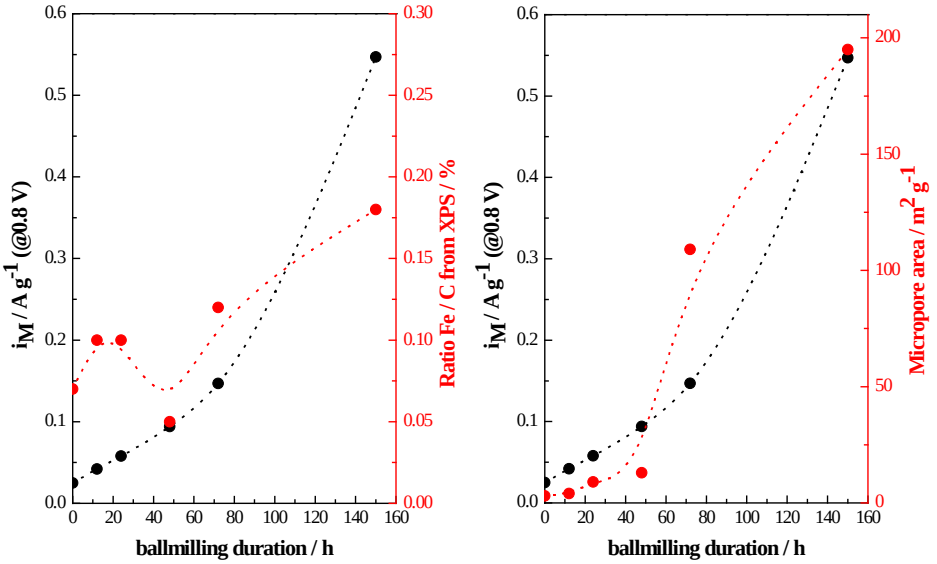

Electrochimica Acta 157 (2015) 158–165

Contents lists available at ScienceDirect

Electrochimica Acta

journal homepage: www.elsevier.com/locate/electacta

Effect of N and S co-doping of multiwalled carbon nanotubes for the oxygen reduction

Carlota Domínguez [a], Francisco J. Pérez-Alonso [a,1,*], Shaeel A. Al-Thabaiti [b], Sulaiman Nassir Basahel [b], Abdullah Y. Obaid [b], Abdurrahman Obaid Alyoubi [b], José L. Gómez de la Fuente [a], Sergio Rojas [a,*]

[a] Grupo de Energía y Química Sostenibles (EQS), Instituto de Catálisis y Petroleoquímica, CSIC, C/Marie Curie, 2, L10. 28049 Madrid, Spain
[b] Chemistry Department, Faculty of Science, King Abdulaziz University, P.O Box 80200-Jeddah 21589, Saudi Arabia

ARTICLE INFO

Article history:
Received 18 September 2014
Received in revised form 25 November 2014
Accepted 7 January 2015
Available online 9 January 2015

Keywords:
ORR
sulfur
nitrogen
non precious metal catalyst
multiwalled carbon nanotubes

ABSTRACT

The co-incorporation of S and N into multiwalled carbon nanotubes (CNTs) and the effects for the catalytic performance for the oxygen reduction reaction (ORR) in acidic and alkaline electrolytes has been studied. Subjecting CNTs to different ballmilling periods results in the formation of defects in their graphitic structure. Heteroatoms such as N and S can be actually incorporated into such defects leading to active catalysts for the ORR. In fact, the ORR activity in acid and alkaline media increases with the increasing amount of heteroatoms, especially N, actually incorporated in the catalysts. The use of precursors containing both N and S into their structure such as thiourea, results in a higher incorporation of surface N atoms than with similar N-containing precursors. As a consequence the ORR activity of the S/N/CNTs based catalysts is higher than that of N/CNT ones. This promotional effect of the presence of S is more significant when the ORR is measured in alkaline media suggesting that S-incorporation into the carbon matrix could actually play a direct role for the ORR.

1. Introduction

Proton exchange membrane fuel cells (PEMFCs) are the most efficient devices to transform chemical energy accumulated in energy carriers such as H_2 or small organic molecules such as methanol or ethanol into electricity. As a consequence, PEMFCs are expected to become key players for transportation and portable devices sectors. The state-of-the-art catalysts for PEMFCs, both in the cathode and in the anode, are based upon carbon supported nanosized Pt and Pt-alloyed particles [1,2]. However, due to the sluggish kinetic of the oxygen reduction reaction (ORR), and despite the impressive achievements obtained in the last decade, Pt loading in the cathode electrode is still too high, of ca. 0.5 mg_{Pt}/cm^2 [3]. As a result, the price of PEMFCs based upon Pt-based electrocatalysts is too high for their wider commercialization. With this motivation in mind, numerous research efforts have been devoted to replacing Pt (or other platinum group metals) catalysts with electrocatalysts based upon non-precious metals (usually referred to as non-precious metal catalysts NPMCs), with high activity for the ORR [4–8]. Amongst those, the most successful ones are based upon Fe, Co or Mn atoms, mainly Fe, coordinated to N atoms (between 2 and 4) and stabilized into a sp^2 C-C graphitic network [4,9,10]. The intrinsic activity of these catalysts, usually referred to as non-precious metal catalysts (NPMCs), for the ORR is usually lower than that of Pt-based ones; however, this feature can be compensated by increasing the amount of NPMCs in the cathode electrode without economic repercussions. Moreover, recent studies about NPMCs for the ORR report current densities as high as 230 A cm^{-3} at 0.8 V, a value comparable to that achieved by Pt/C in acid media [11,12] or even higher than that recorded with Pt/C in alkaline media of 4.8 A cm^{-3} at 0.9 V [13].

Fe/N/C NPMCs are usually prepared via thermochemical routes under inert (N_2 or Ar) or reactive (NH_3) atmospheres of a mixture of N, Fe (or the target metal) and carbon precursors, which in some cases have been previously thoroughly mixed via ballmilling. The thermal process (pyrolysis), are usually conducted at temperatures between 600–1100 °C, depending on the actual precursors used, in order to promote N insertion onto the C—C network while creating optimum textural properties of the final material [14–16]. Next, the catalysts are subjected to acid leaching in order to remove non-stable Fe phases in acidic media. In some cases, pyrolysis and acid leaching steps are conducted several times in order to generate very active

* Corresponding authors. Tel.: +34 91 585 4632.
E-mail addresses: fperez@icp.csic.es (F.J. Pérez-Alonso), srojas@icp.csic.es (S. Rojas).
[1] Active ISE Member.

http://dx.doi.org/10.1016/j.electacta.2015.01.031
0013-4686/

NPMCs. The precise structure of the active site for the ORR of Fe/N/C is still under debate. It is well established, that graphitic carbon is active for the ORR in alkaline media. The activity for the ORR can be increased by incorporating N atoms into the graphitic network, and in fact the ORR activity increases with the amount of N incorporated into the carbon matrix [17,18]. However, it is also well admitted that the ORR activity increases significantly by introducing metals such as Fe or Co, especially the former [19–21] into the N/C matrix. It is also well documented that the most active catalysts are achieved when Fe atoms are bound to N ones although the precise nature of this interaction is still under study. Thus, different Fe/N ensembles, e.g. FeN_4/C, FeN_{2+2}/C, N − FeN_{2+2}/C or N − FeN_{2+2} · · · NH/C have been detected by several groups employing a number of characterization techniques (XPS, Mössbauer spectroscopy, EXAFS etc.) and proposed some of such ensembles as the actual active sites for the ORR [22,23]. Moreover, recent *in situ* studies claim that the spin state of the Fe center plays a key role in the reactivity of Fe in the presence of O_2 [24]. In this line it is also well documented that upon incorporation of N into the C—C network, 4 different N species are formed: pyrrolic, pyridinic, graphitic and oxidized nitrogen. Yasuda et al. have highlighted the importance of pyridinic N for the direct ORR via four-electron pathway [25]. It has also been reported that the ORR activity of NPMCs increases with the increasing amount of N incorporated into the catalysts which increases with the number of defects of the C—C network [26].

Most of the studies dealing with the role of the carbon matrix suggest that the number of active sites for the ORR increases with the microporosity of the catalyst and, as a consequence, that the actual active sites for the ORR with NPMCs are hosted within micropores [27], which can be formed during the pyrolysis step(s). On the other hand, it is also known that the durability of NPMCs, *i.e.*, their resistance to oxidation at high potentials, increases with the degree of graphitization of the carbon matrix. In this sense, NPMCs based on carbon nanotubes usually show better results in terms of durability of the NPMCs [28]. Alas, it is not possible to introduce high amounts of N into the C—C sp^2 graphitic network of nanotubes (or graphene) without destroying the graphitic character of the carbon matrix [17].

A different approach to increase the amount of N into C—C network is by adding heteroatoms other than N, such as B, P and S during the synthesis of N/CNTs. In this sense, it has been reported that the addition of S leads to higher amounts of N actually incorporated onto the carbon sp^2 network, especially the pyridinic form of N [29]. By contrary, other works report that the amount of N actually incorporated into the final catalyst actually decreases after co-doping with S [23,30]. In any case, most reports coincide in that the ORR activity in alkaline media of the S/N- co-doped catalysts increases significantly with respect to the N-doped catalysts, regardless of the actual amount of N in the final catalyst. The actual promotional role of S is, however, unclear. Some studies suggest that the promotional effect for the ORR of heteroatoms such S arise from the modification of the electronic density of the carbon atoms induced by the presence of vicinal S (or other) atoms [30]. Other reports suggest that the promotional effect for the ORR of S co-doping is due to the higher amount of N incorporated in the final catalyst when S-precursors are used during the synthesis of the electrocatalysts.

Although the number of papers dealing with S/N/C-based catalysts for the ORR is high, only very few of them have studied the influence of S for the ORR in acid media with S/N/C catalysts. Recently, Qianqian Shi et al. [31] reported that co-doping CNTs with S and N results in a strong promotion of the ORR activity in alkaline media but the effect is only moderate in acid electrolyte.

In view of the above, we have studied in this work the incorporation of N or S and N into multiwalled carbon nanotubes (CNTs) by using similar precursors, *i.e.*, urea or thiourea as the source of N and of N and S. Previous to the incorporation of the dopants (N and S) the CNTs were subjected to physical treatment to generate defects to promote the incorporation of N and S. The activity for the oxygen reduction reaction (ORR) has been measured in acid electrolyte by means of electrochemical techniques.

2. Experimental

2.1. Chemicals and synthesis of N/CNT or N-S/CNTs

Multiwalled carbon nanotubes (CNTs; SUNANO, purity > 90%, Syn Nanotech Co Ltd) subjected to an acid leaching with HNO_3 20% v/v at 110 °C for 5 h before the synthesis to eliminate possible contaminants [32]. Previous to the incorporation of N and/or N, and in order to generate defects to promote heteroatom insertion, CNTs were treated for different periods of time, 0, 24 and 72 h in a stainless steel planetary ballmilling using 5 stainless steel balls. The CNTs recovered were identified by the suffix–t indicative of the duration of the ballmilling treatment (CNT-0, CNT-24 and CNT-72).

Then, 1.25 g of urea or 1.60 g of thiourea and 0.5 g of CNT-t were subjected to ballmilling for 24 h. The samples recovered were subjected to thermal treatment in a quartz tubular reactor at 800 °C with a heating ramp of 20 °C min^{-1} under an inert atmosphere of 25 mL min^{-1} of N_2 for 1 h.

2.2. Physicochemical characterization

Carbon, nitrogen, sulfur and hydrogen weight contents were measured with an elemental analyser (LECO CHNS-932). X-ray photoelectron spectra (XPS) were acquired with a VG Escalab 200 R spectrometer fitted with an Mg Kα (hυ = 1253.6 eV) 120 W X-ray source. The energy regions of the photoelectrons of interest were scanned until an acceptable signal-to-noise ratio was achieved. Intensities were estimated by calculating the integral of each peak after subtraction of the Shirley-type background and fitting of the experimental curve to a combination of Lorentzian and Gaussian lines of variable proportions. Accurate binding energies (±0.2 eV) were determined by setting the most intense C 1s peak at 284.6 eV.

Raman spectra were recorded in air using a single monochromator Renishaw system 1000 equipped with a thermoelectrically cooled CCD detector and holographic super-Notch filter. The samples were excited with the 532 nm Ar line. The instrument is internally calibrated with a silicon reference at 520 cm^{-1} and gives a peak position resolution of 1 cm^{-1}, the spectrum acquisition time was 10 s and 5 spectra were acquired to ensure an optimal signal to noise ratio.

Textural properties were derermined by recording N_2 adsorption–desorption isotherms of the samples at liquid N_2 temperature with a Micromeritics ASAP 2000 apparatus. Previous to recording the isotherms, samples were evacuated at 140 °C under vacuum for 24 h. Specific areas were calculated by applying the BET method within the relative pressure range P/P^0 = 0.05–0.30.

2.3. Electrochemical characterization

The electrochemical experiments were recorded with a computer controlled Autolab PGstat 302 N potentiostat/galvanostat. A standard three-compartment glass cell and a rotating disk electrode (RDE) (Pine research Intruments) were used. A graphite rod and a homemade RHE electrode were used as counter and reference electrodes, respectively.

A glassy carbon electrode with a thin film of the electrocatalyst under study was used as support for the working electrode. For the thin film preparation, samples were dispersed in a ultrasonic bath

for 10 min in a mixture of Millipore Milli Q® water, isopropyl alcohol (Aldrich, 99.8%) and Nafion (5 wt%) with a final ratio of 80, 18.8 and 0.2 vol%, respectively. The final concentration of the electrocatalyst in the suspension was of 6 $mg_{cat}\cdot mL^{-1}$. A volume of 20 μL of the suspension was pipetted onto the previously polished glassy carbon tip of the RDE.

Previous to the electrochemical testing, the working electrode was subjected to potentials excursions from 0.05 to 1.1 V *vs.* RHE and back for 50 cycles in Ar-saturated 0.1 M $HClO_4$ electrolyte. Cyclic voltammograms (CVs) were recorded between 0.05 and 1.03 V at 10 $mV\cdot s^{-1}$ in Ar-saturated 0.1 M $HClO_4$.

The ORR polarization curves were collected by means of the RDE technique between 0.05 V and 1.03 V at 10 $mV\cdot s^{-1}$ and 1600 rpm in O_2-saturated 0.1 M $HClO_4$ electrolyte. The Faradaic current density (j_F $mA\cdot cm^{-2}$) was obtained by subtracting the current obtained during the anodic sweep scan in the O_2-saturated electrolyte from the capacitive current (density) obtained in the potential sweep recorded in Ar-saturated O_2-free electrolyte under the same experimental conditions. The ORR kinetic current (i_k) was calculated from the Kouteky-Levich equation ($i_k = -i_F \cdot i_{lim}/(i_F - i_{lim})$) where i_K is the kinetic current and i_{lim} is the limiting current. Finally, the ORR mass activity is defined by $i_M = -i_K/m_{cat}$ where m_{cat} is the catalyst loading expressed in grams [33].

H_2O_2 production was recorded by using a rotating ring disk electrode (RRDE) under the same experimental conditions as reported above for the RDE experiments, *i.e.*, recording a linear sweep voltammetry scan beteen 0.05 V and 1.03 V at 10 $mV\cdot s^{-1}$ and 1600 rpm in O_2-saturated 0.1 M $HClO_4$ while appliying a constant ring potential of 1.2 V. The fraction of H_2O_2 produced was calculated according to Eq. (1):

$$X_{H_2O_2} = \frac{2I_R/N}{I_D + I_R/N} \quad (1)$$

where I_D is the disk current and I_R is the ring current and using a ring efficiency (N) of 26% [34].

3. Results and discussion

Fig. 1a and b show the Raman spectra for the N/CNT-t and S/N/CNT-t catalysts. The spectrum of CNT is shown in Fig. 1a for comparison. The graphitic character and the amount of defects of CNTs can be estimated by determining the relative intensity of the D and G bands which appear at ca. 1350 cm^{-1} and 1580 cm^{-1} in the Raman spectra of carbon materials [35]. It is well admitted that the G band is characteristic of graphitic lattice vibration mode whereas D and D′ (a band which appears as a shoulder to the G band at ca. 1620 cm^{-1}) bands are attributed to defects in the graphite plane. A further band at ca. 2710 cm^{-1}, usually referred to as 2D band, is also related to the presence of defects and its intensity increases with the number of defects. The most relevant ways to assess the creation of defects in the graphitic structure of CNTs would be comparing the relative intensity of the D, G and 2D bands. In principle, the generation of defects would lead to an increasing of the I_D/I_G ratio but to a decrease of the I_{2D}/I_G ratio.

As shown in Fig. 1a, the intensity of the G band in the spectra of N/CNT-t samples decreases in the order N/CNT-0 > N/CNT-24 > N/CNT-72 whereas the intensity of the D band remains roughly constant. This trend clearly indicates that the number of defects created on CNTs increases with the duration of the ballmilling treatment. The Raman spectra for the S/N/CNT-t samples are shown in Fig. 1b. First, it can be observed signal/noise ratio of the spectra is lower than that of the spectra shown in Fig. 1a. In addition, a marked decrease of the G band for the samples subjected to longer ballmilling periods is observed. The most significant feature of the Raman spectra for the S/N/CNT-t catalyst is a visible broadening of the D and G bands with respect to the spectra recorded for N/CNT-t samples. This effect can be indicative of the incorporation of higher amounts of heteroatoms, N and S, in the CNTs when using thiourea as precursor resulting in a more significant distortion of the graphitic structure of the S co-doped S/N/CNT-t catalysts.

Table 1 shows the textural properties of the N/CNT-t and S-N/CNT-t catalysts. Clearly, the specific surface area of the catalysts increases with the duration of the ballmilling treatment but is not

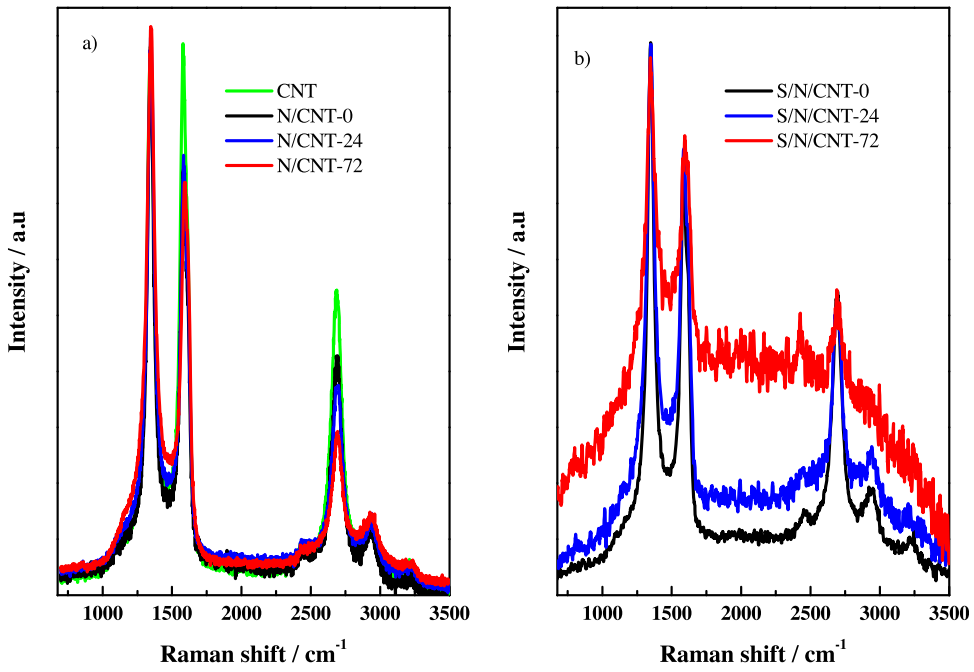

Fig. 1. Raman spectra recorded for a) N/CNT-t and b) S/N/CNT-t catalysts. The spectrum of the fresh CNT is included for comparison. (For interpretation of the references to color in this figure legend, the reader is referred to the web version of this article.)

Table 1
BET area, external surface and micropore surface area of the catalysts under study.

Sample	BET surface area/ $m^2 g^{-1}$	External area/ $m^2 g^{-1}$	Micropore area/$m^2 g^{-1}$
N/CNT-0	229	227	3
S/N/CNT-0	247	247	–
N/CNT-24	237	228	9
S/N/CNT-24	250	245	5
N/CNT-72	392	283	109
S/N/CNT-72	374	314	60

Table 2
C, N, H and S contents and N/C and S/C atomic ratios determined by elemental analysis.

Sample	Weight content (wt.%)				S/C atomic ratio[a]	N/C atomic ratio[a]
	C	H	N	S		
N/CNT-0	93.91	0.14	0.66	0.01	0.00004	0.0060
S/N/CNT-0	93.33	0.16	1.15	0.62	0.00260	0.0106
N/CNT-24	90.76	0.26	1.23	0.01	0.00004	0.0116
S/N/CNT-24	87.95	0.33	2.25	0.73	0.00290	0.0219
N/CNT-72	89.12	0.58	1.75	0.03	0.00010	0.0168
S/N/CNT-72	82.93	0.54	3.43	1.47	0.00660	0.0355

[a] Derived from the actual weight contents.

significantly affected by the incorporation of N and S into the final catalyst. BET surface values remain roughly constant, between 229 and 250 $m^2 g^{-1}$ for the catalysts subjected to ballmilling periods of up to 24 h. The formation of micropores is not observed for these catalysts. On the other hand, a remarkable increasing of the BET surface area is observed for samples subjected to longer ballmilling treatments of 72 h (N/CNT-72 and S/N/CNT-72), and ascribed to the formation of micropores during long ballmilling treatments. This observation coincides with our previous report about the effect of the duration of ballmilling treatment of CNTs [17], showing that the number of defects increases with the duration of the treatment without severe repercussions in carbon nanotubes' morphology for treatments below 48 h. However, extending the duration beyond 72 h results in the collapse of the nanotube structure and amorphous carbon is formed. Irrespectively of the duration of the treatment, it is obvious that the presence of defects promotes the incorporation of N into the C-C network, as deduced from the N and S contents reported in Table 2.

As shown in Table 2, the amount of N incorporated into the catalysts increases with the duration of the ballmilling treatment of the CNTs. Since the amount of defects on the CNTs increases with the duration of the ballmilling process, see Raman spectra in Fig. 1, it is reasonable to conclude that defect sites in the C—C network are prone to incorporate N atoms by forming C—N bonds. The incorporation of S into the S/N/CNT samples follows a similar trend and S content is higher in the CNTs that were subjected to longer ballmilling treatments. Remarkably, the results shown in Table 2 also shows a two fold increase of the N content in the catalysts prepared with thiourea with respect to the ones prepared by using urea as N precursor. This trend indicates that the incorporation of N is promoted by the presence of S during the synthesis of the catalyst.

In order to determine the chemical state and surface abundance of C, Fe, N and S in the catalysts the C 1s, N 1s, Fe 2p and S 2p core-level spectra of all samples under study were recorded. Fig. 2 shows the N 1s core level-regions of the samples under study.

In line with previous reports, the N 1 s core-level region spectra of all samples records a broad band which contains the contribution of four N species; pyridinic-N at 398.5 eV, pyrrolic-N at 400.1 eV, graphitic-N at 401–401.5 eV and oxidized-N at 403.4–404 eV. As shown in Table 3, and in good agreement data shown in Table 2, the surface abundance of N and S is higher for the samples prepared by subjecting CNTs to longer ballmilling treatments. In addition, it seems like the presence of S promotes the incorporation of N into the final catalysts, especially the ones subjected to longer ballmilling treatments S/N/CNT-72. Conflicting results about the effect of the presence of S for the incorporation of N into C—C have been reported. On the one hand, some authors claim that the presence of S results in a lower incorporation of N the graphitic material [30,31]. However, some authors find that the presence of S leads to a higher incorporation of N into the C—C network [36]. Our results clearly show that using precursors containing both S and N leads to materials with higher amounts of N incorporated into the carbon matrix. As shown in Table 2, the atomic N/C ratio is ca. 2 times higher for the S-doped N/CNT-t than for N/CNT-t catalysts. This trend is also fulfilled if the surface atomic ratio derived from XPS (rather than the total atomic ratio shown in Table 2) are analyzed. As shown in Table 3, the amount of surface N (N/C surface atomic ratio) increase upon the incorporation of S into the catalysts. However, this trend is not observed for the CNT-0 series.

On the other hand, results shown in Table 3 illustrate how the relative abundance of the different N species (pyridinic, pyrrolic, graphitic and oxide) remains almost invariable in all samples irrespectively of the N precursor employed during the synthesis. These results indicate that the presence of S plays a strong influence in the total amount of N, but has no visible effect of the distribution of the N-species.

The S 2p and Fe 2p core-level regions of the samples under study are shown in Fig. 3a and b, respectively. The S 2p core-level spectra of all samples can be deconvoluted into two peaks at ca. 164.4 eV and 168.7 eV ascribed to —C—S—C— (*i.e.*, S^{2-}) and SO_4^{-2} species, respectively. The former species have been identified previously by other authors as the one responsible for the increasing ORR activity in alkaline media [30,37,38]. On the other hand, it is known that SOx groups are not active for the ORR [30]

Table 3
Surface abundance of N, Fe and O species and relative distribution of N species in the catalysts.

Sample	Surface atomic ratios				abundance of surface N species			
	Fe/C	N/C	O/C	S/C[a]	$N_{pyridinic}$	$N_{pyrrolic}$	$N_{graphitic}$	N_{oxide}
N/CNT-0	0.0006	0.019	0.045	–	0.51	0.28	0.08	0.13
S/N/CNT-0	0.0011	0.014	0.048	0.0018 (0.0010)[b]	0.59	0.30	0.11	0.00
N/CNT-24	0.0009	0.017	0.047	–	0.57	0.30	0.10	0.02
S/N/CNT-24	0.0031	0.028	0.063	0.0028char_curly (0.0015)[b]	0.59	0.26	0.12	0.03
N/CNT-72	0.0012	0.019	0.062	–	0.51	0.30	0.14	0.04
S/N/CNT-72	0.0029	0.038	0.095	0.0045char_curly (0.0030)[b]	0.51	0.34	0.11	0.04

[a] S/C ratio including all S-species.
[b] atomic ratio of S as —C—S—C— species.

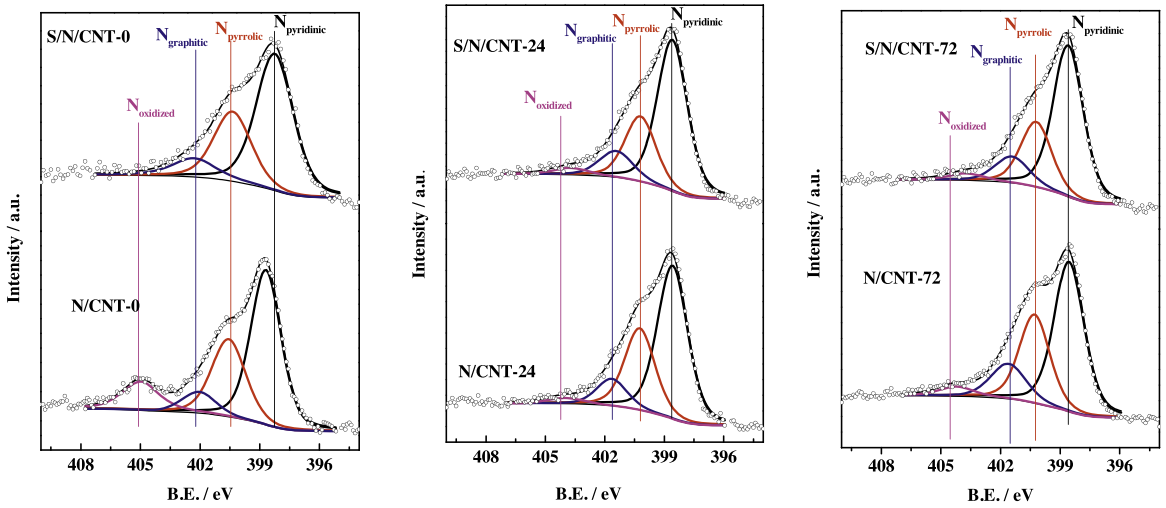

Fig. 2. N 1s core-level spectra (circles) recorded for all catalysts as indicated in the figure. Peaks for N-pyridinic, N-pyrrolic, N-quaternary and oxidized N are shown in black, red, blue and magenta, respectively. (For interpretation of the references to color in this figure legend, the reader is referred to the web version of this article.)

and in fact, the presence of sulfates is detrimental for the ORR activity with Fe/N/C catalysts [39] As shown in Table 3, the content of S decreases in the order S/N/CNT-72 > S/N/CNT-12 > S/N/CNT-0. This trend is due to the increasing formation of —C—S—C—, since as shown in Table 3 the fraction of SO_4^{2-} species remains constant in all S/N/CNT-t samples.

The binding energy of Fe $2p^{3/2}$ core-level region of the samples shows a broad peak centered at ca. 711 eV which can be assigned to iron oxidized species, typically Fe^{2+} or/and Fe^{3+} [40]. Generally, the presence of a shake-up satellite peak at ca. 719 eV is characteristic of Fe^{3+} species, whereas it appears at ca. 715.5 eV for Fe^{2+} species. However, the spectra shown in Fig. 3 lacks of any of such satellite peaks. Previous studies have reported that the XP spectrum of Fe_3O_4 lacks of the characteristic satellite peaks for Fe^{2}+ or Fe^{3+} species [41,42] and as a consequence the Fe peaks observed in Fig. 3b have been assigned the presence of Fe_3O_4 species. It should be remarked that these Fe species are not stable acid media and they lack for ORR activity in alkaline electrolytes [43]. Finally, it should be noted that the amount of Fe actually incorporated on the surface of the samples after ballmilling is very low, of ca. one order of magnitude lower than that of N, see Table 3.

As observed from Table 3, the amount of S incorporated as —C—S—C— species in the catalysts ranges between 0.10 and 0.30 at.%. These values are in line with previous reports about the incorporation of S into CNTs [31] which report S atomic contents of 0.18%, but significantly beyond than other works based upon carbon foams which report S and N atomic contents of ca. 2.9% and 6.5%, respectively [44].

The activity of all catalysts for the ORR was determined by recording cyclic voltammograms in O_2 saturated acid electrolyte until the obtained response was stable. Fig. 3a shows the

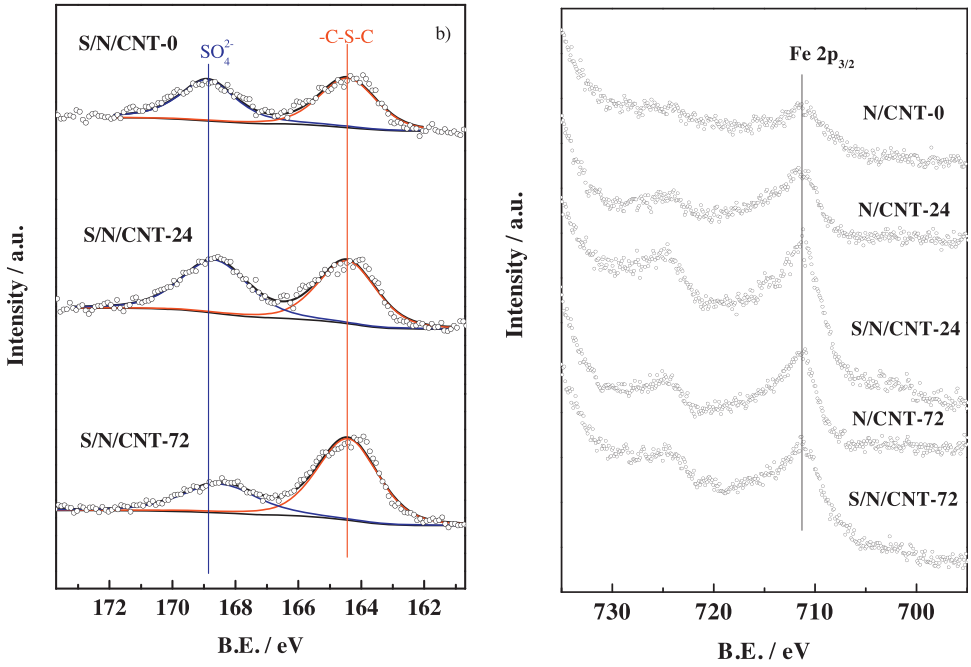

Fig. 3. a) XPS of the S 2p core-level region showing the presence of two types of S species, —C—S—C— (red peaks) and sulfates (blue peaks). b) Fe 2p core-level XP spectra for the samples under study. (For interpretation of the references to color in this figure legend, the reader is referred to the web version of this article.)

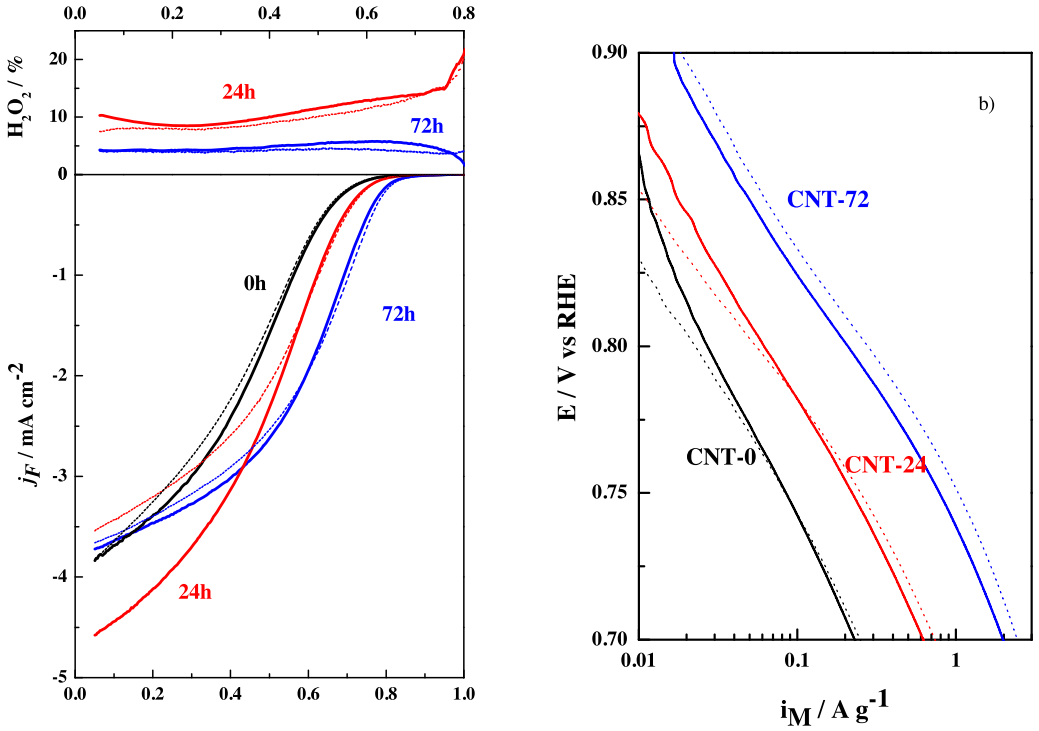

Fig. 4. a) upper panel, positive going sweep with N/CNT-t (straight lines) and S/N/CNT-t (dotted lines) recorded in O_2 saturated 0.1 M $HClO_4$ at 10 mV s^{-1}; lower panel, H_2O_2 production recorded during the ORR by setting the ring E at 1.2 V. b) i_M for the catalysts under study recorded under the same experimental conditions. Blue, red and black lines are for CNT-72, CNT-24 and CNT-0 series.

polarization curves for all samples recorded during the positive going sweep in O_2 saturated 0.1 M $HClO_4$ electrolyte at 10 mV·s^{-1} and 1600 rpm after subtraction of the corresponding capacitive curves recorded under the same experimental conditions only in Ar-saturated electrolytes. E_{onset} and mass-activity measured at 0.8 V are characteristic parameters to define catalytic performances for the ORR of NPMCs. As shown in Fig. 4a, both the onset potentials for the ORR (defined as the potential at which $j_F = 0.1$ mA cm^{-2} [14]) and mass activity at 0.8 V shift to more positive values with the increasing content of N in the catalysts. It can be observed in Fig. 3a that the catalysts do not reach the current limit value expected from the rotation rate at 1600 rpm. This feature, which is usually observed when measuring the activity for the ORR of NMPCs in acid media [45,46], can be indicative of the preferential reduction of O_2 via $2e^-$ pathway instead of the more desired $4e^-$ pathway, *i.e.*, the preferential production of H_2O_2 instead of H_2O. The formation of H_2O_2 has been evaluated with a RRDE experiment by setting the potential of the ring at 1.2 V while recording the ORR. As shown in Fig. 4a (upper panel) the formation of H_2O_2 is clearly observed with all catalysts under study. The production of H_2O_2 with the S/N/CNT-24 and N/CNT-24 is higher than that recorded for S/N/CNT-72 and N/CNT-72, around 10% and 5% respectively. Although it has been reported that the actual production of H_2O_2 in acid media with N/C or Fe/N/C increases with the decreasing loading of catalyst on the electrodes [46,47], similar % H_2O_2 values have been reported during the measurement of the ORR in acid media with N-MWCNTs using high catalysts loading on the electrodes; 0.6 mg cm^{-2} in our work vs 0.8 mg cm^{-2} in ref [46]. On the other hand, the lower production of H_2O_2 with the catalysts subjected to 72 h of ballmilling can be ascribed to the presence of micropores [17]. It should be noted also that the presence of S in the catalysts has a marginal effect for the production of H_2O_2.

The effect of the presence of S in the catalysts is more clearly observed in mass-activities are reported. Fig. 4b clearly shows that the mass activities (i_M) for the ORR increase, almost linearly, with the increasing amount of N actually incorporated into the N/CNT-t catalysts. On the other hand, the effect of S co-doping for the ORR is not straightforward. Thus, a visible improvement (more positive E_{onset} and i_M at 0.8 V) in the ORR activity of S/N/CNT-72 *vs* N/CNT-72 is clearly observed in Fig. 4b. For instance, at 0.8 V, i_M values of 0.25 and 0.19 A g^{-1} are recorded for S/N/CNT-72 and N/CNT-72, respectively, which is an increase in the ORR activity of ca. 30% for the catalyst co-doped with S and N. In fact, S/N/CNT-72 records the highest i_M in the series. In principle this trend can be explained by taking into account that the amounts of N (and S) in N/CNT-72 and S/N/CNT-72 are the highest in the series.

On the other hand, the expected promotional effect of S for the ORR with S/N/CNT-0 and S/N/CNT-24 is not observed. The apparent lack of promotional effect for the ORR observed for S/N/CNT-0 and S/N/CNT-24 *vs* the S-free counterparts can be rationalized in terms of the actual surface content of N in these catalysts. As shown in Table 3, the surface N/C ratio of N/CNT-0 and S/N/CNT-0 is almost the same. On the other hand, the N/C surface atomic ratio of S/N/CNT-24 is only slightly higher than that of N/CNT-24 and as a consequence the promotional effect of the presence of S is less evident. In fact, a careful inspection of Fig. 4b shows that the mass current (i_M) recorded for S/N/CNT-24 are higher than that recorded for S/CNT-24 at potentials less positive than 0.75 V.

As shown above, the surface atomic content of N (see N/C surface atomic ratio in Table 3) in S/N/CNT-72 is ca. 2 times higher than in N/CNT-72 and as a consequence the ORR activity is of around 30% higher in the S co-doped sample. This increasing is somehow lower than the expected, since as stated above the S co-doped samples contains 100% higher amount of surface N atoms than that of N/CNT-72. Moreover, it should be also noted that the promotional effect of the incorporation of S for the ORR shown in this work is smaller than that reported in previous works for S-doped Fe/N/C catalysts for the ORR measured in alkaline media, but similar to that found for S/N/CNT measured in acid media [31]. The ORR activity of the catalysts

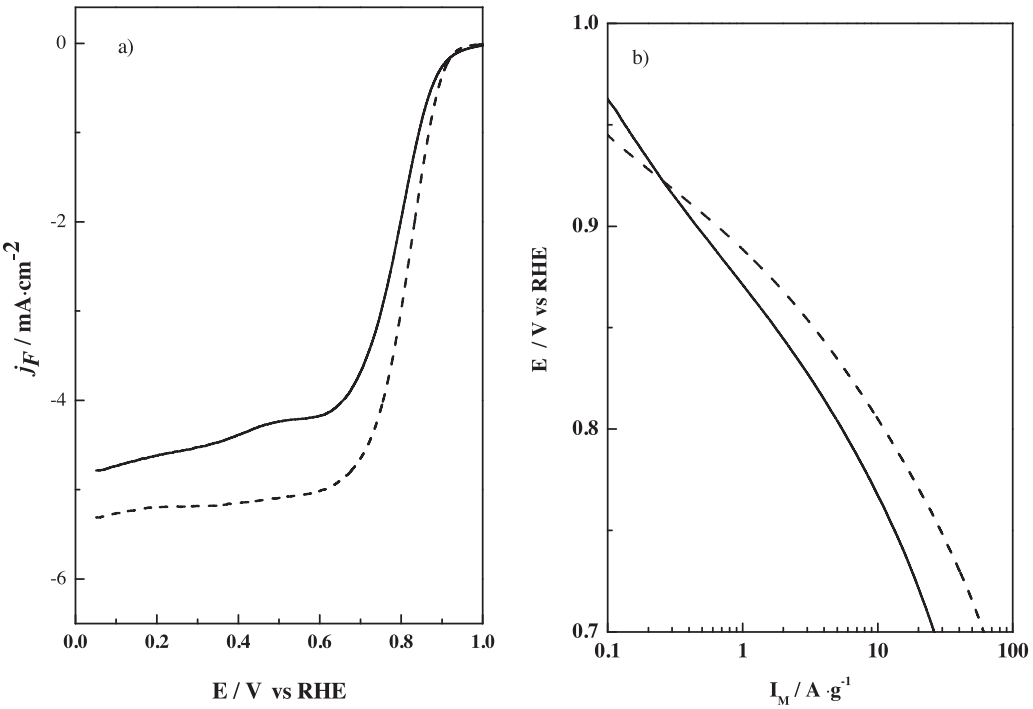

Fig. 5. a) Faradaic current densities (j_F) recorded during the positive going sweep with N/CNT-t (straight lines) and S/N/CNT-t (dotted lines) in O_2 saturated 0.1 M KOH at 10 mV s^{-1}. b) Mass current densities (i_M) derived from Fig. 5a.

prepared with CNT-72 has been also evaluated in alkaline medium. Fig. 5a and 5b show the ORR polarization curves and the i_M for N/CNT-72 and S/N/CNT-72 recorded in 0.1 M KOH. First, it can be observed that the ORR activity of both catalysts is higher than that recorded in acid medium. For instance, E_{onset} for the ORR in acid media is of 0.81 V for both N/CNT-72 and S/N/CNT-72, shifting to ca. 0.93 V in alkaline electrolyte. In the same way, i_M at 0.8 V values of 0.19 and 0.25 A g^{-1} are recorded in acid for N/CNT-72 and S/N/CNT-72, respectively. When measured in alkaline, i_M @ 0.8 V values of 5.1 and 10.5 A g^{-1} are recorded for N/CNT-72 and S/N/CNT-72, respectively. Thus, the i_M for the ORR of S/N/CNT-72 is ca. 100% higher than that of N/CNT-72, indicating that the promotional effect is more relevant in alkaline medium than in acidic one.

Our results clearly show that the ORR activity of (S)/N/CNT-t catalysts increases with the increasing surface N content in the catalysts, both in acid and in alkaline media. The effect of S is, however, unclear. Co-doping with S promotes N incorporation into C—C network, especially in amorphous carbon. On the other hand, the presence of S seems to have no direct effect for the ORR at least when its surface concentration is low. Finally, the promotional effect of S is more evident when measured in alkaline medium since not only higher mass current are recorded with all catalysts but the increasing of the ORR activities due to the presence of S are more significant than in acid media. These results clearly indicate that the ORR proceeds by following different pathways in acidic and in alkaline electrolytes. Whereas at low pH it seems like the N content is the only relevant parameter for the ORR, the presence of S seems also to play a role for the ORR in alkaline media.

4. Conclusions

The incorporation of N and S takes place in defect sites in the C—C network of CNTs. When the graphitic structure of CNTs collapses, the amount of N actually incorporated into the C—C network can be increased by co-doping with S. The ORR activity of N/CNT increases with the increasing content of N in the catalysts, both in acid and alkaline media. As a consequence, co-doping with S results in more active catalysts for the ORR in acid media provided S promotes the incorporation of surface N.

Acknowledgements

This project was funded by the Deanship of Scientific Research (DSR), King Abdulaziz University, Jeddah, under grant number (D-006-432). The authors, therefore, acknowledge with thanks DSR technical and financial support. Economic support from project ENE2013-42322-R from the Spanish Ministry of Economy and Competitiveness is also acknowledged.

References

[1] N.V. Long, Y. Yang, C. Minh Thi, N.V. Minh, Y. Cao, M. Nogami, The development of mixture, alloy, and core-shell nanocatalysts with nanomaterial supports for energy conversion in low-temperature fuel cells, Nano Energy 2 (2013) 636–676.
[2] P. Hernández-Fernández, S. Rojas, P. Ocón, J.L.G. de la Fuente, P. Terreros, M.A. Peña, J.L. García-Fierro, An opening route to the design of cathode materials for fuel cells based on PtCo nanoparticles, Applied Catalysis B: Environmental 77 (2007) 19–28.
[3] H. Gasteiger, S. Kocha, B. Sompalli, F. Wagner, Activity benchmarks and requirements for Pt, Pt-alloy, and non-Pt oxygen reduction catalysts for PEMFCs, Applied catalysis. B Environmental 56 (2005) 9–35.
[4] F. Jaouen, E. Proietti, M. Lefèvre, R. Chenitz, J.-P. Dodelet, G. Wu, H. Chung, C. Johnston, P. Zelenay, Recent advances in non-precious metal catalysis for oxygen-reduction reaction in polymer electrolyte fuel cells, Energy & environmental science 4 (2011) 114–130.
[5] X. Zhou, J. Qiao, L. Yang, J. Zhang, A review of graphene-based nanostructural materials for both catalyst supports and metal-free catalysts in PEM fuel cell oxygen reduction reactions, Advanced Energy Materials 4 (2014) .
[6] G. Liu, X. Li, J.W. Lee, B.N. Popov, A review of the development of nitrogen-modified carbon-based catalysts for oxygen reduction at USC, Catalysis Science and Technology 1 (2011) 207–217.
[7] R. Othman, A.L. Dicks, Z. Zhu, Non precious metal catalysts for the PEM fuel cell cathode, International Journal of Hydrogen Energy 37 (2012) 357–372.
[8] M. Lefèvre, J.P. Dodelet, Recent advances in non-precious metal electrocatalysts for oxygen reduction in PEM fuel cells, ECS Transactions, (2012) , pp. 35–44.

[9] C.W.B. Bezerra, L. Zhang, K. Lee, H. Liu, A.L.B. Marques, E.P. Marques, H. Wang, J. Zhang, A review of Fe–N/C and Co–N/C catalysts for the oxygen reduction reaction, Electrochimica Acta 53 (2008) 4937–4951.
[10] B. Merzougui, A. Hachimi, A. Akinpelu, S. Bukola, M. Shao, A Pt-free catalyst for oxygen reduction reaction based on Fe–N multiwalled carbon nanotube composites, Electrochimica Acta 107 (2013) 126–132.
[11] E. Proietti, F. Jaouen, M. Lefèvre, N. Larouche, J. Tian, J. Herranz, J.-P. Dodelet, Iron-based cathode catalyst with enhanced power density in polymer electrolyte membrane fuel cells, Nature communications 2 (2011) 416.
[12] L. Lin, Q. Zhu, A.W. Xu, Noble-Metal-Free Fe-N/C Catalyst for Highly Efficient Oxygen Reduction Reaction under Both Alkaline and Acidic Conditions, Journal of the American Chemical Society 136 (2014) 11027–11033.
[13] H. Chung, J. Won, P. Zelenay, Active and stable carbon nanotube/nanoparticle composite electrocatalyst for oxygen reduction, Nature communications 4 (2013) 1922.
[14] G. Wu, K.L. More, C.M. Johnston, P. Zelenay, High-performance electrocatalysts for oxygen reduction derived from polyaniline, iron, and cobalt, Science 332 (2011) 443–447.
[15] M. Ferrandon, A.J. Kropf, D.J. Myers, K. Artyushkova, U. Kramm, P. Bogdanoff, G. Wu, C.M. Johnston, P. Zelenay, Multitechnique Characterization of a Polyaniline–Iron–Carbon Oxygen Reduction Catalyst, The Journal of Physical Chemistry C 116 (2012) 16001–16013.
[16] N. Ramaswamy, S. Mukerjee, Fundamental Mechanistic Understanding of Electrocatalysis of Oxygen Reduction on Pt and Non-Pt Surfaces: Acid versus Alkaline Media, Advances in Physical Chemistry 2012 (2012) 1–17.
[17] C. Domínguez, F.J. Pérez-Alonso, M. Abdel Salam, S.A. Al-Thabaiti, A.Y. Obaid, A.A. Alshehri, J.L. Gómez de la Fuente, J.L.G. Fierro, S. Rojas, On the relationship between N content, textural properties and catalytic performance for the oxygen reduction reaction of N/CNT, Applied Catalysis B: Environmental 162 (2015) 420–429.
[18] T. Hibino, K. Kobayashi, P. Heo, Oxygen reduction reaction over nitrogen-doped graphene oxide cathodes in acid and alkaline fuel cells at intermediate temperatures, Electrochimica Acta 112 (2013) 82–89.
[19] A. Dorjgotov, S.-H. Yoon, J. Ok, Y.G. Shul, Y. Jeon, Activity and active sites of nitrogen-doped carbon nanotubes for oxygen reduction reaction, Journal of Applied Electrochemistry 43 (2013) 387–397.
[20] C. Choi, M. Chung, H. Kwon, J. Chung, S. Woo, Nitrogen-doped graphene/carbon nanotube self-assembly for efficient oxygen reduction reaction in acid media, Applied catalysis. B Environmental 144 (2014) 760–766.
[21] J. Tian, A. Morozan, M.T. Sougrati, M. Lefèvre, R. Chenitz, J.P. Dodelet, D. Jones, F. Jaouen, Optimized synthesis of Fe/N/C cathode catalysts for PEM fuel cells: A matter of iron-ligand coordination strength, Angewandte Chemie - International Edition 52 (2013) 6867–6870.
[22] U.I. Kramm, J. Herranz, N. Larouche, T.M. Arruda, M. Lefevre, F. Jaouen, P. Bogdanoff, S. Fiechter, I. Abs-Wurmbach, S. Mukerjee, J.P. Dodelet, Structure of the catalytic sites in Fe/N/C-catalysts for O2-reduction in PEM fuel cells, Physical chemistry chemical physics: PCCP 14 (2012) 11673–11688.
[23] D. Singh, J. Tian, K. Mamtani, J. King, J.T. Miller, U.S. Ozkan, A comparison of N-containing carbon nanostructures (CNx) and N-coordinated iron–carbon catalysts (FeNC) for the oxygen reduction reaction in acidic media, Journal of Catalysis 317 (2014) 30–43.
[24] U. Tylus, Q. Jia, K. Strickland, N. Ramaswamy, A. Serov, P. Atanassov, S. Mukerjee, Elucidating oxygen reduction active sites in pyrolyzed metal-nitrogen coordinated non-precious-metal electrocatalyst systems, Journal of Physical Chemistry C 118 (2014) 8999–9008.
[25] S. Yasuda, L. Yu, J. Kim, K. Murakoshi, Selective nitrogen doping in graphene for oxygen reduction reactions, Chemical communications (London. 1996) 49 (2013) 9627–9629.
[26] F.J. Pérez Alonso, M.A. Salam, T. Herranz, J.L. Gómez de la Fuente, S.A. Al Thabaiti, S.N. Basahel, M.A. Peña, J.L.G. Fierro, S. Rojas, Effect of carbon nanotube diameter for the synthesis of Fe/N/multiwall carbon nanotubes and repercussions for the oxygen reduction reaction, Journal of power sources 240 (2013) 494–502.
[27] F. Jaouen, M. Lefèvre, J.P. Dodelet, M. Cai, Heat-treated Fe/N/C catalysts for O2 electroreduction: Are active sites hosted in micropores? Journal of Physical Chemistry B 110 (2006) 5553–5558.
[28] G. Wu, K.L. More, P. Xu, H.L. Wang, M. Ferrandon, A.J. Kropf, D.J. Myers, S. Ma, C.M. Johnston, P. Zelenay, A carbon-nanotube-supported graphene-rich non-precious metal oxygen reduction catalyst with enhanced performance durability, Chemical communications 49 (2013) 3291–3293.
[29] I. Herrmann, U.I. Kramm, J. Radnik, S. Fiechter, P. Bogdanoff, Influence of Sulfur on the Pyrolysis of CoTMPP as Electrocatalyst for the Oxygen Reduction Reaction, Journal of the Electrochemical Society 156 (2009) B1283.
[30] J. Liang, Y. Jiao, M. Jaroniec, S.Z. Qiao, Sulfur and nitrogen dual-doped mesoporous graphene electrocatalyst for oxygen reduction with synergistically enhanced performance, Angewandte Chemie 51 (2012) 11496–11500.
[31] Q. Shi, F. Peng, S. Liao, H. Wang, H. Yu, Z. Liu, B. Zhang, D. Su, Sulfur and nitrogen co-doped carbon nanotubes for enhancing electrochemical oxygen reduction activity in acidic and alkaline media, Journal of Materials Chemistry A 1 (2013) 14853.
[32] H.-X. Wu, R. Tong, X.-Q. Qiu, H.-F. Yang, Y.-H. Lin, R.-F. Cai, S.-X. Qian, Functionalization of multiwalled carbon nanotubes with polystyrene under atom transfer radical polymerization conditions, Carbon 45 (2007) 152–159.
[33] F. Jaouen, J. Herranz, M. Lefevre, J.P. Dodelet, U.I. Kramm, I. Herrmann, P. Bogdanoff, J. Maruyama, T. Nagaoka, A. Garsuch, J.R. Dahn, T. Olson, S. Pylypenko, P. Atanassov, E.A. Ustinov, Cross-laboratory experimental study of non-noble-metal electrocatalysts for the oxygen reduction reaction, ACS applied materials & interfaces 1 (2009) 1623–1639.
[34] U.A. Paulus, T.J. Schmidt, H.A. Gasteiger, R.J. Behm, Oxygen reduction on a high-surface area Pt/Vulcan carbon catalyst: a thin-film rotating ring-disk electrode study, Journal of Electroanalytical Chemistry 495 (2001) 134–145.
[35] J.-P. Tessonnier, D. Rosenthal, T. Hansen, C. Hess, M. Schuster, R. Blume, F. Girgsdies, N. Pfänder, O. Timpe, D. Su, R. Schlögl, Analysis of the structure and chemical properties of some commercial carbon nanostructures, Carbon 47 (2009) 1779–1798.
[36] R. Nie, X. Bo, C. Luhana, A. Nsabimana, L. Guo, Simultaneous formation of nitrogen and sulfur-doped carbon nanotubes-mesoporous carbon and its electrocatalytic activity for oxygen reduction reaction, International Journal of Hydrogen Energy 39 (2014) 12597–12603.
[37] Z. Yang, Z. Yao, G. Li, G. Fang, H. Nie, X. Liu, X.a. Chen, S. Huang, Sulfur-Doped Graphene as an Efficient Metal-free Cathode Catalyst for Oxygen Reduction, ACS Nano 6 (2012) 205–211.
[38] H. Wang, X. Bo, Y. Zhang, L. Guo, Sulfur-doped ordered mesoporous carbon with high electrocatalytic activity for oxygen reduction, Electrochimica Acta 108 (2013) 404–411.
[39] C. Domínguez, F.J. Pérez-Alonso, J.L. Gómez de la Fuente, S.A. Al-Thabaiti, S.N. Basahel, A.O. Alyoubi, A.A. Alshehri, M.A. Peña, S. Rojas, Influence of the electrolyte for the oxygen reduction reaction with Fe/N/C and Fe/N/CNT electrocatalysts, Journal of Power Sources 271 (2014) 87–96.
[40] T. Herranz, S. Rojas, M. Ojeda, F.J. Pérez-Alonso, P. Terreros, K. Pirota, J.L.G. Fierro, Synthesis, Structural Features, and Reactivity of Fe-Mn Mixed Oxides Prepared by Microemulsion, Chemistry of Materials 18 (2006) 2364–2375.
[41] T. Yamashita, P. Hayes, Analysis of XPS spectra of Fe^{2+} and Fe^{3+} ions in oxide materials, Applied Surface Science 254 (2008) 2441–2449.
[42] M. Muhler, R. Schlögl, G. Ertl, The nature of the iron oxide-based catalyst for dehydrogenation of ethylbenzene to styrene 2. Surface chemistry of the active phase, Journal of Catalysis 138 (1992) 413–444.
[43] Y. Su, H. Jiang, Y. Zhu, X. Yang, J. Shen, W. Zou, J. Chen, C. Li, Enriched graphitic N-doped carbon-supported Fe_3O_4 nanoparticles as efficient electrocatalysts for oxygen reduction reaction, Journal of Materials Chemistry A 2 (2014) 7281–7287.
[44] Z. Liu, H. Nie, Z. Yang, J. Zhang, Z. Jin, Y. Lu, Z. Xiao, S. Huang, Sulfur–nitrogen co-doped three-dimensional carbon foams with hierarchical pore structures as efficient metal-free electrocatalysts for oxygen reduction reactions, Nanoscale 5 (2013) 3283–3288.
[45] C.V. Rao, C.R. Cabrera, Y. Ishikawa, In Search of the Active Site in Nitrogen-Doped Carbon Nanotube Electrodes for the Oxygen Reduction Reaction, The Journal of Physical Chemistry Letters 1 (2010) 2622–2627.
[46] H.R. Byon, J. Suntivich, E.J. Crumlin, Y. Shao-Horn, Fe-N-modified multi-walled carbon nanotubes for oxygen reduction reaction in acid, Physical Chemistry Chemical Physics 13 (2011) 21437–21445.
[47] A. Bonakdarpour, M. Lefevre, R. Yang, F. Jaouen, T. Dahn, J.-P. Dodelet, J.R. Dahn, Impact of Loading in RRDE Experiments on Fe–N–C Catalysts: Two- or Four-Electron Oxygen Reduction? Electrochemical and Solid-State Letters 11 (2008) B105–B108.

Journal of Materials Chemistry A

PAPER

View Article Online
View Journal | View Issue

Cite this: J. Mater. Chem. A, 2015, 3, 24487

Effect of the N content of Fe/N/graphene catalysts for the oxygen reduction reaction in alkaline media†

Carlota Domínguez,[a] F. J. Pérez-Alonso,*[a] Mohamed Abdel Salam,[b] Shaeel A. Al-Thabaiti,[b] Miguel A. Peña,[a] L. Barrio[a] and S. Rojas*[a]

Received 15th June 2015
Accepted 5th November 2015

DOI: 10.1039/c5ta04355g

www.rsc.org/MaterialsA

In this work a series of N–modified graphene composites with different N/C ratios have been synthesised. The incorporation of Fe atoms into the N–modified graphene composites leads to the formation of Fe/N/C ensembles on the outer graphene layers along with Fe_3C and metallic Fe phases in the bulk of the graphite nanoplates as revealed by X-ray absorption and XPS analyses. The adequate choice of the N/C atomic ratio of precursors to prepare Fe/N/graphene based materials is crucial to obtain electrocatalysts with an optimal performance for the ORR. The activity for the oxygen reduction reaction (ORR) of the Fe/N–graphene based electrocatalysts increases with increasing amount of accessible nitrogen, that is, with the amount of nitrogen by surface area.

Introduction

Low temperature fuel cells are one of the most efficient and versatile environmentally friendly energy transformation devices. As a consequence, they are expected to play a chief role in several key energy related sectors including transportation and portable devices.[1] A crucial challenge which cannot be postponed for a longer time is the design and development of highly active and stable electrocatalysts based on cheap, earth-abundant elements.[2] The oxygen reduction reaction, which takes place at the cathode electrode, is the limiting reaction of proton exchange membrane fuel cells (PEMFCs). In order to overcome the sluggish kinetics of the ORR, high loadings of Pt group metals are used in the state-of-the-art PEMFCs, thus resulting in very expensive devices. This is in fact the bottleneck for the wider implementation of these devices.[3] In order to replace Pt in the cathode of PEMFCs, the use of non-precious metal catalysts (NPMCs) with high activity for the ORR has been proposed.[4–6] In addition, the transition from PEMFCs to anion exchange membrane fuel cells (AMFCs) is gaining growing interest and importance, mainly because the kinetics of the ORR are faster in alkaline than in acidic media.[7,8] As a consequence, NPMCs, instead of Pt-based ones, can be used as cathode electrodes in AMFCs.[9,10] Recently, several groups have developed electrocatalysts based on Fe/N/C or N/C structures, or metal oxides with ORR activities that match, or even exceed, the activity of Pt-based catalysts in alkaline media.[11–16] It is well admitted that the active sites for the ORR in Fe/N/C consist of Fe atoms coordinated to several N atoms incorporated into the C–C sp^2 network of graphitic materials such as active carbon, carbon nanotubes or graphene.[17,18] Fe/N/C catalysts are prepared by mixing Fe, N and C precursors followed by one or several thermal treatments under controlled atmospheres. As a consequence, it is expected that the nature of the precursors and of the thermal treatment atmosphere, either reactive or inert, would play a key role in the catalytic performance of the Fe/N/C catalysts for the ORR.[4]

Among the different carbon sources used to prepare NMPCs,[4] graphene based materials are the actual fashion members.[19–21] Due to its special 2D structure, graphene presents a series of features such as very high surface area, ultrahigh electrical conductivity, excellent mechanical properties and high thermal conductivity,[19] which are ideal for improving mass activity, mass transport properties and durability of Fe/N/C based catalysts for the ORR.

Several studies have reported the use of nitrogen–doped graphene or graphene/carbon-based support mixtures in order to obtaining electrocatalysts with high activity and stability for the ORR.[6,11,17,19,22–27] Some authors reported that the use of N precursors with high N/C ratio within their structure increases the amount of active sites for the ORR in Fe/N/C catalysts.[28] The use of metal phthalocyanines as metal precursors for the ORR has been reported.[29]

However, to the best of our knowledge, there is a lack of systematic studies that explore the influence of the relative

[a]Grupo de Energía y Química Sostenibles, Instituto de Catálisis y Petroleoquímica, CSIC, C/Marie Curie 2 L 10, 28049, Madrid, Spain. E-mail: srojas@icp.csic.es; fperez@icp.csic.es

[b]Chemistry Department, Faculty of Science, King Abdulaziz University, PO Box 80200, Jeddah 21589, Saudi Arabia

† Electronic supplementary information (ESI) available: X-ray diffractograms, comparison of ORR activity with Pt/C, graphene and Fe/N/graphene, H_2O_2 production from RRDE, K–L plots and CVs during conditioning. See DOI: 10.1039/c5ta04355g

amounts of the N and C precursors used during the synthesis of Fe/N/C catalysts and the influence of the N/C ratio in the final Fe/N/C catalysts for the ORR activity.

Herein, we explore the synthesis of Fe/N/graphene based electrocatalysts prepared by using commercially available graphene as the main source of carbon. 1,4,8,11-Tetraazacyclotetradecane and urea were used as the N source whereas iron phthalocyanine was used as the Fe source. Note that these precursors contribute as well as C and N sources. In particular, the objective of this study is to identify the optimal N/C ratio between N-precursors and the graphite matrix looking for optimizing the catalytic properties of Fe/N/graphene materials for the ORR in alkaline media.

Results and discussion

Table 1 shows the H, C and N contents of the electrocatalysts as determined by elemental analysis and their nomenclature, where the numeric suffix (*r*) in Fe/N/G-*r* indicates the nominal N/C atomic ratio of each catalyst. This value has been calculated considering all of the N and C atoms in the different precursors used for the synthesis of the final catalysts. As observed, the amount of nitrogen incorporated into the final catalyst increases with the increasing amount of nitrogen in the precursors used for their synthesis.

A comparison between the nominal and actual N/C values shown in Table 1 reveals that the amount of N actually incorporated into the catalysts is significantly lower than the targeted (nominal) value used for their synthesis. Table 1 also shows the BET, micropore and external surface area values obtained from the N_2 adsorption–desorption isotherms. The BET area values of the Fe/N/G catalysts range between *ca.* 100 and 300 $m^2\ g^{-1}$; these values are significantly smaller than the 718 $m^2\ g^{-1}$ of the pristine graphite nanoplate precursor. Table 1 also shows that the contribution of the external area to the total area of all catalysts is more significant than that of their micropore area, irrespective of the N/C ratio.

The Fe 2p, C 1s, N 1s and O 1s core-level region spectra of the Fe/N/G catalysts were recorded in order to estimate the relative surface abundance of these elements and to identify their chemical state. Fig. 1 shows the N 1s core-level spectra of the Fe/N/G catalysts. The spectra of all catalysts show a broad asymmetric peak which can be fitted to four peaks with maxima at BEs of 398.5, 400.1, 401–401.5 and 402–405 eV and assigned

Table 1 Nomenclature, C, H and N atomic contents and BET area of the catalysts under study. Micropore/external area values are shown in brackets

	Weight content/%			
Catalyst	C	H	N	BET/$m^2\ g^{-1}$
Fe/N/G-0.8	78.75	0.85	4.45	105 (30/75)
Fe/N/G-0.6	82.39	0.88	4.15	146 (64/82)
Fe/N/G-0.3	82.88	0.90	3.55	297 (91/206)
Fe/N/G-0.25	85.46	0.94	3.34	263 (80/183)

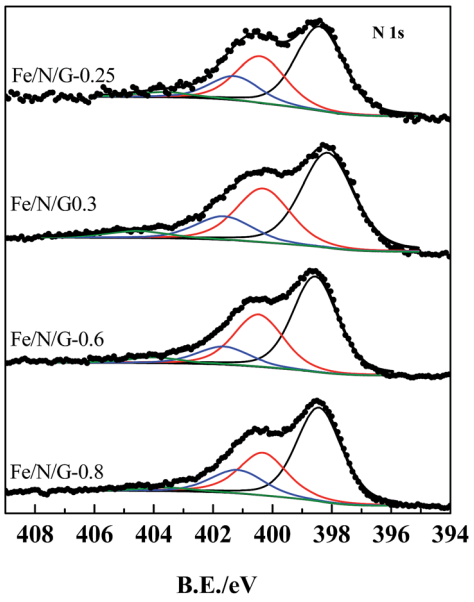

Fig. 1 N 1s core-level spectra of the Fe/N/G samples (open circles). Pyridinic, pyrrolic, graphitic and oxide species are shown in black, red, blue and green lines, respectively.

to pyridinic-*N*, pyrrolic-*N*, graphitic-*N* species and oxide-*N*, respectively.[30,31]

Fig. 2 shows the Fe 2p core-level spectra of the Fe/N/G catalysts. All spectra show two distinct peaks at *ca.* 711 and 724 eV corresponding to the Fe $2p_{3/2}$ and Fe $2p_{1/2}$ core-levels. The Fe $2p_{3/2}$ peak at around 711 eV is characteristic of iron oxidized species in oxides, typically Fe^{2+} or/and Fe^{3+}. The precise assignment of this peak is not straightforward and it is usually done from the analysis of the position of the characteristic shake-up satellite peaks of these iron species.[32] However, the

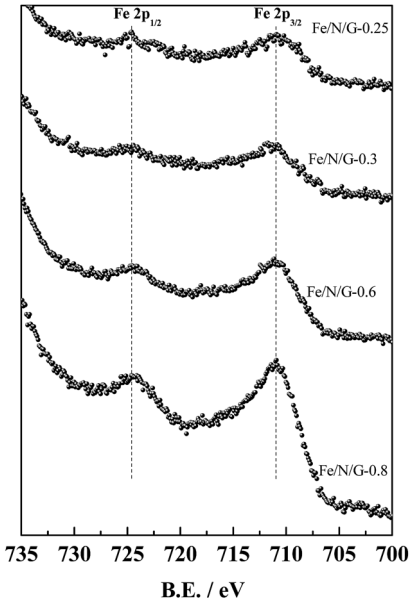

Fig. 2 Fe 2p core-level spectra of Fe/N/G based samples.

spectra shown in Fig. 2 lack the characteristic satellite peaks of Fe^{2+} (at *ca.* 715 eV) or Fe^{3+} (at *ca.* 719 eV) species. The lack of satellite peaks in the XP spectra of iron oxides is usually taken as an indication that both Fe^{2+} and Fe^{3+} species coexist in the sample, most likely in the form of the iron spinel Fe_3O_4.[33]

Nevertheless, it is also reported that the spectra of iron phthalocyanine[34] lack the characteristic satellite peaks of iron oxidized species, despite the fact that the BE of the Fe atoms is characteristic of iron oxidized species. The precise assignment of the iron species in the composites will be addressed below (see the X-ray absorption section).

The surface atomic N/C ratios of the catalysts are shown in Table 2. The atomic ratios derived from the XPS are in good agreement with the N and C contents derived from the elemental analyses. As observed, the N/C ratio increases with the increasing amount of N used for the synthesis of the catalysts. As expected, Fe/N/G-0.8 has the highest total N content (see Table 1) and the highest surface N/C atomic ratio in the series. As shown in Table 2, the N/C atomic ratios derived from chemical analyses are higher than the surface N/C atomic ratios obtained by XPS except for Fe/N/G-0.8. This observation indicates that N atoms are not located exclusively at the surface of the catalysts and in fact a fraction of the N atoms remain within the inner layers of the catalysts. As stated above, 4 types of N-species are detected in all catalysts. In all cases, pyridinic-*N* is the most abundant species, accounting for *ca.* 50% of all N atoms at the catalyst surface. The relative amounts of pyrrolic-*N*, graphitic-*N* and oxide-*N* species are also similar in all catalysts.

Table 2 also shows the relative surface atomic abundance of Fe (expressed as Fe/C or Fe/N) in the catalysts. As observed, the Fe/C ratio in the electrocatalysts increases in parallel with their increasing N (total and surface) content, increasing from 0.0016 in Fe/N/G-0.25 to 0.0059 in Fe/N/G-0.8. It should be recalled that the same amount of the iron precursor, *i.e.*, Fe-phthalocyanine has been used for the preparation of all electrocatalysts and that only the amount of urea and graphite nanoplates has been modified during catalyst preparation.

This trend clearly indicates that the incorporation of surface Fe species into the electrocatalysts is favoured by the presence of N atoms on the outmost graphene layers. This observation is in good agreement with the formation of FeN_x ensembles at the surface of the composites. It is not possible, however, at this stage to determine the actual stoichiometry of such ensembles, *i.e.*, the *x* value. It should be noted though that surface Fe/N atomic ratios are lower than 0.25, the value expected for FeN_4 ensembles, suggesting that N atoms not coordinated to Fe ones exist at the catalyst surface.

The powder X-ray diffractograms of the catalysts and of the pristine graphene precursor present the most intense diffraction line at *ca.* 26–27°, a position usually ascribed to the 002 planes of graphite like materials (Fig. S1†). Additionally, a set of weak diffraction lines between 40 and 50° usually ascribed to Fe_3C can be also observed. In addition, two very small diffraction peaks at 36° and 63° are observed in the diffractograms of Fe/N/G-0.8 and Fe/N/G-0.25 and attributed to the Fe_3O_4 phase. Interestingly, the diffractogram of Fe/N/G-0.6 also shows weak diffraction lines at *ca.* 43.5°, 50.8° and 74.7°, characteristic of iron nitride $FeN_{0.05}$ phases.

Clearly, the nature of the Fe species detected by XPS or by XRD is different. Thus, XPS results show the presence of iron oxidized species, most likely as FeN_x, but fail to show the presence of iron reduced species such as Fe_3C and $FeN_{0.05}$ which are observed by XRD. On the other hand, the X-ray diffractograms do not show reflections characteristic of FeN_x ensembles as in iron phthalocyanine. This discrepancy indicates that the bulk and surface composition of the catalysts are different and Fe_3C and $FeN_{0.05}$ phases (detected only by XRD) are encapsulated within the graphite platelets, hence out of the detection range of the XPS technique. On the other hand, the FeN_x-like species are located at the catalyst surface.

The nature of the iron species and their electronic state has been further studied by X-ray absorption spectroscopy. The XANES spectra of the catalysts under study are presented in Fig. 3. For the sake of comparison, the spectra of each catalyst are compared with the XANES spectra of the selected standards: Fe foil, Fe_3O_4, Fe_3C and iron phthalocyanine (FePhC).

The Fe *K*-edge XANES spectra are sensitive to the bulk oxidation state and local geometry of the sample under study. All Fe/N/G catalysts reported in this work have similar XANES spectra showing almost identical absorption edge positions. The spectral features are a mixture between those of the Fe_3O_4 and FePhC standards. A closer inspection of the energy region of the spectra between 7130 and 7170 eV by analysing its first derivate suggests that the iron species in the catalysts are more similar to those in FePhC than to the iron species in the other standards. This observation is more pronounced for the catalysts with lower N/C ratios. However, the presence of Fe_3O_4 phases cannot be ruled out.

Table 2 N/C, Fe/C, Fe/N and O/C surface atomic ratios and the relative atomic amount of N species derived from XPS analyses. *N/C atomic ratios calculated from the elemental analysis are shown in brackets

	Surface atomic content (XPS)				Relative atomic amount of N species			
Catalyst	N/C*	O/C	Fe/C	Fe/N	Pyridinic *N*	Pyrrolic *N*	Graphitic *N*	Oxide *N*
Fe/N/G-0.8	0.055 (0.048)	0.09	0.0059	0.107	0.54	0.28	0.16	0.02
Fe/N/G-0.6	0.036 (0.043)	0.10	0.0030	0.082	0.53	0.32	0.12	0.03
Fe/N/G-0.3	0.026 (0.037)	0.08	0.0020	0.077	0.52	0.30	0.14	0.04
Fe/N/G-0.25	0.021 (0.033)	0.10	0.0016	0.076	0.52	0.29	0.15	0.04

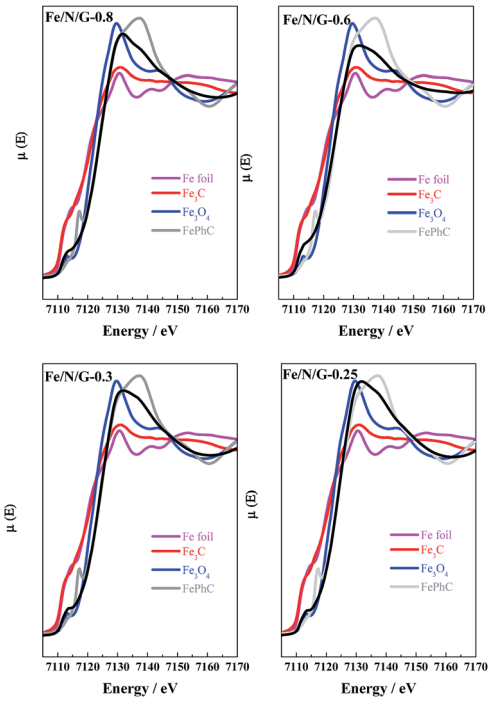

Fig. 3 Fe *K*-edge XANES spectra of all Fe/G/N-based electrocatalysts compared to the spectra of the standard materials, Fe foil, Fe_3C, Fe_3O_4 and FePhC.

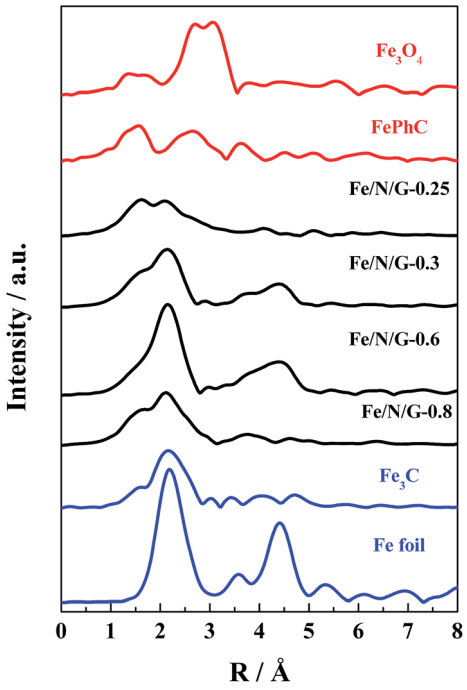

Fig. 4 Radial distribution obtained from EXAF spectra of Fe/N/G-0.8, Fe/N/G-0.6, Fe/N/G-0.3 and Fe/N/G-0.25 (black lines). Red lines correspond to spectra of reference materials, magnetite (Fe_3O_4) and iron phthalocyanine (FePhC), and blue lines correspond to spectra of cementite (F_3C) and iron foil (Fe^0).

Fig. 4 displays the phase uncorrected interatomic distances obtained by Fourier transformation of the EXAFS spectra over the *k*-space range between 3 and 14.5 $Å^{-1}$ of the catalysts studied in this work along with the signals of the Fe foil, Fe_3O_4, Fe_3C and FePhC standards. In good agreement with the XRD and XPS data, the spectra of the catalysts suggest that different Fe species are present in all catalysts. Two intense peaks at 1.6 and 2.1 Å are clearly observed in the spectra of all Fe/N/G catalysts. The first peak is consistent with a Fe–N or Fe–O distance, while the second peak corresponds to the first shell Fe–Fe distance in the metal foil or carbide phases. In addition, the spectra of Fe/N/G-0.6 and Fe/N/G-0.3 show a further intense peak at *ca.* 4.4 Å. This latter peak is assigned to the second shell Fe–Fe bond, observed in the spectra of the Fe foil standard, suggesting that Fe^0 is present in Fe/N/G-0.6 and Fe/N/G-0.3 catalysts. As stated above, the spectra of the Fe/N/G catalysts show an intense peak at *ca.* 1.6 Å. This peak also appears in the spectra recorded for the Fe_3C, Fe_3O_4 and iron phthalocyanine standards. However, the spectrum of the Fe_3O_4 standard shows a very intense peak with two maxima at *ca.* 2.7 and 3.1 Å, the second shell O–Fe–O distances, which are not observed in the spectra of the Fe/N/G catalysts. In view of the radial distribution shown in Fig. 4, the presence of the iron spinel phase in the Fe/N/G catalysts can be ruled out.

On the other hand, along with the peak at *ca.* 1.6 Å, the spectrum of the iron phthalocyanine standard records further peaks at *ca.* 2.6 and 3.6 Å due to backscattering corresponding to the eight carbon atoms of the pyrrole ring bonded to nitrogen and the four bridging nitrogen, respectively.[35] These peaks are, however, not clearly observed in the spectra of the Fe/N/G catalysts suggesting that Fe–N species in the catalysts are not identical to those in the Fe-phthalocyanine used as the reference.

The radial distribution obtained for the samples under study shows a complex mixture of phases in short range order that include Fe–N and Fe–Fe contributions, none of which shows order in a high range ($r > 5$ Å). Nonetheless, X-ray absorption spectra undoubtedly indicate the formation of FeN_x species in the catalysts since the intensity of the peak at 1.6 Å in the spectra of the Fe/N/G catalysts is clearly higher than that observed in the Fe_3C standard, being almost the same in some cases as that of the main peak at *ca.* 2.1 Å observed for that structure. However, a contribution of Fe–C bonds as in Fe_3C to the peak at *ca.* 1.6 Å cannot be ruled out.

The EXAFS spectra of the Fe/N/G catalysts show that, along with Fe^0, FeN_x and probably Fe_3C species are present in all catalysts, but their abundance varies with the actual N/C ratio in the catalyst. Remarkably, the catalyst with the lowest N/C ratio (Fe/N/G-0.25) has the highest fraction of Fe atoms in FeN_x ensembles in the series, with a peak at 1.6 Å as intense as the peak at 2.1 Å assigned to Fe–Fe bonds (1^{st} shell). On the other hand, the relative intensity of the peak at 1.6 Å as compared to that at 2.1 Å in the spectra of Fe/N/G-0.3 and Fe/N/G-0.6 suggests that the fraction of Fe atoms in FeN_x ensembles in these catalysts is lower than that in Fe^0 or Fe_3C phases.

The X-ray absorption spectra clearly identify the presence of zero valence Fe species (metallic Fe and/or Fe_3C) in the

catalysts. However, such Fe^0 species have not been detected in the XPS analysis of the catalysts, neither in the Fe 2p nor in the C 1s core-level regions. The lack of evidence of such species in the XPS spectra indicates that Fe^0 species are not located at the surface of the catalysts and that they are probably encapsulated within the carbon matrix. On the other hand, Fe-oxidized species as FeN_x are the only ones detected in the XPS spectra of the catalysts, *i.e.*, they are located at the surface of the catalysts. The short range order observed for the FeN_x species suggests an amorphous nature and explains its absence in the diffraction patterns.

Altogether, the characterization results shown above reveal that the N/C ratio in the precursor mixture used for the synthesis of Fe/N/G catalysts has a strong influence on their textural properties, elemental composition and nature of the surface and bulk phases in the catalysts. Thus, catalysts with higher total N contents and higher surface atomic N/C ratios are obtained by increasing the N/C ratio in the precursor mixture. However, the surface area of the catalysts decreases with increasing N/C ratio in the precursor mixture. In terms of the nature of phases present in the samples, the characterization results indicate that the Fe/N/G catalysts comprise different Fe species including FeN_x, Fe_3C and metallic Fe. However, FeN_x ensembles are the only species stable at the surface of the catalysts.

Fig. 5 shows the ORR polarization curves and mass normalised kinetic current (i_M) of the Fe/N/G catalysts. For the sake of comparison the performance of Pt/C (40 wt%, Johnson Matthey) is also shown. All catalysts show similar polarization curves with a mixed kinetic-mass controlled region between 1.0 and 0.7 V and a diffusional limited region at potentials less positive than 0.5 V. The onset potentials (E_{onset}) and half-wave ($E_{1/2}$) potentials are characteristic of each catalyst. As observed, Fe/N/G-0.3 and Fe/N/G-0.25 are the most active catalysts in the series showing the same E_{onset} values at 0.98 V and $E_{1/2}$ values of 0.83 and 0.84 V, respectively. Remarkably, this trend suggests that the activity of the catalysts for the ORR increases with decreasing amount of surface Fe and N species. Fig. S3 in the ESI† shows H_2O_2 production for Fe/N/G-0.3 and Fe/N/G-0.6 evaluated with a RRDE. As observed, the production of H_2O_2 is low and the average number of exchanged electrons is *ca.* 3.9 (see the ESI† section for details). Similar results have been obtained from the Koutecky–Levich plots recorded at different rotation rates, as shown in Fig. S4.†

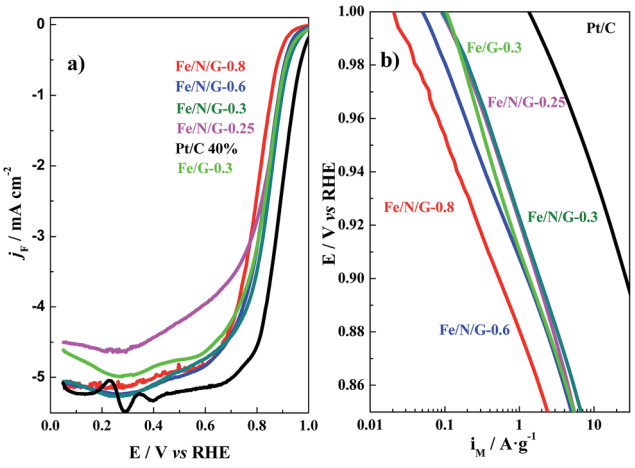

Fig. 5 (a) ORR polarization curves and (b) mass transport corrected mass activities (i_M) in O_2-saturated 0.1 M KOH for the Fe/N/G, Fe/G and Pt/C 40% catalysts recorded at 10 mV s^{-1}, and 1600 rpm. Catalyst loading: 0.06 mg_{cat} cm^{-2} for the Pt/C catalyst and 0.6 mg_{cat} cm^{-2} for Fe/N/G samples.

The ORR activity trend is even more clearly observed in terms of mass activity as shown in Fig. 5b. The mass activities for the ORR of Fe/N/G-0.8, Fe/N/G-0.6, Fe/N/G-0.3 and Fe/N/G-0.25 measured at 0.9 V are 0.5, 1.3, 1.9 and 1.7 A g^{-1}, respectively. The ORR performance of a catalyst prepared without using urea (Fe/G-0.3) is also shown. As observed, the ORR activity at 0.9 V for this catalyst is lower than that obtained for the catalysts containing comparable N/C ratios of *ca.* 0.3, Fe/N/G-0.25 and Fe/N/G-0.3.

The mass activities recorded with the most active catalysts, Fe/N/G-0.25 and Fe/N/G-0.3, are *ca.* one order of magnitude lower than that recorded with benchmark Pt/C catalysts (Pt 40 wt% of 25.8 A g^{-1} at 0.9 V, see Fig. 5b). This value is in line with the DOE's target to replace Pt in fuel cells, *i.e.*, NPMCs with ORR mass activity 10 times lower than that of Pt/C. Admittedly, higher mass activity values of 8–12 A g^{-1} have been reported for other Fe/N/C catalysts.[12,13,22]

The question arises as to how the N/C ratio controls the catalytic performance for the ORR of Fe/N/G electrocatalysts. In principle, higher ORR activities can be due to either (or both) more active sites or/and higher intrinsic activity of such sites, *i.e.*, a higher turnover frequency (TOF). Although the actual nature of the active sites for the ORR is still under debate, it is well accepted that Fe/N-based electrocatalysts exhibit superior performances for the ORR in alkaline electrolytes than in acidic ones.[7,8,36] Most studies argue that FeN_4 and/or FeN_{2+2} ensembles are the active sites for the ORR.[37,38] It has also been reported that the ORR activity increases with the increasing amount of surface N.[39] Mukerjee and co-workers established that these Fe–N sites are involved in the ORR initiation process, O_2 adsorption followed by a $2e^-$ reduction process yielding a peroxide intermediate (HO_2^-) independent of the pH of the electrolyte. They suggest that in alkaline pH the further reduction step of the HO_2^- intermediate to produce H_2O takes place in the same type of Fe–N sites being thermodynamically favoured with respect to the same reduction step in acidic media which would take place in a different site. The authors also propose that this second active site for the production of H_2O in acidic pH comprises metallic Fe nanoparticles although the actual nature of these sites is not established hitherto. Irrespective of the actual nature of the active sites, it seems clear that the ORR activity of Fe/N/C based catalysts is related to the presence of Fe–N ensembles in their structure.

The Tafel slope values calculated for the catalyst reported in this work are around 90 mV per decade, a value in good agreement with that reported for Fe/N/C-based catalysts.[22] This observation suggests that the active sites for the ORR of the Fe/N/G catalysts reported in this work are similar. As shown

above, FeN_x species are the most abundant species at the surface of the Fe/N/G catalysts. In fact, Fe/N_x-like species have been reported as the real active sites for the ORR. As a consequence, it would be expected that a direct relationship between the N surface content (recall that the N and Fe surface contents in the catalyst grow in parallel, see Table 2) and the performance of the Fe/N/G for the ORR exists. However, the ORR performances shown in Fig. 5 clearly point otherwise; and the ORR activity increases with the decreasing N and Fe contents (both surface and bulk contents) in the catalysts. This observation clearly indicates that features other than the N (and Fe) content of the catalysts should also play an important role in the catalytic performance of Fe/N/G catalysts for the ORR. As observed in Table 1, the surface area of the Fe/N/G catalysts decreases with the increasing N/C ratio in the catalysts, *i.e.*, the catalysts with lower N/C ratios exhibit higher BET areas. This trend suggests that a direct relationship between the BET area and their performance for the ORR exists. It should be emphasized, however, that having large BET areas is not enough for exhibiting high ORR activities. For instance, the activity for the ORR of the pristine graphite nanoplate precursor (before the incorporation of N and Fe) is one order of magnitude lower than that of the Fe/N/G catalysts (see Fig. S2†), despite the fact that the BET area of the pristine graphite nanoplates (718 $m^2\ g^{-1}$) is significantly higher than that of the Fe/N/G catalysts, see Table 1. Similar results have been reported for the oxygen reduction reaction by reduced graphene oxide and ascribed to the preferential $2e^-$ pathway with N- and Fe-free graphene-like materials.[40]

Fig. 6 shows the evolution of the mass activity of the catalysts for the ORR at 0.9 V and of the amount of accessible N (N content by surface area) for each catalyst *vs.* the N/C nominal atomic ratio in the precursors used for the synthesis. As observed, both the mass activity and the amount of *accessible* N follow the same trend, confirming that the real active sites for the ORR would be related to the N *accessible* sites.

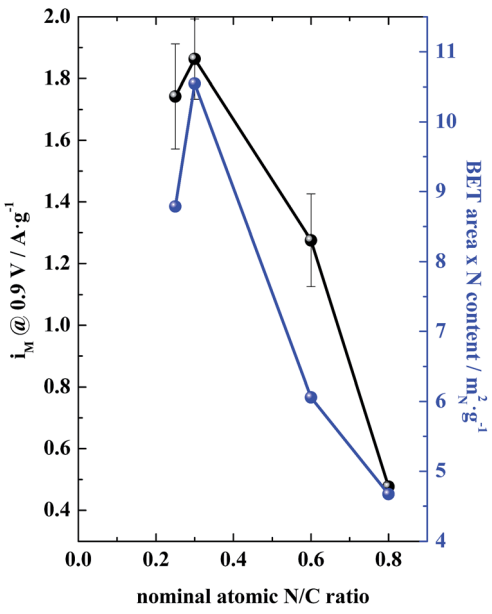

Fig. 6 Relationship between ORR mass activities (i_M) in 0.1 M KOH at 0.9 V for the Fe/N/G electrocatalysts prepared with different N/C molar ratios and N content in the catalyst normalized by surface area.

With these considerations in mind, we propose here that the *accessible* N, *i.e.*, the amount of N by surface area, is a relevant descriptor for the activity of Fe/N/G catalysts for the ORR. As a consequence, not only the amount of N, but also its location, should be optimized during the synthesis of Fe/N based electrocatalysts for the ORR. The results shown in this paper for the synthesis of Fe/N/G from N, Fe and graphene individual precursors indicate that the N/C ratio used for the synthesis of the catalysts not only affects the actual N content on the catalysts, and as a consequence the Fe content, but also affects the actual BET area of the final catalysts. Thus, the catalysts prepared by using high N/C ratios exhibit high surface N/C ratios but lower surface areas. On the other hand, decreasing the N/C ratio during the synthesis of the samples results in catalysts with higher amounts of *accessible* N sites and as a result more active catalysts for the ORR are obtained.

Conclusions

In this paper a series of Fe/N–modified graphene composites with different N/C ratios have been prepared. These materials present a high ORR activity in alkaline electrolytes. The characterization results establish that the N/C ratio in the precursors determines the amount and nature of the N atoms incorporated onto the composite which in turn affects the nature of the FeN_x moieties formed in the final catalysts which are the active sites for the ORR. However, increasing the N/C ratio used for the synthesis of the N/graphene composites results in Fe/N/G materials with lower BET areas and as a consequence with less accessible FeN_x sites and as a consequence exhibiting lower ORR activities. The N/C atomic ratio of the N and C precursor mixture used for the synthesis of Fe/N/graphene should be optimized in order to obtain catalysts exhibiting a high content of accessible Fe/N_x sites, *i.e.*, catalysts with a high content of N and a high surface area.

Experimental

Preparation of electrocatalysts

The catalysts studied in this work were synthesized by three sequential solid state synthesis steps conducted in a planetary ball-milling using 12 mL stainless steel vessels followed by a thermal treatment under inert atmosphere at 800 °C. All catalysts were synthetized by using graphene as the carbon source. Recently, the use of the term "graphene" is creating controversy in the scientific community.[41] Strictly speaking, we have used a two-dimensional (2D) sheet-like carbon material provided by XG Sciences formed by plates with a size of less than two microns and a typical thickness of a few nanometres. In accordance with a recent recommendation for avoiding misinterpretations, the carbon structure used in this work can be defined as graphite nanoplates[41] and it will be referred to as G throughout this manuscript.

In the first step, graphite nanoplates (denoted as G and purchased from XG Sciences, Grade C, 718 $m^2\ g^{-1}$) and the desired amount of the N precursor (1,4,8,11-tetraazacyclotetradecane, Aldrich 98%) to obtain a N/C composite with a N content of 3.5 wt%, were ball-milled at 350 rpm during 4 h. The N/G composite obtained was mixed with an equal amount of the G precursor to that used in the previous step and with different amounts of Urea (CH_4N_2O, PANREAC PRS) to obtain a series of composites with N/C atomic ratios ranging between 0.8 and 0.25. The mixture was ball-milled at 350 rpm during 4 h. In the following step an appropriate amount of iron phthalocyanine (FePhC) (Aldrich) to obtain a Fe loading of 1.4 wt% was added to the N/G composite obtained as described above. The mixture was ball-milled during 10 h at 350 rpm. Note that the nominal N/C atomic ratio of the materials resulting from this last ball milling step ranged between 0.8 and 0.25 The solids obtained were thermally treated (pyrolysed) in a quartz tubular reactor at 800 °C for 1 h in an inert atmosphere of 25 mL min^{-1} of N_2. Table 1 denotes the nomenclature of the different catalysts synthesized with different nominal N/C ratios. The N/C ratios have been calculated by taking into account the contributions of C and N of each of the precursors used for the synthesis of the catalysts. For the sake of comparison, a catalyst with a nominal N/C ratio of 0.3 (Fe/G-0.3) was prepared by using the same procedure as described above but without the addition of 1,4,8,11-tetraazacyclotetradecane and urea.

Physicochemical characterization

Powder X-ray diffractograms (XRD) were collected with a Seifert 3000 powder diffractometer operating with Cu Kα radiation (λ = 0.15418 nm) generated at 40 kV and 40 mA. Scans were recorded at 0.02° s^{-1} between 2θ values of 10° and 90°.

X-ray photoelectron spectra (XPS) of selected core-level elements were recorded with a SPECS customized system for surface analysis equipped with a non-monochromatic X-ray source XR 50 and a hemispherical energy analyser PHOIBOS 150. The X-ray MgKα line (1253.6 eV) was used as the excitation source (operating at 200 W/12 kV), and the medium area mode of the lenses was used for the detector. The energy regions of the photoelectrons of interest were scanned until an acceptable signal-to-noise ratio was achieved. Intensities were estimated by calculating the integral of each peak after subtraction of a Shirley-type background and fitting of the experimental curve to a combination of Lorentzian and Gaussian lines of variable proportions. Accurate binding energies (±0.2 eV) were determined by setting the C 1s core-level peak at 284.6 eV.

Carbon, nitrogen, hydrogen and sulphur contents of the samples were measured with an elemental analyser (LECO CHNS-932).

Textural properties were evaluated from the N_2 adsorption–desorption isotherms of the samples recorded at liquid N_2 temperature with a Micromeritics ASAP 2000 apparatus. Samples were degassed at 140 °C under vacuum for 24 h. Specific areas were calculated by applying the BET method within the relative pressure range P/P^0 = 0.05–0.30.

XAFS data were acquired at the CLAESS beamline of the ALBA Synchrotron facility with the help of ALBA's staff. The Fe *K* absorption edge (7112 eV) was calibrated with the help of a Fe foil. A Si (111) double crystal monochromator working in continuous mode was used for the energy scans. EXAFS spectra are the result of the merging of at least 6 scans.

Analysis of the EXAFS spectra was performed with the software VIPER for Windows. In the spectra of the absorption coefficient μ, a linear fit was made to the pre-edge region in order to normalize the signal. A smooth atomic background μ_0 was evaluated using a smoothing cubic spline.[42]

Electrochemical characterization

The electrochemical experiments were performed by using a computer controlled Autolab PGSTAT 302N potentiostat–galvanostat. A standard three-compartment glass cell and a rotating disk electrode (RDE) (Pine Research Instruments) were used for all electrochemical experiments. A graphite rod was used as the counter electrode. A Reversible Hydrogen Electrode (RHE) prepared prior to each experiment by using the same electrolyte composition as that used for the electrochemical experiments was used as the reference electrode. All potentials in this manuscript are referenced to the RHE.

A glassy carbon electrode with a thin film of the electrocatalyst under study was used as the working electrode. Prior to the electrochemical testing, the working electrode was electrochemically cleaned by potential cycling from 0 to 1.1 V for 50 cycles in Ar-saturated 0.1 M KOH.

The ORR polarization curves were collected by recording cyclic voltammograms between 0 V and 1 V at 10 mV s^{-1} and 1600 rpm in O_2-saturated 0.1 M KOH. The faradaic current density (j_F in mA cm^{-2}) was obtained by subtracting the current obtained during the anodic sweep scan in the O_2-saturated electrolyte from the capacitive current obtained in the potential sweep recorded in the Ar-saturated O_2-free electrolyte under the same experimental conditions. The ORR kinetic current (i_k) was calculated by using the relationship between i_k and i_F as established by the Koutecky–Levich equation [$i_k = -i_F i_{lim}/(i_F - i_{lim})$] where i_k is the kinetic current defined as <0 for reduction reactions and i_{lim} is the limiting current. Finally, the ORR mass activity is defined by $i_M = -i_k/m_{cat}$ where m_{cat} is the catalyst loading on the working electrode expressed in grams. The catalyst loading of Fe/N/G samples for all experiments was 0.6 mg cm^{-2}.

Acknowledgements

This project was funded by the Deanship of Scientific Research (DSR), King Abdulaziz University, Jeddah, under grant number (D-002-436). The authors, therefore, acknowledge DSR technical and financial support. Economic support from projects ENE2013-42322-R from the Spanish Ministry of Economy and Competitiveness, and project 201480E122 from the CSIC is also acknowledged.

References

1 Y. Wang, K. S. Chen, J. Mishler, S. C. Cho and X. C. Adroher, *Appl. Energy*, 2011, **88**, 981–1007.
2 M. S. Faber and S. Jin, *Energy Environ. Sci.*, 2014, **7**, 3519–3542.
3 H. A. Gasteiger, S. S. Kocha, B. Sompalli and F. T. Wagner, *Appl. Catal., B*, 2005, **56**, 9–35.
4 F. Jaouen, E. Proietti, M. Lefèvre, R. Chenitz, J. P. Dodelet, G. Wu, H. T. Chung, C. M. Johnston and P. Zelenay, *Energy Environ. Sci.*, 2011, **4**, 114–130.
5 G. Wu and P. Zelenay, *Acc. Chem. Res.*, 2013, **46**, 1878–1889.
6 H. Shi, Y. Shen, F. He, Y. Li, A. Liu, S. Liu and Y. Zhang, *J. Mater. Chem. A*, 2014, **2**, 15704–15716.
7 C. Domínguez, F. J. Pérez-Alonso, J. L. Gómez de La Fuente, S. A. Al-Thabaiti, S. N. Basahel, A. O. Alyoubi, A. A. Alshehri, M. A. Peña and S. Rojas, *J. Power Sources*, 2014, **271**, 87–96.
8 N. Ramaswamy and S. Mukerjee, *Adv. Phys. Chem.*, 2012, **2012**, 491604.
9 E. H. Yu, X. Wang, U. Krewer, L. Li and K. Scott, *Energy Environ. Sci.*, 2012, **5**, 5668–5680.
10 I. Kruusenberg, L. Matisen, Q. Shah, A. M. Kannan and K. Tammeveski, *Int. J. Hydrogen Energy*, 2012, **37**, 4406–4412.
11 H. T. Chung, J. H. Won and P. Zelenay, *Nat. Commun.*, 2013, **4**, 1922.
12 M. Piana, S. Catanorchi and H. A. Gasteiger, *ECS Trans.*, 2008, **16**, 2045–2055.
13 H. Meng, F. Jaouen, E. Proietti, M. Lefèvre and J. P. Dodelet, *Electrochem. Commun.*, 2009, **11**, 1986–1989.
14 W. Wei, H. Liang, K. Parvez, X. Zhuang, X. Feng and K. Müllen, *Angew. Chem., Int. Ed.*, 2014, **53**, 1570–1574.
15 X.-H. Yan and B.-Q. Xu, *J. Mater. Chem. A*, 2014, **2**, 8617–8622.
16 S. Zhang, H. Zhang, X. Hua and S. Chen, *J. Mater. Chem. A*, 2015, **3**, 10013–10019.
17 Y. Li, W. Zhou, H. Wang, L. Xie, Y. Liang, F. Wei, J. C. Idrobo, S. J. Pennycook and H. Dai, *Nat. Nanotechnol.*, 2012, **7**, 394–400.
18 L. Qu, Y. Liu, J.-B. Baek and L. Dai, *ACS Nano*, 2010, **4**, 1321–1326.
19 M. Liu, R. Zhang and W. Chen, *Chem. Rev.*, 2014, **114**, 5117–5160.
20 N. Mahmood, C. Zhang, H. Yin and Y. Hou, *J. Mater. Chem. A*, 2014, **2**, 15–32.
21 K. Parvez, S. Yang, Y. Hernandez, A. Winter, A. Turchanin, X. Feng and K. Müllen, *ACS Nano*, 2012, **6**, 9541–9550.
22 G. Wu, K. L. More, P. Xu, H. L. Wang, M. Ferrandon, A. J. Kropf, D. J. Myers, S. Ma, C. M. Johnston and P. Zelenay, *Chem. Commun.*, 2013, **49**, 3291–3293.
23 C. Zhang, R. Hao, H. Yin, F. Liu and Y. Hou, *Nanoscale*, 2012, **4**, 7326–7329.
24 P. Chen, T. Y. Xiao, Y. H. Qian, S. S. Li and S. H. Yu, *Adv. Mater.*, 2013, **25**, 3192–3196.
25 G.-L. Tian, M.-Q. Zhao, D. Yu, X.-Y. Kong, J.-Q. Huang, Q. Zhang and F. Wei, *Small*, 2014, **10**, 2251–2259.
26 X. Bo, M. Li, C. Han, Y. Zhang, A. Nsabimana and L. Guo, *J. Mater. Chem. A*, 2015, **3**, 1058–1067.
27 Q. Dong, X. Zhuang, Z. Li, B. Li, B. Fang, C. Yang, H. Xie, F. Zhang and X. Feng, *J. Mater. Chem. A*, 2015, **3**, 7759–7766.
28 V. Nallathambi, N. Leonard, R. Kothandaraman and S. C. Barton, *Electrochem. Solid-State Lett.*, 2011, **14**, B55–B58.
29 K.-K. Türk, I. Kruusenberg, J. Mondal, P. Rauwel, J. Kozlova, L. Matisen, V. Sammelselg and K. Tammeveski, *J. Electroanal. Chem.*, 2015, **756**, 69–76.
30 F. Jaouen, J. Herranz, M. Lefèvre, J. P. Dodelet, U. I. Kramm, I. Herrmann, P. Bogdanoff, J. Maruyama, T. Nagaoka, A. Garsuch, J. R. Dahn, T. Olson, S. Pylypenko, P. Atanassov and E. A. Ustinov, *ACS Appl. Mater. Interfaces*, 2009, **1**, 1623–1639.
31 J. R. Pels, F. Kapteijn, J. A. Moulijn, Q. Zhu and K. M. Thomas, *Carbon*, 1995, **33**, 1641–1653.
32 T. Herranz, S. Rojas, F. J. Pérez-Alonso, M. Ojeda, P. Terreros and J. L. G. Fierro, *Appl. Catal., A*, 2006, **311**, 66–75.
33 M. Muhler, R. Schlögl and G. Ertl, *J. Catal.*, 1992, **138**, 413–444.
34 S. Maroie, M. Savy and J. J. Verbist, *Inorg. Chem.*, 1979, **18**, 2560–2567.
35 S. Kim, T. Ohta and G. Kwag, *Bull. Korean Chem. Soc.*, 2000, **21**, 588–594.
36 U. Tylus, Q. Jia, K. Strickland, N. Ramaswamy, A. Serov, P. Atanassov and S. Mukerjee, *J. Phys. Chem. C*, 2014, **118**, 8999–9008.
37 J. Herranz, F. Jaouen, M. Lefèvre, U. I. Kramm, E. Proietti, J. P. Dodelet, P. Bogdanoff, S. Fiechter, I. Abs-Wurmbach, P. Bertrand, T. M. Arruda and S. Mukerjee, *J. Phys. Chem. C*, 2011, **115**, 16087–16097.
38 U. I. Kramm, J. Herranz, N. Larouche, T. M. Arruda, M. Lefèvre, F. Jaouen, P. Bogdanoff, S. Fiechter, I. Abs-Wurmbach, S. Mukerjee and J. P. Dodelet, *Phys. Chem. Chem. Phys.*, 2012, **14**, 11673–11688.
39 F. J. Pérez-Alonso, M. A. Salam, T. Herranz, J. L. Gómez de La Fuente, S. A. Al-Thabaiti, S. N. Basahel, M. A. Peña, J. L. G. Fierro and S. Rojas, *J. Power Sources*, 2013, **240**, 494–502.
40 S. K. Bikkarolla, P. Cumpson, P. Joseph and P. Papakonstantinou, *Faraday Discuss.*, 2014, **173**, 415–428.
41 A. Bianco, H.-M. Cheng, T. Enoki, Y. Gogotsi, R. H. Hurt, N. Koratkar, T. Kyotani, M. Monthioux, C. R. Park, J. M. D. Tascon and J. Zhang, *Carbon*, 2013, **65**, 1–6.
42 K. V. Klementev, *J. Phys. D: Appl. Phys.*, 2001, **34**, 209.

Effect of the N content of Fe/N/Graphene catalysts for the oxygen reduction reaction in alkaline media

Carlota Domínguez[a], F.J. Pérez-Alonso[a]*, Mohamed Abdel Salam[b], Shaeel A. Al-Thabaiti[b], Miguel A. Peña[a], L. Barrio[a] and S. Rojas[a]*

Supplementary Information

X-ray diffractograms of Fe/NG catalysts

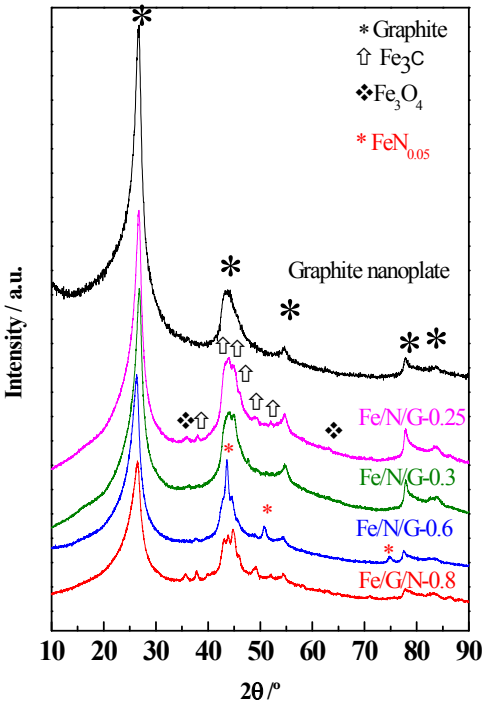

Fig. S1. X-ray diffractograms of Fe/N/G samples with different N/C ratios

A comparison of the catalytic performance for the ORR in KOH of pristine graphite nanoplates (black lines), Fe/N/G-0.3 (green lines) and a commercial Pt/C catalyst purchased from Johnson Matthey (Pt loading 40wt.%) measured under identical reaction conditions as shown in the caption to the figure is shown in Fig S2. As observed, the ORR activity of the pristine nanoplates is significantly lower than that of the Fe/N/G-0.3

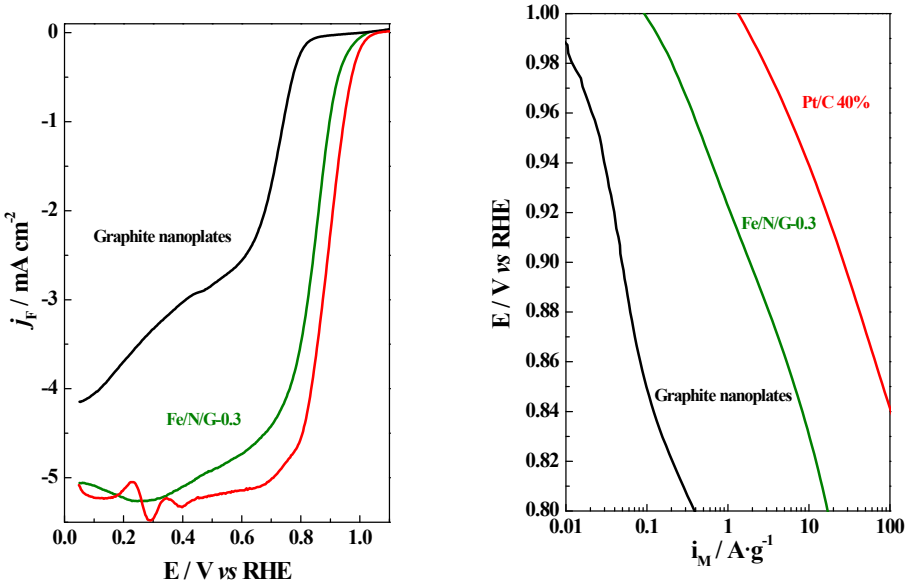

Fig S2. ORR polarization curves and ORR mass activities in 0.1 M KOH at 10 mVs^{-1} and 1600 rpm for Pt/C 40 wt. % and pristine graphite nanoplates. For the sake of comparison, the ORR polarization curve and ORR mass activity of the best catalyst of the series (Fe/N/G-0.3) is also included. Catalyst loading: 0.06 mg_{cat}/cm^2 for Pt/C catalyst and 0.6 mg_{cat}/cm^2 for graphite nanoplates and Fe/N/G-0.3 samples.

Evaluation of H_2O_2 production from Rotating Ring Disk Electrode

H_2O_2 production was evaluated by using a rotating ring disk electrode (RRDE) (with a Pt ring), under the same experimental conditions than that reported above for the RDE applying a constant ring potential of 1.2 V. The fraction of H_2O_2 produced was calculated as shown in Equation 1

$$X_{H2O2} = \frac{\frac{2i_R}{N}}{i_D + \frac{i_R}{N}} \qquad (Eq.1)$$

where iD is the disk current and iR is the ring current. Ring efficiency (N) is of 26%.

The number of exchanged electrons was calculated from Equation 2

$$ne = 4 - \left[\frac{\%H_2O_2}{50\%}\right] \qquad (Eq.2)$$

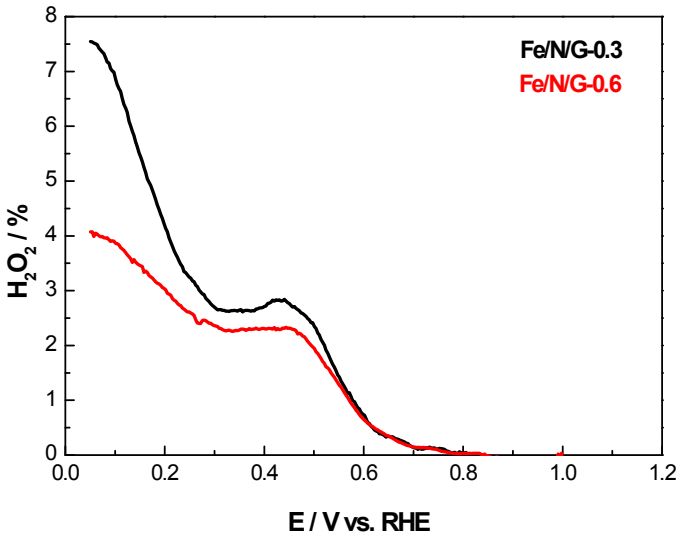

Fig S3. H_2O_2 production in 0.1 M KOH at 10 mVs^{-1} and 1600 rpm for Fe/N/G-0.3 (black line) and Fe/N/G-0.6 (red line). Catalyst loading 0.6 mg_{cat}/cm^2

In addtion, the average number of exchanged electrons during the ORR can be detrermined from the relatinship between the i_D and the rotation rate as defined by the Levich equation:

$$i_D = 0.201nFC_{02}D_{02}^{2/3}v^{-1/6}\omega^{1/2}$$

Where n is the ORR overall electron transfer number, $F = 96487\ C \cdot mol^{-1}$ is Faraday's constant, $C_{02} = 1.1 \times 10^{-6}\ mol \cdot cm^{-3}$ is the concentration (or solubility) of O_2 in the electrolyte solution, $D_{02} = 1.9\ x\ 10^{-5}\ cm^2 \cdot s^{-1}$ is the diffusion coefficient of O_2, $v = 1\ x\ 10^{-2} cm^2 \cdot s^{-1}$ is the viscosity of the

KOH aqueous solution, and ω is the electrode rotating rate (rpm). According with the parameters for a KOH solution of 0.1M [1]

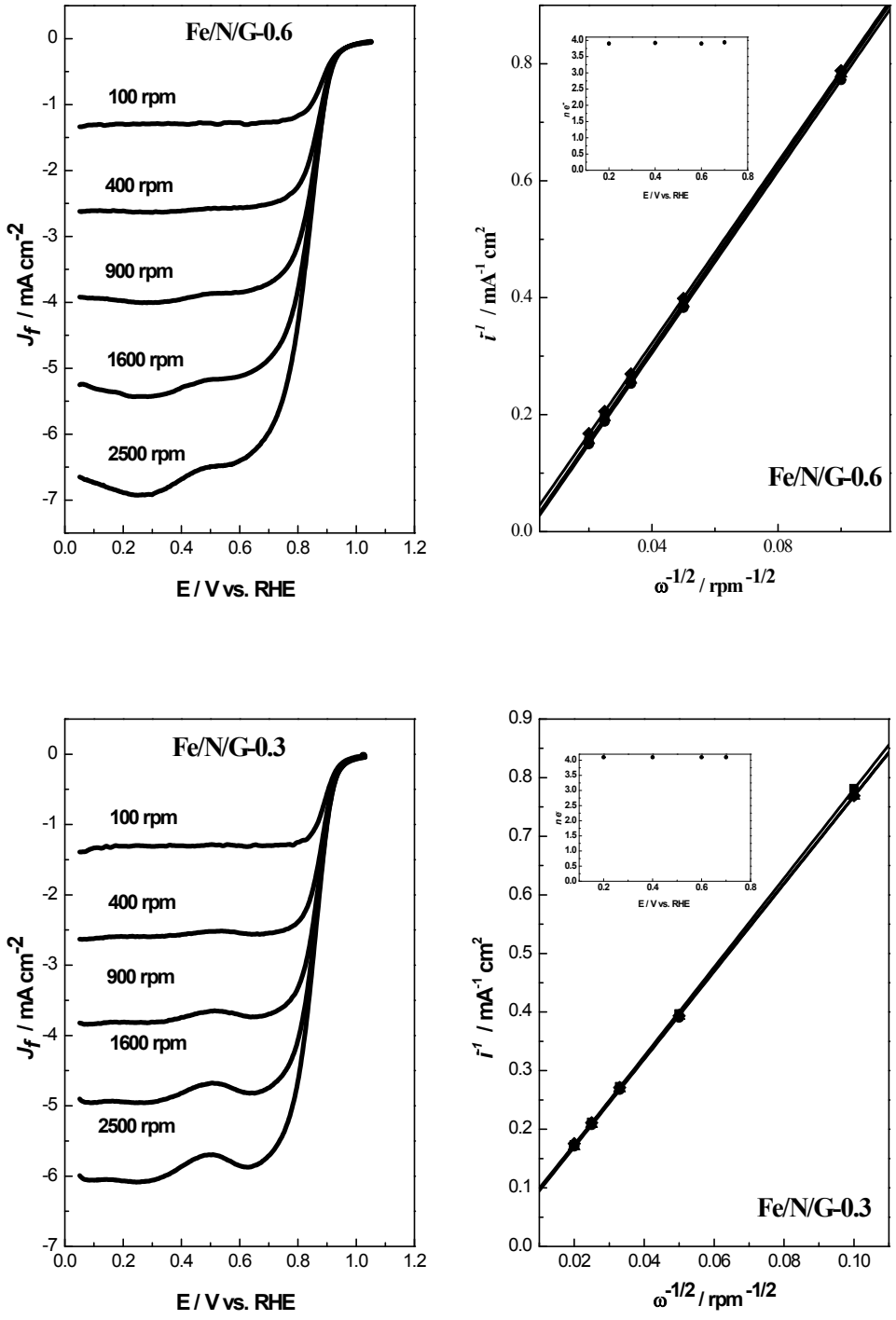

Fig S4. Linear sweep (10 mV/s) recorded in O_2-saturated in 0.1M KOH at different rotation rates and Levich-Koutecky plots for the Fe/N/G-0.6 and Fe/N/G-0.3 at 0.2V (■), 0.4V (●), 0.6V (◊) and 0.7V (○). The insets to the figures are the number of electrons obtained from the Levich-Koutecky equation.

Stability of catalysts

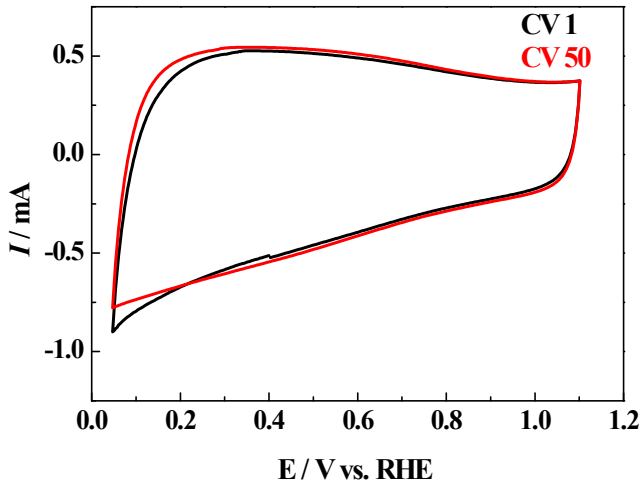

Fig S5. 1st and 50th cyclic voltammogram recorded in Ar-saturated KOH solution.

References

1. Qiao, J., *Effect of KOH concentration on the oxygen reduction kinetics catalyzed by heat-treated co-pyridine/C electrocatalysts.* International Journal of Electrochemical Science, 2013. **8**(1): p. 1189-1208.

Applied Catalysis B: Environmental 183 (2016) 185–196

Contents lists available at ScienceDirect

Applied Catalysis B: Environmental

journal homepage: www.elsevier.com/locate/apcatb

Repercussion of the carbon matrix for the activity and stability of Fe/N/C electrocatalysts for the oxygen reduction reaction

Carlota Domínguez[a], Francisco José Pérez-Alonso[a,*], Mohamed Abdel Salam[b], Shaeel A. Al-Thabaiti[b], Miguel Antonio Peña[a], F. Javier García-García[c], Laura Barrio[a], Sergio Rojas[a,*]

[a] Grupo de Energía y Química Sostenibles, Instituto de Catálisis y Petroleoquímica, CSIC, C/Marie Curie 2, 28049 Madrid, Spain
[b] Chemistry Department, Faculty of Science, King Abdulaziz University, PO Box 80200, Jeddah 21589, Saudi Arabia
[c] Centro Nacional de Microscopía, Universidad Complutense de Madrid, Madrid, Spain

ARTICLE INFO

Article history:
Received 17 August 2015
Received in revised form 15 October 2015
Accepted 21 October 2015
Available online 26 October 2015

Keywords:
Fuel cells
Oxygen reduction reaction
Graphene
Iron
Durability

ABSTRACT

Graphene-like (G), multiwalled carbon nanotubes (CNTs) and active carbon (AC) have been used as carbon matrix for the synthesis of Fe/N/C catalysts for the oxygen reduction reaction. A thorough physicochemical characterization of the electrocatalysts, including X-ray photoelectronic and X-ray absorption spectroscopies, reveal that the formation of Fe/Nx ensembles is favored when the graphene-like or the CNTs are used as the carbon matrix. As a result, the catalyst prepared with the graphene matrix (Fe/N/G) records the highest activity for the ORR in the series of 3.1 A g^{-1} at 0.9 V. This very high ORR activity positions these catalysts as a realistic alternative to replace Pt/C cathodes in alkaline fuel cells. Moreover, using graphene as the carbon matrix endows the catalyst with very high stability during the ORR showing stable catalytic performance for the ORR even after being subjected to severe treatments of 3000 cycles up to 1.4 V. *In situ* IRRA spectra demonstrate that such a high stability for the ORR relates to the excellent resistance against corrosion of the graphene-based catalyst.

1. Introduction

The increasing growth of energy consumption, which is mainly coped with fossil fuels, is causing severe environmental and social issues including climate change, geopolitical tensions and concerns about fossil fuel depletion. As a consequence, numerous efforts to find alternative energy sources, especially renewable ones, have been addressed during the last years. Electrochemical devices such as fuel cells [1] and metal–air batteries [2] are expected to power environmentally friendly vehicles in a near future. Some of the most relevant environmentally friendly energy related processes such as the hydrogen evolution reaction (HER), the hydrogen oxidation reaction (HOR), the oxygen evolution reaction (OER) and the oxygen reduction reaction (ORR), are conducted in the presence of electrocatalysts [3,4] which usually contain high amounts of scarce and expensive Platinum group metals (PGM). The urgent and great challenge is to design and develop highly active and more durable electrocatalysts based upon low cost, earth-abundant elements with comparable activity to that of the benchmark PGM based catalysts [5]. In recent times, non-precious metal catalysts (NPMCs) based upon the incorporation of transition metals such as Fe onto N/C composites (usually denoted as Fe/N/C) have emerged as the most suitable candidates for replacing Pt as electrocatalysts for the ORR in Proton Exchange Membrane Fuel Cells (PEMFC) [6–15]. The lower kinetics of this type of NPMCs for the ORR can be compensated by using higher NPMCs loadings without economic penalties [7,13]. Moreover, in the last years, NPMCs with comparable ORR kinetic currents in acid media than that obtained with benchmark carbon supported PGM have been reported [8,11,12,16]. The results are even more promising in alkaline media and several groups have developed electrocatalysts based upon Fe/N/C structures [17,18] with ORR activity that match, or even exceed, the activity of Pt/C.

Although the actual nature of the active sites for the ORR in Fe/N/C catalysts remains elusive it is well accepted that their activity increases when Fe atoms are coordinated to the N heteroatoms incorporated onto the C-C sp^2 network of a carbon matrix, usually

* Corresponding authors.
E-mail addresses: fperez@icp.csic.es (F.J. Pérez-Alonso), srojas@icp.csic.es (S. Rojas).

http://dx.doi.org/10.1016/j.apcatb.2015.10.043
0926-3373/

active carbon [9,13,19,20]. In addition, it is also proposed that the formation of the active sites takes place inside the micropores of the carbon network [21], resulting in catalysts with high active surface area. However, the presence of micropores results in severe mass transportation limitations when high current densities are demanded to PEMFCs [8].

The state-of-the-art mesoporous carbon supports used in the cathodes of fuel cells are prone to suffer severe corrosion phenomena due to the strong oxidizing environment in the cathode electrode of PEMFCs. Due to their special 1D and 2D structures, carbon nanotubes and graphene-based materials possess unique properties such as high conductivity, high surface area and stability [10,22,23], thus being very attractive alternative carbon matrixes or supports for the synthesis of electrocatalysts. Several works have explored the use of nitrogen-doped graphene and/or carbon nanotubes as supports for the synthesis electrocatalysts for the ORR, resulting in more active and stable electrocatalysts for the ORR [9,10,17,18,22,24–28]. Despite the utter importance of the carbon matrix for the synthesis and performance of the Fe/N/C catalysts for the ORR, there is a lack of systematic studies addressing this issue. It seems to be widely accepted that the activity of Fe/N/C based catalysts for the ORR increases by using graphene like or carbon nanotubes or even carbon nanotube-graphene complexes as the carbon matrix [9,13,17]. However, it has been recently reported that the activity for the ORR in KOH of Fe/N/C-based catalysts prepared with high area carbon black is significantly higher than when prepared with graphene nanosheets [18].

In this work we explore the effect of the carbon matrix for the synthesis and catalytic performance of Fe/N/C catalysts by preparing series of catalysts using the same Fe and N precursors, but different types of carbons, namely graphite nanoplates (graphene, G), multiwalled carbon nanotubes (CNTs) or active carbon (AC). The formation of Fe/Nx-like ensembles is favoured when CNTs or graphene are used as support. The catalyst prepared with graphene, Fe/N/G, exhibits very high ORR activity in alkaline electrolyte which compares well against that of Pt/C benchmark catalyst. Equally important, this catalyst displays an outstanding stability against corrosion in alkaline media after repeated cycling up to 1.4 V *vs.* RHE.

2. Experimental

2.1. Synthesis of catalyst

The following commercially available carbons are used for the synthesis of the catalysts: Graphene (graphite nanoplates, from XG Sciences, Grade C), multiwalled carbon nanotubes (from Nanocyl) and active carbon (Norit GSX). The catalysts studied in this work were synthesized by a series of sequential ballmilling steps in a 12 mL stainless steel vessel followed by pyrolysis at 800 °C. In a first step, 0.75 g of the desired carbon matrix and 0.0027 g of the N precursor (1,4,8,11-tetraazacyclo-tetradecane, Aldrich 98%) were ballmilled at 350 rpm during 4 h. The N/C composite obtained was mixed with 0.75 g of the same carbon material than that used in the previous step and 1.3 g of Urea (CH_4N_2O, Panreac, PRS) and ballmilled at 350 rpm during 4 h. The N/C composite obtained was mixed with 0.52 g of iron phthalocyanine (Aldrich) and ballmilled for 10 h. The solid obtained was thermally treated (pyrolised) in a quartz tubular reactor at 800 °C for 30 min in an atmosphere of 50 mL min^{-1} of NH_3 (5%)/Ar. The catalysts obtained are labelled as Fe/N/G, Fe/N/CNT or Fe/N/AC where G, CNT and AC are used to identify graphene, carbon nanotubes or active carbon, respectively. Note that Fe/N/C will be used as a generic term to identify the family of Fe/N-based catalysts reported in this work irrespectively of the actual carbon matrix

2.2. Physicochemical characterization

X-ray photoelectron spectra (XPS) were acquired with a SPECS customized system for surface analysis equipped with a non-monochromatic X-ray source XR 50 and a hemispherical energy analyser PHOIBOS 150. X-ray MgKα line (1253.6 eV) was used as excitation (operating at 200 W/12 kV), and the medium area mode of the lenses was used for the detector. The energy regions of the photoelectrons of interest were scanned at increments of 0.1 eV and fixed pass energy of 25 eV until an acceptable signal-to-noise ratio was achieved. Atomic abundances were estimated by calculating the integral of each peak, determined by subtraction of the Shirley-type background and fitting of the experimental curve to a combination of Lorentzian and Gaussian using the appropriate sensitivity factors for each element [29]. Binding energies (±0.2 eV) were determined by setting the C 1s peak at 284.6 eV.

C, H and N contents of the samples were measured with an elemental analyser (LECO CHNS-932). Total iron content of the catalysts was analysed by inductively coupled plasma with an ICP–OES Optima 3300DV (PerkinElmer) after acidic microwave digestion of the samples.

Textural properties were evaluated by N_2 adsorption–desorption isotherms of the samples recorded at liquid N_2 temperature with a Micromeritics ASAP 2000 apparatus. Samples were degassed at 140 °C under vacuum for 24 h. Specific areas were calculated by applying the BET method within the relative pressure range $P/P^0 = 0.05–0.30$.

XAFS data were acquired at CLAESS beam line at ALBA Synchrotron facility with the help of ALBA staff. A Si (1 1 1) double crystal monochromator working in continuous mode was used for the energy scans. Fe K absorption edge (7112 eV) was calibrated with the help of a Fe foil, placed between second and third ionization chambers, and measured simultaneously with the sample spectra. Catalysts samples were pressed in self-supporting pellets. The spectra were recorded in the transmission mode at ambient temperature. EXAFS spectra are the result of the merge of at least 6 scans. The following selected standard materials were analyzed: Fe foil, Fe_3O_4, Fe_3C and iron phthalocyanine (FePhC). The analysis of the EXAFS spectra was performed with the software VIPER for Windows. In the spectra of the absorption coefficient μ, a linear fit was made to the pre-edge region in order to normalize the signal. A smooth atomic background μ_0 was evaluated using a smoothing cubic spline [30].

TEM and STEM images were recorded with at TEM/STEM JEOL 2100F microscope operated at 200 kV. The microscope was equipped with an OXFORD INCA detector for EDS analyses. Specimens for TEM analyses were prepared by dispersing the catalysts in butanol and placing one drop onto a holey-carbon-coated copper supported grid.

2.3. Electrochemical tests

The electrochemical tests were performed with a computer controlled Autolab Pgstat 302N potentiostat/galvanostat. A standard three-compartment glass cell and a rotating disk electrode (RDE) (Pine research instruments) were used for all electrochemical experiments. The counter electrode was a graphite rod and the reference electrode was a Reversible Hydrogen Electrode (RHE). A glassy carbon electrode with a thin film of the electrocatalyst under study was used as the working electrode. The electrocatalyst was deposited on the electrode by means of an ink prepared by ultrasonically dispersing 6 mg of the catalyst in 800 μL of water, 200 μL of isopropyl alcohol and 20 μL of 5 wt.% Nafion. 20 μL of the ink were deposited on the electrode resulting in a catalyst loading of 0.6 mg_{cat} cm^{-2}. Previous to the electrochemical testing, the work-

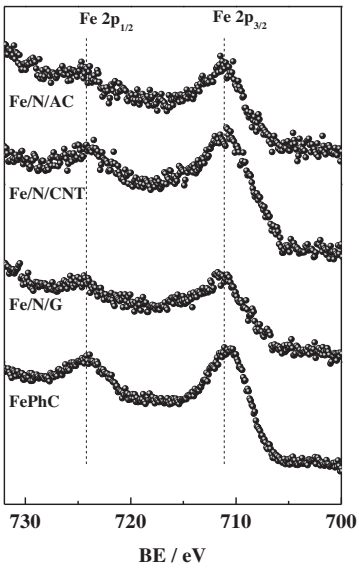

Fig. 1. Fe 2p core-level spectra of Fe/N/G, Fe/N/CNT and Fe/N/AC. The spectrum for iron phthalocyanine (FePhC) is shown for comparison.

ing electrode was cleaned by potential cycling from 0 to 1.1 V for 50 cycles in Ar-saturated electrolyte: 0.1 M KOH or 0.1 M $HClO_4$.

The ORR polarization curves were collected at 10 mV s^{-1} and 1600 rpm between 0.0 and 1.2 V or 0.0 and 1.0 V in O_2 saturated 0.1 M KOH or 0.1 M $HClO_4$ electrolytes, respectively. The Faradaic current density (j_F mA cm^{-2}) was obtained by subtracting the current obtained during the anodic sweep in the O_2 saturated electrolyte from the capacitive current recorded in Ar-saturated electrolyte under the same experimental conditions.

H_2O_2 production was evaluated by using a rotating ring disk electrode (RRDE) (with a Pt ring), under the same experimental conditions than that reported above for the RDE applying a constant ring potential of 1.2 V. The fraction of H_2O_2 produced was calculated as shown in Eq. (1) [31],

$$X_{H_2O_2} = \frac{\frac{2i_R}{N}}{i_D + \frac{i_R}{N}} \quad (1)$$

where i_D is the disk current and i_R is the ring current. Ring efficiency (N) is of 26%.

The number of exchanged electrons was calculated from Eq. (2).

$$ne = 4 - \left(\frac{\%H_2O_2}{50\%}\right) \quad (2)$$

The ORR kinetic current (i_k) was calculated from the Koutecky–Levich equation as shown in Eq. (3)

$$i_k = -\frac{i_F \times i_{lim}}{i_F - i_{lim}} \quad (3)$$

where i_k is the kinetic current defined as <0 for reduction reactions and i_{lim} is the limiting current. Finally, the ORR mass activity is defined in Eq. (4),

$$i_m = -\frac{i_k}{m_{cat}} \quad (4)$$

where m_{cat} is the catalyst loading in grams [6].

For the stability tests simulating fuel cell operation, the working electrode was cycled between 0.6 and 1.0 V at 50 mV s^{-1} for 3000 cycles in O_2 saturated electrolyte without rotation. With the aim of simulating the severe oxidizing environments during start-up and stop cycles of a fuel cell, the working electrode was cycled between 0.4 and 1.4 V at 1 V s^{-1} for 3000 cycles in O_2 saturated electrolyte without rotation. The ORR polarization curves were collected before and after the stability tests following the procedure described above.

In situ electrochemical IRRAS studies of the corrosion of Fe/N/C catalysts were performed with a NICOLET 6700 FT-IR spectrometer equipped with a MCT detector and fitted with a PIKE Technologies VeeMAX II spectroscopic accessory. A poly (methyl methacrylate) (PMMA) cell with a CaF_2 prism bevelled at 60° at its bottom was used. FTIR spectra were acquired from the average of 64 interferograms, obtained with 4 cm^{-1} resolution at selected potential, by applying single potential steps from a reference potential (E_0 = 0.6 V *vs.* RHE) in the positive direction up to 1.4 V. The reflectance ratio R/R_0 was calculated, where R and R_0 are the reflectance measured at the sample and the reference potential, respectively. Electrochemical control was carried out using an Autolab PGstat 302 N.

3. Results and discussion

3.1. Catalyst characterization

The H, C, N and Fe contents of the Fe/N-based electrocatalysts as determined by elemental analysis (H, C and N) and ICP-OES analysis (Fe content) are reported in Table 1. The amount of nitrogen incorporated into the catalysts are of 2.8, 2.6 and 2.3 wt.% for Fe/N/G, Fe/N/AC and Fe/N/CNT, respectively. These similar values suggest that the amount of nitrogen actually incorporated into the catalysts is not strongly influenced by the nature of the carbon material used for the synthesis of the catalysts.

Table 1 also shows the BET, micropore and external surface area values obtained from the N_2 adsorption–desorption isotherms. In all cases, the BET surface area of the catalysts is smaller than that of the pristine carbon material of 718, 233 and 850 m^2 g^{-1}, for graphene, CNT and AC, respectively.

The surface composition of the catalysts was studied by XPS. Table 2 shows the relative abundance of Fe, C and N as calculated from X-ray photoelectron spectroscopy of the Fe/N-based catalysts.

All catalysts have similar N/C contents ranging between 0.021 for Fe/N/G and 0.026 or 0.028 for Fe/N/CNT and Fe/N/AC, respectively. These values are in good agreement with the atomic ratios derived from the elemental analysis indicating the lack of N segregation onto catalyst surface. In order to identify and quantify the N atoms incorporated into the C-C network, the N 1s core-level spectra were analysed (Fig. S1 in Supplementary material). The peaks

Table 1
Weight contents and specific surface areas of the catalysts.

Catalyst	C (wt.%)	H (wt.%)	N (wt.%)	Fe (wt.%)	BET (m^2 g^{-1})
Fe/N/G	86.4	0.7	2.8	2.4	415 (162/253)
Fe/N/CNT	89.0	0.5	2.3	2.0	166 (21/145)
Fe/N/AC	83.6	1.1	2.6	2.4	362 (164/198)

C, H, and N wt.% as determined from elemental analysis; Fe wt.% as determined from ICP-OES analyses. Specific surface areas determined form the BET method. The values in parentheses indicate micropore/external areas.

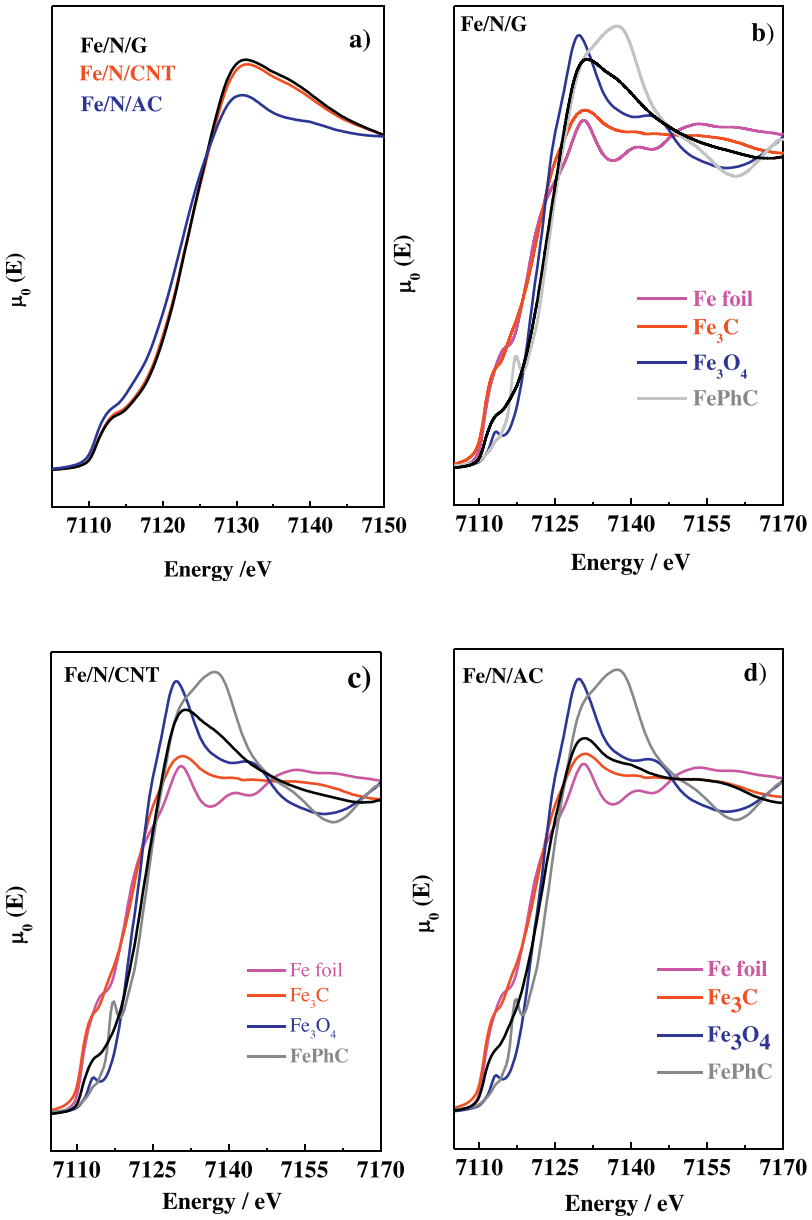

Fig. 2. (a) Fe K-edge XANES spectra of Fe/N/G, Fe/N/CNT and Fe/N/AC. (b), (c) and (d) XANES spectrum of each catalyst compared with the spectra of the standard materials.

were fitted to four components with peak maxima at 398.5, 400.1, 401.0–401.5 and 402–405 eV and assigned to pyridinic-N, pyrrolic-N, graphitic-N species and oxide-N, respectively [6,32]. As shown in Table 1, the relative amount of the N species, *i.e.*, pyridinic-N pyrrolic-N, graphitic-N and oxide-N species is similar in all catalysts regardless of the nature of the carbon matrix. Pyridinic-N is the predominant species in all catalysts, followed by pyrrolic-N and graphitic-N.

Fig. 1 shows the Fe 2p core-level spectra of the Fe/N/C electrocatalysts. All spectra show a broad peak centred at *ca.* 711 eV which is usually ascribed to the presence of iron oxidized species, typically Fe^{2+} or/and Fe^{3+}. The precise assignment of this peak is usually done from the position of the characteristic shake-up satellite peaks of

Table 2
Surface elemental chemical composition.

Sample	Surface atomic content			Relative atomic amount of N species			
	N/C	O/C	Fe/C	Pyridinic	Pyrrolic	Graphitic	Oxide
Fe/N/G	0.021 (0.028)	0.050	0.0018 (0.0060)	0.46	0.32	0.19	0.03
Fe/N/CNT	0.026 (0.022)	0.034	0.0028 (0.0048)	0.51	0.32	0.11	0.06
Fe/N/AC	0.028 (0.027)	0.090	0.0023 (0.0062)	0.46	0.32	0.17	0.05

N/C, Fe/C and O/C surface atomic ratios and relative atomic amount of N species derived from XPS analyses; for the sake of comparison bulk N/C and Fe/C atomic ratios (from Table 1) are shown in parentheses.

these iron species [33]. However, the spectra shown in Fig. 1 lack of the characteristic, well defined, satellite peaks for Fe^{2+} (at *ca.* 715 eV) or Fe^{3+} (at *ca.* 719 eV) species in oxide structures. This feature is indicative of the presence of Fe_3O_4 [34,35] and/or of iron phthalocyanine (spectrum also shown in Fig. 1). The surface concentration of Fe in the catalysts (see Fe/C atomic ratio in Table 2) is of *ca.* 0.002 for Fe/N/G and Fe/N/AC and slightly higher in Fe/N/CNT (Fe/C = 0.0028). As also shown in Table 2, the surface concentration of iron (Fe/C = 0.0018–0.0028) is indeed lower than the bulk concentration (Fe/C = 0.0048–0.0062). This feature indicates that a significant fraction of the iron atoms (of around 66%) is not exposed at the catalyst surface suggesting Fe atoms become covered by several carbon layers during the synthesis of the catalysts.

The nature of the iron species and their electronic state was further studied by X-ray absorption spectroscopy. The XANES and EXAFS spectra of the catalysts are shown in Figs. 2 and 3 respectively. For the sake of comparison, the XANES and EXAFS spectra of selected standards: Fe foil, Fe_3O_4, Fe_3C and iron phthalocyanine (FePhC), are also shown. The Fe K-edge XANES spectra for Fe/N/G and Fe/N/CNT are almost identical showing no significant shifts of the absorption edge positions. However, the spectra for Fe/N/AC is slightly different showing an evident shift to lower energy which can be taken as a clear indication of the different electronic state of the Fe atoms in Fe/N/AC as compared to Fe/N/G or Fe/N/CNT. The XANES spectra for each catalyst are compared with the spectra of the standard materials in Fig. 2b–d. The shifting of the adsorption edge of the Fe species in Fe/N/AC could be indicative of the presence of Fe_3C or Fe^0 (as in Fe foil) species in this catalyst. A careful inspection of the energy region of the spectra between 7130 and 7170 eV by analysing its first derivative shows that the iron species in Fe/N/AC are more similar to Fe_3C than to Fe foil. On the other hand, the adsorption edge of Fe in Fe/N/G and Fe/N/CNT is closer to that recorded for FePhC or Fe_3O_4.

A careful inspection of the energy region of the spectra between 7158 and 7170 eV shows that the iron species in Fe/N/G and Fe/N/CNT are more similar to those in FePhC than in Fe_3C.

The phase uncorrected interatomic distances obtained by Fourier transformation of the EXAFS spectra over the k-space range between 3 and 14.5 $Å^{-1}$ of the catalysts studied in this work along with the signals for the Fe foil, Fe_3O_4, Fe_3C and FePhC standard materials are shown in Fig. 3. As observed, the most intense peak in the spectra for all catalysts is centred at *ca.* 2.1 Å. However, this peak is asymmetric and the contribution from another peak at *ca.* 1.6 Å is evident, especially in the spectra for Fe/N/G and Fe/N/CNT. The first peak is consistent with a Fe—N or Fe—O distance, while the second peak corresponds to the first shell Fe-Fe distance in the metal foil or carbide phases. The intensity of the peak (shoulder) at ca. 1.6 Å is significantly smaller in the spectrum of Fe/N/AC. The most intense peaks in the spectra of the standard materials appear at *ca.* 1.6 (Fe_3O_4, FePhC, shoulder in Fe_3C), 2.1 (Fe foil, Fe_3C), 2.7 (Fe_3O_4), and 4.4 (Fe foil) Å.

The peak at 1.6 Å can be assigned to the distances Fe—C (Fe_3C), Fe—N (FePhC) and Fe—O (Fe_3O_4), whereas the rest of the peaks correspond to the distance FeFe in Fe foil 1st shell (2.1 Å), Fe_3C (2.1 Å), Fe_3O_4 (2.7 Å) and Fe foil 2nd shell (4.4 Å) [36–39].

The local structure of Fe in the catalysts under study resembles to that of the Fe_3C standard showing a peak at 2.1 Å (distance Fe—Fe) and shoulder at ca. 1.6 Å (distance Fe—C), indicating that Fe_3C is the most abundant iron phase in the catalysts (Fig. 3). However, the intensity of the peak at 1.6 Å in the spectra for Fe/N/G and Fe/N/CNT is almost the same than that of the main peak at *ca.* 2.1 Å suggesting that other iron species are present in these catalysts. As shown in Fig. 3, the peak at 1.6 Å is characteristic of Fe—N or Fe—O distances; however the presence latter species should be ruled out because the spectra for the catalysts lack of the most intense peaks at *ca.* 2.5 and 3.0 Å which are clearly observed in the spectra of

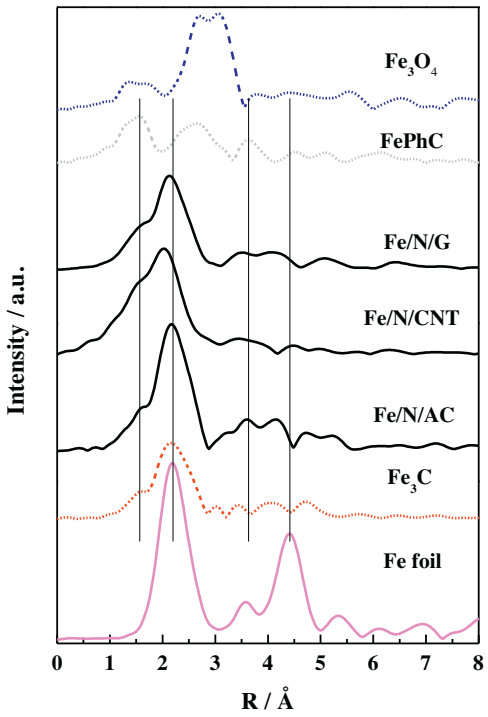

Fig. 3. FT EXAFS spectra for samples Fe/N/G, Fe/N/CNT and Fe/N/AC. Spectra of Fe foil, Fe_3O_4, Fe_3C and iron phthalocyanine (FePhC) are included for comparison.

the Fe_3O_4 standard. The formation of Fe_3N upon thermal treatments in highly concentrated NH_3 (>60 vol.%) has been proposed by other authors [40]. These phases are not protected by graphitic layers and can be passivated after air exposure forming Fe—O bonds. However, we found no evidences of the formation of iron nitride (Fe_3N) crystalline phases in our catalysts. Fig. S2 shows the X-ray diffractograms for the Fe/N/C catalysts (and for the pristine carbons). Although several diffraction lines for Fe_3C and Fe_3N appear at similar 2 theta values, the presence of small peaks between 48 and 49° along with the stronger diffraction line at 45° indicate the presence of Fe_3C. On the other hand, the most intense peak for Fe_3N at 43.55° is not observed in the diffractograms of the Fe/N/C catalysts. It should be noted that the small diffraction peak at 43.8° in the diffractograms for the Fe/N/C coincides better with the diffraction line for Fe_3C at 43.86° than with the one for Fe_3N at 43.55°. In fact, the absence of iron nitrides phases could be due to the low volume percentage of NH_3 (5%) used in the pyrolysis step during the synthesis of the Fe/N/C catalysts reported in this work, (see Section 2). As a consequence, the peak at 1.6 Å is assigned to Fe—N distance similar to those found in FePhc that are present in Fe/N/G and Fe/N/CNT. It should be noted that the Fe—N species in these catalysts are not identical to those in the Fe-phthalocyanine used as reference; the X-ray absorption spectra clearly indicate the formation of FeNx species in the catalysts. The abundance of these FeNx-like species is higher in Fe/N/G and Fe/N/CNT than in Fe/N/AC, which is mainly composed by Fe_3C-like iron species. This conclusion is also supported by the XANES (Fig. 2), where the Fe absorption edge of Fe/N/G and Fe/N/CNT is shifted toward higher energies. However, the formation of Fe—O bonds in the surface of the carbon matrix can be produced in a small extend, and it is compatible with the EXAFS spectroscopic results.

As shown above, Fe_3C species were not detected by XPS (neither in the Fe 2p nor in the C 1s core-level regions) indicating that such Fe_3C species are encapsulated within the carbon matrix rather than exposed at the catalyst surface. This conclusion is in line with the surface and bulk Fe/C atomic ratios calculated from XPS and

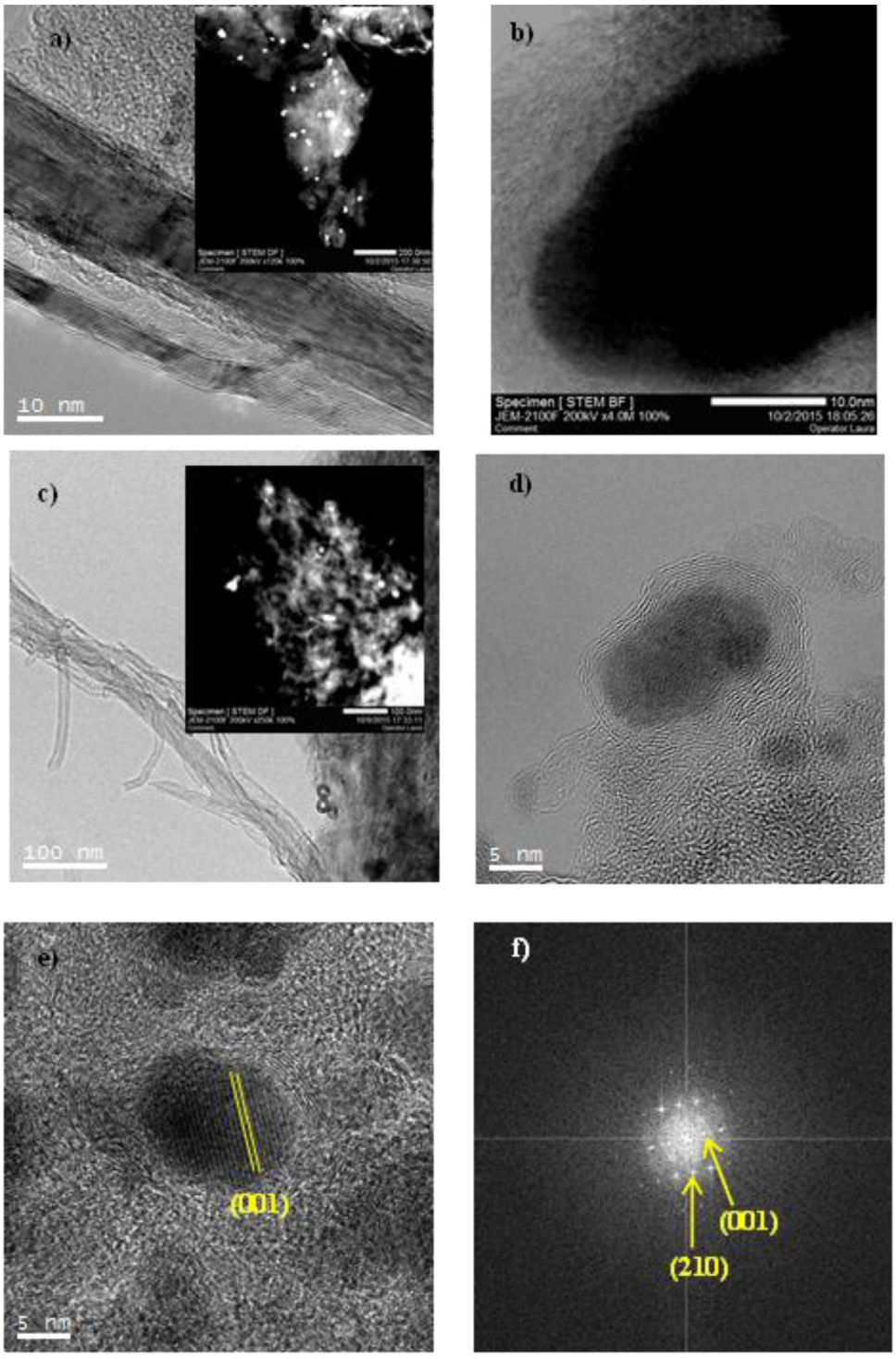

Fig. 4. (a) and (b) TEM and STEM (bright field) images of Fe/N/G. The inset to figure (a) is a STEM image for Fe/N/G. (c) and (d) TEM images of Fe/N/CNT. The inset to figure (c) is a STEM image for Fe/N/CNT. (e) HR-TEM for an iron particle in Fe/N/CNT showing the (0 0 1) planes of Fe_3C. (f) Digital diffraction pattern of the iron particle shown in (e) highlighting the spots for the (0 0 1) and (2 1 0) planes in Fe_3C.

ICP-OES analyses (see Table 2), respectively, which show that an important fraction of the iron atoms remain in the catalyst bulk rather than at the catalyst surface.

As stated above the XPS analyses indicate the presence of iron oxidized species either as Fe–Nx and/or Fe_3O_4, at the catalyst surface. Taking into account that the presence of the latter species has been ruled out by XAS, the iron species responsible for the XPS peaks are assigned to nitrogen coordinated Fe species similar to those in iron phthalocyanine suggesting that Fe–Nx-like species are the only iron species at the catalysts surface.

The characterization results clearly indicate that the nature of the carbon matrix used for the preparation of Fe/N/C electrocatalysts has a strong influence in the actual nature of the Fe species formed in the final catalysts. The use of graphene-like and CNTs matrixes lead to the stabilization of Fe/Nx ensembles at the catalyst surface. In addition, the nature of carbon material also determines

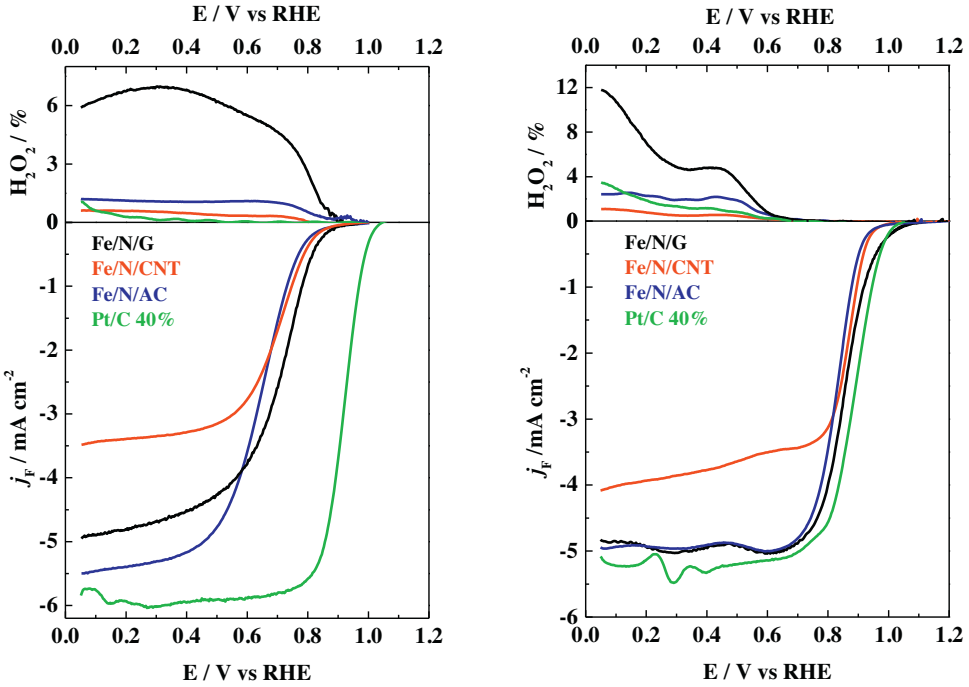

Fig. 5. ORR polarization curves and% H_2O_2 obtained in 0.1 M $HClO_4$ (left panel) and 0.1 M KOH (right panel) with Fe/N/G Fe/N/CNT and Fe/N/AC recorded at 10 mV s^{-1} and 1600 rpm. The performance of Pt/C (40 wt.% from Johnson Matthey) is included for the sake of comparison.

the surface area and textural properties of the catalysts obtained after the pyrolysis step. Hence, the utilization of graphene or active carbon renders Fe/N/C electrocatalysts with higher surface areas than CNTs.

3.2. Catalyst morphology

Representative STEM and TEM images for Fe/N/G and Fe/N/CNT are shown in Fig. 4. Fig. 4a,c shows low magnification images for Fe/N/G and Fe/N/CNT, respectively. The characteristic layers the graphene nanoplates and of the carbon nanotubes can be observed in Fig. 4a,c, respectively, indicating that the structure of the carbon materials used for the synthesis of the catalysts maintained during the synthesis of the catalysts. Representative STEM images for Fe/N/G and Fe/N/CNT are shown as the insets to Fig. 4a,c, respectively. The brighter spots are indicative of the areas containing elements with high *Z* values, *i.e.*, these areas pinpoint the presence of iron particles. Fig. 4b,d shows HR-STEM and HR-TEM micrographs of the iron particles in Fe/N/G and Fe/N/CNT, respectively. As clearly observed in the images, the iron particles are encapsulated within several layers of graphene. The thickness these graphene layers is of *ca.* 3 nm or higher thus preventing the identification of these iron particles by a surface characterization technique such as XPS. As discussed above, EXAFS and XRD analyses indicate the presence of iron carbide (Fe_3C) phases in the catalysts but such species were not detected by XPS. It should be recalled that XRD also fails to indicate the presence of iron nitride (Fe_3N). The nature of the iron particles encapsulated into the graphene layers has been further studied by TEM. Fig. 4e shows a high resolution transmission electron microscopy image for a representative iron particle in Fe/N/CNT. The corresponding digital diffraction pattern is shown in Fig. 4f. The particle was found to lie on the grid oriented along a direction close to the zone axis [−120]. The particle has been indexed according to the unit cell parameters and space group for the Fe_3C structure type. Note that the indexation of this particle for any other crystalline phase of all those present in the Fe–C phase diagram, including the Fe metal itself was not possible.

3.3. Oxygen reduction performance

Fig. 5 shows the ORR polarization curves and hydrogen peroxide yields recorded in 0.1 M $HClO_4$ or 0.1 M KOH with the Fe/N/C catalysts. Irrespectively of the electrolyte, Fe/N/G exhibits the highest activity for the ORR within the range between 0.7 and 1.0 V (*i.e.*, in the kinetically controlled region), followed by Fe/N/CNT and Fe/N/AC.

The ORR can follow two reaction pathways; the so-called 4 electron pathway via the complete reduction of O_2 to H_2O, or the 2 electron pathway where H_2O_2 is formed. As observed in Fig. 5, Fe/N/G records the highest H_2O_2 production of the catalysts under study in both acid and alkaline electrolytes.

The amount of H_2O_2 produced is calculated from Eq. (1). The average number of electrons transferred per O_2 molecule (ne) can be calculated from the H_2O_2 yield calculated from Eq. (2). Thus, Fe/N/G shows a decrease from ne = 4 (no peroxide generation) at 0.75 V to ne = 3.89 at 0.05 V in alkaline media. In acid media, the average number of electron varies from 3.95 at 0.80 V to 3.88 at 0.05 V with a maximum yield of hydrogen peroxide of 7% (ne = 3.86) at 0.30 V. In both cases, the results are very close to the desired value of 4 in line with the results obtained for other non-precious metal catalysts [17]. Fe/N/CNT and Fe/N/AC record lower hydrogen peroxide yields ranging between 1 and 2%, respectively, in both alkaline and acid media.

Fig. 6 shows the mass transport corrected mass activities (i_M) for the Fe/N/C catalysts calculated from Eqs. (3) and (4) recorded in the kinetically controlled region in both acid and alkaline media. The ORR activity trend is more clearly observed, and the i_M for the ORR follows the order Fe/N/G > Fe/N/CNT > Fe/N/AC, irrespectively of the pH of the electrolyte.

The Fe/N/C catalysts reported in this work exhibit higher ORR activity in the alkaline electrolytes, in good agreement with previous results for Fe/N/C based catalysts [41,42]. Although the reason for this fact remains unclear, it is accepted that in alkaline media the ORR is an outer-sphere process whereby the production of H_2O_2 is the predominant reaction pathway [43]. Ramaswamy and Muk-

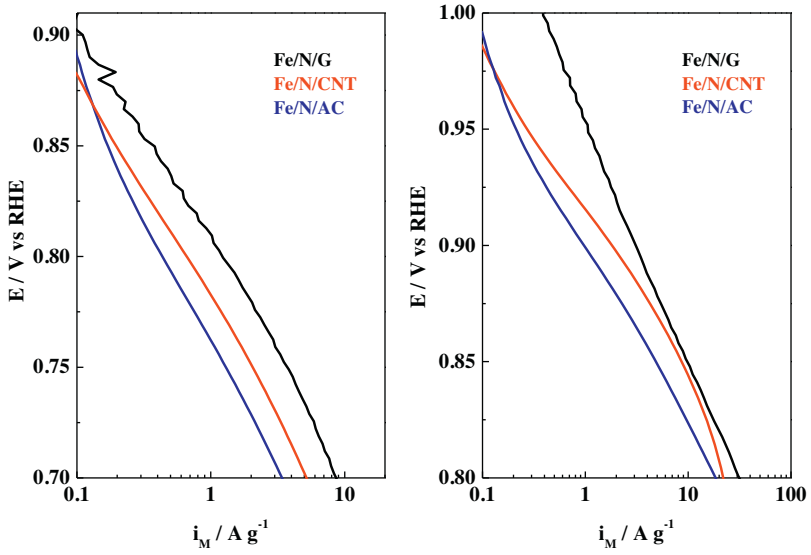

Fig. 6. ORR mass activities in 0.1 M $HClO_4$ (left panel) and 0.1 M KOH (right panel) for the Fe/N/G, Fe/N/CNT and Fe/N/AC recorded at 10 mV s^{-1} and 1600 rpm.

erjee [43] claim that Fe^{2+} sites in Fe/N/C catalysts are capable of stabilizing the peroxide intermediate species in alkaline media, *i.e.*, HO_2^- thus promoting the complete reduction of O_2 to H_2O. On the other hand, Blizanac et al. [44] studied the effect of pH in the ORR with noble metals and concluded that whereas the rate determining step (the transfer of one electron to $O_{2,ad}$ to $O_{2,ad}^-$) is a pH independent process, the reversible potential for the protonation of O_2^- and the formation of peroxide (HO_2^-) is pH dependent. Hence, the thermodynamic potential for peroxide formation shifts to more negative values at alkaline pH and overlaps with the thermodynamic potential of formation of O_2^-. Due to this overlap in equilibrium potentials, the overpotential required to reduce oxygen to peroxide is very low and only weak adsorption of O_2^- in alkaline media is needed to bring the potential of the rate determining step into a useful potential (*vs.* RHE) range.

The mass activity for the ORR in alkaline media with Fe/N/G measured at 0.9 V is of 3.1 ± 0.3 A g^{-1}, or a volumetric activity of 1.25 A cm^{-3} if an effective catalysts density of 0.4 g cm^{-3} is assumed [45]. This value is amongst the highest mass activities reported in literature for similar Fe/N/C based catalysts [17,46,47]. This mass activity value is of only 8 times lower than that recorded with benchmark Pt/C catalyst (Pt 40 wt.%) of 25.8 A g^{-1} at 0.9 V (Fig. S3), a factor that allows to consider Fe/N/G as a feasible alternative to replacing Pt/C catalysts [45]. Moreover, the onset potential (E_{onset}) for the ORR with Fe/N/G, defined as the potential required for generating an ORR current density of 0.1 mA cm^{-2} in a steady-state RDE experiment [12], records a very positive value of 1.04 V, which is close to the best E_{onset} values reported for other Fe/N/C catalysts [17] and higher than the best onset potentials reported for Pt-free or Pt based catalysts in acid media of ca. 1.0 V with Fe- and Co-ordered mesoporous catalysts [16] and single-crystal Pt_3Ni [48] and of 1.05 V with nanoporous PtNi [49]. Also, Fe/N/G and Fe/N/CNT exhibit the same $E_{1/2}$ values of 0.86 V, shifting to 0.83 V for Fe/N/AC. These values are in line with the best $E_{1/2}$ values reported for Fe/N/C-based catalysts for the ORR in alkaline media of 0.86 V (catalyst loading 0.2 mg cm^{-2}) [17].

The question arises as to why Fe/N/G is more active for the ORR than the catalysts prepared with active carbon or carbon nanotubes. In principle, the ORR activity accounts to a combination of the following features, (i) number of active sites, (ii) intrinsic activity of those sites, *i.e.*, the turnover frequency (TOF) and/or (iii) accessibility to the active sites. As discussed above, Fe/N/G and Fe/N/AC exhibit similar BET areas of 415 and 362 m^2 g^{-1}, respectively, which are significantly higher than that of Fe/N/CNT (145 m^2 g^{-1}). On the other hand, all catalysts exhibit similar total N contents and a similar distribution of the N-species. However, the amount of surface Fe in Fe/N/G is 36% lower than in Fe/N/CNT and 22% lower than in Fe/N/AC. These results clearly indicate that the ORR activity is not directly related to the total amount of N or Fe atoms in the catalyst and that the nature of the surface exposed Fe/Nx ensembles actually determines the final performance of the catalysts. According to the X-ray absorption spectra (XANES and EXAFS in Figs. 2 and 3, respectively) Fe/N/G and Fe/N/CNT have higher amount of FeNx like species than Fe/N/AC. Taking into account that most studies coincide in that N-coordinated Fe atoms, typically FeN_4 and/or FeN_{2+2} moieties [36,50], are the most active sites for the ORR [6,36] the higher ORR activity of Fe/N/G and Fe/N/CNT can be ascribed to a higher amount of active sites for the ORR available in those catalysts as compared with the Fe/N/AC counterpart.

3.4. Long term stability tests

Displaying high electrocatalytic activity for the ORR is not the only requirement for NPMCs to replace Pt/C as cathode electrodes of commercial fuel cells. Durability is in fact a serious issue to be addressed with Fe-based electrodes for the ORR [51]. An improved durability both during operation and start up and stop cycles of a fuel cell is an essential feature of a commercial catalyst. A benchmark protocol for O_2 saturated the assessment of stability and durability of Fe/N/C based catalyst has not been reported hitherto. Different groups report different protocols based upon repeated cycling typically between 0.6 and 1.0 V [16,17], or between 0.6 and 1.3 V [52] in N_2 saturated electrolytes. Other protocols are based upon square-wave programs in N_2 saturated electrolytes between 0.9 and 1.4 V [51]. Recently, the DOE recommended to increase the upper potential limit up to 1.4 V in order to better simulate start-up/shutdown processes in a fuel cell [53].

In a first step, the stability of the catalysts was assessed by subjecting all of catalysts to 3000 consecutive cycles between 0.6 and 1.0 V at 50 mV s^{-1} in O_2 saturated 0.1 M KOH. Fig. 7 shows the mass activities (i_M) for Fe/N/G, Fe/N/CNT and Fe/N/AC in the kinetically controlled region before and after the stability tests.

As observed, Fe/N/G and Fe/N/CNT are very stable recording identical i_M at 0.9 V before and after recording 3000 consecutive potential cycles in O_2 saturated electrolytes. On the other hand, Fe/N/AC becomes severely degraded, recording a mass activity loss

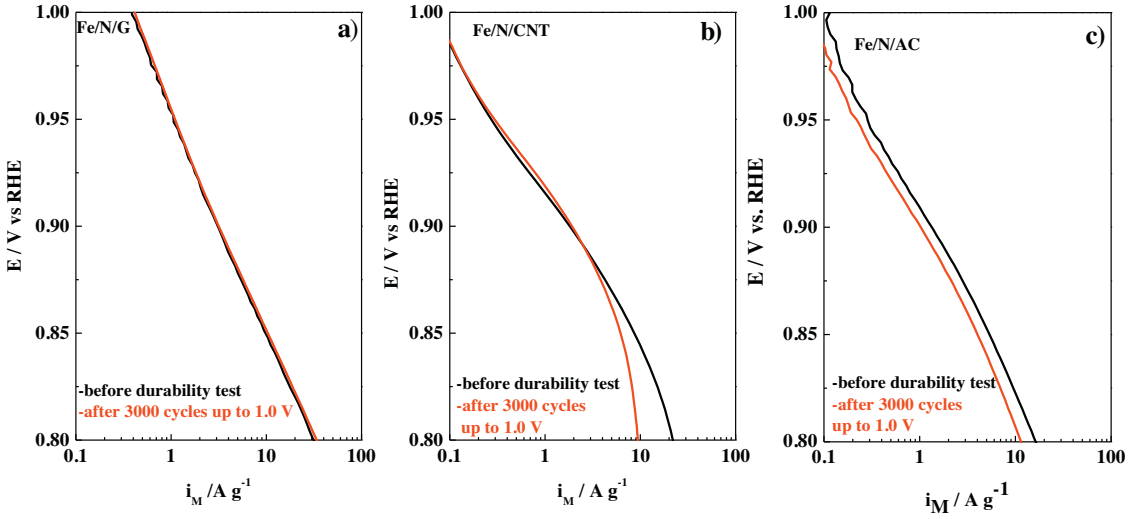

Fig. 7. ORR mass activities in 0.1 M KOH at 10 mV s^{-1} and 1600 rpm for Fe/N/G (a), Fe/N/CNT (b) and Fe/N/AC (c) before (black lines) and after (red lines) the stability tests: 3000 cycles between 0.6 and 1.0 V at 50 mV s^{-1}. (For interpretation of the references to color in this figure legend, the reader is referred to the web version of this article.)

of *ca.* 24% at 0.9 V. The stability of these Fe/N-based catalysts in alkaline electrolyte is higher than that of the benchmark Pt/C (40 wt.%) catalyst which records a severe mass activity loss of *ca.* 64% at 0.9 V after cycling at same conditions (see Fig. S3). The most stable catalysts in alkaline media (Fe/N/G and Fe/N/CNT) were subjected to the same stability test but in acid media (0.1 M $HClO_4$). Fig. S4 shows the mass activities for the catalysts before and after the stability tests. As observed, the stability of, Fe/N/G and Fe/N/CNT in the acidic electrolyte is significantly lower than in the alkaline one showing mass activity losses at 0.9 V of 42% and 54%, respectively.

In view of the high stability of these catalysts, especially Fe/N/G, we have conducted a more severe degradation test which consists in consecutive cycling of the electrode in O_2 saturated alkaline electrolyte between 0.4 and 1.4 V at 1 V s^{-1}. This protocol is similar to that reported for the study of Pt/C catalysts [54], but more severe than those reported recently for Fe/N/C based catalysts [52]. Fig. 8 shows the ORR polarization curves and the mass transport corrected mass activities (i_M) in the kinetically controlled region recorded with Fe/N/G, Fe/N/AC and Fe/N/CNT catalysts in alkaline media before and after the stability test. Again, Fe/N/G exhibits an excellent stability showing almost identical j_F and i_M values within the potential region between E_{onset} and $E = 0.8$ V.

These results suggest that the use of graphene as carbon matrix for the preparation of NPMCs confers unique properties to the final material for ORR in terms of activity and especially in terms of stability. As shown in Fig. 8, the ORR activity of Fe/N/G remains very stable after being subjected to repeated cycling up to potential values of 1.4 V for 3000 consecutive cycles. The mass activity decreases *ca.* 10% after this severe durability test. This value translates into a ΔE of ≈10 mV to less positive values for obtaining a current density of 3.1 A g^{-1} before and after the stability test. When subjected to the same harsh duration test (3000 cycles up to 1.4 V), the Fe/N/CNT catalyst records a severe a mass activity loss of 28% at 0.9 V as shown in Fig. S3. This ORR activity decay is very similar to the one observed for Fe/N/AC catalyst after cycling up to 1.4 V.

To the best of our knowledge this is the first time that such a high stability for the ORR with Fe/N/C based catalysts has been reported under severe degradation conditions, demonstrating the potential benefits of the use of graphene as carbon matrix for the preparation of NPMCs for the ORR in alkaline media.

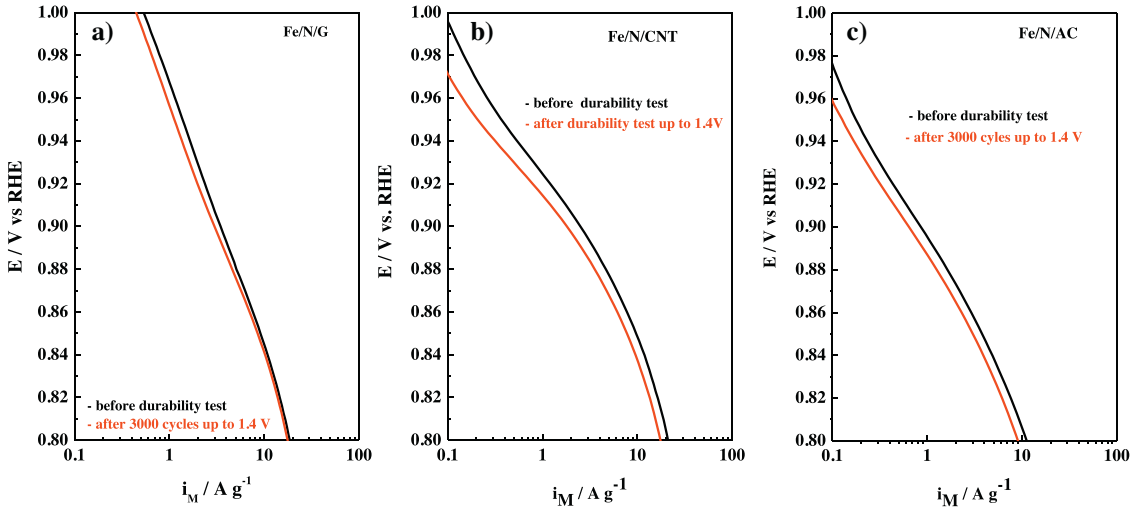

Fig. 8. ORR mass activities for Fe/N/G, Fe/N/CNT and Fe/N/AC catalysts recorded in O_2 saturated 0.1 M KOH at 10 mV s^{-1} and 1600 rpm before (black line) and after (red line) the stability test: 3000 cycles between 0.4 and 1.4 V at 1 V s^{-1}. (For interpretation of the references to color in this figure legend, the reader is referred to the web version of this article.)

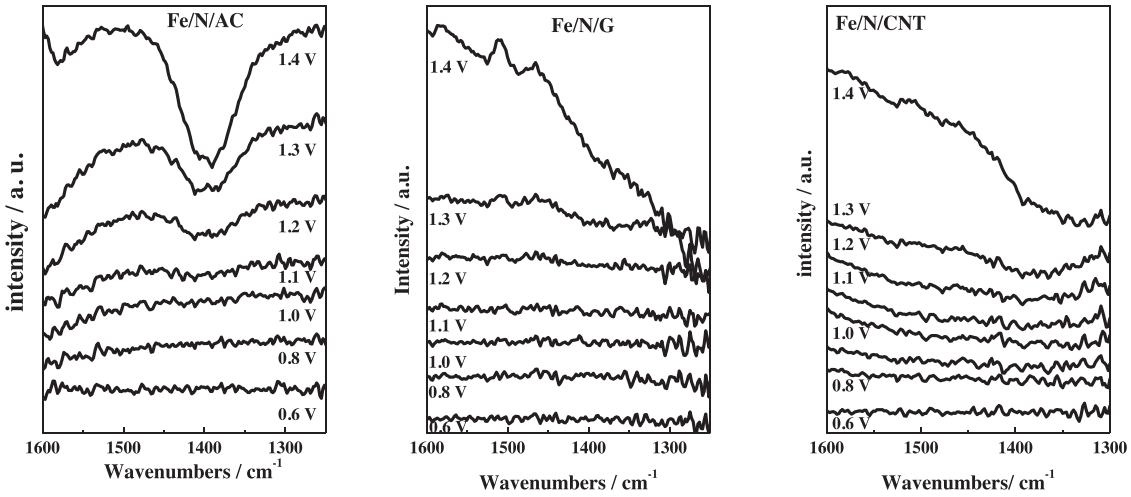

Fig. 9. *In situ* IRRA spectra recorded at different potentials up to 1.4 V in KOH 0.1 M Ar-saturated electrolytes for Fe/N/AC, Fe/N/G and Fe/N/CNT catalysts.

In principle, several effects can contribute to the degradation of Fe/N/C catalysts such as the oxidation of the iron cations coordinated to nitrogen leading to demetallation and/or the elimination of FeNx sites embedded in carbon matrix due to corrosion of the surrounding carbon support [51]. In order to assess whether the higher stability of Fe/N/G catalyst is related to a better resistance against corrosion, we studied the evolution of the catalysts with the applied potential by means of in situ electrochemical infrared reflection adsorption spectroscopy (EC-IRRAS). In principle, carbon corrosion can be monitored by following the evolution of evolved CO_2 with potential. However, CO_2 is not a stable species in alkaline electrolyte forming carbonates at high pH values. Carbonates are characterized by an IR band at *ca.* 1400 cm^{-1}. Note that negative going bands in the IRRA spectra are indicative of the formation of species.

Fig. 9 shows the 1600 and 1250 cm^{-1} region of the IR spectra recorded during the ORR in alkaline electrolyte. A negative going band at 1400 cm^{-1} is clearly observed in the spectra for Fe/N/AC recorded at $E \geq 1.1$ V. This band, which is ascribed to the formation of carbonate species, is indicative of the formation of CO_2 due to the over oxidation of the active carbon at $E \geq 1.1$ V. On the other hand, the spectra recorded for Fe/N/G are featureless, and IR bands indicative of the formation of carbonates (or CO_2) or other oxidized species are not observed. The spectra recorded for Fe/N/CNT resemble to those recorded for Fe/N/G and the formation of carbonate species is not as clearly observed as with Fe/N/AC. Nonetheless, the spectra recorded at $E \geq 1.3$ V show a low intense broad band at *ca.* 1400 cm^{-1} which could be indicative of the incipient formation of carbonates.

In order to verify the formation of CO_2 with the applied potential, the IR spectra were also recorded in acid electrolyte (0.1 M $HClO_4$) under the same experimental conditions. In line with the experiments in alkaline electrolyte, the formation of CO_2 (characterized by an IR band at 2343 cm^{-1}) is clearly observed in the spectra recorded at $E \geq 1.2$ V with Fe/N/AC (Fig. S4). On the other hand, the spectra recorded with Fe/N/G or Fe/N/CNT only show a very low intense band at *ca.* 2343 cm^{-1} ascribed to the formation of CO_2 at $E \geq 1.4$ V and 1.3 V, respectively. This behavior indicates that graphene and CNTs are more stable supports towards corrosion than active carbon. It should be noted that CO_2 formation with CNT is slightly higher than with graphene suggesting that CNTs are more prone to be oxidized than graphene, *i.e.*, they are more stable than AC but less stable than graphene. With these results in mind, and taking into account that the nature of the Fe–Nx sites at the catalyst surface is similar in all catalysts, it is clear that the loss of the catalytic activity of Fe/N/C catalysts is directly related with the stability of the carbon matrix against corrosion (CO_2 formation) than with the stability of the Fe/Nx ensembles. It should be remarked that catalyst deactivation is only observed once carbon corrosion takes place. Therefore, using highly graphitized materials such as graphene-like or, to a lesser extent CNTs, prevents carbon corrosion and as a result the Fe/Nx moieties remain stable at the catalyst surface (see the high ORR stability of Fe/N/G shown in Fig. 8), especially with Fe/N/G. On the contrary, Fe/N/AC is the most prone of the catalysts under study to suffer carbon corrosion through a 4 electron mechanism producing CO_2 (leading to the formation of carbonates in alkaline electrolytes). As a consequence, upon carbon oxidation the Fe/Nx active sites are no longer stable at the catalyst surface probably leaching into the electrolyte. As a consequence the ORR activity of Fe/N/AC drops more significantly than that of Fe/N/G or Fe/N/CNT in which Fe/Nx ensembles remain stable within the resistant carbon matrix. It should be remarked that the stability of the Fe/N/C catalysts is only affected by the stability of the carbon matrix and that once the threshold potential for carbon corrosion is reached a severe loss in the catalytic performance for the ORR is observed regardless of the actual nature of the carbon matrix. Thus, Fe/N/CNT losses *ca.* 29% of its mass activity for the ORR when subjected to potentials above 1.3 V; this value is the onset potential for the corrosion of the CNTs.

Conclusions

This paper shows that the nature of the carbon matrix (graphene, carbon nanotubes or active carbon) is an important parameter for the designing of NPMCs based upon Fe/N/carbon. Catalysts prepared with graphitic materials such as graphene or CNTs result in the preferential formation of FeNx-like species at the catalyst surface and as a result to a higher activity for the ORR in acid and alkaline electrolytes. In addition, graphene is highly resistant towards corrosion at potentials up to 1.4. As a consequence the Fe/Nx ensembles formed on graphene are also extremely stable for the ORR in alkaline media. In fact, the activity of Fe/N/G for the ORR in alkaline electrolyte remains stable even after severe degradation protocol consisting in subjecting the electrode to 3000 consecutive cycles up to 1.4 V.

Acknowledgments

This project was funded by the Deanship of Scientific Research (DSR), King Abdulaziz University, Jeddah, under grant number

(D002/436). The authors, therefore, acknowledge with thanks DSR technical and financial support. Economic support from projects ENE2013-42322-R from the Spanish Ministry of Economy and Competitiveness, and project 201480E122 from the CSIC are also acknowledged. XAS experiments were performed at CLAESS beamline at ALBA Synchrotron with the collaboration of ALBA staff.

Appendix A. Supplementary data

Supplementary data associated with this article can be found, in the online version, at http://dx.doi.org/10.1016/j.apcatb.2015.10.043.

References

[1] Y. Wang, K.S. Chen, J. Mishler, S.C. Cho, X.C. Adroher, A review of polymer electrolyte membrane fuel cells: technology, applications, and needs on fundamental research, Appl. Energy 88 (2011) 981–1007.
[2] G. Girishkumar, B. McCloskey, A.C. Luntz, S. Swanson, W. Wilcke, Lithium–air battery: promise and challenges, J. Phys. Chem. Lett. 1 (2010) 2193–2203.
[3] C.C.L. McCrory, S. Jung, I.M. Ferrer, S.M. Chatman, J.C. Peters, T.F. Jaramillo, Benchmarking hydrogen evolving reaction and oxygen evolving reaction electrocatalysts for solar water splitting devices, J. Am. Chem. Soc. 137 (2015) 4347–4357.
[4] I. Katsounaros, S. Cherevko, A.R. Zeradjanin, K.J.J. Mayrhofer, Oxygen electrochemistry as a cornerstone for sustainable energy conversion, Angew. Chem. Int. Ed. 53 (2014) 102–121.
[5] M.S. Faber, S. Jin, Earth-abundant inorganic electrocatalysts and their nanostructures for energy conversion applications, Energy Environ. Sci. 7 (2014) 3519–3542.
[6] F. Jaouen, J. Herranz, M. Lefèvre, J.P. Dodelet, U.I. Kramm, I. Herrmann, P. Bogdanoff, J. Maruyama, T. Nagaoka, A. Garsuch, J.R. Dahn, T. Olson, S. Pylypenko, P. Atanassov, E.A. Ustinov, Cross-laboratory experimental study of non-noble-metal electrocatalysts for the oxygen reduction reaction, ACS Appl. Mater. Interface 1 (2009) 1623–1639.
[7] F. Jaouen, E. Proietti, M. Lefèvre, R. Chenitz, J.P. Dodelet, G. Wu, H.T. Chung, C.M. Johnston, P. Zelenay, Recent advances in non-precious metal catalysis for oxygen-reduction reaction in polymer electrolyte fuel cells, Energ. Environ. Sci. 4 (2011) 114–130.
[8] M. Lefèvre, E. Proietti, F. Jaouen, J.P. Dodelet, Iron-based catalysts with improved oxygen reduction activity in polymer electrolyte fuel cells, Science 324 (2009) 71–74.
[9] Y. Li, W. Zhou, H. Wang, L. Xie, Y. Liang, F. Wei, J.C. Idrobo, S.J. Pennycook, H. Dai, An oxygen reduction electrocatalyst based on carbon nanotube-graphene complexes, Nat. Nanotechnol. 7 (2012) 394–400.
[10] M. Liu, R. Zhang, W. Chen, Graphene-supported nanoelectrocatalysts for fuel cells: synthesis properties and applications, Chem. Rev. 114 (2014) 5117–5160.
[11] E. Proietti, F. Jaouen, M. Lefèvre, N. Larouche, J. Tian, J. Herranz, J.P. Dodelet, Iron-based cathode catalyst with enhanced power density in polymer electrolyte membrane fuel cells, Nat. Commun. 2 (2011).
[12] G. Wu, K.L. More, C.M. Johnston, P. Zelenay, High-performance electrocatalysts for oxygen reduction derived from polyaniline, iron, and cobalt, Science 332 (2011) 443–447.
[13] G. Wu, P. Zelenay, Nanostructured nonprecious metal catalysts for oxygen reduction reaction, Acc. Chem. Res. 46 (2013) 1878–1889.
[14] Z.S. Wu, S. Yang, Y. Sun, K. Parvez, X. Feng, K. Müllen, 3D nitrogen-doped graphene aerogel-supported Fe_3O_4 nanoparticles as efficient electrocatalysts for the oxygen reduction reaction, J. Am. Chem. Soc. 134 (2012) 9082–9085.
[15] C. Domínguez, F.J. Pérez-Alonso, M. Abdel Salam, J.L. Gómez De La Fuente, S.A. Al-Thabaiti, S.N. Basahel, M.A. Peña, J.L.G. Fierro, S. Rojas, Effect of transition metal (M: Fe, Co or Mn) for the oxygen reduction reaction with non-precious metal catalysts in acid medium, Int. J. Hydrog. Energy 39 (2014) 5309–5318.
[16] J.Y. Cheon, T. Kim, Y. Choi, H.Y. Jeong, M.G. Kim, Y.J. Sa, J. Kim, Z. Lee, T.H. Yang, K. Kwon, O. Terasaki, G.G. Park, R.R. Adzic, S.H. Joo, Ordered mesoporous porphyrinic carbons with very high electrocatalytic activity for the oxygen reduction reaction, Scientific Rep. 3 (2013).
[17] H.T. Chung, J.H. Won, P. Zelenay, Active and stable carbon nanotube/nanoparticle composite electrocatalyst for oxygen reduction, Nat. Commun. 4 (2013).
[18] S. Zhang, H. Zhang, X. Hua, S. Chen, Tailoring molecular architectures of Fe phthalocyanine on nanocarbon supports for high oxygen reduction performance, J. Mat. Chem. A 3 (2015) 10013–10019.
[19] D.W. Wang, D. Su, Heterogeneous nanocarbon materials for oxygen reduction reaction, Energy Environ. Sci. 7 (2014) 576–591.
[20] C. Domínguez, F.J. Pérez-Alonso, M. Abdel Salam, S.A. Al-Thabaiti, A.Y. Obaid, A.A. Alshehri, J.L. Gómez de la Fuente, J.L.G. Fierro, S. Rojas, On the relationship between N content, textural properties and catalytic performance for the oxygen reduction reaction of N/CNT, Appl. Catal. B: Environ. 162 (2015) 420–429.
[21] F. Jaouen, M. Lefèvre, J.P. Dodelet, M. Cai, Heat-treated Fe/N/C catalysts for O2 electroreduction: are active sites hosted in micropores? J. Phys. Chem. B 110 (2006) 5553–5558.
[22] X. Zhou, J. Qiao, L. Yang, J. Zhang, A review of graphene-based nanostructural materials for both catalyst supports and metal-free catalysts in PEM fuel cell oxygen reduction reactions, Adv. Energ. Mater. 4 (2014), n/a-n/a.
[23] A.O. Al-Youbi, J.L. Gómez de la Fuente, F.J. Pérez-Alonso, A.Y. Obaid, J.L.G. Fierro, M.A. Peña, M. Abdel Salam, S. Rojas, Effects of multiwalled carbon nanotube morphology on the synthesis and electrocatalytic performance of Pt supported by multiwalled carbon nanotubes, Appl. Catal. B: Environ. 150-151 (2014) 21–29.
[24] G. Wu, K.L. More, P. Xu, H.L. Wang, M. Ferrandon, A.J. Kropf, D.J. Myers, S. Ma, C.M. Johnston, P. Zelenay, A carbon-nanotube-supported graphene-rich non-precious metal oxygen reduction catalyst with enhanced performance durability, Chem. Commun. 49 (2013) 3291–3293.
[25] C. Zhang, R. Hao, H. Yin, F. Liu, Y. Hou, Iron phthalocyanine and nitrogen-doped graphene composite as a novel non-precious catalyst for the oxygen reduction reaction, Nanoscale 4 (2012) 7326–7329.
[26] P. Chen, T.Y. Xiao, Y.H. Qian, S.S. Li, S.H. Yu, A nitrogen-doped graphene/carbon nanotube nanocomposite with synergistically enhanced electrochemical activity, Adv. Mater. 25 (2013) 3192–3196.
[27] G.-L. Tian, M.-Q. Zhao, D. Yu, X.-Y. Kong, J.-Q. Huang, Q. Zhang, F. Wei, Nitrogen-doped graphene/carbon nanotube hybrids: in situ formation on bifunctional catalysts and their superior electrocatalytic activity for oxygen evolution/reduction reaction, Small 10 (2014) 2251–2259.
[28] R. Zhang, S. He, Y. Lu, W. Chen, Fe, Co N-functionalized carbon nanotubes in situ grown on 3D porous N-doped carbon foams as a noble metal-free catalyst for oxygen reduction, J. Mater. Chem. A 3 (2015) 3559–3567.
[29] C.D. Wagner, L.E. Davis, M.V. Zeller, J.A. Taylor, R.H. Raymond, L.H. Gale, Empirical atomic sensitivity factors for quantitative analysis by electron spectroscopy for chemical analysis, Surf. Interface Anal. 3 (1981) 211–225.
[30] K.V. Klementev, Extraction of the fine structure from X-ray absorption spectra, J. Phys. D: Appl. Phys. 34 (2001) 209.
[31] U.A. Paulus, T.J. Schmidt, H.A. Gasteiger, R.J. Behm, Oxygen reduction on a high-surface area Pt/vulcan carbon catalyst: a thin-film rotating ring-disk electrode study, J. Electroanal. Chem. 495 (2001) 134–145.
[32] J.R. Pels, F. Kapteijn, J.A. Moulijn, Q. Zhu, K.M. Thomas, Evolution of nitrogen functionalities in carbonaceous materials during pyrolysis, Carbon 33 (1995) 1641–1653.
[33] T. Herranz, S. Rojas, M. Ojeda, F.J. Pérez-Alonso, P. Terreros, K. Pirota, J.L.G. Fierro, Synthesis, structural features, and reactivity of Fe–Mn mixed oxides prepared by microemulsion, Chem. Mater. 18 (2006) 2364–2375.
[34] M. Muhler, R. Schlögl, G. Ertl, The nature of the iron oxide-based catalyst for dehydrogenation of ethylbenzene to styrene 2. Surface chemistry of the active phase, J. Catal. 138 (1992) 413–444.
[35] A.P. Grosvenor, B.A. Kobe, M.C. Biesinger, N.S. McIntyre, Investigation of multiplet splitting of Fe 2p XPS spectra and bonding in iron compounds, Surf. Interface Anal. 36 (2004) 1564–1574.
[36] U.I. Kramm, J. Herranz, N. Larouche, T.M. Arruda, M. Lefèvre, F. Jaouen, P. Bogdanoff, S. Fiechter, I. Abs-Wurmbach, S. Mukerjee, J.P. Dodelet, Structure of the catalytic sites in Fe/N/C-catalysts for O_2-reduction in PEM fuel cells, Phys. Chem. Chem. Phys. 14 (2012) 11673–11688.
[37] U. Tylus, Q. Jia, K. Strickland, N. Ramaswamy, A. Serov, P. Atanassov, S. Mukerjee, Elucidating oxygen reduction active sites in pyrolyzed metal-nitrogen coordinated non-precious-metal electrocatalyst systems, J. Phys. Chem. C 118 (2014) 8999–9008.
[38] H.R. Byon, J. Suntivich, E.J. Crumlin, Y. Shao-Horn, Fe–N-modified multi-walled carbon nanotubes for oxygen reduction reaction in acid, Phys. Chem. Chem. Phys. 13 (2011) 21437–21445.
[39] D. Singh, J. Tian, K. Mamtani, J. King, J.T. Miller, U.S. Ozkan, A comparison of N-containing carbon nanostructures (CNx) and N-coordinated iron–carbon catalysts (FeNC) for the oxygen reduction reaction in acidic media, J. Catal. 317 (2014) 30–43.
[40] H. Meng, N. Larouche, M. Lefèvre, F. Jaouen, B. Stansfield, J.-P. Dodelet, Iron porphyrin-based cathode catalysts for polymer electrolyte membrane fuel cells: effect of NH_3 and Ar mixtures as pyrolysis gases on catalytic activity and stability, Electrochim. Acta 55 (2010) 6450–6461.
[41] C. Domínguez, F.J. Pérez-Alonso, J.L. Gómez De La Fuente, S.A. Al-Thabaiti, S.N. Basahel, A.O. Alyoubi, A.A. Alshehri, M.A. Peña, S. Rojas, Influence of the electrolyte for the oxygen reduction reaction with Fe/N/C and Fe/N/CNT electrocatalysts, J. Power Sources 271 (2014) 87–96.
[42] N. Ramaswamy, S. Mukerjee, Fundamental mechanistic understanding of electrocatalysis of oxygen reduction on Pt and non-Pt surfaces: acid versus alkaline media, Adv. Phys. Chem. 2012 (2012).
[43] N. Ramaswamy, S. Mukerjee, Influence of inner- and outer-sphere electron transfer mechanisms during electrocatalysis of oxygen reduction in alkaline media, J. Phys. Chem. C 115 (2011) 18015–18026.
[44] B.B. Blizanac, P.N. Ross, N.M. Markovic, Oxygen electroreduction on Ag(111): the pH effect, Electrochim. Acta 52 (2007) 2264–2271.
[45] H.A. Gasteiger, S.S. Kocha, B. Sompalli, F.T. Wagner, Activity benchmarks and requirements for Pt, Pt-alloy, and non-Pt oxygen reduction catalysts for PEMFCs, Appl. Catal. B Environ. 56 (2005) 9–35.
[46] M. Piana, S. Catanorchi, H.A. Gasteiger, Kinetics of non-Platinum group metal catalysts for the oxygen reduction reaction in alkaline medium, ECS Trans. 16 (2008) 2045–2055.

[47] H. Meng, F. Jaouen, E. Proietti, M. Lefèvre, J.P. Dodelet, pH-effect on oxygen reduction activity of Fe-based electro-catalysts, Electrochem. Commun. 11 (2009) 1986–1989.
[48] V.R. Stamenkovic, B. Fowler, B.S. Mun, G. Wang, P.N. Ross, C.A. Lucas, N.M. Markovic, Improved oxygen reduction activity on $Pt_3Ni(111)$ via increased surface site availability, Science 315 (2007) 493–497.
[49] J. Snyder, T. Fujita, M.W. Chen, J. Erlebacher, Oxygen reduction in nanoporous metal–ionic liquid composite electrocatalysts, Nat. Mater. 9 (2010) 904–907.
[50] J. Herranz, F. Jaouen, M. Lefèvre, U.I. Kramm, E. Proietti, J.P. Dodelet, P. Bogdanoff, S. Fiechter, I. Abs-Wurmbach, P. Bertrand, T.M. Arruda, S. Mukerjee, Unveiling N-protonation and anion-binding effects on Fe/N/C catalysts for O_2 reduction in proton-exchange-membrane fuel cells, J. Phys. Chem. C 115 (2011) 16087–16097.
[51] V. Goellner, C. Baldizzone, A. Schuppert, M.T. Sougrati, K. Mayrhofer, F. Jaouen, Degradation of Fe/N/C catalysts upon high polarization in acid medium, Phys. Chem. Chem. Phys. 16 (2014) 18454–18462.
[52] N. Ranjbar Sahraie, J.P. Paraknowitsch, C. Göbel, A. Thomas, P. Strasser, Noble-metal-free electrocatalysts with enhanced ORR performance by task-specific functionalization of carbon using ionic liquid precursor systems, J. Am. Chem. Soc. 136 (2014) 14486–14497.
[53] P. Zelenay, Non-PGM Target Update, 2015. http://energy.gov/sites/prod/files/2014/07/f17/fcto_cwg_june2014_zelenay.pdf.
[54] J.C. Meier, I. Katsounaros, C. Galeano, H.J. Bongard, A.A. Topalov, A. Kostka, A. Karschin, F. Schuth, K.J.J. Mayrhofer, Stability investigations of electrocatalysts on the nanoscale, Energy Environ. Sci. 5 (2012) 9319–9330.

SUPPLEMENTARY MATERIAL FOR MANUSCRIPT

Repercussion of the carbon matrix for the activity and stability of Fe/N/C electrocatalysts for the oxygen reduction reaction

Carlota Domínguez, Francisco José Pérez-Alonso, Mohamed Abdel Salam, Shaeel A. Al-Thabaiti, Miguel A. Peña, F. Javier García-García, Laura Barrio and Sergio Rojas

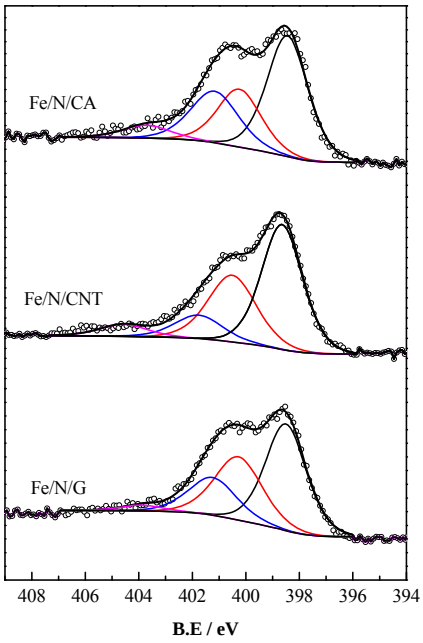

Fig. S1. N 1s core-level spectra for Fe/N/G, Fe/N/CNT and Fe/N/AC.

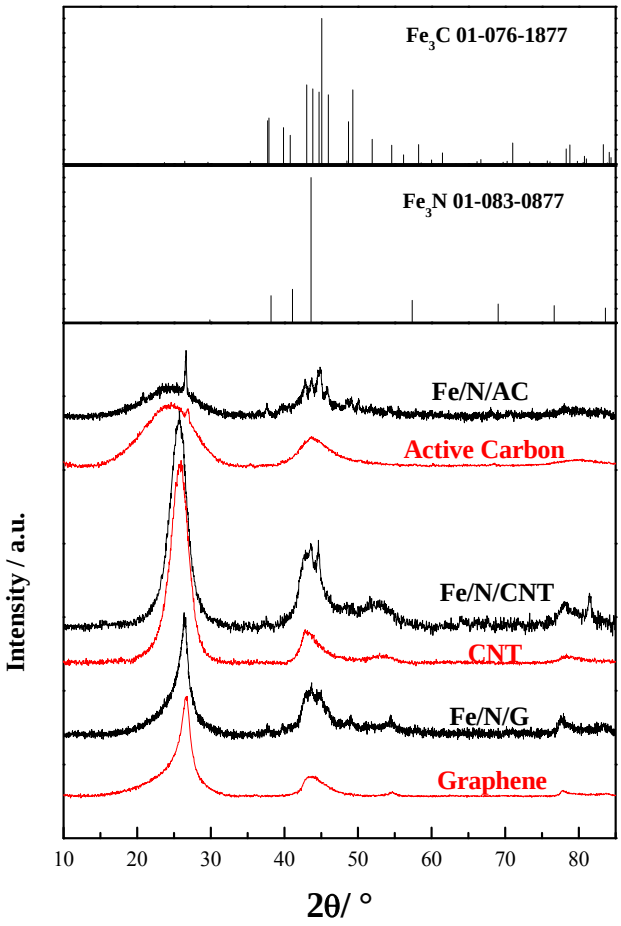

Figure S2. X-ray diffractograms of Fe/N/G, Fe/N/CNT and Fe/N/AC and the corresponding pristine carbon supports.

The activity for the ORR in O_2-saturated 0.1 M KOH electrolyte was tested by LSV in a RDE configuration. Long term stability tests were conducted by subjecting the catalyst to 3000 consecutive cycles between 0.6 and 1.0 V at 50 mV s^{-1}.

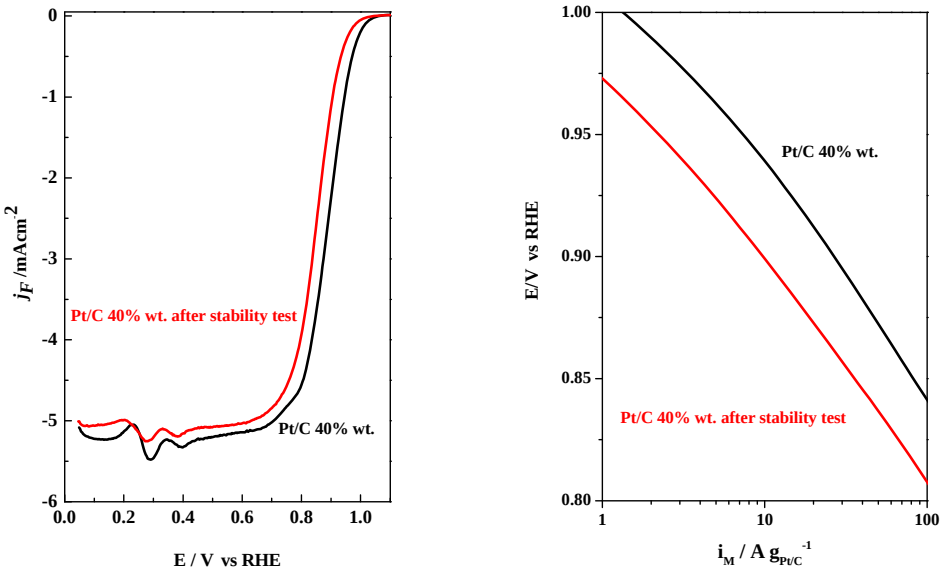

Fig. S3 ORR polarization curves (left figure) and ORR mass activities (right figure) in 0.1 M KOH at 10 mVs^{-1} and 1600 rpm for Pt/C 40% wt. before (black lines) and after (red lines) the stability tests: 3000 cycles between 0.6 and 1.0 V at 50 mVs^{-1}.

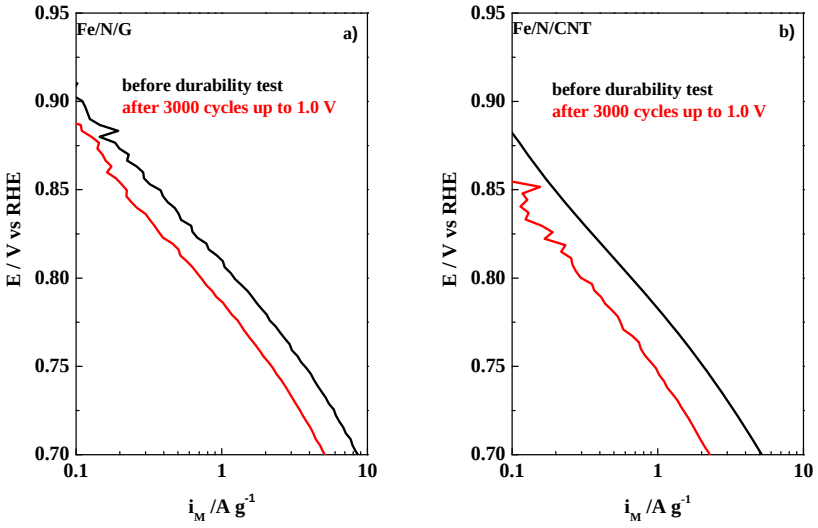

Figure S4. ORR mass activities in 0.1 M $HClO_4$ at 10 mVs^{-1} and 1600 rpm for Fe/N/G and Fe/N/CNT before (black) and after (red) the stability tests: 3000 cycles between 0.6 and 1.0 V at 50 mV s^{-1}.

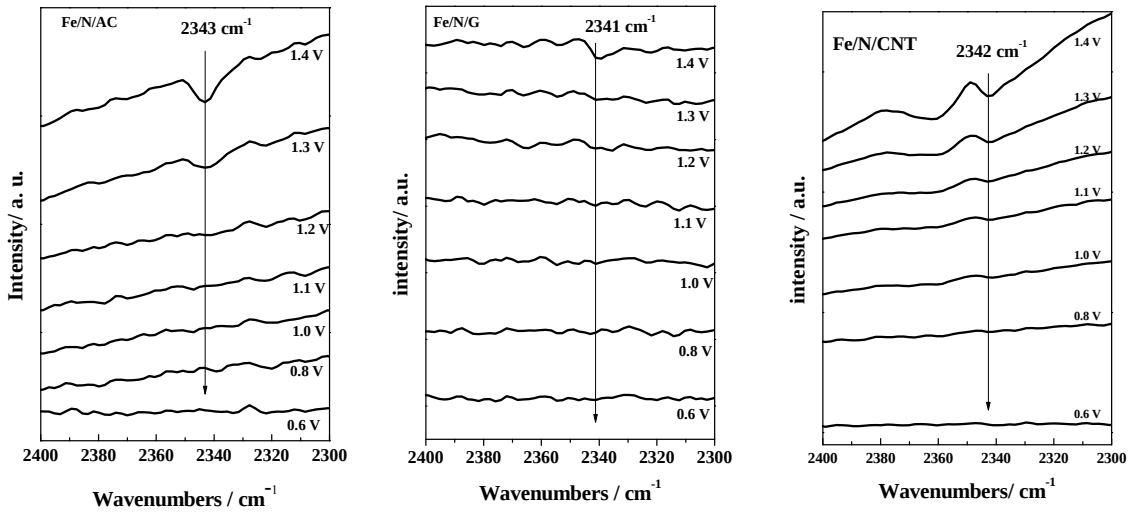

Fig S5. *In situ* IRRA spectra (64 scans) recorded at selected potentials (as indicated in the Figure) in 0.1 M $HClO_4$ Ar-saturated electrolytes for Fe/N/A, Fe/N/G and Fe/N/CNT catalysts.

The spectra were recorded in situ by applying by applying single potential steps between 0.6 and 1.4 V (RHE) in Ar- saturated 0.1 M $HClO_4$ electrolytes. 64 scans were accumulated during the collection of each spectrum. The spectra are referenced to a R^0 spectra collected at 0.6 V, as a consequence negative going bands account for appearing species.

The band at 2343 cm^{-1} is ascribed to the formation of CO_2 which is observed at $E \geq 1.3$ V with Fe/N/AC. A similar, less intense band is observed at 1.4V in the spectra with Fe/N/G

Chapter 4

Conclusions

This thesis addresses one of the most relevant challenges in the field of electrocatalysis for the oxygen reduction reaction, *i.e.*, the designing of optimized Fe/N/C catalysts for the ORR based on the understanding of their structure/activity relationships. The most relevant conclusions are:

- C/N composites are active for the ORR. The incorporation of N atoms into the carbon network of CNTs is favoured by the creation of defects in the C-C sp^2 network. Defects can be created by mechano-chemical methods such as ballmilling.
- The amount of N incorporated to the carbon network can be promoted by co-doping with other heteroatoms such as S.
- The presence of a transition metal in the N/C network increases the activity of the catalysts. Fe/N/C catalysts are more active for the ORR than Co/N/C and Mn/N/C.
- Active and stable Fe/N/C catalysts for the ORR are only successfully created after the pyrolysis treatment which leads to the formation of Fe-N_x moieties in the carbon matrix. The use of a reactive atmosphere of NH_3 during the pyrolysis treatment results in more active catalysts due to the gasification of the material and as a consequence higher BET surface areas were obtained.
- The fraction of Fe-N_x moieties increases when carbon matrixes with high graphitic character such as graphene or CNTs are used. The ORR activity increases with the amount of Fe-N_x moieties.

- The use of mechano-chemical methods such as planetary ballmilling, for the mixing step of different precursors used for the preparation of Fe/N/C-based catalysts, results in more active catalysts for the ORR than their mixture by wet impregnation method.

- The performance of the Fe/N/C catalysts is severe affected by the pH of the electrolyte. Higher ORR activities are recorded in alkaline electrolytes as compared to acidic ones. However, the effect of the counter ion is almost negligible in all (acid and alkaline) electrolytes studied.

- The use of acid treatments during the synthesis of Fe/N/C catalysts, to remove the unstable Fe species obtained after pyrolysis step, decreases the ORR performance of the final catalysts. This effect is produced by the strong adsorption of anions (sulphates when sulphuric acid is used for leaching treatment) onto the active sites. The activity can be only partially recovered after a thermal treatment at a temperature of at least 400 ^{o}C.

- Fe/N/C-based catalysts prepared with graphene or CNT carbon supports presents high resistance towards corrosion. Both Fe/N/G and Fe/N/CNT catalysts showed high durability after 3000 consecutive cycles at potentials up to 1.0 V and Fe/N/G presents an outstanding stability even after severe degradation tests of 3000 consecutive cycles at potentials up to 1.4 V.

Conclusiones

Esta tesis aborda uno de los retos más importante en el campo de la electrocatálisis para la reacción de reducción de oxígeno, como es el diseño y optimización de catalizadores Fe/N/C para la ORR y el estudio de su relación estructura/actividad. Las conclusiones más relevantes de este trabajo son:

- Los composites C/N son activos para la ORR. La incorporación de átomos de N dentro de la red de carbonos de los CNTs está favorecida por la creación de defectos en la red sp^2 C-C. Estos defectos se pueden crear mediante el uso de métodos mecano-químicos tales como el uso del molino de bolas.

- La cantidad de N incorporado a la red de carbonos se ve favorecida por el co-dopado con otros heteroátomos como el S.

- La presencia de metales de trasición en la red N/C aumenta la actividad de los catalizadores. Los catalizadores Fe/N/C son más activos para la ORR que los catalizadores Co/N/C y Mn/N/C.

- Se han creado catalizadores Fe/N/C activos y estables para la ORR despñues del tratamiento de pirolisis, el cual implica la formación de fracciones Fe-Nx en la matriz de carbón. El uso de una atmósfera reactiva de NH_3 durante el tratamiento de pirolisis da lugar a catalizadores más activos debido a la gasificación del material y como consecuencia se obtienen catalizadores con áreas superficiales BET más altas.

- La cantidad de fracciones Fe-N_x aumenta cuando se emplean matrices de carbón con estructuras más grafíticas como por ejemplo grafeno o CNTs. La actividad en la ORR aumenta con el aumento de las fracciones Fe-N_x.

- El uso de métodos mecano-químicos como el molino de bolas planetario para la etapa de mezcla de los diferentes precursores usados en la preparación de catalizadores basados en Fe/N/C, da lugar a catalizadores más activos para la ORR que la mezcla de los precursores mediante el uso de la impregnación húmeda.

- La actividad de los catalizadores Fe/N/C se ve fuertemente afectada por el pH del electrolito. Estos catalizadores son más activos para la ORR en electrolitos alcalinos que en electrolitos ácidos. Sin embargo, el efecto del contraión es despreciable en todos (ácido y alcalino) los electrolitos estudiados.

- El uso de tratamientos ácidos durante la síntesis de los catalizadores Fe/N/C, para eliminar las fases no estables de Fe obtenidas después de la etapa de pirolisis, disminuye la actividad final de los catalizadores en la ORR. Este efecto se produce por la fuerte adsorción de aniones (aniones sulfatos, cuando se usa ácido sulfúrico para el tratamiento ácido) en los centros activos. La actividad puede recuperarse parcialmente después de un tratamiento térmico a una temperatura de al menos 400 ^{o}C.

- Los catalizadores basados en Fe/N/C preparados con soportes de grafeno o CNT presentan una alta resistencia a la corrosión. Tanto los catalizadores Fe/N/G y Fe/N/CNT mostraron una gran durabilidad después de 3000 ciclos consecutivos hasta un potencial de 1.0 V y el catalizador Fe/N/G presenta una excelente estabilidad incluso después de someterlo a un severo test de degradación consistente en 3000 ciclos consecutivos hasta un potencial de 1.4 V.

Chapter 5

Practical applications of catalysts Fe/N/G

5.1 Activity study in anion exchange membrane fuel cell

The best Fe/N/C catalyst prepared during this thesis has been used as cathode catalyst in an anion exchange membrane fuel cell (AEMFC) feed with ethanol in the anode and pure O_2 in the cathode. Studies with this class of catalysts as cathode in direct alcohol (ethanol) AEMFC have been conducted hitherto. These studies show a possible approach to a real application of this new generation of catalysts.

5.1.1 Preparation of the membrane electrode assembly (MEA)

For the construction of the MEA, the anode and cathode electrodes were placed on both sides of the anion exchange membrane. The alkaline polymer membrane is based on a polybenzimidazole material (M40 Dapozol, Danish Power System) doped in a 6 M solution of KOH during 5 days. The electrodes are formed by a gas diffusion layer of carbon cloth (ELAT GDL-LT 1200W) where the catalyst layer is sprayed by means of an ink which is prepared by ultrasonically dispersing the catalyst in a solution of isopropyl, water and 5 wt.% of Nafion. In particular, the inks used in this study were prepared with a catalyst content of 1.3 mgPt·cm^{-2} for a PtRu/C 45 wt.% (30% Pt - 15% Ru, Johnson Matthey) in the anode and 2.5 mgcat·cm^{-2} of

Pt/40 wt.% (Johnson Matthey) or 5 mgcat·cm^{-2} of Fe/N/C in the cathode. The catalysts are suspended in a solution of 150 μL of Milli-Q water, 380 μL of isopropyl and 5 wt.% of Nafion. The amount of Nafion used is optimized according to the Eq. 5.1, because a high amount of Nafion results in an increment in the resistance of the electrodes as a consequence lower performance of the fuel cell.

$$0.55 = \frac{mg_{catalyst}}{mg_{catalyst} + mg_{Nafion5\%}} \tag{5.1}$$

After an ultrasonically dispersion of the catalysts in the solution by the use of an ultrasonic probe sonicator (UP100H, Heilscher), the ink was sprayed on the gas diffusion layer. The carbon cloth has one side covered by a fine carbon microporous layer treated with PTFE, where the catalyst ink is sprayed. The carbon microporous layer favoured the absorption of the catalyst ink resulting in a more homogeneous catalyst layer. The other side of gas diffusion layer allows a good management of the water formed in the cathode side and the humidity of the membrane, favouring the evacuation of the excess water.

The assembly of the membrane and the electrodes is made by a hydraulic press between two metal plates with cylindrical resistors inside and connected to a temperature control. The pressing is done at $5 \cdot 105$ Pa, rising the temperature up to 100 °C for 2 min. The final MEA is showed in Figure 5.1.

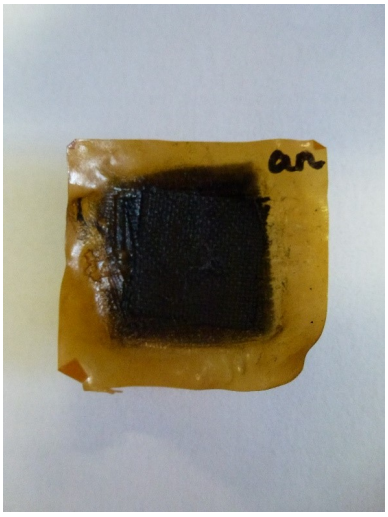

Figure 5.1: Membrane electrode assemble after assembly.

5.1.2 Electrochemical performance of Fe/N/G-based cathode in direct ethanol alkaline membrane fuel cell

The electrochemical tests consist on recording polarization curves and obtaining the corresponding power curves of the fuel cell. Polarization curves were collected by a linear voltammetry sweep, from the open circuit potential (OCP) to the corresponding potential (close to the short-circuit potential) by applying different electric currents to the system. From the measurements of the potential vs. current, it is possible calculate the power curve ($P = V \cdot I$). The data obtained provide useful information about power generation capacity of the fuel cell.

The electrochemical tests were performed with a computer controlled Autolab Pgstat 302N potentiostat/galvanostat and the experimental set up is a fuel cell provided by Electrochem Inc. controlled in a FCTS (Arbin) (Figure 5.2) by using the software MITS Pro. The working electrode (WE) was connected to the cathode of the fuel cell and the reference electrode (RE) and counter electrode (CE) were connected to the anode. The fuel cell is fed by 1 mL min^{-1} flow of 2 M ethanol/ 2 M KOH to the anode and 200 mL min^{-1} O_2 (P_{O_2} = 3 bar) to the cathode. The temperature of operation is 90 ^{o}C. Previously to the polarization curves, the MEA is activated by subjecting the system to several polarization curves previous to the measurement, activating the MEA at high currents close to the short-circuit in order to produce water capable to humidify the MEA. Once the conditioning polarization curves are reproducible, the electrochemical test were performance at 10 mV·s^{-1}.

As thoroughly discussed throughout this work, the main aim of the thesis was to obtain an active and durable non-precious metal based catalyst for the ORR that can replace Pt-based catalysts usage in fuel cells. In this work, the best results measured in an electrochemical cell for the NPMCs studied were obtained with the electrocatalyst derived from FePhC/Urea/Graphene and identified by Fe/N/G, prepared according to the work presented in **paper VI**.

The high activity and durability showed by the Fe/N/G catalyst in alkaline electrolyte added to the tolerance of this kind of catalysts to the alcohol crossover, make this electrocatalyst an ideal candidate for its use as cathode catalysts in direct ethanol AEMFCs.

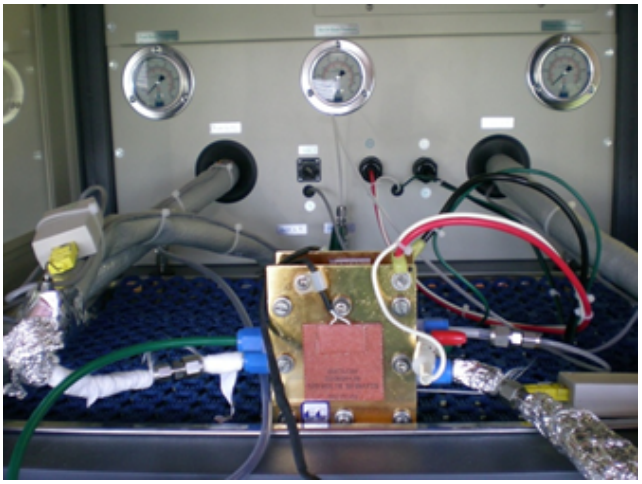

Figure 5.2: Set-up of fuel cell in the fuel cell test station (FCTS) provided by Arbin.

The polarization and power density curves recorded with Fe/N/C as cathode and PtRu/C and anode are shown in Figure 5.3. For the sake of comparison, the curves obtained with a benchmark Pt/C catalysts (2.5 mgPt/cm^{-2}) at the cathode are also shown.

As observed, the polarization curves obtained with Fe/N/C or Pt/C cathodes show similar profiles. Thus, open circuit voltages, OCP, of 0.85 V and 0.86 are recorded by using Fe/N/G or Pt/C, respectively, as cathodes. Nevertheless, from potentials below 0.6 V the power density is slightly superior for the Pt/C cathode. The peak power density for Fe/N/G is 80 mW·cm^{-2} compared with 90 mW·cm^{-2} for Pt/C. This close performance of Fe/N/G cathode compared to Pt/C was achieved only with two-fold amount of Fe/N/G catalyst with respect to that of Pt/C. This result emphasizes the possibility of replacing Pt/C catalysts by Fe/N/C-based catalysts for the direct ethanol AEMFCs, since the amount of catalyst could be increased without economic consequences.

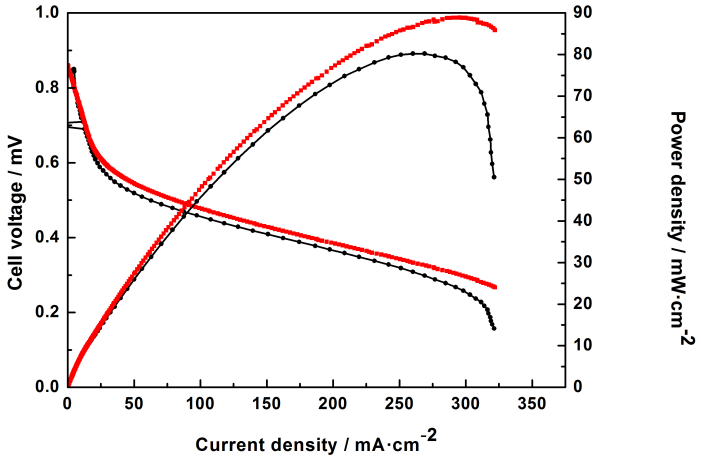

Figure 5.3: Polarization and power curves for MEAs prepared with Fe/N/G (black) and Pt/C (red) Pas cathodes and PtRu/C as anode in both MEAs.The fuel cell is fed by 1 mL min^{-1} flow of 2 M ethanol/ 2 M KOH to the anode and 200 mL min^{-1} O_2 (PO_2 = 3 bar) to the cathode. The temperature of operation is 90 °C